SHM-BASED SEISMIC PROGRESSIVE COLLAPSE ANALYSIS OF RC BRIDGE STRUCTURES

ZHENG YUE

Ph.D

The Hong Kong Polytechnic University

2015

The Hong Kong Polytechnic University

Department of Civil and Environmental Engineering

SHM-BASED SEISMIC PROGRESSIVE COLLAPSE ANALYSIS OF RC BRIDGE STRUCTURES

ZHENG YUE

A thesis submitted in partial fulfillment of the requirement for the Degree of **Doctor of Philosophy**

May 2015

CERTIFICATE OF ORIGINALITY

I hereby declare that this dissertation entitled "*SHM-based Seismic Progressive Collapse Analysis of RC Bridge Structures*" is my own work and that, to the best of my knowledge and belief, it reproduces no material previously published or written, nor material that has been accepted for the award of any other degree or diploma, except where due acknowledgement has been made in the text.

_______________________________ (Signed)

ZHENG YUE (Name of student)

To my big family

for their love and support

ABSTRACT

As one of the most damaging natural disasters, strong earthquakes often cause numerous structures to collapse and many people to die, which were reflected over again in recent Wenchuan Earthquake in 2008, Tohoku Earthquake in 2011, and Nepal Earthquake in 2015. To prevent buildings from collapse when they are subjected to strong earthquakes, the dynamic collapse of reinforced concrete (RC) building structures has been investigated actively and extensively, in which the finite element (FE)-method-based collapse analysis of RC building structures is an effective method. However, all the current FE-method-based seismic collapse analyses are based on the removal of entire element, but the actual seismic collapse of a structure often starts from the failure of an element at some degree-of-freedoms (DOFs). The removal of an element without the failure at all its DOFs may lead to false structural collapse. More importantly, the current FE-method-based collapse analysis methods contain many uncertainties. The time-dependent compressive strength of concrete, the confinement effect of core concrete due to the stirrup, the creeping and shrinking effects of concrete, the strength enhancement effect of the reinforcement embedding in the concrete, and the existing damage in concrete and reinforcement due to previous earthquakes, among others, cannot be fully or partially considered in the current collapse analyses, which again may produce false structural collapse.

On the other hand, as a cutting-edge technology, structure health monitoring (SHM) systems have been installed in some important buildings and bridges to

monitor their functionality, safety, and integrity with the ultimate goal of preventing the buildings and bridges from collapse. Nevertheless, there are seldom studies on how to utilize the information recorded by a SHM system to eliminate the uncertainties existing in the current collapse analysis method and provide an evolutionary and accurate collapse analysis method including collapse prognosis.

In view of the problems outlined above, this thesis aims at developing a SHM-based seismic collapse analysis (prognosis) method for RC structures under earthquake excitation. In consideration that the existing studies on RC bridge structures are much less than RC building structures and the collapse mechanism of RC bridge structures may be very different from that of RC building structures, this thesis focuses on seismic collapse analysis of RC bridge structures.

A refined collapse analysis method for RC structures considering the DOF release other than the element removal is first proposed in this thesis. By considering the DOF release, the catenary effect of RC beams and the effect of axial force on RC columns can be considered. Three numerical case studies were performed to examine the feasibility and accuracy of the proposed DOF release method. The numerical results of the collapse analysis of a two-span RC continuous beam with its two ends fixed under a concentrated static load was first compared with the experimental results. The result comparisons show that the refined method gives a better agreement with the experimental results compared with the traditional element removal method. The refined dynamic collapse analysis method was then applied to a two-story RC frame structure to demonstrate the entire progress of dynamic collapse. The numerical results demonstrate again that the refined method gives more reasonable collapse results by taking the catenary effect into account than the traditional element removal method. Finally, a two-span continuous RC bridge with a two-column pier at its middle was taken as an example to demonstrate the applicability of the refined method to RC bridge structures. The results show that the collapse of the RC columns does not occur immediately after the DOFs associated with bending moment and shear force of the two columns are released, and that the final collapse of the two columns is due to excessive axial loads. This failure mode could not be predicted by the traditional element removal method. Therefore, the refined method based on DOF release is preferable for the collapse analysis of RC structures including RC bridge structures.

A 1:12 scaled RC cable-stayed bridge model was then elaborately designed and constructed to experimentally study the seismic collapse of the RC bridge that was not designed for the seismic resistance and to provide measurement data for implementing the proposed SHM-based collapse analysis method. A comprehensive measurement (SHM) system was designed and installed on the RC bridge to record both the global responses and local responses of the bridge. Before the shaking table tests, each cable force of the as-built RC bridge was measured by the frequency method to ensure that the bridge configuration meets the design requirement. The dynamic characteristic test was then conducted to gain an insight of the properties of the bridge. Finally, a series of earthquake tests, which include small earthquake, moderate earthquake, large earthquake and collapse earthquake in terms of their peak ground accelerations (PGA) and spectra, were conducted. It was observed from the four shake table tests that: (1)

the RC bridge performed linearly and elastically under the small earthquake excitation and the RC bridge kept intact conditions after the small earthquake excitation; (2) the RC bridge performed slightly nonlinearly and plastically under the moderate earthquake excitation. The concrete in the failure-vulnerable components cracked slightly; (3) the RC bridge performed severely nonlinearly and plastically under the large earthquake excitation. The concrete in the failure-vulnerable components crushed severely and the reinforcement in the failure-vulnerable components yielded severely; and (4) the RC bridge partially collapsed under the collapse earthquake excitation. The concrete in the failure-vulnerable components crushed severely and the reinforcement in the failure-vulnerable components yielded severely. The measured data acquired from the SHM system together with the dynamic characteristics provide plentiful information for the subsequent linear model updating of the intact bridge, the nonlinear model updating of the damaged bridge, and collapse prognosis for the damaged bridge, respectively.

A 3-D FE model of the physical RC cable-stayed bridge subject to shake table tests is established for conducting seismic collapse analysis. To get an accurate FE model of the bridge for further collapse prognosis, a linear model updating strategy using two types of objective functions, the objective function based on natural frequencies and the objective function based on acceleration and strain responses, is proposed with the purpose of updating key parameters of the intact bridge so as to eliminate the uncertainties related to the linear RC bridge structure. A total of 12 key parameters are identified by virtue of sensitivity-based FE model analyses and updated using natural frequencies as the objective function. Three accelerometers and three strain gauges are selected as the key sensor locations and their responses are used for the further model updating in the time domain. Various seismic response time histories computed using the two different updating methods are compared with the measured responses. The comparison results indicate that the two objective functions both can improve the quality of the FE model. The second objective function not only can be used as an alternate of the first one for nonlinear model updating but also provides better updating results than the first objective function.

A nonlinear model updating method by using the measured acceleration responses and reinforcement strains of the RC cable-stayed bridge in the time domain is proposed to update the envelop curves of the materials of the nonlinear bridge without knowing its previous loading history. In the nonlinear model updating, the degradations of both unloading stiffness and reloading stiffness are accomplished in addition to the strength degradation. A total of 58 key parameters divided into the five groups are introduced to be updated. The optimization objective function used in the time domain is the same as the one presented for the linear model updating. Three accelerometers and three strain gauges are selected as the key sensor locations and their responses are used for the nonlinear model updating. The updated 58 key parameters are used to configure the envelop curves of the materials of the bridge due to the previous earthquakes and these curves are then used to calculate the seismic responses of the bridge subject to current earthquake excitation. Various seismic response time histories computed using the nonlinear updated results are compared with the measured responses. The comparison results indicate that the updated results of the key parameters are correct and the nonlinear model updating method is feasible.

To further verify the SHM-based seismic collapse prognosis method, it is applied to the RC bridge subject to the collapse test. Since the seismic collapse prognosis of a structure shall be carried out based on the current damage conditions of the structure, the SHM-based nonlinear model updating is necessary to find out the current damage conditions of the structure. In this regard, the 58 key parameters of the RC bridge were updated by considering the bridge subject to the latest earthquake ground motion and using the nonlinear model updating method proposed. The results show that the values of the most updated parameters of the bridge under the latest large earthquake excitation became much smaller compared with those identified for the bridge subject to a moderate earthquake excitation. The values/thresholds of the failure criteria of the four zero-length failure elements of the RC bridge were also determined based on the current damaged conditions and compared with those from the undamaged conditions. The comparative results show that the values/ thresholds of the failure criteria of the four zero-length failure elements of the RC bridge determined based on the current damaged conditions are very different from those based on the undamaged conditions. The collapse prognosis of the RC bridge subject to two future earthquake ground excitations were finally performed base on the updated FE model of the bridge to find out which earthquake will cause the true bridge collapse. The computed results showed that the RC bridge did not collapse when it was subjected to the first future earthquake excitation of relatively small intensity. The computed results showed that when the bridge was subjected to the second earthquake excitation of relatively large intensity, the RC southwest pier, as one of the failure-vulnerable component, triggered the flexure failure at 3.133 second of the earthquake excitation and it was separated from the RC bridge structure. The other three failure-vulnerable components experienced severe damage but not failed. A series of computed seismic responses such as acceleration, strain and reaction force of the RC bridge subject to the second earthquake excitation were compared with the shake table test results recorded by the SHM system installed on the bridge. The comparison results showed that the computed results and collapse process are compatible with the test results recorded by the SHM system. The SHM-based collapse prognosis proposed in this chapter is feasible and effective.

An ideal SHM system installed on a bridge is useful in monitoring the loading conditions, updating the FE model, assessing the linear and nonlinear performance, and making collapse prognosis of the bridge. Two sets of SHM systems for the prototype RC bridge are established using two different methods. These systems have demonstrated significantly different results in terms of sensor location and sensor number. The SHM system that uses the multi-sensor placement method includes 16 strain gauges and 12 accelerometers, whereas the proposed SHM system includes 24 strain gauges and 10 accelerometers. The sensors of the strain gauge in the proposed SHM system are all placed in the failure-vulnerable components, such as the tower legs beneath the girder and the two south piers, whereas only several strain gauges in the current SHM system are placed on the girder, transverse beam, and stay cable.

These differences can be attributed to the fact that the current SHM system is utilized to assess the linear performance of the bridge under service loadings, whereas the proposed SHM system is used to make a collapse prognosis of the RC bridge under seismic loadings.

To demonstrate the difference of the current collapse analysis method and the proposed SHM-based collapse analysis method, an SHM-based collapse prognosis of the earthquake-damaged bridge was conducted. In reality, the damage condition of the bridge can be determined using the nonlinear model updating technique in Chapter 6 and the information that is acquired from the proposed SHM system installed on the bridge. In this way, the uncertainties in the FE model of the bridge can be eliminated and provide a critical support for the collapse prognosis. In this study, the damaged state was specified by conducting a nonlinear seismic analysis for absence of SHM system. For comparison, a collapse analysis of the prototype RC bridge is also conducted using the current collapse analysis method. The entire collapse processes from the two collapse analysis/prognosis methods are significantly different: (1) the seismic intensity used for the current collapse analysis method is larger than that used for the proposed SHM-based collapse prognosis method; and (2) the proposed method has detected a partial collapse in the southwest pier, whereas the current collapse analysis method has detected a partial collapse in the southeast pier. Therefore, the proposed SHM-based collapse prognosis is a promising method to prognosticate the behavior of the existing RC bridges under future earthquakes, whereas the current collapse analysis can be only used for the bridge at design stage.

PUBLICATIONS

Journal papers

1. L. Hu, Y.L. Xu, and **Y. Zheng**, Conditional Simulation of Spatially Variable Seismic Ground Motions Based on Evolutionary Spectra, *Earthquake Engineering and Structural Dynamics*, 41(15): 2125-2139, 2012.

2. Qi Li, You-lin Xu, **Yue Zheng**, An-xin Guo, Kai-yuen Wong and Yong Xia. SHM-Based F-AHP Bridge Rating System with Application to Tsing Ma Bridge, *Frontiers of Architecture and Civil Engineering in China*, 5(4): 465-478, 2011.

3. **Y. Zheng**, Y.L. Xu, and Q. Gu. Refined Seismic Collapse Analysis of RC Structures, *Computers and Structures*, submitted.

4. Y. L. Xu, **Y. Zheng** and Q. Gu. SHM-Base Seismic Collapse Analysis of a RC Cable-Stayed Bridge, *Earthquake Engineering and Structural Dynamics*, submitted.

5. **Y. Zheng**, Y. L. Xu and S. Zhan. Seismic Collapse Tests of a RC Cable-Stayed Bridge under Earthquake Excitations, *Engineering Structures*, submitted.

Conference papers

1. Y.L. Xu, **Y. Zheng**, Q. Li, K.Y. Wong, Y. Xia, and A.X. Guo. SHM-Based Bridge Rating System for Long-Span Cable-Supported Bridge, *14th Asia Pacific Vibration Conference*, 5-8 December 2011, Hong Kong, China.

2. **Y. Zheng**, Y.L. Xu and L. Hu. Seismic Response of Analysis of Long-Span Cable-Stayed Bridge Subjected to Multi-Support Excitation, *5th International Symposium on Environmental Vibration*, 20-21, October, 2011, Chengdu, China. (Invited Report)

ACKNOWLEDGEMENTS

I would like to express my sincere gratitude to Prof. You-Lin Xu, my chief supervisor, for his excellent guidance, invaluable advice, high responsibility, and deep insight in this scientific research. I sincerely appreciate his efforts to provide me with the unique opportunity to pursue my PhD study, which will definitely shape my research career in years to come.

I also own a special debt of gratitude to Associate Prof. Sheng Zhan for his invaluable help in the shake table tests. Without his help, I would not be able to complete my PhD project.

High tribute shall be paid to Prof. Wei-zhen Chen and Prof. Wan-cheng Yuan from Tongji University and Associate Prof. Lin Lu from The Hong Kong Polytechnic University for their constant encouragements during the five-year course of my PhD study (2010-2015).

Great acknowledgment is made to the three-year scholarship (2010-2013) from a collaborative research project between The Hong Kong Polytechnic University and Hong Kong Highways Department on the development of structural health rating and evaluation system for the Stonecutters Bridge in Hong Kong.

Special thanks should go to the staff members in the Department of Civil and Environmental Engineering, Library, Research Office, and Finance Office in The Hong Kong Polytechnic University for their kindly help.

I am greatly indebted to Prof. Quan Gu from Xiamen University, China, for his selfishness help in the numerical simulation. Also, I am grateful to Prof. Bo Chen from Wuhan University of Technology, China, for his immediate help and encouragements.

I own much to my friends and colleagues, Dr. Dan Zhong, Dr. Gui-ping Bi, Dr. Song-ye, Zhu, Dr. Yong Xia, Dr. Hua-fu Pei, Dr. Yong-fang Rao, Dr. Juan Zhang, Dr. Zhi-wei Chen, Dr. Xiao-hua Zhang, Dr. Xian-ting Du, Dr. Liang Hu, Dr. Wen-feng Huang, Dr. Qin Huang, Ms. Ying-jie Jin, Mr. Feng-yang Wang, Dr. Bin Wang, Dr. Wen-ai Shen, Dr. Qing Zhu, Dr. Wen-yu He, Mr. Jin-hua Lin, Mr. Chao-dong Zhang, Ms. Yi-xin Peng, Mr. Xiao-liang Meng, Dr. Xiang Xiao, Dr. Jia He, Mr. Jian-fu Lin, Mr. Rong-pan Hu, Dr. Ling Ding, Mr. Wei-li Luo, Mr. Hai-quan Jing, Mr. Yi Yang, Dr. Bin Zhang and Dr. Kun Liu for their valuable suggestions and critiques which are of importance in making the thesis a reality.

Last but not the least, my gratitude extends to my farther, deceased mother, deceased uncle, my brothers and sister, my wife and two daughters, as well as my parents-in-law. All of them have, over the past six years, bestowed on me their love and support without which the completion of my PhD study is impossible.

CONTENT

LIST OF FIGURES

LIST OF TABLES

CHAPTER 1

INTRODUCTION

1.1 Research Motivation

As one of the most damaging natural disasters, strong earthquakes often cause numerous RC bridges to collapse and many people to die, which were reflected over again in recent Northridge earthquake in 1994, Kobe earthquake in1995, Chi-Chi earthquake in 1999, Wenchuan Earthquake in 2008, Tohoku Earthquake in 2011, and Nepal Earthquake in 2015. The painful lessons, learned from the severely damaged or collapsed RC bridges due to strong earthquakes, emphasize that it is imperative to conduct seismic collapse analysis for gaining insight into the collapse mechanism of RC bridges, assessing the present damage conditions of the bridges, and taking effective measures to prevent them from collapse.

A significant amount of research has been performed on the collapse analysis of civil structures and relevant research has accelerated in recent years (Administration 2003; DoD 2009; Elwood and Moehle 2003; Ghannoum 2007; GSA 2003; Kim et al. 2009; Kim et al. 2012; Kim et al. 2012; Lignos et al. 2011; Lu et al. 2013; Sagiroglu 2012; Sasani 2008; Sasani et al. 2007; Talaat and Mosalam 2009; Wu et al. 2009). To assess the resistant capacity against progressive collapse for the building structures, the US General Services Administration (GSA 2003) and the US Department of Defence (DoD 2009) issued guidelines, respectively. In the two design codes, a simple approach, named alternate path method (APM), is presented for engineers to conduct the progressive collapse analysis of new or existing structures by the nominal removal of major supporting structural components. Actually, the APM has inherent shortcomings: (1) it is based on the system response after several types of specified critical elements are removed rather than it detects the initial components that trigger the damage and collapse; (2) the dynamic effect could not or only roughly be taken into account in the progressive collapse analysis, and therefore it is not a conservative approach to evaluate the risk of collapse for structures; and (3) there is a major obstacle for engineers to use APM confidently because of a lack of detailed information in the aforementioned guidelines (Marjanishvili 2004). In brief, all the current collapse analysis of reinforced concrete (RC) structures is based on the removal of element one by one rather than the release of degree of freedoms (DOFs) one by one (Lu et al. 2013; Talaat and Mosalam 2009). Careful observations of test results (Elwood and Moehle 2003; Sagiroglu 2012) reveal that the collapse of a RC structure often starts from the failure of an element at some DOFs and that the removal of the element without the failure at all the DOFs may lead to false structural collapse. Therefore, it is a top priority to find a rigorous dynamic collapse analysis/prognosis method for the structure based on the release of DOFs one by one. Besides, the current collapse analysis method for RC structures is established based on a series of assumptions (Lu et al. 2013) and it can only be used to conduct collapse analysis for structures at design stage, which may yield incorrect collapse analysis results for as-built RC structures (Sasani 2008; Sasani and Sagiroglu 2008). The assumptions involving in the current collapse analysis method mainly include: (1) the strength of reinforcement can be increased if it is embedded in concrete, but this strengthening effect can only be considered empirically; (2) the internal forces in different components of a RC structure may redistribute because of different construction procedures and/or the shrinking and creeping effects of concrete, but such effects cannot be taken into consideration in the current collapse analysis; (3) a RC structure may already suffer from some damage during its service time and its material properties are no longer linear and elastic, but such damaged conditions cannot be estimated and taken into account in the current collapse analysis. Therefore, the current collapse analysis method needs to be improved and it is an urgent task to propose a rigorous collapse analysis method considering the explicit DOF release one by one for the as-built RC structures subject to future earthquake, which is, however, scarcely explored.

Many studies have conducted various seismic collapse tests on building structures. However, almost all the collapse tests focused on RC building structures, and experimental investigations on seismic collapse mechanism of RC bridges are very limited. The structural systems of building and bridge structures for bearing external loadings are significantly different. For example, the bearing conditions in bridge structures are more complex than those in buildings; but the redundancy of building structures are larger than that of bridges.

In view of the above, a practical framework to conduct accurate seismic collapse analysis/prognosis for structures based on the concept of DOF release and its implementation in a soft package are required. Furthermore, how to accurately evaluate the present conditions of RC bridges are essential for further seismic collapse analysis/prognosis. Otherwise, the collapse analysis/prognosis of the bridge with inaccurate material properties will result in unreliable failure mode of the bridge. Fortunately, the SHM systems installed on important bridges can provide useful information for us to eliminate the uncertainties and accurately assess the present conditions of the bridges by virtue of model updating techniques. Therefore, new linear and nonlinear FE model updating techniques in the time domain that update the FE models to reflect the current conditions of the existing RC structures are required for further accurate seismic collapse analysis.

The traditional linear model updating method using either the dynamic characteristics or the static strain/stress/displacement responses of structures as the updating objectives (Brownjohn and Xia 2000; Cantieni 1996; Catbas and Aktan 2002; Catbas et al. 2007; Chajes et al. 1997; Enevoldsen et al. 2002; Jaishi and Ren 2005; Pavic et al. 1999; Schlune et al. 2009; Wong 2004) is not the best choice to obtain an accurate FE model for the structure subject to dynamic loadings. Bridge structures subject to seismic loadings that select the transit responses of strain or acceleration in time domain as the updating objectives may be a wise solution for the linear model updating, but research in this area is limit.

The material nonlinearity in civil structures can be assumedly represented by hysteretic material models. Therefore, the issue of nonlinear model updating a time-varying system is changed to the issue of nonlinear model updating time-varying parameters of hysteretic material models. Asgarieh et al. (2014) and

Kunnath et al. (1997) proposed an approximate nonlinear relationship between hysteretic model parameters and force-deformation hysteretic curve to identify the damage in the civil structures. A new nonlinear model updating method in the frequency domain is proposed for a RC shear wall subject to low ambient vibration (Song et al. 2012; Song et al. 2008). The main contribution is that a relationship between damage parameters employed in numerical simulation and FE model stiffness at the zero-load crossings was thus presented. However, most of these nonlinear model updating applications were demonstrated by single-degree-freedom or simple multi-degree-freedom numerical cases. Therefore, it is urgent to propose a new nonlinear model updating method for real-world civil structures (including bridge structures).

In view of the problems outlined, a practical framework, implemented with new SHM system design, linear and nonlinear FE model updating techniques in the time domain and rigorous seismic collapse analysis method, is required for accurate SHM-based collapse analysis of the existing RC bridge structures.

1.2 Research Objectives

This thesis focuses on the SHM-based seismic collapse analysis of RC bridge structures under earthquake excitations with the following major objectives:

1. To propose a rigorous progressive collapse analysis method based on the concept of DOFs release for RC structures; to implement the refined collapse analysis method in an open software of OpenSees (McKenna et al. 2007); and to present a series of rules for DOFs release corresponding to different failure modes of both RC beam

and column.

2. To design and construct a 1/12 scaled RC bridge for conducting seismic collapse tests on a shake table; to install a sophisticated SHM system on the bridge to record the base seismic loadings of the bridge; to record responses of strain and acceleration at critical positions for conducting linear and nonlinear model updating of the FE model of the bridge; and to record responses of strain, acceleration and reaction forces for verifying the proposed model updating methods.
3. To establish a nonlinear fiber-element FE model of the bridge in OpenSees (McKenna et al. 2007); to select key parameters for model updating using sensitivity method; to perform linear model updating of the bridge using two updating objective functions in the frequency and time domains, respectively; to verify the correctness and feasibility of the proposed linear updating method by partially measured responses of strain, acceleration and reaction forces in the time domain; and to obtain an accurate FE model of the intact bridge based on the linear model updating method.
4. To present the evolution principles for the envelop curves of both concrete and reinforcement together with the degradation rules of stiffness; to conduct the nonlinear model updating of the bridge under moderate earthquake using the responses of strain and acceleration at critical positions in the time domain as the updating objectives; to verify the correctness and feasibility of the nonlinear model updating method by partially measured responses of strain, acceleration and reaction forces in the time domain; and to obtain an accurate FE model of the

damaged bridge based on the nonlinear model updating method.

5. To conduct the nonlinear model updating of the bridge under large earthquake; to determine the failure criteria of the four failure zero-length elements based on the present damage conditions of the RC bridge; to conduct seismic collapse analysis of the damaged bridge; and to verify the correctness and feasibility of the seismic collapse analysis method by partially measured responses of strain, acceleration and reaction forces in the time domain.
6. To establish a three dimensional FE model of the prototype RC stay-cable bridge for the SHM system design and the seismic collapse analysis/prognosis; to design two set of SHM systems according to two different methods, respectively; to conduct seismic collapse analysis of the prototype bridge using the current collapse analysis method; to conduct seismic collapse analysis of the prototype bridge using the proposed SHM-based collapse analysis method; and to declare the importance of the proposed SHM-based collapse analysis for existing RC bridges.

1.3 Assumptions and Limitations

The development and application of the seismic collapse analysis framework proposed by this study are subjected to the following assumptions and limitations:

1. It is assumed that the release sequence of DOFs in a damaged element of a FE model of a RC structure accords to a series of rules related to different failure modes of RC beams and columns.
2. The 1/12 scaled bridge was divided into three parts to cast at different time. The properties of the concrete are assumed as identical at each cast stage. The

properties of the same type of reinforcement are assumed as identical.

3. It is assumed that the conditions of the bearings in the 1/12 scaled bridge are ideal. The concrete experiences linear performance under small earthquake whereas the possibly slight nonlinearity is negligible.
4. The tensile strength of concrete is not considered in the FE models of both the 1/12 scaled bridge and the prototype bridge.
5. Four failure modes of RC structures are not discussed in this thesis: (1) the failure of a RC member is controlled by inadequate development length of lap-spliced reinforcement or straight/hooked bars along the beam span or column clear height; (2) the failure of a RC beam is controlled by inadequate embedment into the beam-column joint; (3) the RC column with axial load exceeds 0.7 times the nominal load strength at zero eccentricity; and (4) the failure of beam-column joints.
6. When the RC bridge subject to moderate, large and collapse earthquakes, the RC bridge is divided into five groups for convenient execution of nonlinear model updating. It is assumed that the material properties of concrete and reinforcement in each group are identical.
7. It is assumed that the reloading path is along a quadratic parabola of the damaged concrete that has experienced strength degradation.
8. For the limitation of the size of the shake table, the SHM-based seismic collapse test of the prototype RC bridge could not be conducted.
9. The damage conditions of the prototype bridge are specified before collapse for

demonstration of the numerically SHM-based seismic collapse method applying to a prototype bridge.

10. During the collapse process, the movement of rigid body, contact and collision of debris are not involved in the seismic collapse analysis/prognosis.

1.4 Outline of the Thesis

To achieve the aforementioned objectives, this thesis covers a variety of research topics elaborated in 9 chapters organized as follows:

Chapter 1 introduces the motivation for this study and states its objectives, assumptions and limitations.

Chapter 2 contains an extensive literature review on the relevant topics, including, first, the numerical collapse analysis on structures; then, the experimental collapse analysis on structures; third, the linear and nonlinear model updating techniques; and finally, the information of SHM system installed typical bridges as well as the SHM-based collapse prognosis.

Chapter 3 refines FEM-based collapse simulation by introducing the concept of DOF release. With the concept, an element removal (failure) is a natural consequence of time-varying release (failure) of all DOFs of the element one by one. The concept is implemented in OpenSees (McKenna et al. 2007). The test results of collapse analysis of a RC beam with two ends fixed under a concentrated static load are first used to demonstrate the advantages of DOF release over the traditional element removal. The rigorous collapse analysis method is then applied to a two-story reinforced concrete frame to demonstrate the collapse for a complicated RC frame structure. At last, a two-span continuous RC bridge with a two-column pier is taken as an example to demonstrate the applicability of the refined method to RC bridge structures, the seismic collapse of which is seldom investigated.

Chapter 4 describes a 1/12 scaled RC cable-stayed bridge constructed for seismic collapse tests on a shake table to examine the feasibility and correctness of the proposed SHM-based dynamic progressive collapse prognosis method. The scaled RC cable-stayed bridge model was built with reference to a real RC foot cable-stayed bridge located in an earthquake-prone zone. This chapter also introduces the design and constriction details of the RC bridge structure. A comprehensive SHM system was designed and installed on the bridge structure. A series of the shaking table tests was performed until the bridge structure partially collapsed. The shaking table tests were carried out in four stages in terms of four intensity levels of earthquake: small earthquake, moderate earthquake, large earthquake, and collapse earthquake. For the small earthquake test, the test data acquired from the SHM system will be used to update the FE model of the intact RC bridge through the linear model updating method discussed in Chapter 5. For the moderate earthquake test, the test data acquired from the SHM system will be used to update the FE model of the slightly damaged RC bridge through the nonlinear model updating method discussed in Chapter 6. For the large earthquake test, the tests data acquired from the SHM system will be used to update the FE model of the severely damaged RC bridge in Chapter 7. The updated FE model will then be assigned with the zero-length failure elements and the corresponding failure criteria which will be finally used for seismic collapse analysis and prognosis in Chapter 7. For the collapse earthquake test, the tests data acquired from the SHM system will be compared with the numerical results from the collapse prognosis to examine the feasibility and accuracy of the proposed collapse prognosis method in Chapter 7. Of course, in addition to the test data recorded for the subsequent analyses, the structural behavior and the collapse process of the RC bridge structure under four levels of earthquake excitations were clearly observed during the entire shaking table tests.

Chapter 5 aims to establish an accurate FE model and conduct a linear model updating of the RC cable-stayed bridge, investigated experimentally in Chapter 4, for seismic collapse analysis in OpenSees (McKenna et al. 2007). The characteristic FE model of the RC bridge structure for seismic collapse analysis is elaborately established accounting for not only material nonlinearity but also geometric nonlinearity. Besides, the zero-length elements with appropriate failure criteria are assigned at failure-vulnerable locations in the FE model to detect the potential failures. To ensure the accuracy of the FE model of the bridge structure, a two-stage model updating method (linear model updating and nonlinear model updating) are proposed in this study. The most recent linear model updating of RC structures is performed in the frequency domain, but in this study the linear model updating will be performed in both the frequency and time domains in consideration of the subsequent nonlinear model updating. Only the linear model updating is discussed in this chapter while the nonlinear model updating will be discussed in Chapter 6. In the linear model updating stage, twelve parameters are selected through sensitivity-based FE analyses and two different optimization objective functions are used. Measurement data acquired from the SHM system installed in the cable-stayed bridge model subject to small ground motion and presented in Chapter 4 are used for the linear model updating and for the validation of the proposed model updating method.

Chapter 6 discusses the evolution principles for the envelop curves of both concrete and reinforcement together with the degradation rules of stiffness. The preliminary nonlinear seismic analysis of the RC bridge subject to moderate earthquake will then be carried out using the updated linear FE model obtained in Chapter 5 as well as the initial envelop curves of the materials and the degradation rules of stiffness. Based on the calculated response magnitudes, the configurations and locations of the structural members, all the members are classified into five groups. Except for the group of linear members whose key parameters have been updated using the linear model updating method in Chapter 5, the key parameters of other groups of nonlinear members will be identified and updated. The nonlinear model updating will then conducted using the acceleration and strain responses at the critical locations decided in Chapter 5 as the optimization objectives to update the key parameters of the nonlinear elements. To confirm the correctness of the updated key parameters, the calculated seismic responses are compared with the so-called measured responses which are used in the model updating. Furthermore, the feasibility and accuracy of the proposed nonlinear model updating method is finally verified through the comparison between the predicted responses and the measured responses which are not used in the model updating.

Chapter 7 proposes a SHM-based seismic collapse analysis for not only RC building structures but also RC bridge structures. A nonlinear model updating analysis is first performed to identify the key parameters of the FE model of the RC cable-stayed bridge subjected to a large earthquake. The failure criteria for the zero-length failure elements are then determined based on the updated FE model and in terms of the provisions described in Chapter 3. Finally, a number of seismic collapse analyses are performed against a number of earthquake excitations of different intensity levels to find out which earthquake will finally cause the true collapse of the bridge. Such a seismic collapse analysis is also called the collapse prognosis of a RC structure.

Chapter 8 establishes a three dimensional FE model of the prototype RC stay-cable bridge for the SHM system design and the seismic collapse analysis/prognosis. Then, two set of SHM systems are designed according to two different methods, respectively. Finally, the current progressive collapse method is used to perform the collapse analysis of the prototype bridge. The proposed collapse prognosis method is subsequently demonstrated based on the prototype bridge with specified damage.

Chapter 9 summarizes the contributions, findings, and conclusions of this study. Limitations of thesis study are discussed and some recommendations for future study, provided.

CHAPTER 2

LITERATURE REVIEW

2.1 Numerical and Code Studies on Collapse of Structures

Progressive collapse is described as the spread of an initial local failure from element to element, eventually resulting in the collapse of an entire structure or a disproportional large part (ASCE 2010). Post-earthquake reconnaissance shows that a reinforced concrete (RC) structure without aseismic design in earthquake-prone regions is vulnerable to seismic collapse. In recent years, Wenchuan Earthquake (2008), Chile Earthquake (2010), Tohoku Earthquake (2011), and Nepal Earthquake (2015) all have caused heavy casualties and countless structure collapses. To gain an extensive insight into the collapse mechanism of structures so as to reduce structure collapses under earthquake, both numerical and experimental studies on the collapse of structures appeal to more and more administration institutes and researchers in the world.

2.1.1 Code studies on progressive collapse of building structures

To assess the resistant capacity against progressive collapse of building structures, the US General Services Administration and the US Department of Defense issued guidelines (GSA 2003; DoD 2009), respectively. In the two design codes, a simple approach, named alternate path method (APM), is presented to conduct the progressive collapse of new or existing structures by the nominal removal of major supporting structural components. The GSA method recommends that the middle column of the long side, middle column of the short side, and the corner column of the building at the ground floor be removed as the candidate components. It should be noted that the column is removed only one at a time. On the other hand, the DoD method recommends the same, but adds that each floor level should be considered. Four analytical methods of APM analyses are permitted by the two codes: linear static, nonlinear static, linear dynamic, and nonlinear dynamic.

In fact, the APM has inherent shortcomings: (1) it is based on the system response after several types of specified critical elements are removed rather than detects the initial components that trigger the damage and collapse; (2) the dynamic effect could not or only roughly consider the progressive collapse analysis, and therefore it is not a conservative approach to evaluate the risk of collapse for structures; and (3) there is a major obstacle for engineers to use APM confidently for lack of detailed information in the aforementioned guidelines (Marjanishvili 2004). Hence, it is necessary to propose a new accurate method that can automatically detect failure-vulnerable components for seismic collapse analysis of structures.

2.1.2 Progressive collapse analysis of structures using DEM

The discrete element method (DEM) suggested by Cundall (1971) as a promising numerical technique is widely used in soil and rock engineering. Conventionally, a set of point contacts, or edge-to-edge contacts are used to simulate the interaction between discrete blocks ignoring the continuous stress distribution throughout a contact surface. That is, deformable blocks may be discretized independently from their neighbors. The study results from many references (Alexandris et al. 2004; Azevedo 2003; Baggio and Trovalusci 2000; Lemos 2007; Papantonopoulos et al. 2002) indicating that application of the DEM to complex structures is still a challenge task for critical examination of modeling methodologies (e.g., the representation of the units, contact physical laws, fracture criteria). Moreover, it is unable to conduct collapse analysis for real RC structures. In this regards, a modified discrete element method (MDEM) for collapse analysis of RC structures by introducing the Iwashita's model (Iwashita and Hakuno 1988) is respectively proposed by Meguro and Hakuno (1988) and Meguro and Hakuno (1989). For concrete materials, the gravel in concrete was idealized as circular element and the mortar as nonlinear springs (pore-springs). The Mohr-Coulomb yielding rules were used as the failure criteria of a reinforced concrete. The RC structure can be discretized into very small elements respectively connected by pairs of spring elements (element-spring and pore-spring) in normal and tangential directions, as shown in Figure 2.1. Before the nonlinear pore-springs in the model fail, the model will behave as a continuous medium. Nevertheless, if the pore-springs fail, the model will become a perfect discrete body. In such a way, the EDEM can be employed to conduct collapse analysis of simple RC structures.

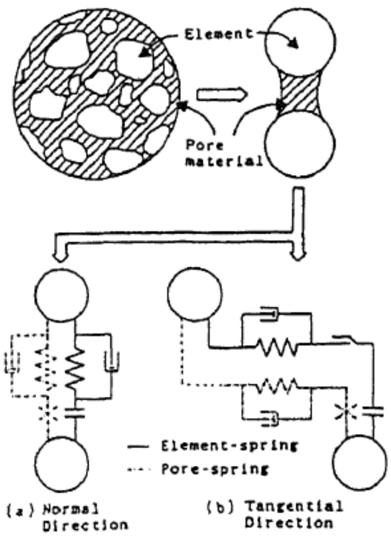

Figure 2.1 Modeling medium (Meguro and Hakuno 1989)

A multi-story RC frame and a continuous RC bridge using the EDEM was investigated by Hakuno (1996). He summarized several limitations of the EDEM to solve real RC structures: (1) enormous calculation time is required because explicit numerical integration is unstable unless the integration time step is very short; and (2) the effect of reinforcement in concrete cannot be directly considered, but equivalent values are assigned to the parameters of the pore-springs for failure criteria of reinforcement. Meguro and Tagel-Din (2001) point out that the EMED is unable to model the fracture performance accurately where cracks occur in many directions. In addition, the accuracy of the EMED in a small deformation range is less than that of the finite element (FE) method.

2.1.3 Collapse analysis of structures using AEM

To partially overcome the drawbacks of the EDEM aforementioned, an applied element method (AEM) is presented for collapse analysis of structures via the concept of discrete crack (Meguro and Tagel-Din 2001; Meguro and Tagel-Din 2002;

Tagel-Din and Meguro 2000; Tagel-Din and Meguro 2000; Tagel-Din and Rahman 2004). A structure is always meshed by an assembly of small discrete elements and each element is connected by pairs of normal and shear springs to transfer the normal and shear stresses, respectively. Constitutive laws of material are inevitably involved for conducting collapse analysis of RC structures. For reinforcement springs, reinforcing bars are modeled as bare bars for the envelope curve (Okamura and Maekawa 1991) while the model proposed by Ristic et al. (1986) is used for interior loops, as shown in Figure 2.1(a). The main advantage of this model is that it can take both the effects of partial unloading and Baushinger's effect. For normal concrete springs, the Mackawa model presented by Okamura and Maekawa (1991) is adopted, as shown in Figure 2.2(b). After reaching the peak compression stresses, stiffness is assumed as a minimum magnitude to avoid obtaining a singular stiffness matrix. For shear concrete springs, the model shown in Figure 2.2(c) is assumed. Before cracking, point stresses are assumed to be proportional to strains, and after cracking, stiffness is assumed as a minimum value to avoid yielding a singular stiffness matrix. In Figure 2.2(c), the redistributed value (RV) is used to account for the effects of friction and interlocking of concrete between two elements. Given the material models of concrete and reinforcement, the pairs of springs between two elements can be calculated at each analysis step. If the springs are subjected to compression, Mohr-Coulomb's failure criteria will be used for compression shear failure. When the springs trigger the compression shear failure, shear force is redistributed and shear stiffness is assumed to be zero in later increments. The pairs of springs will be removed if the failure criteria are triggered. A typical model of a RC structure for collapse analysis is established using AEM (Salem 2011), as shown in Figure 2.3. The AEM is able to capture the structure's performance during entire collapse by introducing a set of failure criteria.

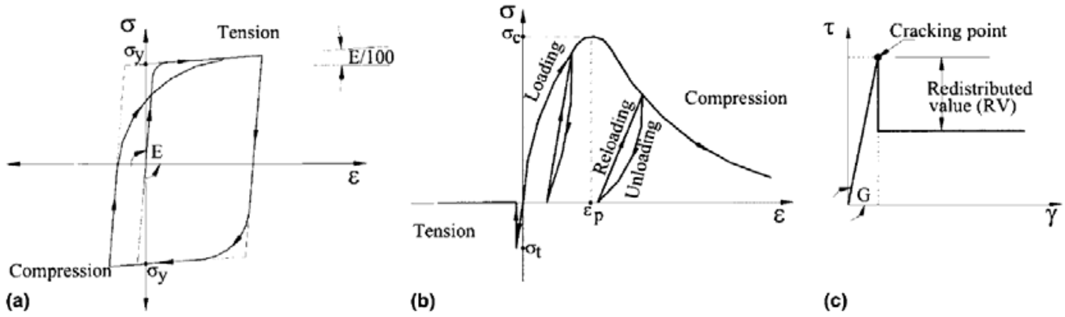

Figure 2.2 Material model for concrete and reinforcement

(a) Reinforcement (b) Concrete (c) Concrete (Shear direction)

(Meguro and Tagel-Din 2001)

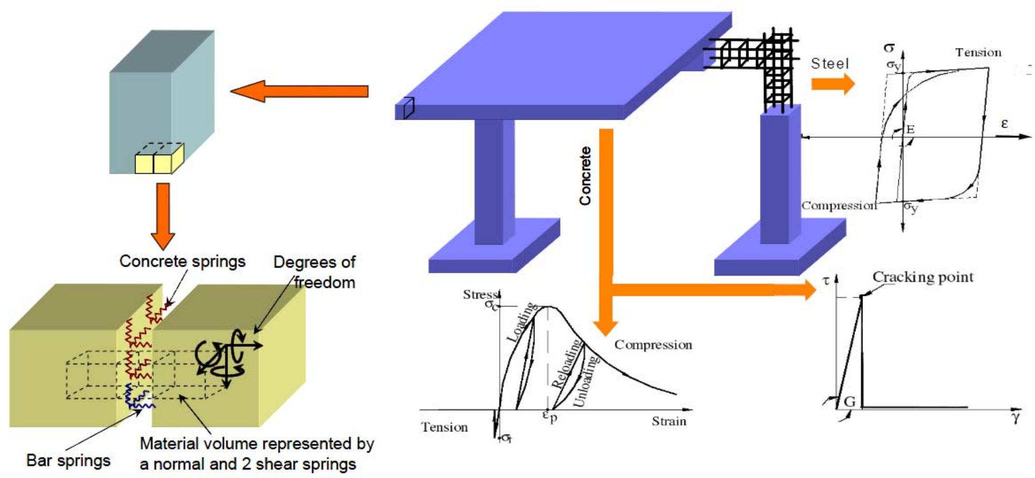

Figure 2.3 Sample analysis model using AEM (Salem 2011)

The response of Hotel San Diego was investigated using AEM by Sasani (2008) and Sasani and Sagiroglu (2008), respectively. It is a RC infilled-frame structure with removal of two exterior neighboring columns. The compressive strength of concrete was obtained from compression tests on two concrete samples. The yield and ultimate tensile strengths were also obtained from two reinforcing steel samples. The ultimate strain of the reinforcing steel was measured at 0.17. The structure resisted collapse with the measured and analytical maximum vertical displacements of 6.4 and 5.3 mm, respectively. Although the RC structure did not fail after removal of two columns, the analytical results indicate that the bi-directional Vierendeel (frame) action of transversal and longitudinal frames with the participation of infill walls is identified as the major mechanism for redistribution of loads in this structure. The collapse of a multi-story RC framed structure from soil scour under its foundation was investigated using AEM (Salem 2011). The collapse propagation of the building reappeared. To prevent collapse of the structures subjected to such extreme loading, three strengthening measures (floor beams, tie beams connecting footings and diagonal bracings) were proposed and investigated. The analysis results indicated that the tie beam played an effective role to enhance the redundancy of the structure. A three-dimensional (3D) discrete crack model based on AEM to conduct economic design for RC structures against collapse was presented by Salem et al. (2011). Firstly, a four-bay and three-story one-third scale RC frame was taken as the study objective and the applied element model of the frame was established. The analytical and experimental results of the force versus download displacement at the lower middle column were found to be well-matched. Then, an applied element model of a five-story RC building was established with 10885 elements. Two different cases of column removal were considered: the central column was removed in the first case and the two central columns were removed in the second case. According to the analytical result of the first case, the building did not collapse after the removal of the central column. In other words, the building was able to resist collapse. The analytical result also showed that a progressive collapse of about one-third of the building was observed. Nevertheless, the collapsed area was 142 m^2, lying within the allowable limits. A ten-story RC frame structure which is designed according to ACI 318-08 using AEM according to GSA code was investigated numerically (Helmy et al. 2009). A two-dimensional (2D) and 3D applied element models were used to conduct the progressive collapse analyses. Six different cases of column removal were considered: a corner column, an edge column, an edge shear wall, internal columns, an internal shear wall, and a corner shear wall. The results indicated that neglecting slabs in collapse analysis for both 2D and 3D frame analyses may lead to incorrect structural response and uneconomic design. Therefore, it suggested that the applied element model of building structure with slabs for collapse analysis might be an economical design. A RC bridge subjected to earthquake excitation using AEM was studied (Wibowo et al. 2009). The Kobe earthquake ground motions with 0.6g, 0.82g and 0.34g in X-, Y-, and Z- axes of the RC bridge were used as the seismic input. The analysis results showed that the cracks were firstly found at the connection between the deck and the pier, and then propagated through full width of the deck. Finally, the joint of the deck and the girder failed.

However, all the aforementioned applied element models used for collapse analysis consisted of numerous very small size elements and the explicit numerical integration for collapse analysis needs very small time step, making it difficult to deal with AEM in real-world civil structures.

2.1.4 Collapse analysis of structures using FE method

2.1.4.1 Failure modes

RC beams and columns are the main components of RC structures for force transfer, the primary failure modes of which are flexural failure, shear failure, and their combination as described below

- ***Flexure Failure Model***

It needs to be emphasized that the flexure failure model considers the interaction between the flexure and the axial forces. In the 1990's, the displacement consideration and capacity design for seismic design of RC structures, and developed the concept of performance-based seismic design were emphasized (Priestley 1997). It is essential and significant for RC components in structure to have ductility capacity in order to avoid brittle shear collapse during strong earthquakes.

At member (element) level, the flexural failure model can be interpreted by the ultimate limit state, which is sometimes taken to correspond to a critical physical event, such as fracture of confined reinforcement in a potential plastic hinge zone of a concrete member. Another common definition is related to a specified strength drop (20% is often used) from the maximum attained strength. A true ultimate limit state would refer to inability to carry imposed loads, such as gravity loads on a beam, or axial forces in a column.

At structure level, the flexural failure model can be interpreted by the survival limit state and it is ensured that during strong ground shaking considered feasible for the site, collapse of the structure should not take place. Although the survival limit state is of critical importance for seismic collapse analysis, its determination has drawn comparatively little attention (Priestley et al. 2007). Clearly, this limit is exceeded when the structure, unable to sustain any more gravity loads, collapses. This occurs when the gravity-load capacity is reduced below the level of existing gravity loads as a result of total shear failure of a critical column. A perfect hysteretic model is capable of representing all the important modes of deterioration that are observed in excremental studies. The monotonic test result shows that strength is "capped" and followed by a negative tangent stiffness. Ibarra et al. (2005) indicated that: (1) the cyclic hysteretic response indicates that the strength in large cycles deteriorates with the number and amplitude of cycles, even if the displacement associated with the strength cap is not reached; (2) It also indicates that strength deterioration occurs in the post-capping range; and (3) that the unloading stiffness may also deteriorate. Furthermore, it is observed that the reloading stiffness may deteriorate at an accelerated rate. Several hysteretic models have been developed to present the behavior of components exhibiting characteristics of the type aforementioned (Kunnath et al. 1991; Sivaselvan and Reinhorn 2000; Song and Pincheira 2000). Council (2000) introduced an envelope relation of force verse displacement for nonlinear dynamic analysis. The unloading and reloading properties should consider the significant stiffness and strength degradation characteristics. However, few models integrate all the important deterioration sources such as strength deterioration in the backbone curve (post-capping stiffness branch) and cyclic deterioration of strength and stiffness. Ibarra et al. (2005) developed a series of deteriorating models including bilinear, peak-oriented and pinched hysteretic systems and implemented in a computer program (Allahabadi and Powell 1988). Aviram et al. (2008) presented a backbone of the moment verse curvature for dynamic analysis, which can be used to consider the degradation of the stiffness after the ultimate state of the element section.

The non-deteriorate failure model had been reviewed for predicting the damage of reinforced concrete members (Chung et al. 1987; Williams and Sexsmith 1995). The indices are classified into cumulative and non-cumulative. Non-cumulative indices relate the state of damage to peak response quantities such as displacement, ductility, rotation, drift or other physical quantity like stiffness, but they do not account for cyclic loading effects. Cumulative indices include part of all of the loading histories to predict the capacity reduction due to cyclic repetitive loading. Such indices are computed cumulatively using various measures such as energy, total or plastic deformation, or a combination (Park and Ang 1985). Some other models attempt to predict low-cycle fatigue by applying the Coffin-Manson (Coffin and Wesley 1952), either directly to global member behavior or to the behavior of the underlying materials (Kunnath et al. 1997).

The non-deteriorating model counts cumulative damage and uses the count to indicate degree of damage and complete “failure” (usually identified by the counter taking on a value of 1.0). They do not consider that cumulative damage causes a decrease in strength and stiffness and as a result leads to an increase in deformations.

However, it is the loss of strength and the increase in deformation that will ultimately cause collapse of a structure.

- ***Flexure-Shear Failure Model***

The contribution of the axial force to the collapse of the structure is also considered in the flexure-shear failure model just like the flexure failure model. Although the displacement-based philosophy of design in civil engineering has been accepted by engineers in the past 20 years, lightly confined reinforced concrete beams and columns are found in use for the reconnaissance after earthquake (Wenchuan, 2008). As a matter of fact, there are approximately 40,000 non-ductile RC structures in California, USA. Although many non-ductile structures are built in small earthquake districts (such as Hong Kong), when the bridges in this area are subjected to some severe earthquake in future, brittle shear collapse will occur, resulting in a catastrophe because the columns are not in built with detailing seismic design.

Up to now, several flexure-shear failure models have been developed to estimate the degradation of column shear strength with increasing inelastic deformations (Priestley 1997; Sezen and Moehle 2004; Watanabe and Ichinose 1991). These models are useful for estimating the maximum shear demand that a column can withstand, but they do not provide a reliable estimate of the drift capacity at shear failure. Only a limited number of drift capacity models have been developed for columns experiencing flexural before shear failure (Kato and Ohnishi 2002; Pujol 2002; Pujol et al. 1999). With the recent efforts to develop displacement-based seismic design methodologies, researchers have begun to recognize the need to understand not only the shear capacity of reinforced concrete columns without aseismic design but also the capacity to sustain axial loads after shear failure. The results of large-scale shear-critical reinforced concrete columns tests demonstrated that the loss of axial loads capacity did not necessarily follow immediately after a loss of lateral load capacity (Lynn 2001; Lynn et al. 1996; Su and Wong 2007). Several pseudo-static tests were performed in Japan to investigate the axial capacity of shear-damaged columns (Kabeyasawa et al. 2002; Tasai 1999). These tests suggested that axial failure occurred when the shear capacity was reduced to approximately zero, and that the drift at axial failure decreased with increasing axial stress. Based on 50 laboratory tests on the reinforced concrete columns yielding flexural failure prior to shear failure, the shear failure model (Elwood and Moehle 2005) defined the drift at shear failure as the drift at which the shear capacity degraded to 80% of the maximum measures shear. Experimental research has shown that axial failure of a shear-damaged column due to sliding along inclined shear cracks is related to several variables including axial stress on the column, the amount of transverse reinforcement, and the drift demand. Based on these observations, the onset of axial failure was described using a shear-friction model (Elwood and Moehle 2003). Similar to the shear failure model described above, this capacity model defines a limit surface at which axial failure is expected to occur. The column can conduct seismic collapse analysis by coupling the shear failure model and axial failure model in series to experience the damage procedure during strong earthquake.

- ***Shear Failure Model***

The shear failure is always found in the masonry structures suffering from strong earthquake. The shear failure is a brittle and dangerous behavior which should be avoided in the reinforced concrete bridges.

2.1.4.2 Failure indices

To conveniently categorize the damage of a structure, a simple classification based on visual signs of damage was presented by Park et al. (1987):

None -no damage or localized minor cracking;

Minor -minor cracking throughout;

Moderate -severe cracking and localized spalling;

Severe -crushing of concrete and exposure of reinforcing steels;

Collapse.

Obviously, it is easy to apply both experimental and post-earthquake inspection. Commonly, a dimensionless index, between 0.0 for an intact element and 1.0 for a completely failed element, is used to measure the degree of damage for structures. For RC structures, the damage may be caused by the concrete, the reinforcement or a combination of the both. Cyclic loading may accumulate damage in the component caused by strength degradation, stiffness deterioration, and low-cycle accumulation. Low-cycle accumulated damage is a critical issue in terms of the amplitude and number of inelastic cycles because seismic loading may result in large inelastic reversals. Existing damage modes can be typically classified into:

➢ ***Non-Cumulative Models***

The ductility ratio in terms of rotation, curvature or displacement is the earliest and simplest damage model. The rotational ductility (μ_θ) for a component is defined as the ratio of the maximum rotation in the component (θ_m) to the yield rotation (θ_y):

$$\mu_\theta = \frac{\theta_m}{\theta_y} \tag{2.1}$$

The yield rotation (θ_y) is computed assuming that the element yields in anti-symmetric bending (Banon et al. 1981) suggested that. The curvature ductility (μ_ϕ) for an element is defined as the ratio of the maximum curvature along the element (ϕ_m) to the yield curvature (ϕ_y):

$$\mu_\phi = \frac{\phi_m}{\phi_y} \tag{2.2}$$

The displacement ductility (μ_δ), is defined as the ratio of the maximum displacement of the component (δ_m) to the yield displacement (δ_y):

$$\mu_\delta = \frac{\delta_m}{\delta_y} \tag{2.3}$$

Another widely used damage model is the drift. Both the maximum drift and the permanent drift remaining after earthquake were taken as the damage indices (Toussi and Yao 1983).

➢ ***Deformation-based Cumulative Models***

The deformation-based damage model is usually used for the components subjected to cyclic loading. The damage index is taken as a function of the accumulated plastic deformation, or by combining a term with respect to the hysteretic energy absorbed during the loading. Banon et al. (1981) presented a normalized cumulative rotation index expressed as:

$$NCR = \frac{\sum \left|\theta_m - \theta_y\right|}{\theta_y} \tag{2.4}$$

The damage model is widely applied to flexure dominated component.

- ***Energy-based Cumulative Models***

A damage index in terms of energy absorption is firstly presented (Gosain et al. 1977), expressed as:

$$D = \sum_i \frac{F_i \delta_i}{F_y \delta_y} \tag{2.5}$$

where F_i and F_y are the force of cycle *i* and the yield force respectively; and δ_i and δ_y are the displacement of cycle *i* and the yield displacement respectively. Only cycles with $\frac{F_i}{F_y} \geq 0.75$ are considered in the calculation, because the remaining capacity can be ignored when it is less than 25%.

- ***Combined Models***

The model presented by Park and Ang (1985) is the best known and most widely used damage index. This model is taken as function of normalized deformation and energy absorption:

$$D = \frac{\delta_m}{\delta_u} + \beta_e \frac{\int dE}{F_y \delta_u} \tag{2.6}$$

where δ_m is the maximum displacement reached in the loading; δ_u is the monotonic ultimate displacement; F_y is the yield force; $\int dE$ is the absorbed hysteretic energy; and β_e is an energy parameter. The first term is a pseudo static displacement measure, the second term considering accumulated damage.

2.1.4.3 Progressive Collapse due to Blast or Impact Loading

Apart from the AEM and DEM aforementioned, the finite element (FE) method used to study the progressive collapse of structures under explosive loading appeals to many researchers over the world. The dynamic collapse analysis of the structure is a complex issue when the structure is subjected to blast loading (Farnam et al. 2010; Hao and Tang 2010; Li and Hao 2013; Li and Hao 2013; Tang and Hao 2010; Uenishi et al. 2010). Because the high amplitude blast loading in a short duration often performs strong time variation that yields a varying strain rate for both the concrete and the reinforcement. The dynamic strain increase factor that is defined as a ratio of the dynamic-to-static strength against strain rate is used to consider the material strength enhancement with strain rate effect. Most of the failure criteria of concrete and reinforcement in the literature are the ultimate compressive and tensile strength multiplied by the dynamic strain increase ratios, respectively. To accurately capture such high velocity response of structures under blast loading, very small size element and very small integration time step are essential, which make the collapse analysis of structures both computational resource and time consuming. To avoid the difficulty of the convergence check at the end of each time step of the collapse analysis experiencing strong material and geometrical nonlinearities, an explicit numerical algorithm is always used.

2.1.4.4 Collapse due to Seismic Loading

Most disastrous collapse of civil structures is caused by strong earthquakes and seismic collapse is a focused issue drawing an increasing attention. Extensive investigation on collapse analysis has been conducted by many researchers around the world in recent years. A modified member stiffness procedure to release all the degrees of freedom (DOF) at the failed end of an element using the APM was investigated (Kaewkulchai and Williamson 2004). A new damage index as a function of degradations of both stiffness and strength was proposed. A quasi-static approach using stiffness degradation factors to determinate the post-elastic bending, shearing, and axial stiffness properties was proposed (Grierson et al. 2005). Two planar steel moment frames to subsequently conduct collapse analysis by removing specified components. Progressive collapse analyses of steel frame structures using macro-model based simulation technique were conducted using APM (Khandelwal et al. 2008). The FE model was established in the commercial code LS-DYNA (Hallquist 2006). For failure criteria of material, the tensile response of steel takes strain hardening and fracture into consideration, while the compressive response accounts for the effects of local and global bucking. The collapse of RC frame structures by virtue of macro-model based simulation technique was studied using APM (Bao et al. 2008). The FE models were established in the commercial code DIANA (Witte and Kikstra 2005) and OpenSees (McKenna et al. 2007), respectively. The total strain rotating crack model in DIANA (Witte and Kikstra 2005) is used for the concrete. The Von Mises isotropic plasticity model in DIANA (Witte and Kikstra 2005) was used for the reinforcement, the failure strain of which is defined as 0.2. On the other hand, Concrete02 model in OpenSess (McKenna et al. 2007) was used for the concrete and

Steel02 model was used for the reinforcement with failure strain of 0.2. An integrated system for progressive collapse analysis based on the two major guidelines (DoD 2009; GSA 2003) was developed, in which generating a new node close to the plastic hinge of the failed member to separate the failed member from the hinge in the analysis was suggested (Kim et al. 2009). In the literature, the generalized damage index is expressed as:

$$D = 1 - \frac{M_{ac}}{M_{y0}} \tag{2.7}$$

$$M_{ac} = M_{y0} \cdot f(\beta_1, \mu) \tag{2.8}$$

$$f(\beta_1, \mu) = (1 - \frac{\mu_{\max}}{\mu_u})^{1/\beta_1} \tag{2.9}$$

where M_{ac} is the deteriorated value of the yield moment and M_{y0} is the theoretical yield moment of undamaged members. $f(\beta_1, \mu)$ is a function of the maximum attained deformation (μ) and the accelerator factor (β_1). The progressive collapse of a multistory building using nonlinear quasi-static FE method simulations and following the guidelines (GSA 2003) was investigated by Kwasniewski (2010). The FE model was established in the commercial code LS-DYNA (Hallquist 2006). The strain-stress model proposed by Galambos (2000) was used for the reinforcement. The failure strains were 0.33 and 0.22 corresponding to different steel grade of s275 and s335, respectively. The sophisticated material model with three invariant formulations for the failure surfaces, the so-called Karagozian & Case Concrete Model, was applied. The failure strain of the concrete was 0.0035.

Actually, the APM has inherent shortcomings: (1) it is based on the system response after several types of specified critical elements are removed rather than detects the initial components triggering the damage and collapse; (2) the dynamic effect cannot or is only roughly taken into account in the progressive collapse analysis, and therefore it is not a conservative approach to evaluate the risk of collapse for structures; and (3) there is a major obstacle for engineers to use APM confidently for the lack of detailed information in the aforementioned guidelines (Marjanishvili 2004).

To have a better collapse analysis, the dynamic approach with an explicit element removal technique has been proposed. The dynamic approach calculates dynamic response of a structure, checks the damage level of every element against its failure criteria at end of each time step, and removes the failed element one by one until the structure collapses. An analytical formulation of an element removal algorithm based on dynamic equilibrium and the resulting transient change in system kinematics was proposed by Talaat and Mosalam (2009). A one-story RC frame with seismically deficient reinforcement details in RC columns were used to conduct seismic collapse analysis. Additionally, a three-bay five-story RC frame infilled with unreinforced masonry wall in the middle bay of each story was employed to carry out seismic collapse analysis. The material-level damage indices define two aggregated cross-section damage indices, D_{A} and D_{M} , as expressed below, to reflect the loss of a cross-section's capacity to resist axial loads and bending moments, respectively

$$D_{\mathrm{A}} = 1 - I_{conf}\left(1 - \sum_{fiber}\left(D_{fiber}A_{fiber} / A_{cross-section}\right)\right) \tag{2.10}$$

$$D_{\mathrm{M}} = 1 - I_{conf}\left(1 - \sum_{fiber}\left(D_{fiber}A_{fiber}h_{fiber}^2 / I_{cross-section}\right)\right) \tag{2.11}$$

where A and I refer to transformed area and moment of inertia, and h refers to the distance between the fiber's center and the uncracked section centroid. Areas and inertias are transformed using the ratio between the initial stiffness moduli of the individual fiber material to obtain a homogeneous section. D_{fiber} is the material-specific damages index previously defined for individual fibers. I_{conf} is an indicator for the loss of confinement whose value is 0.0 if the confining medium fracture is detected and 1.0 otherwise. The two FE models of RC structures were all established in OpenSees (McKenna et al. 2007). The potential collapse processes of high-rise RC buildings using an element deactivation technique implemented by virtue of the second development of a commercial software of Marc (2010) was investigated by Lu et al. (2013). A total of four typical material deactivating criteria (i.e. unconfined concrete crushing, confined concrete crushing, fracture tensile strain of rebar, and bucking compressive stain of reinforcement) were proposed. More seismic collapse analyses and their comparison with the experimental results can be found in the references (Elwood and Moehle 2003; Ghannoum 2007; Kim et al. 2012; Lignos et al. 2011; Wu et al. 2009; Yavari et al. 2009).

However, all the aforementioned collapse analyses are based on the removal of element one by one rather than the release of DOFs one by one. Careful observations of test results (Elwood and Moehle 2003; Sagiroglu 2012) reveal that the seismic collapse of a structure often starts from the failure of an element at some DOFs and that the removal of the element without the failure at all the DOFs may lead to false structural collapse. A new rigorous collapse analysis method based on the DOF release is imperious to accurately reproduce the earthquake-induced collapse process of structures under severe earthquakes.

2.2 Experimental Studies on Seismic Collapse of Structures

In the past two decades, many seismic collapse tests on building structures have been conducted in the world. The experimental studied on three real RC buildings (Hotel San Diego in San Diego, University of Arkansas Medical Center Dormitory in Little Rock and Baptist Memorial Hospital in Memphis) that were demolished by implosion were conducted (Sasani 2008; Sasani and Sagiroglu 2008). The Hotel San Diego was a 6 story RC structure. Two neighboring exterior columns were removed, one of which was a corner column. The maximum vertical displacement was 0.635cm at the top of the corner column. The dominant collapse resistant mechanism was the bi-directional Vierendeel (beam) action of the beams and columns on the top of the removed columns. The University of Arkansas Medical Center Dormitory was a 10 story RC structure. The initial damage scenario was the removal of an exterior column. The corresponding resisting mechanism was completely formed by the performance of structural elements. The Baptist Memorial Hospital was a 20 story RC structure composed of four wings connected to a core. Each wing was separated from the core by an expansion. The initial damage scenario was the removal of an interior column. The dominant collapse mechanism is similar to that of the Hotel San Diego. A 1:8 scaled RC frame to study the progressive collapse mechanism according to the guidelines (DoD 2009; GSA 2003) was constructed (Sagiroglu 2012). The center first floor column was removed firstly, and then a monotonically increased displacement of 41.28cm imposed on the top of the removed column. Finally, the catenary effect of the center two span beams was studied. Test specimens composed of three columns fixed at their bases and interconnected by a beam at the upper level was designed (Elwood and Moehle 2003). The central column had wide spacing of transverse reinforcement, making it vulnerable to shear failure, and subsequent axial load failure during testing. For a building containing columns susceptible to combined flexure-axial-shear load failure, it is reasonable to expect that some components will experience limited yielding before the columns failed in shear. Hence, to achieve the desired response, the outside columns were designed to have a yield displacement and yield moment equal to two thirds of the central column. The results of these shake table tests verified that the shear-axial failure model they developed was correct and efficient. A 2D, three-bay, three-story 1:3 reinforced concrete frame that was used to study collapse performance under intensive earthquake was designed and constructed (Ghannoum 2007). The frame contained non-seismically detailed columns whose proportions and reinforcement details allow them to yield in flexure prior to initiating shear strength degradation and ultimately reaching axial collapse (these columns are therefore referred to as flexure-shear-critical columns). A two-dimensional specimen frame, composed of two non-ductile and two ductile columns by a stiff beam to allow for load distribution was designed, which was subjected to a unidirectional base motion on the shake table until global collapse occurred (Wu et al. 2009; Yavari et al. 2009). The test demonstrated two types of column failure, including flexure-shear and pure flexural failure. The test data were compared with various simplified failure numerical models commonly used by practicing engineers and researchers to identify older buildings at high risk of structural collapse during severe earthquake. Two 1:8 scale models of a 4-story code-compliant prototype moment-resistant frame was constructed and tested (Lignos et al. 2011). The research results demonstrated that prediction of collapse was feasible using relatively simple analytical models. The stiffness deterioration was adequately represented in the analytical model. Response of the framing system near collapse had sensitive cyclic loading histories that were routinely used to test components, however, providing insufficient information for modeling deterioration near collapse. A full-scale shake table test on a six-story reinforced concrete wall frame structure was carried out (Kim et al. 2012). Story collapse induced from shear failure of shear critical members (e.g. short columns and shear walls) was successfully produced in the test. Numerical simulation was also carried out to predict the post-peak behavior using different kinds of deteriorating models, the simulation results gave a good match with the strength-degrading features observed in the post-peak regions where shear failure of members and concentrated deformation occurred in the first story. The effects of member model characterize, torsional response, and earthquake load dimensions (i.e. three-dimension effects) on the collapse process of the specimen were also investigated through comprehensive dynamic analyses. Two 1:3 scaled RC frames with asymmetric plan composed of columns and a wall frame in the first story to generate considerable eccentricity for seismic motion were designed and constructed (Kim et al. 2012). The test results showed that torsional response resulting from the eccentricity in the 1st story induced a displacement concentrated in the weak frame, and eventually the independence column of the RC specimen failed in shear and lost their axial load carrying capacity. The specimen super-reinforced with flexibility survived an identical earthquake load, although significant strength deterioration and considerable lateral and vertical deformation were generated at the end of the test. Actually, the structural systems of building and bridge structures are significantly different, which renders different collapse modes. Shale-table tests of a 2/3-scale, three-story, RC frame with unreinforced masonry infill walls were conducted (Stavridis et al. 2012). The reinforced components of the RC frame did not have an earthquake-resistant design. The RC frame was subjected to a series of dynamic tests including white-noise base excitations and 14 scaled historical earthquake ground motion records of increasing intensity. All the collapse tests aforementioned are focused on the study of RC building structures; experimental investigation of collapse mechanism on RC bridges is seldom conducted, though.

2.3 Model Updating for Structures

Current condition assessment of bridge structures mainly depends on visual inspection and is depicted by subjective criteria without establishing a systematic method for evaluating the bridge dynamics, serviceability and safety (Brownjohn et al. 2001). The various promising model updating techniques (i.e. linear and nonlinear model updating methods) can be used to assess condition of bridge structures by eliminating uncertainties in initially established FE models of structures to ensure modeling accuracy (Aktan et al. 1996; Brownjohn et al. 2001; Friswell and Mottershead 1995; Mottershead and Friswell 1993). If a bridge structure experiences linear and elastic performance under external applied loading, the linear model updating technique is adequate for an accurate FE model of the structure. Nevertheless, if the bridge structure performs severe nonlinear behavior under external applied loading, the nonlinear model updating technique needs to be employed.

2.3.1 Linear model updating for bridge structures

To improve the efficiency of linear model updating for real civil structures, sensitivity-based linear model updating with modal frequencies and mode shapes is often used to ignore insensitivity parameters (Brownjohn and Xia 2000; Cantieni 1996; Jaishi and Ren 2005; Pavic et al. 1999). Mode shapes are difficult to identify accurately because the number of sensors were limited and the signal acquired from the field measurement data for mode shape analysis was contaminated by environmental noise. Therefore, measured modal frequencies are the most appropriate updating objectives for real bridge structures (Catbas and Aktan 2002). The linear model updating for bridges using curvatures of mode shapes was conducted (Wahab and Roeck 1999). Then, the FE-method-based model updating was carried out to minimize the discrepancies between the analyzed results and the measurement results. Static-based linear model updating was also used for moderate scale bridges (Chajes et al. 1997; Enevoldsen et al. 2002; Xiao et al. 2014). Static responses such as displacement and strain could be used as updating objectives for linear model updating of bridges (Ren and Chen 2010). Static strain response that can capture local performance of the structures was selected as updating objectives for linear model updating of structures (Wang et al. 2013). A long-span bridge using identified dynamic characteristics together with static stress responses was successfully updated (Catbas et al. 2007). The global and local updating steps were conducted separately. A long-span bridge using static displacement, stress together with modal frequencies and mode shapes was updated (Wang et al. 2013).

In view of these developments, the traditional linear model updating method uses either the dynamic characteristics or static strain/stress/displacement responses as the updating objectives. But for bridge structures subject to seismic loading, selecting the transit responses of strain or acceleration in time domain as the updating objectives may be a promising solution for linear model updating, but researches in this area are limited.

2.3.2 Nonlinear model updating for structures

Although linear FE model updating method has been successfully used to predict damage represented by loss of effective stiffness, nonlinear FE model updating is preferable to identify damage conditions of structures or damage prognosis. It is urgent to implement nonlinear FE model updating that is in preference to linear FE model updating because of the three facts (Asgarieh et al. 2014): (1) all real structures are actually nonlinear, having uncertainties in their nonlinear performance; (2) the nonlinear response of a structure subjected to large seismic loadings exhibits more severe damage than does the linear response to small seismic loadings; and (3) an accurate nonlinear FE model can be used for damage prognosis. It is necessary to make numerical models accurate for nonlinear structural dynamics and resolve difficult problems concerning the nonlinear FE model updating (Hemez and Doebling 2001). Additionally, the opinion that the nonlinear model updating conducted in time-domain gain advantages over that in frequency domain was introduced. The principal component decomposition method to conduct the nonlinear model updating for a structure containing a hyper elastic polymer under impact loading was introduced (Beardsley et al. 1999). The harmonic balance method to carry out the nonlinear model updating of weak nonlinear structures in frequency domain was introduced (Meyer and Link 2003).

The material nonlinearity in civil structures can be assumedly represented by the hysteretic material (i.e. concrete and reinforcement). Therefore, the issue of nonlinear model updating a time-varying system becomes an issue of nonlinear model updating time-varying parameters of hysteretic material models (Asgarieh et al. 2014). An approximate nonlinear relationship between hysteretic model parameters and force-deformation hysteretic curve to identify the damage in the civil structures was proposed (Kunnath et al. 1997). A new nonlinear model updating method for structural system subjected to low ambient vibration was proposed (Song et al. 2012; Song et al. 2008). The main contribution is that a relationship between damage parameters employed in numerical simulation and FE model stiffness at the zero-load crossings was presented.

However, most of these nonlinear model updating applications were demonstrated by single-degree-freedom or simple multi-degree-freedom numerical cases. Therefore, it is urgent to propose a new nonlinear model updating method for real-world civil structures (including bridge structures).

2.4 Structural Health Monitoring of Bridge Structures

2.4.1 Definition of SHM

Structural health monitoring (SHM) system installed in bridge structure is the implementation of a damage detection and safety assessment strategy for the bridge. Damage is defined as changes to the material and/or geometric properties of these systems, including changes to the boundary conditions and system connectivity. Damage affects the current or future behaviors of these systems. The damage identification process is generally structured into four levels: (1) damage detection, (2) damage location, (3) damage typification, and (4) damage extent.

2.4.2 Condition assessment

Condition assessment of a bridge is one of the most important aims for installing a sophisticated SHM system. Generally, five levels are categorized to determine the depths of investigation:

- ***Level 1: Rating.*** This represents the conventional assessment of the bridge with a visual field inspection that provides a subjective impression of the condition of the bridge.
- ***Level 2: Condition assessment.*** A rough visual inspection has to be an element of any SHM campaign. Then a decision has to be made whether the conventional method is satisfied or an extended or even sophisticated additional

approach is used.

- ***Performance assessment.*** This intermediate level uses the same procedure as described for Level 2. The level of assessment always needs additional information such as dynamic characteristics of bridges.
- ***Detailed assessment and rating.*** The next step is to establish an analytical model representing the bridge. The simulated results using the model will be compared with the measurement data. If the identification is simple, a step back towards Level 3 might be taken; otherwise, the most obvious thing is to introduce a permanent record over some period of time to capture the necessary phenomena valid for this specific case.
- ***Level 5: Lifetime prediction.*** For a serious lifetime prediction, the records available have to be long enough to cover at least three cycles relevant for the bridge. Simulation should be run from the analytical model in order to achieve a theoretical performance for comparison.

Figure 2.4 demonstrates how these procedures are developed from simple inspection routines to highly sophisticated monitoring campaigns.

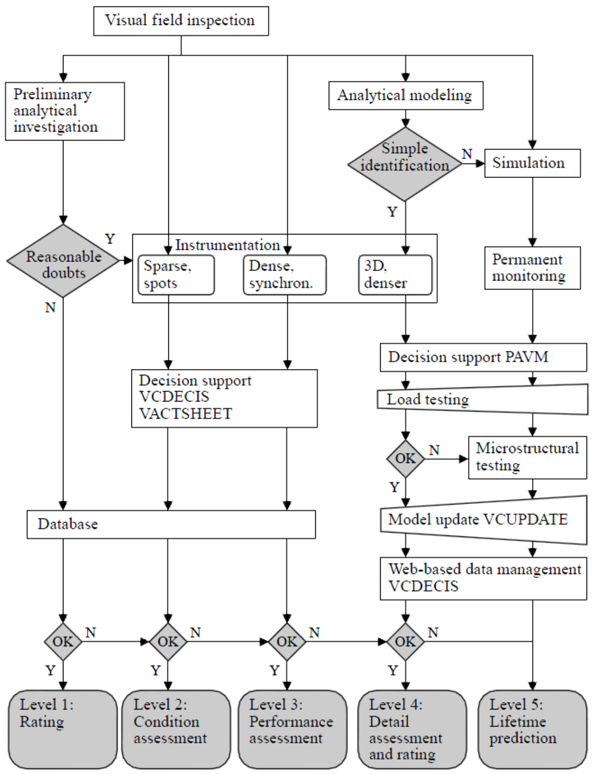

Figure 2.4 Typical hierarchical concept for the SHM procedure for bridge (Wenzel 2008)

On-structure health monitoring systems have been equipped on bridges in Europe (Andersen and Pedersen 1994; Brownjohn et al. 2005; Casciati 2003; Myrvoll et al. 2000), the Unite States (Pines and Aktan 2002), Canada (Cheung and Naumoski 2002; Mufti 2002), Japan (Fujino and Abe 2004; Wu and Fujino 2005), Korea (Koh et al. 2003; Yun et al. 2003), China (Ou 2004; Wong 2004; Xiang 2000; Xu and Xia 2011), and other countries (Nigbor and Diehl 1997; Thomson et al. 2001). Table 2.1 presents the sensor information of 20 typical long-span bridges installed with SHM systems (Ko and Ni 2005). Although so many SHM systems have been installed on the bridges, how to optimize the number and placement of sensors still remains a critical issue.

Table 2.1 Major bridges equipped with SHM systems (Ko and Ni 2005)

No.	Bridge Name	Bridge Type	Location	Main Span (m)	Sensors Installed
1	Akashi Kaikyo Bridge	Suspension Bridge	Japan	1991	(1),(2),(4),(5),(6),(7),(16)
2	Great Belt East Bridge	Suspension Bridge	Denmark	1624	(1),(2),(3),(4),(5),(9),(12),(13),(20),(21)
3	Runyang South Bridge	Suspension Bridge	China	1490	(1),(2),(3),(4),(7)
4	Humber Bridge	Suspension Bridge	UK	1410	(1),(2),(3),(4),(6),(9)
5	Jiangyin Bridge	Suspension Bridge	China	1385	(1),(2),(3),(4),(5),(7),(10),(11),(14)
6	Tsing Ma Bridge	Suspension Bridge	China	1377	(1),(2),(3),(4),(5),(7),(8),(13)
7	Golden Gate Bridge	Suspension Bridge	USA	1280	(1),(4),(16)
8	Minami Bisan-Seto Bridge	Suspension Bridge	Japan	1100	(4),(7),(9),(16)
9	Forth Road Bridge	Suspension Bridge	UK	1006	(2),(3),(7),(9),(18)
10	Humen Bridge	Suspension Bridge	China	888	(3),(7),(12),(13)
11	Ohnaruto Bridge	Suspension Bridge	Japan	876	(1),(2),(3),(4),(5),(7),(16)
12	Hakucho Bridge	Suspension Bridge	Japan	720	(1),(4),(16)
13	Gwangan Bridge	Suspension Bridge	Korea	500	(1),(2),(3),(4),(12),(18),(19),(20)
14	Namhae Bridge	Suspension Bridge	Korea	404	(1),(2),(3),(4),(12),(19)
15	Tamar Bridge	Suspension Bridge	UK	335	(1),(2),(3),(13),(19),(20)
16	Youngjong Bridge	Suspension Bridge	Korea	300	(1),(2),(3),(4),(12),(18),(19),(20)
17	Sutong Bridge	Cable-stayed Bridge	China	1088	(1),(2),(3),(4),(5),(7),(8),(9),(11),(12),(21),(22)
18	Stonecutters Bridge	Cable-stayed Bridge	China	1018	(1),(2),(3),(4),(5),(7),(8),(9),(11),(12),(21),(22)
19	Tatara Brdige	Cable-stayed Bridge	Japan	890	(4),(16)
20	Normandie Bridge	Cable-stayed Bridge	France	856	(1),(2),(3),(4),(7)

Note: (1) anemometer; (2) temperature sensor; (3) strain gauge; (4) accelerometer; (5) displacement transducer; (6) velocimeter; (7) global positioning system; (8) weight-in-motion sensor; (9) corrosion sensor (11) optic fiber sensor; (12) tiltmeter; (13) level sensing station; (14) dynamometer; (15) total station; (16) seismometer; (17) fatigue meter; (18) cable tension force; (19) joint meter; (20) laser displacement sensor; (21) meteorological station; (22) video camera; (23) jacking pressure sensor; (24) potentiometer; (25) water level sensor.

2.4.3 SHM system installed in Tsing Ma Bridge

A Wind and Structural Health Monitoring System for the Tsing Ma Bridge was devised and used by the Highways Department of Government of Hong Kong Special Administrative Region. The sophisticated system included six integrated modules: the sensory system, data acquisition and transmission system, data processing and control system, structural health evaluation system, portable data acquisition system, and portable inspection and maintenance system.

The layout of the sensory system for the Tsing Ma Bridge is illustrated in Figure 2.5. A total of 276 sensors are provided in seven types: anemometers, temperature sensors, weight-in-motion sensors, accelerometers, displacement transducers, level sensing stations, and strain gauges, as listed in Table 2.2.

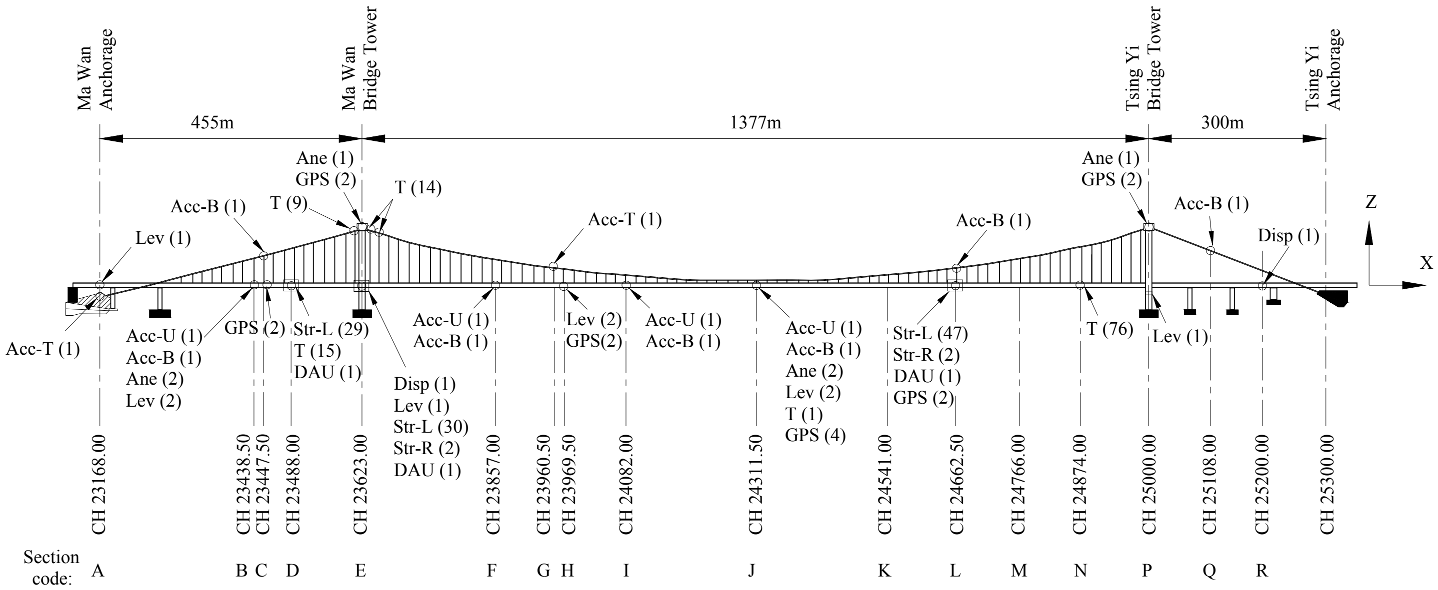

Figure 2.5 Layout of sensors and DAUs of the Tsing Ma Bridge (Xu and Xia 2011)

Note: (1) Number in parameters are the number of sensors;

(2) Lev: Level sensing (9); Ane: Anemometer (6); Acc-U: Uniaxial Accelerometer (4); Acc-B: Biaxial accelerometer (7); Acc-T: Triaxial Accelerometer (2); Str-L: Linear strain gauge (106); Str-R: Rosette strain gauge (4); T: Temperature sensor (115); Disp: Displacment tranducer (2); DAU: Data acquisition unit (3).

(3) Weight-in-motion sensors are not located on the bridge and not shown in the figure.

Table 2.2 Sensors deployed on Tsing Ma Bridge (Xu and Xia 2011)

Monitoring Item	Sensor Type	Sensor Code	No. of Sensor	Position
Wind speed and direction	Anemometer	WI	6	2: deck of main span;
				2: deck of Ma Wan side span;
				2: top of two towers
Temperature	Thermometer	P1~P6, TC	115	6: ambient;
				86: deck section;
				23: main cables
Highway traffic	Weigh-in-motion	WI	7	approach to Lantau Toll Plaza
Displacement	Displacement transducer	DS	2	1: lowest portal beam of the Ma Wan tower (lateral);
				1: deck at the Tsing Yi abutment (longitudinal)
	GPS station	TM	14	4: top of towers;
				2: middle of main cables;
				2: middle of Ma Wan side span;
				6: ¼, ½ and ¾ of main span
	Level sensing station	LV	9	1: abutment; 2: two towers;
				2: deck of Ma Wan side span;
				4: deck of main span
Acceleration	Accelerometer	AS	13	4: uniaxial, deck;
		AB		7: biaxial, deck and main cables;
		AT		2: triaxial, main cables and Ma Wan abutment
Strain	Strain gauge	SP	110	29: Ma Wan side span
		SR		32: cross frame at Ma Wan tower
		SS		49: main span

According to the sensors statistics in Table 2.2, thermometers and strain gauges, more than 100 in number, were installed mainly on the deck and main cables. Only 13 accelerometers were installed on the deck, cable and abutment. No accelerometer was placed on the failure-vulnerable sections of the tower and piers. Therefore, the current SHM system installed on Tsing Ma Bridge cannot be employed for the collapse prognosis under future earthquakes. A new SHM system that can not only monitor the linear performance of the bridge under service loading but also provide useful information for collapse prognosis of the bridge under future earthquake is urgently needed to be developed.

2.4.4 SHM-based collapse prognosis

Prognosis is an advanced technique for assessing future behavior of a structure based on an accurate calibration of the present conditions of the structure. Three factors are critical to create accurate prognosis for a structure: (1) a set of SHM system including appropriate sensor number and sensor placement; (2) a reliable and accurate method for calibration of current conditions of the structure; (3) a series of evolution rules for materials and computational capacity of large deformation of the structure. An accurate prognosis of a structure is very important for authorities to know the performance and timely maintenance of a structure or to deal with accidental damage. The current seismic collapse analysis of a RC bridge is a direct analysis process that starts from intact condition of the bridge which is applicable for the bridge at design stage. That is, the current collapse analysis based on an ideal condition of the bridge cannot reflect the real conditions of the bridge. It is incapable of making prognosis for the bridge. Then, the current SHM systems installed on important bridges are mainly used to monitor the linear performance of the bridge under specific service loading. However, these systems provide insufficient information for predicting the collapse of bridges subject to future earthquakes. Hence, the world sees a pressing need to have an SHM system for the collapse prognosis of bridges subject to earthquakes. SHM-based prognosis for fatigue damage of the Tsing Ma bridge under combined highway, railway and wind loadings was discussed (Xu 2015). Although, this is not an easy task, for the dynamic stress responses of a long-span suspension bridge are induced by multiple types of dynamic loads, such as railway, highway, and wind loads, and uncertainty and randomness are inherent in these dynamic loads. The prognosis of fatigue damage to long-span suspension bridges under multiple types of dynamic loads can be made by integrating computer simulation with the measurement data from SHM system. However, how to prognosticate the bridge structures based on the existing SHM systems is an interesting issue, which is seldom discussed. If a bridge structure is prognosticated under various loadings (i.e., service loadings, wind loading and seismic loading), then the remaining life of the bridge can be predicted (Li et al. 2011; Xu and Xia 2011).

CHAPTER 3

RIGOROUS COLLAPSE ANALYSIS OF RC STRUCTURES

3.1 Introduction

As reviewed in Chapter 2, the alternate path method (APM) approach does not account for the type of triggering event, but rather considers building system response after the triggering event has destroyed critical structural components (Khandelwal et al. 2008). Therefore, it is not a reliable approach to evaluate risk of collapse for RC structures. The dynamic collapse analysis on RC structure with explicit element removal technique is extensively conducted, though. Seismic collapse analyses are all based on one-by-one element removal rather than one-by-one DOFs release. Careful observations of test results (Elwood and Moehle 2003; Sagiroglu 2012) reveal that the collapse of a structure often starts from the failure of an element at some DOFs and that the removal of the element without failure at any DOFs may lead to false structural collapse. A rigorous seismic collapse analysis shall be based on the release of DOFs one by one rather than the removal of elements one by one.

In this regard, this paper refines FE-method-based seismic collapse simulation by introducing a concept of degree-of-freedom (DOF) release. With the concept, an element removal (failure) is a natural consequence of time-varying release (failure) of all DOFs of the element one by one. The concept is implemented in an open-source finite element code OpenSees (McKenna et al. 2007). The test results of static collapse of a RC beam with two ends fixed under a concentrated static load are first used to demonstrate the advantages of DOF release over the traditional element removal. The refined seismic analysis method is then applied to a two-story reinforced concrete frame to demonstrate the collapse process for a complicated RC frame structure. At last, a two-span continuous RC bridge with a two-column pier is taken as an example to demonstrate the applicability of the refined method to RC bridge structures, to which seismic collapse investigation is seldom applied.

3.2 DOF Release and Element Removal

Experiments of structural collapse show that the seismic collapse of a RC structure often triggers from the failure of some DOFs of an element rather than the failure of the entire element. However, the current FE-method-based seismic collapse simulation depends on the one-by-one element removal when the element meets its designated failure criteria. The current simulation method therefore could not account for the catenary effect of a RC beam and the axial bearing effect of a RC column due to flexure-shear failure, resulting in different collapse modes. To overcome these drawbacks, the concept of DOF release is presented in this study. The failure modes and criteria of RC beams and RC columns in line with the new strategy are first discussed in this section. Due to space limitations, the following failure modes or conditions will not be considered in this study as stipulated (ASCE/SEI 2007): (1) the failure of a RC member is controlled by inadequate development length of lap-spliced reinforcement or straight/hooked bars along the beam span or column clear height; (2) the failure of a RC beam is controlled by inadequate embedment into the beam-column joint; (3) the RC column with axial load exceeds 0.7 times the nominal load strength at zero eccentricity; and (4) the beam-column joint fails.

3.2.1 Failure modes and criteria of RC beams

The failure modes have three DOFs at each end of a planar RC beam (i.e., DOFs associated with axial, shear forces and bending moment). The failure modes of a RC beam are currently classified as either the failure controlled by flexure or the failure controlled by shear (Elwood et al. 2007). For the failure controlled by flexure, the flexural strength of a RC beam depends on three major factors: the magnitude of shear force acting on the beam, the arrangement of longitudinal reinforcement, and the transversal reinforcement, respectively. For the failure controlled by shear, hoop spacing affects shear strength of a RC beam. The three parameters *a*, *b* and *c* in the backbone curve, which were updated by Elwood (Elwood et al. 2007) and are illustrated in Figure 3.1, can be used to find the threshold point (E) as the failure criteria of RC beams controlled by either flexure or shear. The backbone curve, which envelopes the entire cyclic response, is defined as the moment-rotation responses and can be derived from experiments or a standard cross-section analysis. The abscissa in Figure 3.1 denotes the rotation response and the ordinate indicates the ratio of bending moment response (Q) over yield moment capacity of a RC beam (Q_y). The segment on the backbone curve from point A to point B represents an elastic and linear range. A small percentage (about 0 to 15%) of the elastic slope from point B to point C is introduced to represent the phenomena such as strain hardening. The ordinate value of point C indicates the maximum moment capacity of the RC beam. The abscissa value of point C is the rotation where remarkable strength degradation occurs. To avoid the inability to converge in computation, a small slope (10 vertical to 1 horizontal) is provided to the segment from point C to point D. Beyond point D, the beam will respond with its residual strength until the failure of point E. If the rotation exceeds a designated value in terms of the importance of the component type (Elwood et al. 2007), the entire RC beam is said to fail and it will be entirely removed from the structure according to the current element removal algorithm.

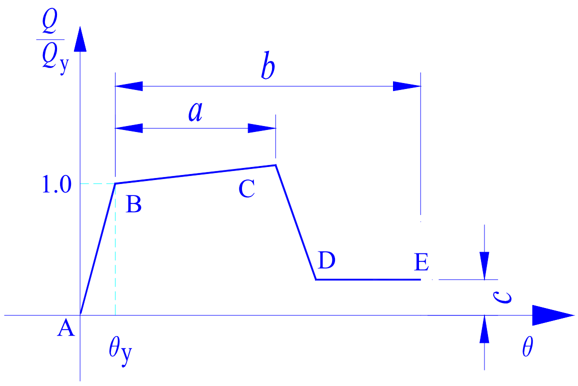

Figure 3.1 Generalized moment-rotation relationship for RC beams

The currently-used element removal algorithm used in seismic analysis, however, ignores the catenary effect. Actually, after a RC beam fails by flexure or shear, longitudinal reinforcements or part of longitudinal reinforcements still remain so that they can take tension forces and form the so-called catenary effect. Thus, after a RC beam fails by either flexure or shear, the DOFs of the RC beam associated with moment and shear can be released but the DOF associated with axial force will remain to consider the catenary effect. The consideration of catenary effect may result in different collapse modes in the numerical simulation.

3.2.2 Failure modes and criteria of RC columns

The failure modes of a RC column are different from those of a RC beam because of their distinguished characteristics: the beam mainly sustains bending moments and shear forces while the column bears axial and shear forces in addition to bending moment. Three failure modes classified in terms of the demand-capacity ratio (DCR) V_{p} / V_0 can be explicitly illustrated by Figure 3.2, where the shear demand (V_{p}) of a RC column can be determined by the yield moment capacity divided by the shear span. V_0 is the shear capacity of a RC column. The shear capacity V_0 is composed of two parts: one part V_{c} is carried by concrete; the other part V_{s} is sustained by transverse reinforcement through a 45° truss model. $\mu_{\mathrm{d}} = \Delta_{\mathrm{u}} / \Delta_{\mathrm{y}}$ is the lateral displacement ductility, in which Δ_{u} denotes the lateral displacement beyond the yield displacement Δ_{y}. The dash-dot line in Figure 3.2 shows the nominal shear capacity, which degrades with the development of displacement ductility. A model for the nominal shear capacity ($V_{\mathrm{n}} = kV_0$) of a RC column with light transverse reinforcement was presented (Sezen and Moehle 2004) as follows:

$$V_{\mathrm{n}} = kV_0 = k(V_{\mathrm{c}} + V_{\mathrm{s}}) = k\frac{0.5\sqrt{f_{\mathrm{c}}^{'}}}{a_1 / d}\sqrt{1 + \frac{P}{0.5\sqrt{f_{\mathrm{c}}^{'}}A_{\mathrm{g}}}}0.8A_{\mathrm{g}} + k\frac{A_{\mathrm{st}} f_{\mathrm{st}} d}{s} \tag{3.1}$$

$$k = \begin{cases} 1.0 & \mu_{\mathrm{d}} \le 2.0 \\ 1.15 - 0.075\mu_{\mathrm{d}} & 2.0 < \mu_{\mathrm{d}} \le 6.0 \\ 0.7 & \mu_{\mathrm{d}} > 6.0 \end{cases} \tag{3.2}$$

where the coefficient k is the function of the displacement ductility (μ_{d}), $f_{\mathrm{c}}^{'}$ is the 28-day concrete compressive strength (MPa) of the standard cylinder, a_1 is the shear span, d is the depth to the centerline of the extreme tension reinforcing steel, s is the hoop spacing, A_g is the gross cross-section area of columns, P is the axial load, A_{st} is the area of transverse reinforcement, and f_{st} is the yield strength of transverse reinforcement.

The dash-dot line in Figure 3.2 shows that the nominal shear capacity degrades with the development of displacement ductility from 2.0 to 6.0. The conceptual definition of three categories of failure modes can now be illustrated by means of Figure 3.2 (Elwood et al. 2007; Wu et al. 2009). When the shear demand denoted by the curve (a) is more than the shear capacity ($V_p / V_0 \geq 1$), the shear failure occurs before the first yielding of longitudinal reinforcement. When the shear demand denoted by the curve (b) exceeds the shear capacity ($0.7 < V_p / V_0 < 1$), the shear failure occurs after the first yielding of the longitudinal reinforcement due to the shear degradation in the column. This failure is called flexure-shear failure. It should be emphasized that if the RC column sustains a high axial load, the column will perhaps experience axial failure after the flexure-shear failure (Elwood and Moehle 2003). This failure is called the flexure-shear-axial failure. When the shear demand denoted by the curve (c) in Figure 3.2 is less than 70% of the shear capacity ($V_p / V_0 \leq 0.7$), the flexure failure occurs for excessive flexural deformation. Points (1), (2) and (3) in Figure 3.2 represent the onset of shear failure, flexure-shear failure, and flexure failure, respectively. This classification is conceptual based on DCR, and the failure criteria will be described in the next paragraph.

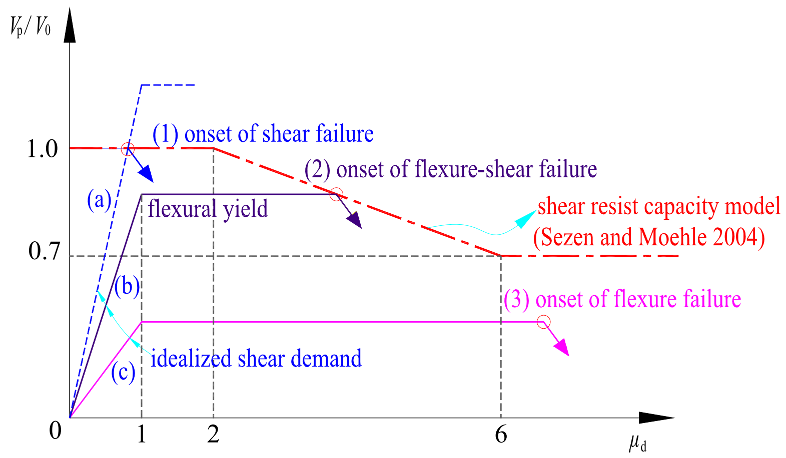

Figure 3.2 Definition of three failure modes of a RC column

The currently-used flexural or shear failure criteria for a RC column are similar to those for a RC beam controlled by flexure or shear. With reference to Figure 3.1, the abscissa and ordinate values of point B on the backbone can be calculated through a standard cross-section analysis of the column with the detailed information of both concrete and reinforcement. The three parameters *a*, *b* and *c* can be found from the literature (Elwood et al. 2007). Then, the backbone curve in Figure 3.1 can be constructed and point E can be located. If the actual rotation of the column exceeds the abscissa value of point E while the residual moment retains *c* per cent of the yield moment capacity, the entire RC column is said to fail in flexure or shear.

However, RC columns are often subjected to significant compressive forces compared with RC beams. Therefore, once a RC column fails in flexure or shear, the column cannot bear its compressive forces, resulting in the complete collapse of the column. Correspondingly, the DOFs of the column associated with the bending moment, shear and axial forces should be released simultaneously. This is different from the RC beam related to the catenary effect.

For flexure-shear failure, the degradation of the lateral capacity occurs after yielding of the longitudinal reinforcement but results from the shear effect in the column. Furthermore, it is understood from Figure 3.2 that the flexure-shear damage of a RC column will occur when the drift ratio (Δ_s / L) of the RC column reaches to a certain level at which the nominal shear capacity degrades and equals the shear demand of the RC column. An empirical drift capacity model expressed by Eq.(3.3) regarding the flexure-shear failure of a RC column was presented (Elwood and Moehle 2005).

$$\frac{\Delta_s}{L} = \frac{3}{100} + 4\rho'' - \frac{1}{40}\frac{v}{\sqrt{f_c'}} - \frac{1}{40}\frac{P}{A_g f_c'} \geq \frac{1}{100} \quad \text{(MPa units)} \tag{3.3}$$

where Δ_s is the lateral displacement at which flexure-shear damage occurs, L is the clear height of the RC column, ρ'' is the transverse reinforcing steel ratio ($A_{st} / b_1 s$), b_1 is the width of cross section of the column, v is the shear stress equals to $V / b_1 d$, and V is the shear force in the column.

As the flexure-shear damage of the RC column further develops until its residual shear capacity becomes very small (e.g. less than 10%), the flexural and shear failure is said to occur and the corresponding DOFs of the column can be released. However, whether or not the DOF associated with the compressive force can be released is subject to the further analysis of compression force. If the compressive force on the column is small, the compression failure may not occur and therefore the DOF associated with the compressive force will not be released. If the RC column bears a high compression load, it will be vulnerable to axial failure after the flexure-shear failure. An axial failure model expressed by Eq.(3.4), based on the shear-friction model to predict the point where axial damage occurs was presented (Elwood and Moehle 2005).

$$\frac{\Delta_a}{L} = \frac{4}{100}\frac{1+(\tan\theta)^2}{\tan\theta + P(\frac{s}{A_{st} f_{st} d_c \tan\theta})} \qquad \text{(MPa units)} \tag{3.4}$$

where Δ_a is the lateral displacement at which axial damage occurs, θ is the critical angle of the shear failure plane, and d_c is the depth of the column core from center line to center line of the hoops. As the axial damage of the column further develops until its axial capacity becomes very small (e.g., less than 10%), the flexural-shear-axial failure is said to occur and the DOF of the column associated with the compressive force is further released in addition to the two DOFs released before for both shear and flexure.

In summary, when step-by-step DOF release is considered in collapse analyses of a RC structure, the entire RC beam will not be removed even though the beam is subject to both shear and flexure failures. Only when the reinforcing tensile reinforcements in the beam reach their ultimate strength, the DOF associated with the tension will then be released. In such a way, the catenary effect can be taken into account in the collapse analysis when the DOF associated with the axial force is not released.

For RC column failure by either shear or flexure, the DOFs of the column associated with bending moment, shear and axial forces are all released simultaneously. However, for RC columns fail in flexure-shear mode, whether the DOF of the column associated with the axial force will be released depends on the magnitude of the compressive force. In most cases, the release of the DOF associated with the compression follows the release of the DOFs associated with the bending moment and shear force. This is different from the currently-used approach in which the entire RC column is removed once triggering the criteria of flexure-shear failure.

3.3 Algorithm for DOF Release and Element Removal Implemented in OpenSees

To conduct the seismic collapse analysis of a RC structure, a nonlinear FE model shall be established first for the structure. In this study, the fiber element in an open-source finite element code of OpenSees (McKenna et al. 2007), which can account for the material nonlinearities of concrete and reinforcement as well as the geometrical nonlinearity of the structure, are used to construct the FE model for the RC structure. The FE model has three levels: fiber level, section level, and element level. At the element level, the forces and displacements of each element can be computed by virtue of the global displacements obtained by solving the global system of equations. At the section level, the forces and deformations are obtained by virtue of the forces and deformations of each element. At the fiber level, the stress and strain of each fiber can be calculated according to the constitutive laws of concrete and reinforcement and following the assumption that plane section remains plane and normal to the reference longitudinal axis. The bonding/debonding effects between reinforcement and concrete are not considered in the fiber element. The nonlinear analysis of the FE model is then performed to find potential failure locations (member section) of the RC structure. Certain types of zero-length elements accounting for the DOF release and element removal are then inserted into the potential failure sections of the FE model. The failure criteria are defined at the section level. In such a way, the failure criteria of the failure-vulnerable elements can be compared with the calculated results for failure detection. The collapse analysis is finally performed by releasing DOFs in the zero-length elements and removing elements according to the limited state failure criteria. Clearly, the collapse analysis is different from traditional nonlinear analysis.

The potential failure locations of both RC beams and RC columns can be determined by comparing the maximum bending moment response with the maximum moment capacity of a component, as shown in Figure 3.1, through a nonlinear seismic analysis. If the maximum bending moment response of the beam or the column is more than the maximum moment capacity at a particular section, this section is taken as a potential failure location. For a given potential failure location, the possible failure mode will then be identified and the corresponding zero-length element will be inserted into the potential failure location.

For a RC beam, the maximum moment capacity and the shear capacity can be determined in accordance with its material properties as well as its detailed cross-sectional reinforcement information (ACI/318 2005). The shear demand can then be calculated by taking the maximum moment capacity over the shear span. The failure mode of the RC beam can be acquired by comparing the shear capacity with the shear demand. If the shear capacity is more than the shear demand, the failure of the RC beam is controlled by flexure; otherwise, the failure of the RC beam is controlled by shear.

For a planar RC beam as shown in Figure 3.3, nonlinear fiber beam elements are used to model the beam. If the section *j* or *k* of the beam is a potential failure location, the zero-length element (*j* and *k* share the identical coordinates in Figure 3.3) is then inserted into the potential failure location to simulate the flexure or shear failure. The zero-length element shown in Figure 3.3 consists of three DOFs associated with bending moment, shear and axial forces which are respectively represented by three zero-length springs (i.e., rotation spring, shear spring and axial spring). The axial stiffness of the axial spring is set as 100 times stiffer than the axial stiffness of the beam elements to ensure that there is no additional axial deformation introduced by the zero-length element. The shear stiffness of the shear spring is also set as 100 times stiffer than the shear stiffness of the beam elements for the same reason. The backbone model for hysteretic material, as shown in Figure 3.1, is then assigned to the rotation spring with appropriate parameters (*a*, *b*, and *c*) to detect the potential flexure or shear failure. When the flexure or shear failure criterion of the rotation spring is reached, the DOFs associated with the bending moment and shear force will be released simultaneously. The axial spring, however, is kept to consider the catenary effect of the RC beam. When the reinforcement in the beam reaches its ultimate tension strength, the axial DOF will then be released finally.

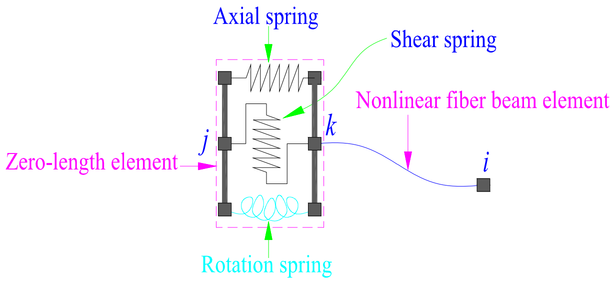

Figure 3.3 Illustration of the zero-length element for a RC beam

For RC columns, experimental results of several research programs that the boundaries of $V_p/V_0 = 1$ and $V_p/V_0 = 0.7$, as discussed in Section 2, are not sufficient to distinguish the three failure modes were found (Elwood et al. 2007; Zhu et al. 2007). They then proposed the revised criteria to predict potential failure modes. These revised criteria, presented by a flowchart shown in Figure 3.4, rely on the three major parameters: the transverse reinforcement ratio ρ'', the hoop spacing to depth ratio *s*/*d*, and the parameter of DCR (V_p/V_0). Clearly, the details of transverse reinforcement are indispensable for predicting the potential failure mode for a RC column. To judge the potential failure mode for a given RC column, the first step is to calculate the DCR of the RC column. If the DCR is more than 1.0, the RC column is susceptible to shear failure. If the DCR of the RC column is less than 0.6, the RC column is susceptible to flexure or flexure-shear failure, depending on their details of transverse reinforcement. If the DCR of the RC column is more than 0.6 and less than or equal to1.0, the RC column is susceptible to shear or flexure-shear, depending on the configuration details of the hoops.

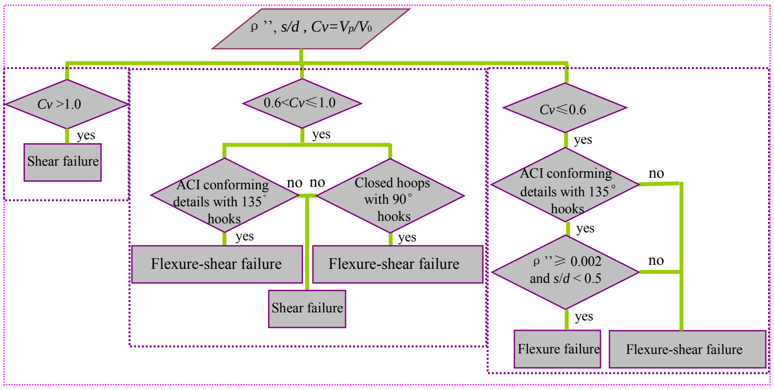

Figure 3.4 Flowchart for judging potential failure modes of a RC column

For the planar RC column shown in Figure 3.5, nonlinear fiber beam elements are used to model the column. If the section j or k of the column is a potential failure location, the zero-length element (j and k share the identical coordinates in Figure 3.5) is then inserted into the potential failure location to simulate the flexure or shear failure (Figure 3.5(a)) or flexure-shear-axial failure (Figure 3.5(b)). The zero-length element consists of three DOFs associated with bending moment, shear and axial forces represented by three zero-length springs (i.e., rotation spring, shear spring, and axial spring). The axial and shear stiffness for the axial and shear spring is set as 100 times stiffer than the axial and shear stiffness of the column element, respectively, to ensure that there are no additional axial and shear deformations introduced by the zero-length element. For a RC column with either flexure or shear failure, the backbone model for hysteretic materials as shown in Figure 3.1 is assigned to the rotation spring with appropriate parameters (i.e., a, b and c) to detect the potential flexure or shear failure. When the flexure or shear failure criterion of the rotation spring is reached, all the three DOFs associated with the bending moment, shear and axial forces will be released simultaneously. Similarly, the zero-length element that consists of three DOFs associated with bending moment, shear and axial forces representing by three zero-length springs as shown in Figure 3.5(b) is proposed and inserted into the potential failure location to simulate the flexure-shear or flexure-shear-axial failure for the RC column. Two hysteretic material models (Elwood and Moehle 2005) with appropriate parameters (Δ_s / L, Δ_a / L and others) are assigned to the shear and axial springs, respectively, to detect the potential flexure-shear and flexure-shear-axial failure, respectively. The initial axial stiffness of the axial spring in its hysteretic model is set as 100 times stiffer than the axial stiffness of the column element to ensure that no additional axial flexibility is introduced by the zero-length element. The initial shear stiffness of shear spring in its hysteretic model is taken as the stiffness of the uncracked RC column with an effective shear area. The elastic flexure stiffness of the rotation spring is set as 100 times stiffer than the flexure stiffness of the column element to ensure that no additional flexure deformation is introduced by the zero-length element. When the failure criterion of the shear spring is reached, the DOFs associated with the bending moment and the shear force will be released simultaneously. Nevertheless, the DOF associated with the axial force will be released until the failure creation of the axial spring is triggered.

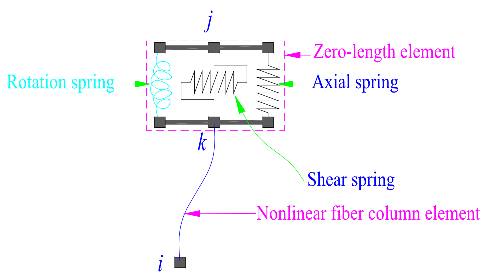

(a)

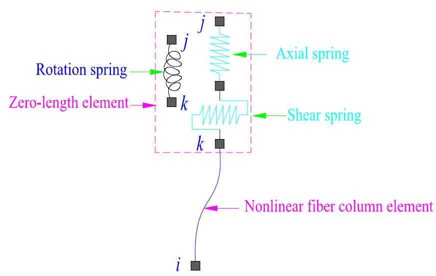

(b)

Figure 3.5 Illustration of zero-length elements for RC columns

(a) Zero-length element for flexure or shear failure

(b) Zero-length element for flexure-shear-axial failure

The seismic collapse analysis with the DOF release and element removal proposed in this study is implemented using the open source soft package of OpenSees (McKenna et al. 2007). An efficient algorithm is designed and implemented in the OpenSees (McKenna et al. 2007) for automated DOF release and element removal during an ongoing simulation. The nonlinear FE model of a RC structure for collapse analysis is described at material level, section level, element level and structure level in a hierarchical order. The zero-length elements are then inserted into the potential failure sections of the FE model identified by the nonlinear analysis. Each zero-length element consists of three zero-length springs representing three DOFs. Each zero-length spring is assigned with appropriate material properties and failure criterion. The DOF release is accomplished by removing the zero-length spring when its failure criterion is triggered.

To detect failure and release a DOF, two steps are added in the original computer algorithm, as shown in the flowchart in Figure 3.6. The current stress state of each zero-length spring is first checked to see if the failure criterion is reached at material level. If so, the information of the zero-length spring is recorded into a specified file. Each specified file is an execute file that includes the command of removing the zero-length spring. After all zero-length springs are checked at the material level at a given time step, the second step is taken to check the specified file and execute the command in the file and reset the file for the next time step. It is worth mentioning that when the zero-length spring is removed, all the associated information such as loads and masses to this zero-length spring will also be removed. Furthermore, the nodes connected by this zero-length spring have to be checked after the removal of the zero-length spring. If the node is 'free', it has to be removed to avoid stiffness singularity.

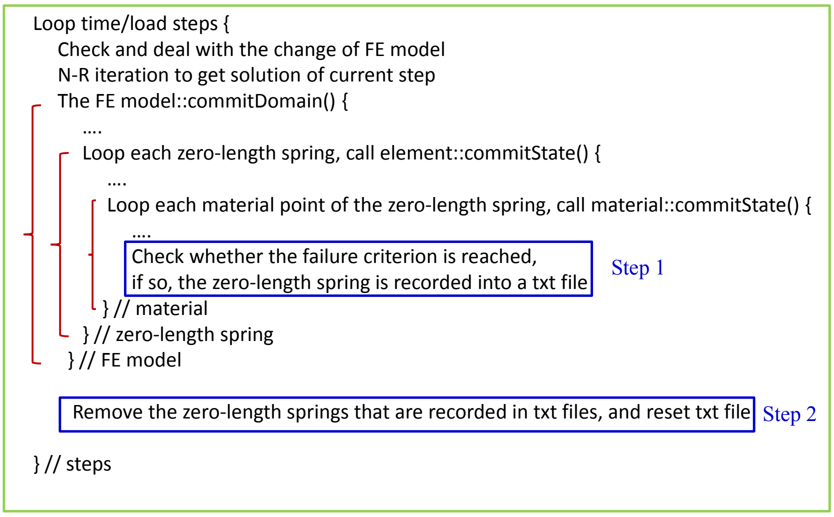

Figure 3.6 Flowchart for DOF removal

3.4 Case Studies

Three case studies are conducted to examine the feasibility and accuracy of the proposed collapse analysis procedure and the associated computer algorithms. A two-span continuous RC beam that is firmly fixed at the two ends and bears a concentrated static load at its middle support is first used to demonstrate the catenary effect by the DOF release method. Seismic collapse analysis is then carried out for a two-story RC frame using both the proposed DOF release method and the traditional element removal method, from which two different failure modes can be found.

Finally, the refined seismic collapse method is applied to a two-span RC continuous bridge structure, which is seldom investigated before.

3.4.1 DOF release to simulate catenary effect

A static collapse experiment of a two-span (2m+2m) continuous RC beam with its two ends fixed and a concentrated static load (P) acting at its middle support was conducted at Tsinghua University, China, as shown in Figure 3.7 (Lu 2013). A strongly fixed boundary condition was applied to both ends of the specimen and the boundary blocks were connected by two strong beams to control the horizontal displacement. The two boundary blocks were welded to the supporting blocks to prevent rotation. A constant vertical load was imposed on the middle support of the beam by two hydraulic jacks. The hydraulic jack above the beam imposed a constant vertical load on the top of the supporting column at the middle of the beam while the hydraulic jack under the beam is unloaded gradually to simulate the pseudo-static removal of the supporting column. The dimensional configuration and reinforcement details of the RC beam are graphed in Figure 3.8. The experimental result of the vertical load versus vertical displacement at the middle support of the beam is plotted in Figure 3.10 in solid line. It can be seen in Figure 3.10 that the vertical displacement increases gradually with increasing load until the occurrence of the plastic hinges at both ends of the RC beam. The vertical load then decreases gradually after the full development of the plastic hinges with the vertical displacement about 0.14m. Owing to the catenary effect, the vertical load can be further increased with the stiffer strength of the longitudinal reinforcement of the beam. Finally, the RC beam failed when the longitudinal reinforcement in the beam reached its ultimate strength and the vertical load reached its maximum magnitude.

Figure 3.7 Profile of a RC beam specimen (Lu 2013)

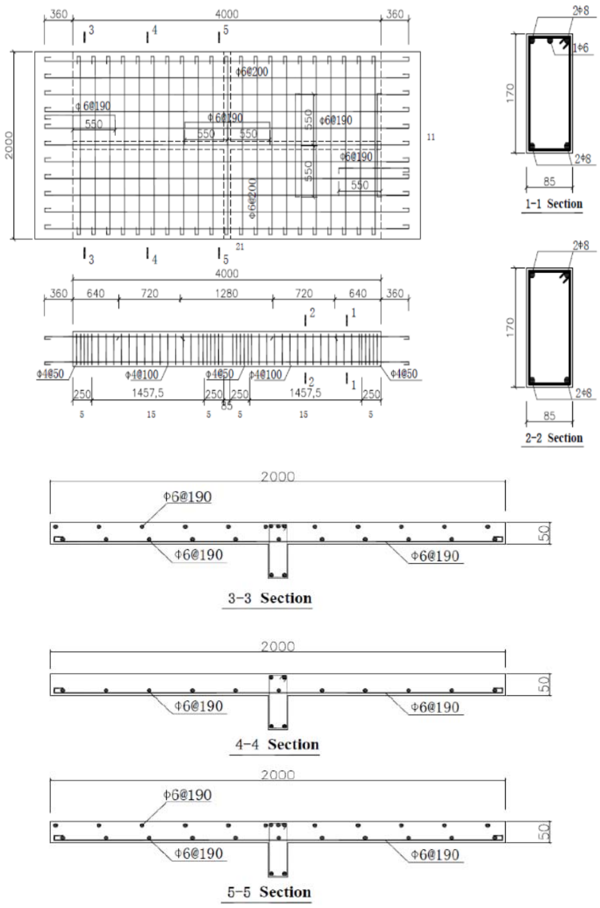

Figure 3.8 Sectional information of RC beam (Lu 2013) (Unit: mm)

The experiment above provides an opportunity to examine the proposed collapse analysis method. The FE model of the RC continuous beam is first established to perform a static nonlinear analysis. The 2-D FE model consists of 30 horizontal nonlinear fiber beam-column elements to model the RC continuous beam and one vertical zero-length spring of a constant axial stiffness to model the middle column. The Concrete and hysteretic material models in OpenSess (McKenna et al. 2007) are selected to account for the constitutive laws for concrete and reinforcement, respectively, of the RC beam. The potential failure locations are determined through the static nonlinear analysis and the failure mode for the RC beam is predicted in accordance with the provisions aforementioned. The simulation results show that the potential failure locations of the continuous RC beam are located at the two ends because the middle part of the beam was stiffened and the possible failure modes are flexural. Consequently, the zero-length element is inserted into the two ends of the RC beam to detect the flexure failure, and the final FE model for collapse analysis of the RC beam consists of the two zero-length elements, 30 fiber beam-column elements and a zero-length spring, as shown in Figure 3.9. The displacement control strategy is employed to conduct the collapse analysis. The computed relations between the vertical force and vertical displacement at the middle support of the beam are displayed in Figure 3.10, in which the curves by dash and dot-dash lines are the results acquired by the DOF release method and the traditional element removal method, respectively. There is a significant difference in the results between the test and the element removal method: the beam fails much earlier when using the element removal method because of the ignorance of the catenary effect. The proposed DOF release method, on the other hand, does predict the catenary effect. The ultimate vertical force of the RC beam obtained by the DOF release method is 75.27kN, which is close to the measured ultimate force of 78.26kN, but the ultimate force obtained from the element removal method is 50.07kN only. The ultimate force acquired from the element removal method is underestimated remarkably.

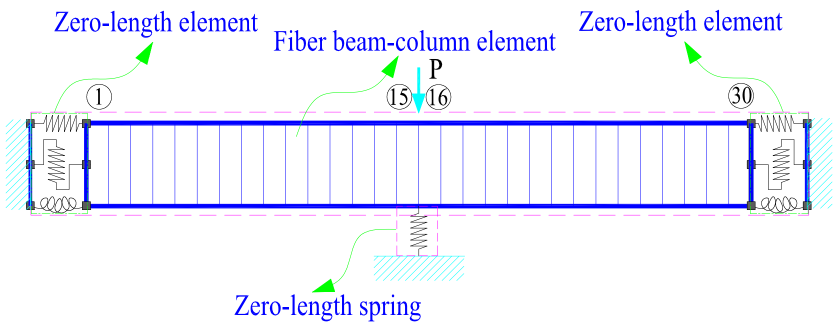

Figure 3.9 2-D FE model for static collapse analysis

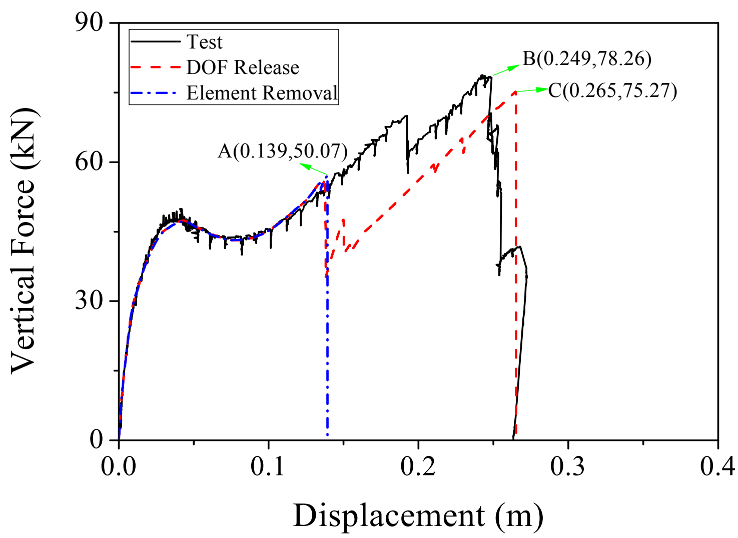

Figure 3.10 Comparison of vertical force versus vertical displacement

3.4.2 Different failure modes between element removal method and DOF release method

A two-story planar RC frame structure is taken as another case study to demonstrate the difference between the traditional element removal method and the DOF release method for seismic collapse analysis. The configuration of the RC frame is shown in Figure 3.11(a) with detailed cross-sectional reinforcement design. The total height of the RC frame is 12.0m with each story height of 6.0m and the total width of the RC frame is 16.0m with each bay of 8.0m at the second story. The cross section of all the RC columns is 90 × 90cm, whereas the cross section of all the RC beams is 80 × 80cm. The elastic modules of concrete and reinforcement are 3.0×10^4 and 2.0×10^5MPa, respectively. The diameters of longitudinal and transversal reinforcing steel are 32mm and 16mm, respectively. The longitudinal reinforcement is arranged uniformly all around the RC beams and columns with 60mm cover. The space between two neighboring hoops is 0.20m for all the columns and beams. The density of the RC frame structure is 2600kg/m^3. The 28-day compressive strength of the concrete is 30.0MPa and the yielding strength of the reinforcement is 280.0MPa.

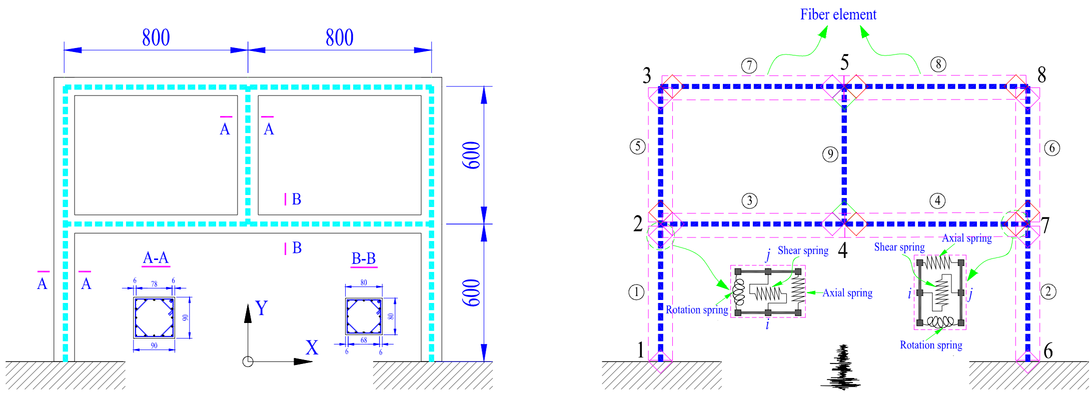

(a) (b)

Figure 3.11 Configuration for RC frame and FE model of RC frame (Unit: cm)

(a) Configuration for a RC frame (b) FE model

As mentioned before, a nonlinear FE model of the RC frame structure is essential to detect the potential failure locations before conducting a collapse analysis. The FE model of the RC frame consists of 9 nonlinear fiber beam-column elements, each of which models one structural member, as shown in Figure 3.11(b). To make sure the computation accuracy, force interpolation shape function is used for each fiber beam-column element (Neuenhofer and Filippou 1997). The Concrete 02 and hysteretic material models in OpenSess (McKenna et al. 2007) are selected to account for the constitutive laws for concrete and reinforcement of the RC frame, respectively. The lump masses are used in the FE model. The Rayleigh damping assumption is adopted to construct the structural damping matrix and the damping ratio is assumed as 0.05 for the first two mode shapes of the frame in the vertical direction.

The potential failure locations and their failure modes can be determined through a dynamic nonlinear analysis in accordance with the provisions aforementioned. An earthquake record, as shown in Figure 3.12, of an adjusted PGA of 1.326g is selected as the input excitation in the vertical direction of the RC frame for the nonlinear dynamic analysis. The maximum bending moment responses of the beam elements 3 and 4 are respectively 1991.4kN.m and 1991.5kN.m at the ends, which are more than the maximum moment capacity of 1702.0kN.m. The maximum bending moment responses of the column elements 1 and 2 are respectively 4960.5kN.m and 3375.6kN.m at the ends, which are also more than the maximum moment capacities of

2375.0kN.m and 2239.0kN.m. Nevertheless, the maximum bending moment response of the column element 5 is 65.0kN.m only at the ends, which is smaller than the maximum moment capacity. In consideration of symmetric configuration of the RC frame, the ends of all the beam elements and column elements, except the column element 5, are identified as the potential failure locations. Furthermore, the failures of all the RC beams are controlled by flexure because the shear demands of the RC beams are smaller than their shear capacities. All the RC columns are susceptible to flexure failure in terms of the flowchart plotted in Figure 3.3.

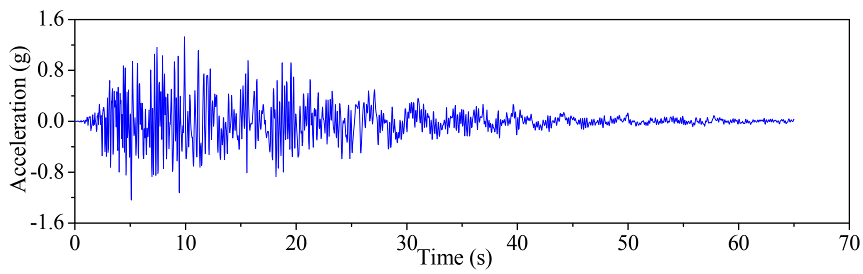

Figure 3.12 An earthquake record of an adjusted PGA of 1.326g

According to the failure locations and failure modes identified above, zero-length elements of flexural failure mode are inserted into all the potential failure locations. Consequently, the FE model of the RC frame for collapse analysis consists of 9 fiber beam-column elements and 16 zero-length elements, as shown in Figure 3.11(b).

The evolutionary seismic collapse of the RC frame predicted by the DOF release method and the traditional element removal method is demonstrated in Figures 3.13 and 3.14, respectively. From Figure 3.13, it can be seen that the flexure failure first occurs at the left end of Element 7 at 11.74s, and accordingly the zero-length element with 3-DOFs inserted into the failure location is completely removed. The second flexure failure occurs at the right end of Element 4 at 15.28s and the corresponding zero-length element is subsequently removed. The third flexural failure occurs at the left end of Element 6 at 16.0s and accordingly the corresponding zero-length element is completely removed. The fourth flexure failure occurs at the left end of Element 3 at 16.88s, and when the corresponding zero-length element is completely removed, the disproportional part of the RC frame collapses although the remaining part of the RC frame is still subject to ground excitation.

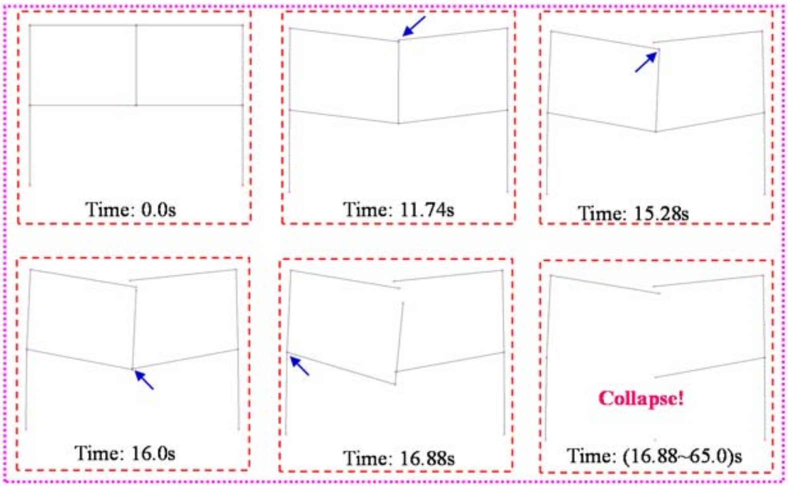

Figure 3.13 Collapse process of RC frame predicted by element removal method

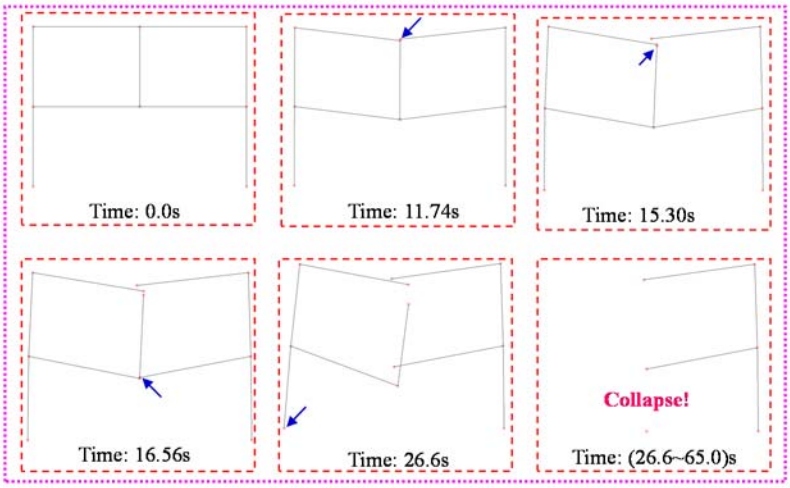

Figure 3.14 Collapse process of RC frame predicted by DOF release method

From Figure 3.14, it can be seen that the flexure failure also occurs at the left end of Element 7 at 11.74s. The rotation and shear springs in the zero-length element inserted into the failure location are accordingly released, but the axial spring still remains. The second flexure failure occurs at the right end of Element 4 at 15.3s, and accordingly the rotation and shear springs in the zero-length element inserted into the failure location are released, but again the axial spring still remains. The third flexure failure occurs at the left end of Element 6 at 16.56s, and again the rotation and shear springs in the zero-length element inserted into the failure location are released. The fourth flexure failure occurs at the bottom end of Element 1 at 26.6s, and when the zero-length element is completely removed, the disproportional part of the RC frame collapses.

The evolutionary seismic collapse analyses indicate that the first three failure locations and the corresponding failure time predicted by the traditional element removal method and the proposed DOF release method are similar but the final failure location and the failure time are quite different. The different collapse modes predicted by the two methods are used mainly because the element removal method could not consider the catenary effect but the axial springs still remain in the DOF release method that makes the failure modes different. To further demonstrate the differences in the collapse analyses by the two methods, Figure 3.15 produces the displacement time histories of Node 5 in the X and Y- directions before it detaches from the remaining frame structure. Predicted by the traditional element removal method, Node 5 detaches from Element 7 firstly and Element 4 secondly and finally it detaches from the RC frame together with Element 5 at 16.88s. Predicted by the DOF release method, Node 5 detaches from Element 7 firstly and Element 4 secondly and finally it detaches from the RC frame together with Element 5 at 26.6s. The displacement responses of Node 5 in both X and Y- directions, predicted by the DOF release method, are much larger than those using the element removal method, which demonstrates that the catenary effect plays an important role in seismic collapse. Moreover, the collapse time of the RC frame is postponed 9.72s if the refined collapse analysis method involving DOF release strategy is used.

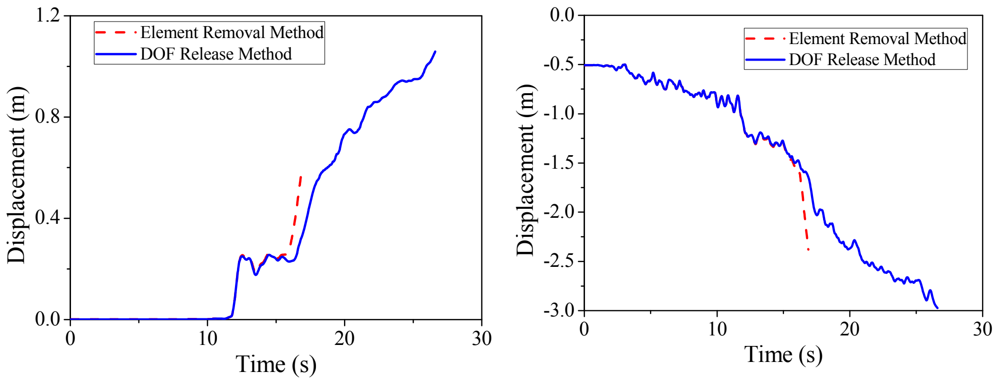

(a) (b)

Figure 3.15 Displacement time histories of Node 5 in X and Y- axes

(a) X-axis (b) Y-axis

Figure 3.16 plots the time histories of bending moment of Element 7 at its right end and Element 1 at its bottom end, respectively. It can be clearly seen that the bending moment at the right end of Element 7 fluctuates sharply around -1487.0kN.m until 11.74s when the DOFs are released at the left end of Element 7 and the bending moment varies around zero until 15.28s and 15.30s, as predicted by the element removal method and the DOF release method, respectively. By using the DOF release method, the bending moment of Element 7 then further decreases approximately from zero at 15.30s to -769.6kN.m at 26.6s when the 3-DOFs associated with the bending moment, axial and shear forces at the bottom of Element 1 are released. Afterwards, the bending moment of Element 7 increases gradually until the ground excitation disappears. However, by using the traditional element removal method the bending moment of Element 7 does not experience a sharp decrease after the zero-length element inserted into the left end of Element 7 is removed due to the so-called catenary effect. For Element 1, the bending moment at its bottom increases from a small value to about -2255.2kN.m at about 15.30s, predicted by either the method. When the element removal method is used, the bending moment then increases to about -677.7kN.m during a very short time period of 0.78s after Elements 3 and 5 are removed from the frame at time 16.88s. Afterwards, the bending moment gradually increases to about 250kN.m. It can be seen in Figure 3.13 that although Element 1 experiences severe damage, it does not collapse at the end of earthquake excitation.

However, if the DOF release method is employed, the bending moment of Element 1 at its bottom further decreases to about -2375kN.m and after 10.04s it collapses at 26.6s due to flexure failure.

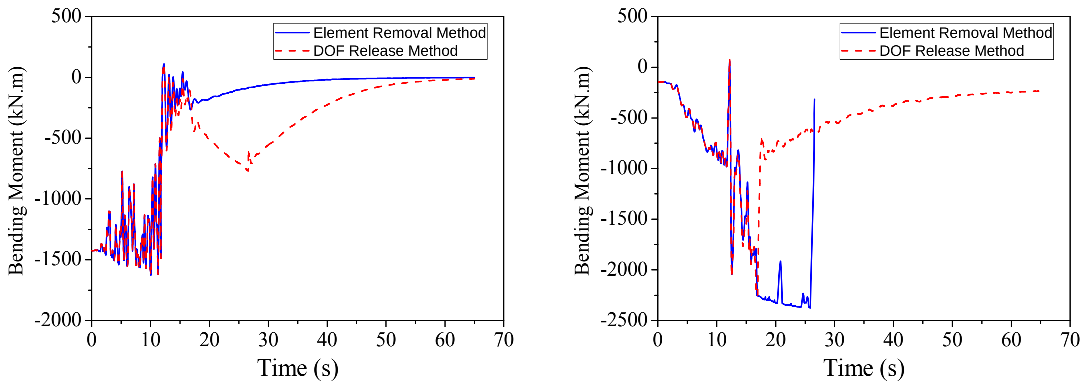

(a) (b)

Figure 3.16 Time histories of bending moment of Elements 7 and 1

(a) Element 7 (b) Element 1

3.4.3 Application of DOF release method to a continuous RC bridge

The DOF release method is now applied to a continuous RC bridge with two equal spans (2×20 m), as shown in Figure 3.17. The RC two-box girder is supported by two RC abutments at its two ends and a two-column pier at its middle. The pile foundation is employed for the two-column pier and the shallow foundation is selected for the two abutments. The height and the width of the RC two-box girder are 1.2m and 12.5m, respectively. The thickness of the top and bottom plates of the two boxes is 250mm, the thickness of two flange slabs is 300mm, and the width of the three webs is 400mm (see Figure 3.18). The clear height of the RC columns is 5.8m, and the cross section of the RC column is 0.9×0.9m. The detailed reinforcement arrangement of the two-box girder is also shown Figure 3.18. The longitudinal thread reinforcing steels are uniformly arranged around the top and bottom plates of the two boxes, the two flange slabs and the three webs of the two-box girder. The diameter of the longitudinal reinforcement along the top side and bottom side of the two-box girder is 32mm, and other longitudinal reinforcement is 26mm in diameter. The larger size hoop is arranged for the three webs and the smaller size hoop is arranged for other components of the two-box girder. The cover thickness of the two-box girder is 60mm. A total of 24 longitudinal thread reinforcing steels with a diameter of 32mm are arranged uniformly in each column with 60mm cover. The hoop spacing in the column and the girder are 400mm and 100mm, respectively. All the close hoops in the column and the girder have both 135 degree hooks at its two ends with an extension length more than 6 times the diameter of the transverse reinforcing steel. Therefore, the longitudinal reinforcing steel ratio ($A_{sl}/b_0 h$, where A_{sl} is the area of the longitudinal reinforcement and b_0 and h are the width and height of the column section, respectively) and the transverse reinforcement ratio ($A_{st}/b_0 s$) of the RC column are 0.024 and 0.00251, respectively. The density of the RC bridge is $2600\,\mathrm{kg/m^3}$. The compressive strengths of unconfined concrete (f_c') and confined concrete (f_{cc}') of the column are 30.0MPa and 30.3MPa, respectively. The compressive strengths of unconfined concrete and confined concrete of the RC girder are 40.0MPa and 52.0MPa, respectively. The yield strength and yield strain of the reinforcement are 280.0MPa and 0.0014, respectively. The ultimate tensile strain of reinforcement is 0.012 and the strain-hardening modulus is $0.015E_s$ (E_s is the elastic modulus of the reinforcement) after yielding point.

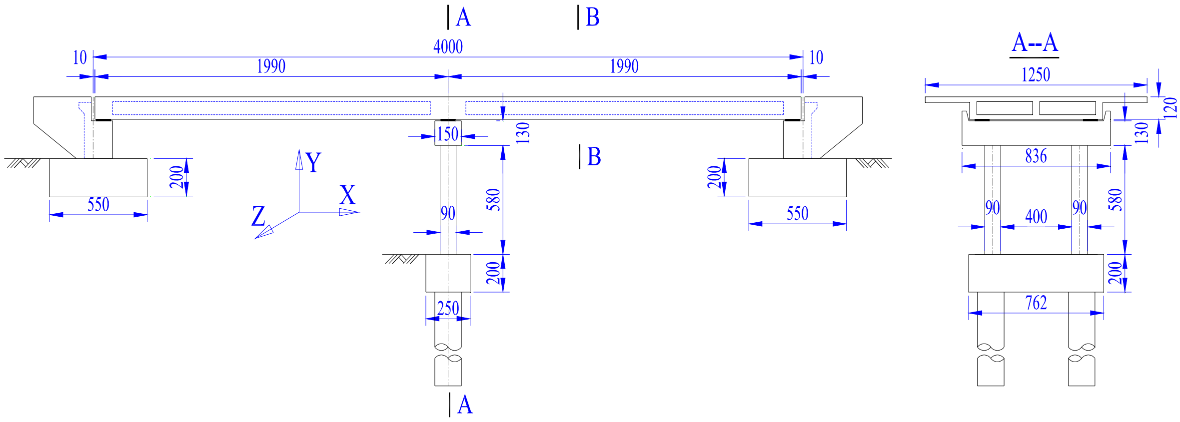

Figure 3.17 Configuration for a continuous RC bridge (Unit: cm)

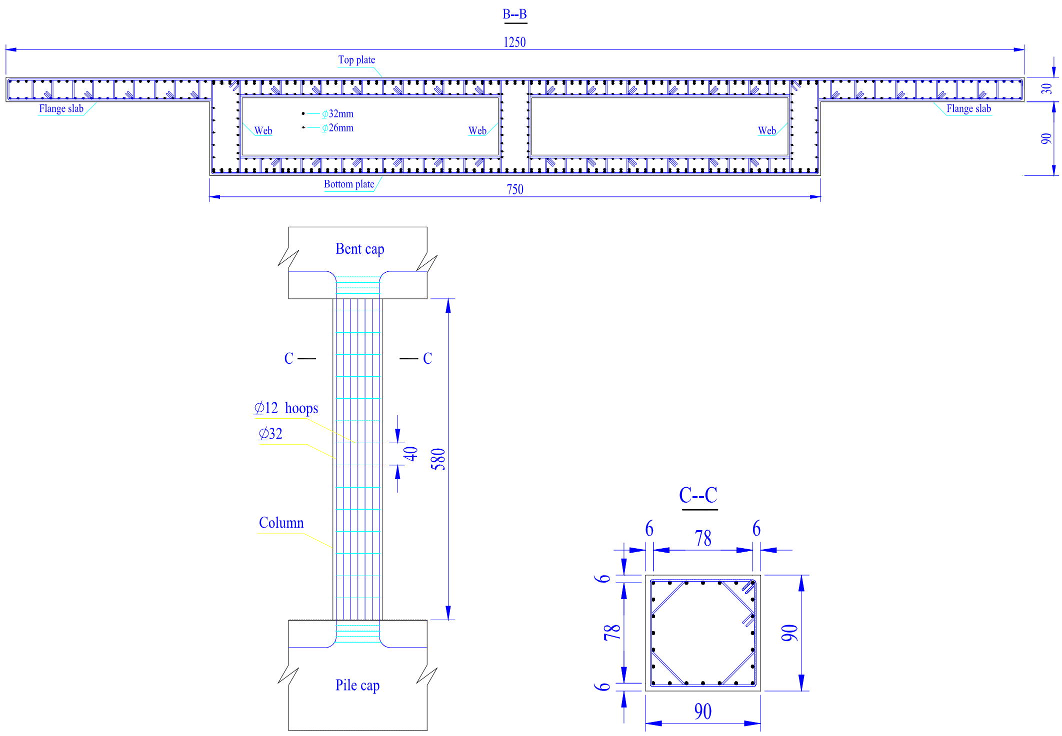

Figure 3.18 Reinforcement details of column and girder (Unit: cm)

3.4.3.1 FE model of a continuous RC bridge for seismic collapse analysis

As mentioned before, a nonlinear FE model of the RC bridge structure should be established to predict the potential failure locations before conducting a collapse analysis. The Concrete02 and hysteretic uniaxial models are respectively selected to account for the constitutive laws for concrete and reinforcement of the RC bridge structure in OpenSess (McKenna et al. 2007). A total of 28 nonlinear fiber beam-column elements and 4 elastic beam-column elements are used to model the RC bridge girder. The 4 elastic beam-column elements are used to model the transverse solid beams at both ends and the middle support of the girder because the stiffness of the transverse solid beam is very large. The bent cap and the pile cap are modeled by 6 and 4 elastic beam-column elements, respectively. Each column of the RC pier is modeled by 10 nonlinear fiber beam-column elements. The cross section of each column is discretized using 10×10 confined concrete fibers for the core concrete and 20 unconfined concrete fibers for each side of the cover concrete. The joint connections of the bent cap and the two columns are simulated by rigid elements. The similar approach is employed in the joint connections between the pile cap and the two columns. Co-rotational geometric transformations (Crisfield 1990) are employed for all the beam-column elements to account for the geometric nonlinearity. For simplicity, the soil and structural interaction is not considered in this study, and the pile cap is fixed on the ground directly without consideration of pile deformation. Since the axial and flexural stiffness of the two RC abutments is very strong, the deformation of the abutment is also negligible and the bridge girder is assumed to be connected to the ground directly. The supporting conditions of the bridge and the connection condition between the girder and the bent cap are illustrated in Figure 19 and tabulated in Table 3.1, in which the numbers 0 and 1 denote respectively free and constrained conditions of the related DOFs in the global coordinate system. The earthquake record shown in Figure 3.12 and with an adjusted PGA of 1.21g is used as the input excitation to the bridge along the Z-axis for a nonlinear seismic analysis.

Table 3.1 Supporting and connecting conditions

Bearing No.	UX	UY	UZ	ROTX	ROTY	ROTZ
I	0	1	0	0	0	0
II	0	1	0	0	0	0
III	1	1	1	0	0	0
IV	1	1	0	0	0	0
V	0	1	0	0	0	0
VI	0	1	0	0	0	0

The nonlinear seismic analysis shows that the RC girder does not experience any yielding and the two columns of the bridge pier are potential failure components. The failure mode of the RC columns is discussed as follows. The sectional bending moment capacity of the RC column is 2928.0kN.m, obtained from a standard cross-section analysis. The shear demand (V_p) is 940.8kN, acquired by the maximum moment capacity over the shear span. The shear capacity (V_0) is 1288.8kN, calculated by Eq. (3.1). Then, the DCR ($C_v = V_p / V_0$) equals to 0.73 and locates within the range $0.6 < C_v \leq 1.0$. In addition, each hoop has 135 degree hooks at both ends and each hook has a length longer than 6 times the diameter of the hoop. Consequently, the two columns are susceptible to flexure-shear-axial failure when the bridge suffers from strong earthquakes in the transverse direction of the RC bridge in accordance with the provisions described in Section 3.3 as well as the flowchart shown in Figure 3.3. Therefore, two zero-length elements are respectively inserted into the top of each RC column to detect the flexure-shear-axial failure. Consequently, the FE model for collapse analysis of the RC bridge consists of 28 nonlinear fiber beam-column elements, 13 elastic beam-column elements, 5 rigid elements and 2 zero-length elements, as shown in Figure 3.19. Each pair of nodes (Nodes 39 and 41, Nodes 40 and 42) shares the same coordinates. Node 18 is located at the middle section of the RC girder.

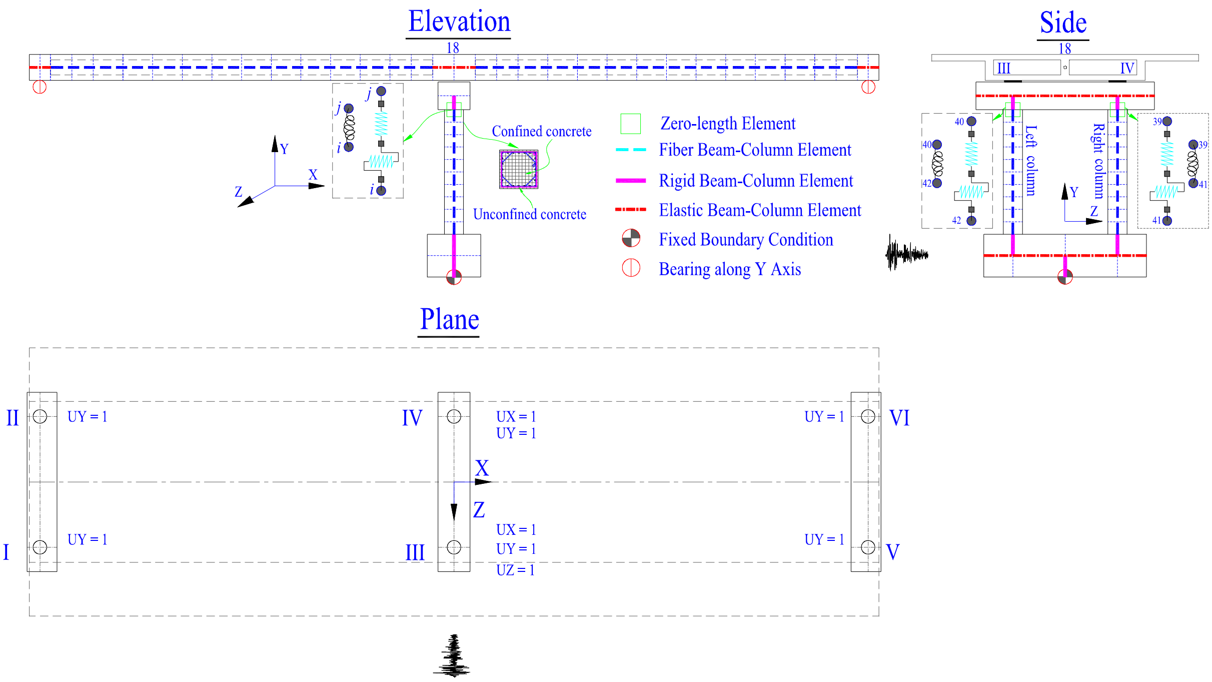

Figure 3.19 FE model for seismic collapse analysis of a RC bridge

There are totally 3250 time steps and each step is 0.02s in the collapse analysis. Two main factors are considered when selecting a proper ground motion. One is that the ground motion should have such intensity that the columns will experience flexure-shear-axial failure; the other is that the duration should be long enough so that the phenomena of axial failure after the flexure-shear failure of the columns can be observed. The Rayleigh damping (Chopra 1995) is assumed, with a damping ratio of 0.05 for the first and second modes of vibration of the bridge in the Z-axis. The

Newmark-beta method (Newmark 1959) is adopted and the minimum integration time step is 1.0×10^{-4} to ensure convergence at each time step.

3.4.3.2 Results of seismic collapse analysis

The entire progress of dynamic collapse of the RC bridge under the earthquake excitation, from flexure-shear failure to axial failure and eventually collapse, is demonstrated in Figure 3.20 and described in Table 3.2. The flexure-shear failure of the RC bridge occurs first in the left column at 6.74s and then in the right column at 8.22s. The absolute story drift ratios of the left column and the right column are 0.0297 and 0.0294, respectively, which are more than the flexure-shear failure threshold of 0.029. The two columns retain only 10% shear capacity and the story drift ratios of both columns reach 0.0396 at 12.34s, and accordingly the DOFs of the two columns associated with the shear force and bending moment about the X-axis are released. The axial failure occurs in the right column at 12.44s and in the left column at 12.46s. The story drift ratios of the left column and the right column are 0.0579 and 0.0547, respectively, which are more than the axial failure threshold of 0.051. The two columns lose their 90% axial compressive capacity and the story drift ratios of both columns reach 0.099 at 12.74s, resulting in the disproportional collapse of the continuous bridge. Fortunately, the RC girder is designed with sufficient ductility to survive earthquake without collapse. This case study demonstrates that the axial failure of the RC columns occurs later than the flexure-shear failure. The DOFs associated with the bending moment and shear forces as well as the axial force of each column are released at two different times (i.e., 12.34s and 12.74s), which cannot be predicted by using the traditional element removal method.

Table 3.2 Failure characteristics of collapse process of a RC bridge

Time	Failure condition	Story drift ratio	Absolute failure threshold	Failure location
6.74s	Detect flexure-shear failure	-0.0297	0.029.	Left column
8.22s	Detect flexure-shear failure	0.0294	0.029	Right column
12.34s	Flexure-shear failure	0.0396		Both columns
12.44s	Detect axial failure	0.0547	0.051	Right column
12.46s	Detect axial failure	0.0579	0.051	Left column
12.74s	Axial failure	0.099		Both columns

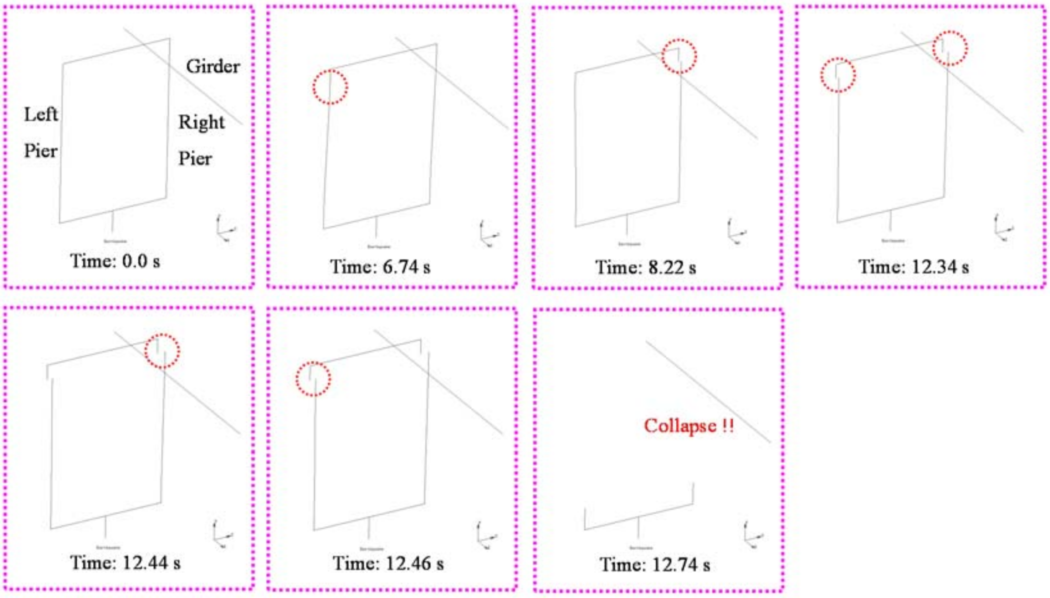

Figure 3.20 Progress of dynamic collapse of a RC bridge

As mentioned before, only the earthquake excitation in the transverse direction of the RC bridge is considered to perform a seismic collapse analysis of the bridge. The time histories of Nodes 18, 41 and 42 along the Y-axis are graphed in Figure 3.21. It can be seen that the two columns completely fail due to excessive axial load at time 12.74s. After the two columns are removed, the vertical deflection of the girder at its middle span (Node 18) drops to about -0.059m in the Y-axis. Afterwards, the RC girder experiences a free vibration and is stabilized at a vertical deflection of about -0.024m.

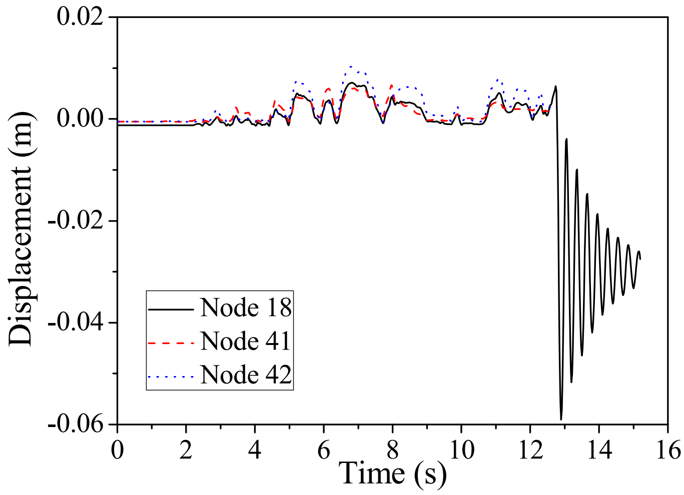

Figure 3.21 Displacement time histories of Nodes 18, 41 and 42 along Y-axis

The hysteretic response of the shear force versus story drift ratio of the left column is shown in Figure 3.22. The point A denotes that the flexure-shear failure is detected first because the absolute abscissa of the point A is 0.0297 that is more than the flexure-shear failure threshold of 0.029. The point B indicates that the left RC column fails due to the flexure-shear failure. The corresponding DOFs of the zero-length element associated with the bending moment and shear force are thus released. The point C is the failure threshold of axial failure in terms of story drift ratio and the point D presents the final story drift ratio when the left RC column fails.

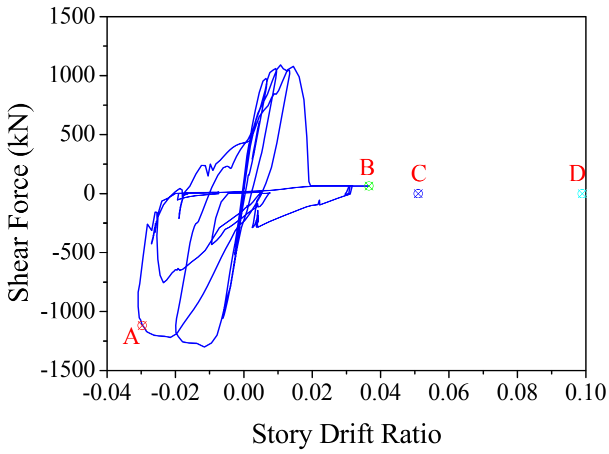

Figure 3.22 Shear force vs. story drift ratio of the left column

The hysteretic response of the shear force versus story drift ratio of the right column is shown in Figure 3.23. The point A denotes that the flexure-shear failure is detected first because the abscissa of the point A is 0.0294 that is more than the flexure-shear failure threshold of 0.029. The point B indicates that the right RC column fails due to the flexure-shear failure. The corresponding DOFs of the zero-length element associated with the bending moment and shear force are thus released. The point C is the failure threshold of axial failure in terms of story drift ratio and the point D presents the final story drift ratio when the right RC column fails.

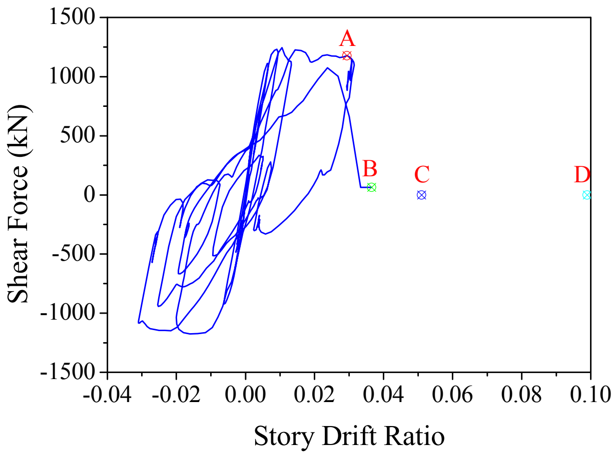

Figure 3.23 Shear force vs. story drift ratio of the right column

The vertical reaction force time-histories of the bridge girder from the left and right abutments during the earthquake are graphed in Figure 3.24. It can be seen that the vertical reaction forces at the two ends of the girder increase suddenly when the two columns at the middle span fail and are removed at time 12.74s. The dead load supported by the middle pier transfers completely to the two abutments when the axial failure occurs in the two columns. Table 3.3 lists the values of reaction forces at the two abutments and pile cap before earthquake and after collapse.

Table 3.3 Reaction forces before earthquake and after collapse (Unit: kN)

	Left abutment	Pile cap	Right abutment
Before earthquake	2943.6	5862	2943.6
Bridge collapse	4960.7	1444.3	4960.7

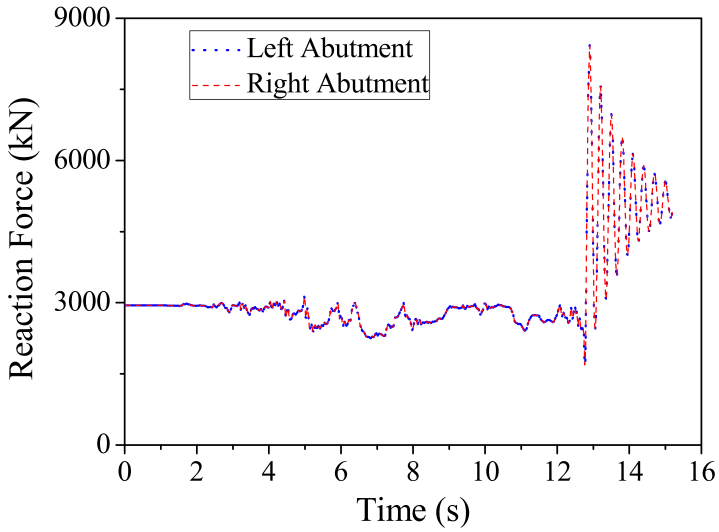

Figure 3.24 Time histories of reaction forces

3.5 Conclusions

The FE-method-based seismic collapse simulation of RC structures has been refined by introducing a new strategy of DOF release. This refined method can consider the catenary effect for RC beams and the effect of axial forces on the failure modes of RC columns. With the refined method, the zero-length element removal is a natural consequence of the release of all DOFs of the element. The refined method is implemented in an open source finite element code of OpenSees (McKenna et al. 2007). First the numerical results of the collapse of a two-span RC continuous beam with its two ends fixed under a concentrated static load was compared with the test results, with the comparison results showing that the DOF release method gave a better agreement with the measured results than the traditional element removal method. Then, the refined seismic analysis method was applied to a two-story RC frame structure to demonstrate the entire progress of dynamic collapse, with the numerical results demonstrating again that the proposed method gave more reasonable collapse results by taking the catenary effect into account than the traditional element remove method. At last, a two-span continuous RC bridge with a two-column pier at its middle was taken as an example to demonstrate the applicability of the refined method to RC bridge structures. The results showed that the collapse of the RC columns did not occur immediately after the DOFs associated with bending moment and shear force of the two columns were released, and that the final collapse of the two columns was due to excessive axial loads. This failure mode could not be predicted by the traditional element remove method. Therefore, the refined method based on DOF release is preferable to the seismic collapse analysis of RC structures including RC bridge structures.

CHAPTER 4

SHAKE TABLE COLLAPSE TESTS OF A RC CABLE-STAYED BRIDGE

4.1 Introduction

Many reinforcement concrete (RC) building structures that did not have sufficient detailing in earthquake-prone zones experienced severe damage or collapse, as presented in Chapter 2 and Chapter 3. Various kinds of numerical failure models have been proposed and developed for investigating the collapse mechanism of such failure-vulnerable RC building structures. Meanwhile, researchers have conducted experimental investigations on the earthquake-induced collapse of RC building structures. However, few numerical studies are conducted to find the collapse mechanism of RC bridge structures and even less experimental studies are performed on the earthquake-induced collapse of RC bridge structures.

Although many numerical collapse investigations on RC building structures have been performed, many uncertainties exist in the current finite element (FE) model-based dynamic collapse analyses. The material properties of concrete and reinforcement used in the current numerical collapse analysis are selected according to the design codes or specification, but the material properties of concrete actually vary with time. The compressive strength of concrete can be enhanced by confinement of stirrups, but such confinement effect can be considered only in terms of the empirical formula (Priestley et al. 2007) in the current numerical collapse analysis. The strength of reinforcement can also be increased if it is embedded in concrete, but this strengthening effect can only be considered empirically. The internal forces in different components of a RC building structure may redistribute because of different construction procedures and/or the shrinking and creeping effects of concrete, but such effects cannot be taken into consideration in the current numerical collapse analysis. A RC building structure may already suffer from some damage during its service time and its material properties are no longer linear and elastic. Such damaged conditions cannot be estimated and taken into account in the current numerical collapse analysis. The aforementioned uncertainties also exist in the FE model-based seismic collapse analysis of RC bridge structures. Although researchers carried out experimental investigations trying to verify the numerical results of seismic collapse, the aforementioned uncertainties related to long-term effects of RC structures were not considered. The accuracy of the current seismic collapse analysis of RC structures is therefore a problem.

In recent years, structural health monitoring (SHM) systems have been installed in some of important RC structures to monitor their functionality and safety. This thesis aims to propose a SHM-based seismic collapse prognosis method for RC structures subject to earthquake excitation. The measurement results (structural responses and ground motions) from the SHM system will be used to update the FE model of the RC bridge structure in two stages: (1) linear updating of the RC structure under small earthquake; and (2) nonlinear updating of the RC structure under moderate and severe earthquake. The updated FE model will best represent the prototype because the adverse effects of the uncertainties are eliminated through the model updating. The seismic collapse prognosis will then be conducted using the updated FE model. The future performance of the RC structure subject to future earthquake will be predicted, and the collapse prognosis of the future earthquake causing structure collapse will be performed.

To examine the feasibility and correctness of the proposed SHM-based seismic collapse prognosis method, a scaled RC cable-stayed bridge is designed, constructed, and tested in the Structural Dynamic Laboratory of The Hong Kong Polytechnic University. The scaled RC cable-stayed bridge model was built with reference to a real RC foot cable-stayed bridge located in an earthquake-prone zone. The design and constriction details of the RC bridge structure will be introduced in this chapter. A comprehensive SHM system was also designed and installed on the bridge structure. A series of the shaking table tests was performed until the bridge structure partially collapsed. The shaking table tests were carried out in four stages in terms of four intensity levels of earthquake: small earthquake, moderate earthquake, large earthquake, and collapse earthquake. For the small earthquake test, the test data acquired from the SHM system will be used to update the FE model of the intact RC bridge through the linear model updating method discussed in Chapter 5. For the moderate earthquake test, the test data acquired from the SHM system will be used to update the FE model of the slightly damaged RC bridge through the nonlinear model updating method discussed in Chapter 6. For the large earthquake test, the tests data acquired from the SHM system will be used to update the FE model for the severely damaged RC bridge in Chapter 7. The updated FE model will then be assigned with the zero-length failure elements and the corresponding failure criteria and it will be finally used for seismic collapse analysis and prognosis in Chapter 7. For the collapse earthquake test, the tests data acquired from the SHM system will be used to compare with the numerical results from the collapse prognosis to examine the feasibility and accuracy of the proposed collapse prognosis method in Chapter 7. Of course, in addition to the test data recorded for the subsequent analyses, the structural behavior and the collapse process of the RC bridge structure under four levels of earthquake excitation were clearly observed during the entire shaking table tests.

4.2 Bridge Model Design and Construction

4.2.1 Prototype RC cable-stayed foot bridge

The RC cable-stayed foot bridge built in 2004 and located at Jiangsu Province of China is used as the prototype for the bridge model design and construction. It is a single tower RC cable-stayed bridge with two stay cable planes. The bridge has a main span (on the west side) of 24.4m and an overall length of 38.9m. The width of the Π type girder cross section is 10.9m. The height of the tower is 19.27m, measured from the base to the top of the tower. A partial east span of 3.6m near the east side pier, where the cross section is heightened from 1.0m to 1.44m, is designed to balance the dead loads of the east side span and the main span. The RC girder and transverse beam are rigidly connected to the RC tower. The bearing conditions at the two south and north side piers are of different types: (1) the movements of the twin-girder at the north piers are free in the longitudinal and transversal directions but fixed in the vertical direction; (2) the movements of the twin-girder at the south piers are free only in the longitudinal direction. The stay cables are anchored to the twin-girder and the tower legs. Because this cable-stayed bridge was not designed against earthquake, the spacing between the two neighboring stirrups in both the RC tower legs and the side RC piers is 0.48m only. The configuration of the entire RC cable-stayed bridge and the detailed reinforcements of each component are shown in Figure 4.1.

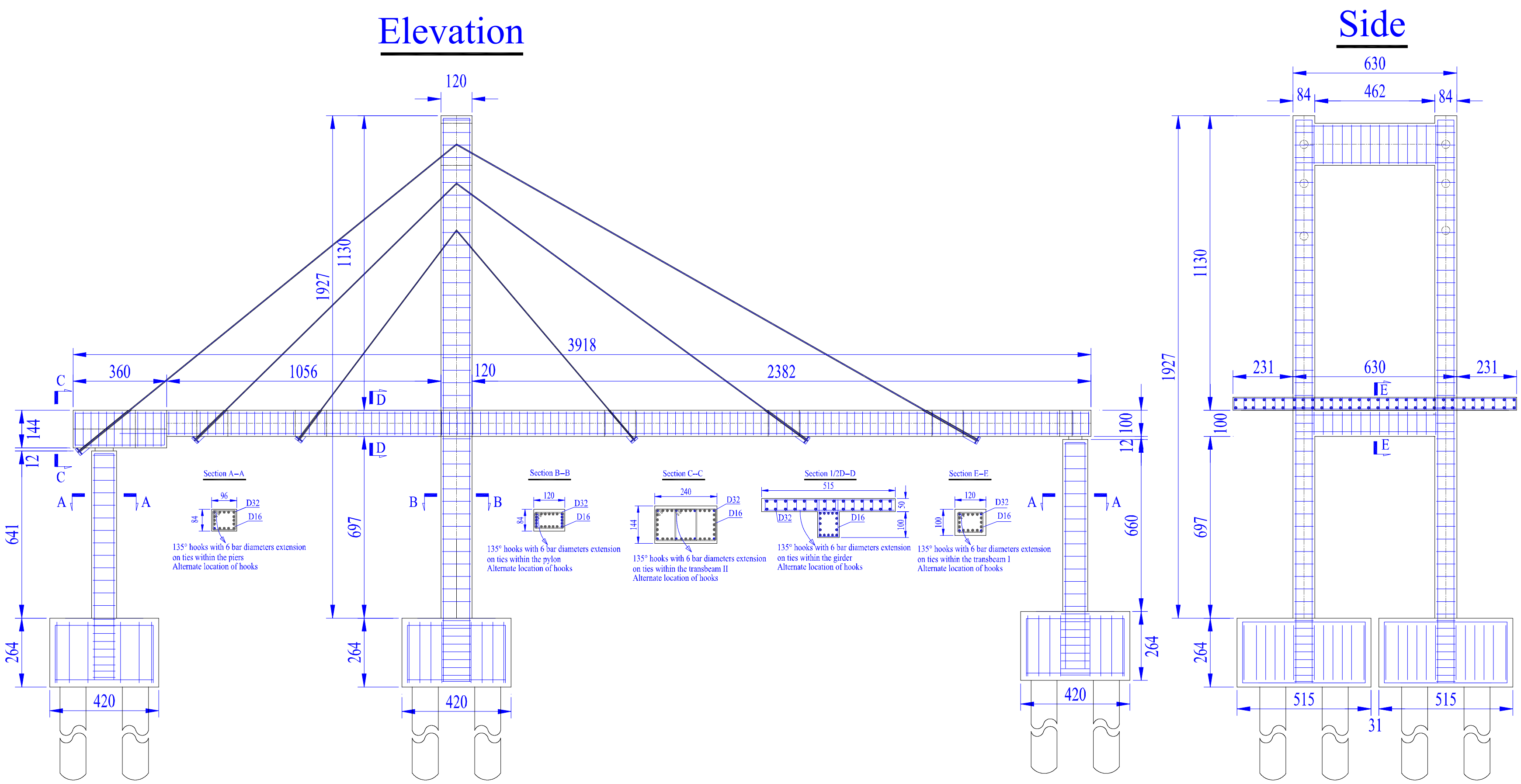

Figure 4.1 Configuration of the prototype RC cable-stayed bridge with detailed design of reinforcement (Unit: mm)

4.2.2 Design principles of the bridge model

The main information of the shake table in The Hong Kong Polytechnic University is available before the design of the RC cable-stayed bridge model. The shake table size is 3×3m. The maximum displacement and velocity of the shake table are 100mm and 500mm/second, respectively. The maximum peak acceleration of the shake table is 1.0g along single direction. The range of working frequency of the table is from 0 to 50Hz and the maximum overturning moment of the shake table is 100kN.m. In consideration of the maximum table length available, the geometric (length) ratio (length of model over length of prototype) is selected as 1/12 with reference to the laws of similarity (Moncarz and Krawinkler 1981), as shown in Figure 4.2. Similar to the prototype bridge, the RC was used as the main material to construct the scaled bridge model. According to the laws of similarity (Moncarz and Krawinkler 1981), if the construction materials of the prototype and the scaled model are the same, the Young's modulus ratio (modulus of model over modulus of prototype) is equal to 1.0. If the laws of similarity are satisfied, the test results should not be affected. To satisfy the fully similarity with respect to the density, a total of 3.06 tons supplementary mass should be added on the bridge model to yield a density ratio (density of model over density of prototype) of 12.0. However, for limited space available on the bridge model, only 1.51 tons supplementary masses were added on the girder and tower of the bridge. As a result, the density ratio is 6.4. The law of similarity also requires a time ratio (time of model over time of prototype) of 0.21. Because the capacity of the shake table is limited, only a time ratio of 0.25 is used. Therefore, the test results of the bridge model could not be scaled back exactly to the prototype.

According to this length ratio, the physical bridge model has a main span (west side) of 2.035m and a side span (east side) of 1.230m. The heights of east and west RC piers are 0.52m and 0.55m, respectively. The height of the RC tower is 1.606m, measured from the base level to the top of the tower. Similar to the prototype bridge, a length of 0.3m girder is designed at the end of the east span, where the cross section is heightened from 0.083m to 0.12m, to balance the dead loads due to the different lengths of two spans. The entire RC twin-girder is 3.265m long and connected by 8 RC transverse beams. To well simulate the damaged conditions of the RC bridge suffered from earthquakes, the original materials of concrete and reinforcement are chosen for the scaled RC bridge model. The similarity laws require the similarity of the reinforcement ratio rather than the size of the reinforcement. Therefore, the similar reinforcement ratios of the prototype and the model shall be used. In this study, the ratios of longitudinal reinforcement in the tower of the prototype and bridge model are 1.44% and 1.61%, respectively, which are quite similar. The ratios of transverse reinforcement in the tower of the prototype and bridge model are 0.38 % and 0.46%, respectively. The ratios of longitudinal reinforcement in the pier of the prototype and bridge model are 1.60% and 2.02%, respectively. The ratios of transverse reinforcement in the pier of the prototype and bridge model are 0.48% and 0.59%, respectively. In consideration that the sizes of the cross sections of the pier, tower and girder of the bridge model are small, the largest aggregate size used in concrete mixing is 10 mm. The twisted reinforcing steel with a nominal diameter of 6mm is used as the longitudinal reinforcement, and the reinforcing wire with a diameter of 3.25mm is used as the stirrup. Each stay cable consists of 19 strands of parallel steel wires with a diameter of 0.6mm, and the resultant cable has an overall diameter of approximately 3mm. Although these sizes do not follow the length ratio of 1/12, they will not significantly affect the test results. The primary properties of the materials (concrete, reinforcing steel and stay cable) of the RC bridge model are tested at the beginning of the shaking table tests and tabulated in Tables 4.1 and 4.2, respectively. The tested strain versus stress relationships of the longitudinal reinforcing steels and the stirrups are plotted in Figures 4.3, respectively. A group of three cylinder concrete specimens are tested to find out the compressive strengths and the elastic modulus, where the average values are taken as the initial values for establishing the FE model of the RC bridge in Chapter 5. Similarly, three twisted reinforcing steel specimens and three stirrup specimens are respectively tested to determine the yielding strength and the elastic modulus, where the average values are also taken as the initial values for establishing the FE model of the RC bridge in Chapter 5.

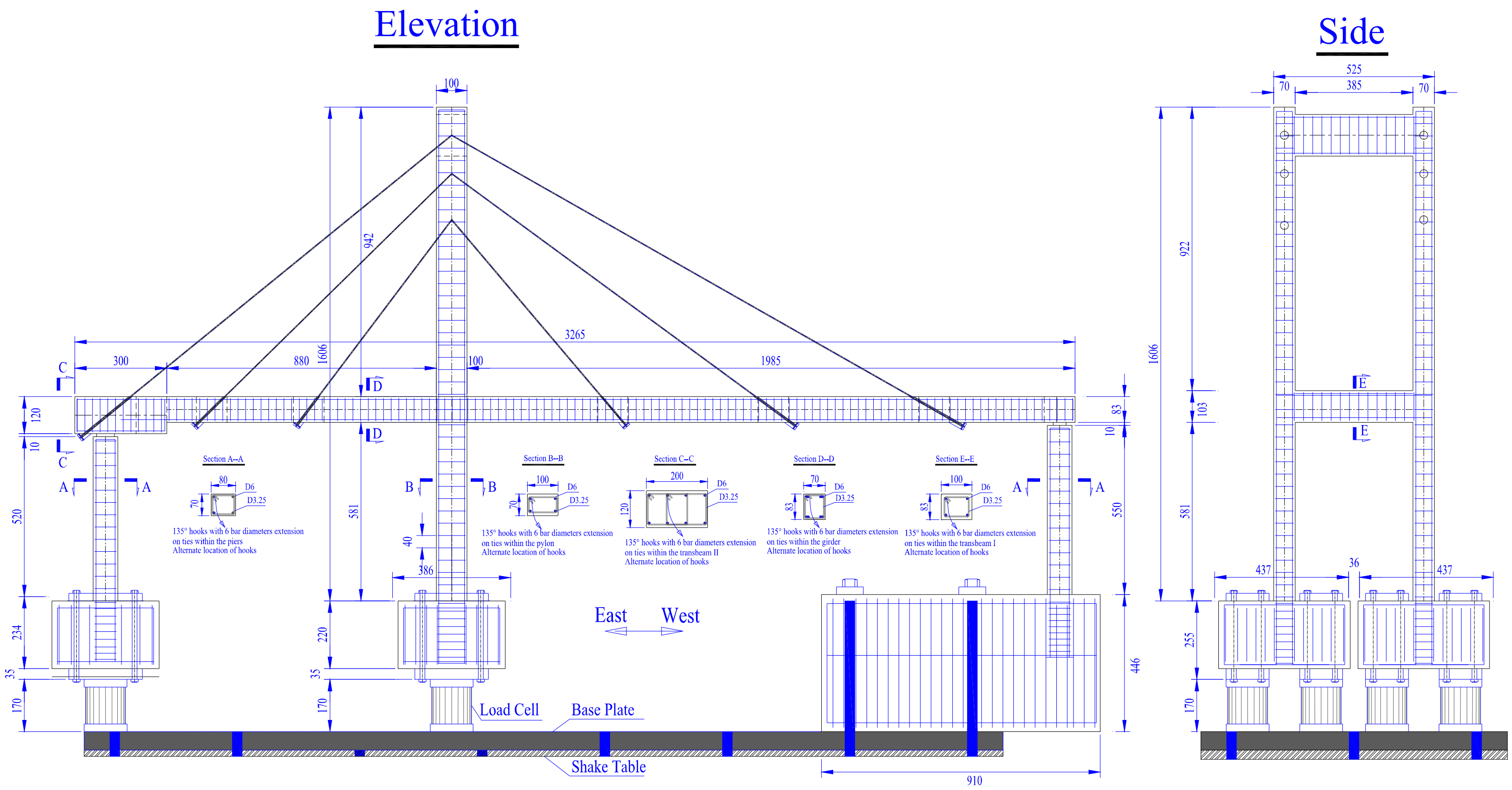

Figure 4.2 Configuration of the 1:12 scaled RC cable-stayed bridge and detailed design of reinforcement (Unit: mm)

As the twin-girder bear a large amount of additional masses in the shake test, it is elaborately designed strong enough to prevent damage. The design of the RC piers and tower of the prototype do not comply with the specifications of seismic codes and the spacing of stirrup in these components is quite light. In the bridge model, these components are also designed relatively weak so that these components will trigger collapse of the RC bridge model subject to severe earthquakes. In brief, the two RC tower legs are designed and expected to sustain flexure-shear failure as described in Chapter 3. The four side RC piers are designed and expected to be flexure failure.

Table 4.1 Average values from concrete tests

f_c' (Transverse beam)	44.2 MPa
f_c' (Foundation)	44.5 MPa
f_c' (Girder, Tower and Pier)	36.7 MPa
E_c (Transverse beam)	3.4×10^4 MPa
E_c (Foundation)	3.4×10^4 MPa
E_c (Girder, Tower and Pier)	3.3×10^4 MPa

(a)

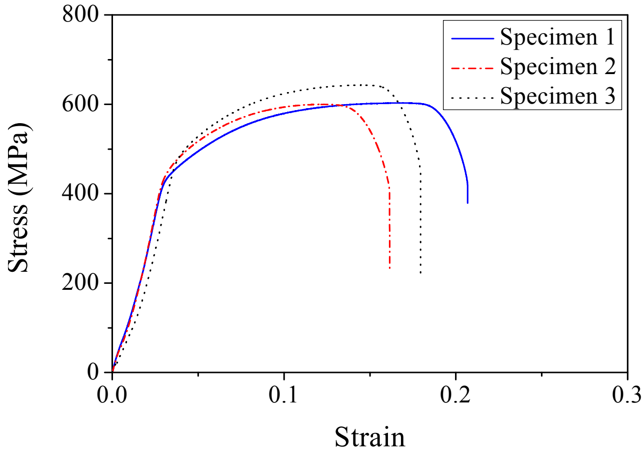

(b)

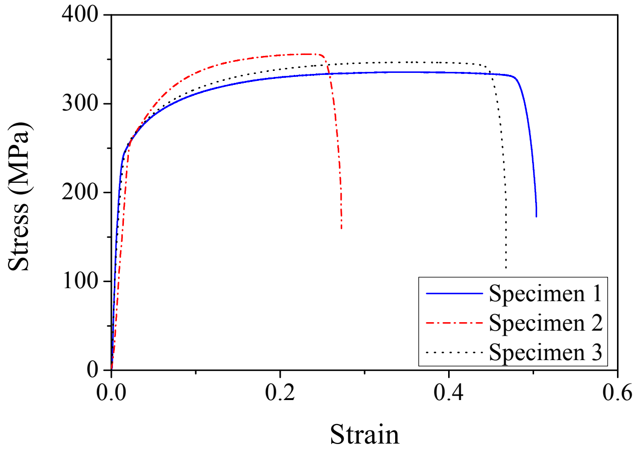

(c)

Figure 4.3 Strain-stress relationships of reinforcing steel specimens

(a) Tensile test of reinforcing steel (b) Strain vs. stress relationship of longitudinal reinforcing steel specimens (c) Strain vs. stress relationship of stirrup specimens

Table 4.2 Average values from reinforcement and stay cable tests

f_y (Longitudinal reinforcement)	446.0 MPa
E_y (Longitudinal reinforcement)	2.33×10^5 MPa
f_y (Stirrup)	245.7 MPa
E_y (Stirrup)	2.13×10^5 MPa
E_y (Stay cable)	6.18×10^4 MPa

4.2.3 Component design

The properties of the concrete and reinforcement designed to construct different RC components of the cable-stayed bridge model are identical.

4.2.3.1 RC Piers

The cross section of the four RC piers is 0.070m wide and 0.08m high. The heights of the east and west piers are 0.52 and 0.55m, respectively. The longitudinal reinforcing steel has a nominal diameter of 6mm with an average yielding strength of 446.0MPa. The internal distance of neighboring stirrups is 0.04m with a diameter of 3.25mm and with the yielding strength of 245.7MPa. All stirrup hooks are 135° bend plus 6 bar diameters extension. The Figure 4.4 shows the configuration and reinforcing steel of the four side RC piers.

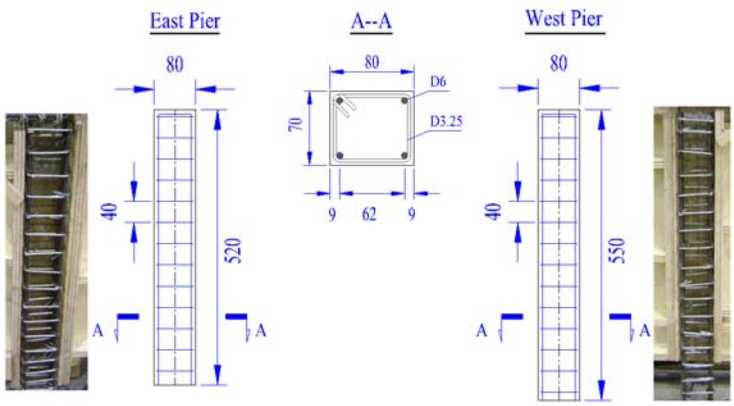

Figure 4.4 Configuration of piers and detailed design of reinforcing steel (Unit: mm)

4.2.3.2 RC tower

The RC tower consists of two tower legs and two transverse beams. The height of the two tower legs is 1.606 m. The cross section of each tower leg is 0.07m wide and 0.1m high. The cross section of the top transverse beam of the tower is 0.1m wide and 0.135m high, and the cross section of the bottom transverse beam is 0.103m wide and 0.115m high. The spacing between neighboring stirrups in the tower leg is 0.04m, and it is the same as that in the side RC piers. The spacing between neighboring stirrups of the two transverse beams is 0.25m. The Figure 4.5 shows the configuration and reinforcing steel of the RC tower.

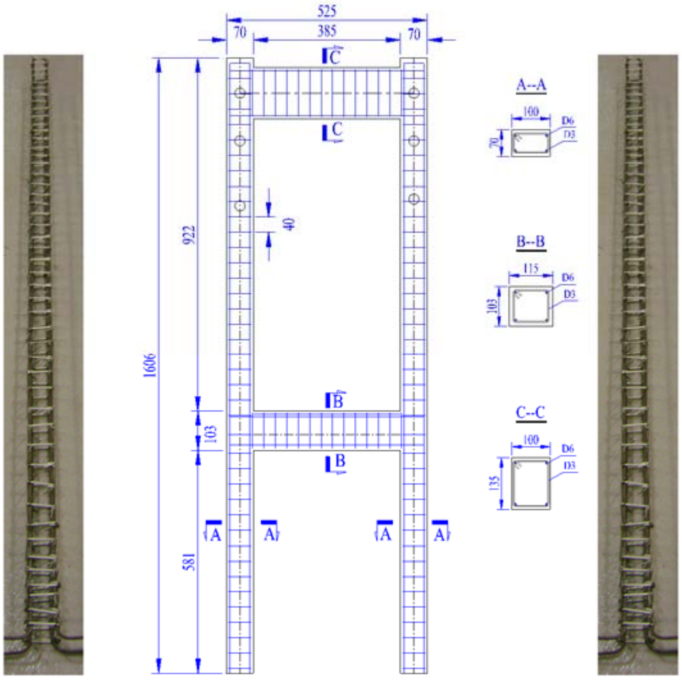

Figure 4.5 Configuration of tower and detailed design of reinforcing steels

(Unit: mm)

4.2.3.3 RC twin-girder and transverse beams

The RC twin-girder consists of two girders and eight RC transverse beams (including the bottom transverse beam of the tower), as shown in Figure 4.6 (a). The RC twin-girder is 3.265m long, and each of the RC transverse beams is 0.455m long measured from the centerlines of the two girders. The standard cross section of the girder is 0.07m wide and 0.083m high but the cross section of the east-side girder of 0.3m long is 0.07m wide and 0.12m high. The standard cross section of the transverse beam is 0.1m wide and 0.083m high but the heightened cross section of the east-side transverse beam is 0.2m wide and 0.12m high. Apart from the heightened part of the girder, a total of 8 longitudinal reinforcing steels are arranged with two at each of the four corners of the girder, as shown in Section B-B in Figure 4.6 (b). In the heightened part of the girder, four more longitudinal reinforcing steel are added. Similarly, a total of 4 longitudinal reinforcing steels are arranged at the four corners of each transverse beam. The spacing between neighboring stirrups in the two girders and the transverse beams is 0.025m. The detailed arrangement of the longitudinal reinforcement of the girders and the transverse beams can be seen from Figure 4.6 (b). Since the two girders and eight transverse beams are the main components to sustain the additional mass blocks, the areal ratio of the longitudinal reinforcement of the girder is much higher than those of the tower leg and side pier. The volumetric ratios of the stirrup of the girder and transverse beam are higher than those of the tower leg and side pier. Thus, they are not expected to be damaged during the tests.

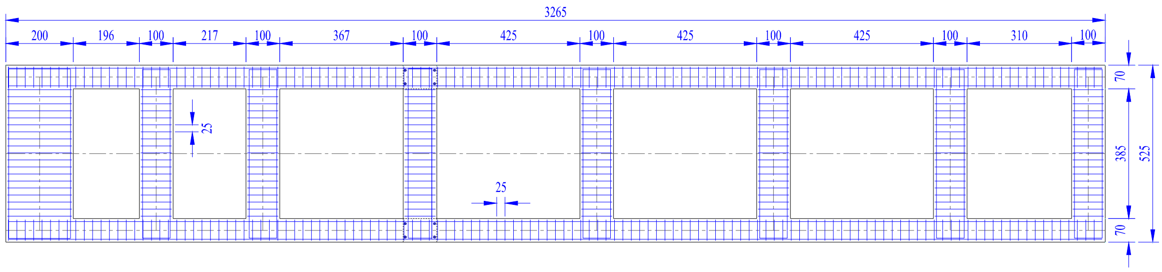

(a)

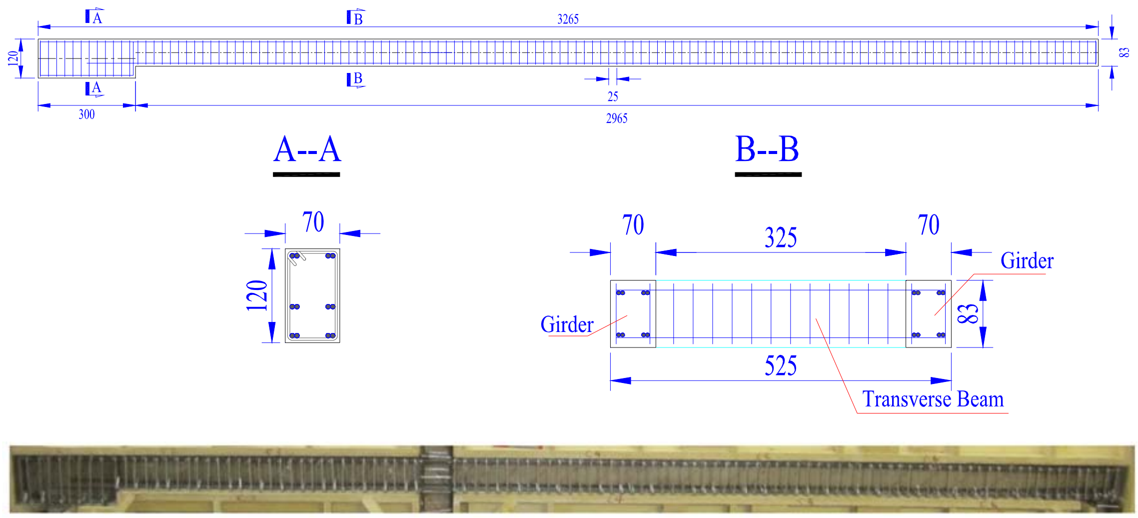

(b)

Figure 4.6 Configuration of girders and transverse beams with detailed design of reinforcing steels (Unit: mm)

4.2.3.4 Stay cable

A total of 12 stay cables are used to connect the bridge girder to the tower. Each stay cable consists of 19 parallel steel wires with a diameter of 0.6mm, and the resultant cable has an overall diameter of approximately 3mm. The six pairs of stay cables and their cable numbers are plotted in Figure 4.7. Each of the stay cables is anchored to the bottom of the main girder and rigidly connected to the tower leg, as shown in Figure 4.7. The length of each cable, measured from the connection point of the cable at the centerline of the girder to the connection point at the centerline of the tower, is listed in Table 4.3.

Table 4.3 Length of stay cables

Cable (No.)	Length (m)	Cable (No.)	Length (m)
c1	1.445	c7	1.445
c2	1.096	c8	1.096
c3	0.773	c9	0.773
c4	0.810	c10	0.810
c5	1.300	c11	1.300
c6	1.810	c12	1.810

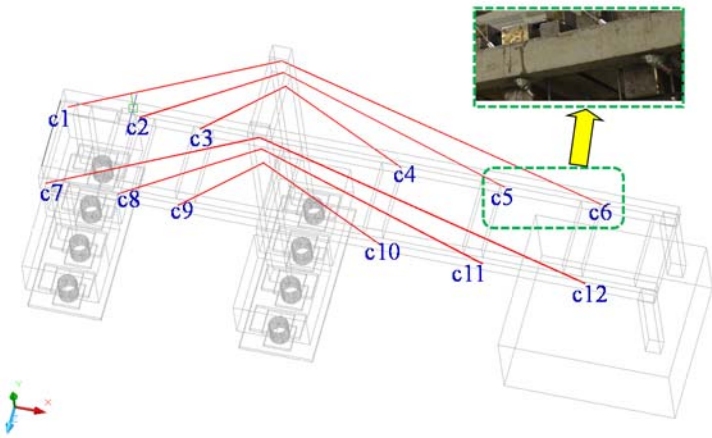

Figure 4.7 Number and anchorage of stay cables

4.2.3.5 Bearing conditions

In the bridge model, the RC girder and transverse beam are rigidly connected to the RC tower. The bearing conditions at the two south and north side piers are of different types: (1) the movements of the twin-girder at the south piers are free only in the longitudinal direction, and (2) the movements of the twin-girder at the north piers are free in the longitudinal and transversal directions but fixed in the vertical direction. Accordingly, in the bridge model, the bearing at the south pier was fabricated by two steel plates with a narrow gap and a steel bolt, as shown in Figure 4.8 (a), and the bearing at the north pier was fabricated by two steel plates with a wide gap and a steel bolt, as shown in Figure 4.8 (b).

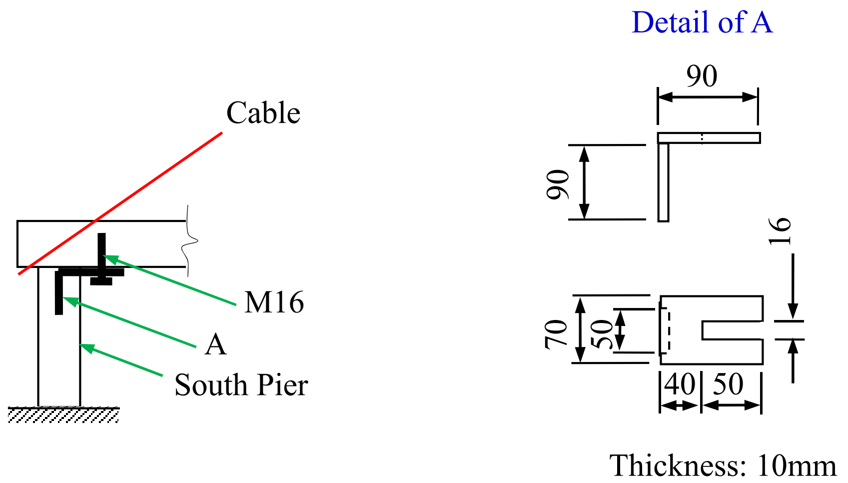

(a)

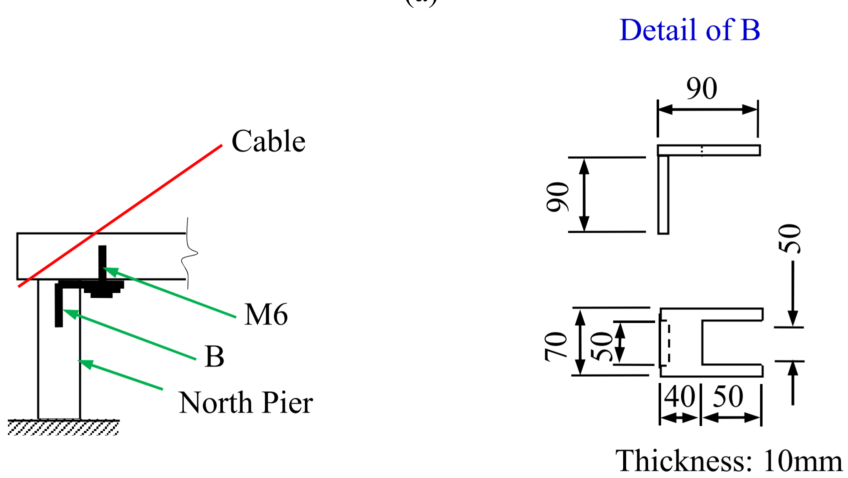

(b)

Figure 4.8 Bearing conditions between girders and side piers (Unit: mm)

(a) At the south side (b) At the north side

4.2.4 Construction of the bridge model

4.2.4.1 Fabrication of bridge components

As the size of the bridge model and the spacing of the stirrup both are small, it is very difficult casting and vibrating concrete during the construction of the bridge model. Therefore, two cross frames respectively made up of one girder and one tower leg were placed at full length on the ground for casting and vibrating concrete in situ (see Figure 4.9). A total of 6 steel tubes were embedded in each girder so that the stay cable can be anchored on the girder afterwards. In addition to the reinforcement work of the girder and tower, the partial reinforcement works of the nine transverse beams were also made before the concrete casting of the cross frames. The four RC side piers were also casted together with the cross frame in situ. Nevertheless, because the two side piers were separated from the cross frame in structure, two pieces of wood plate were placed at the connective locations between the frame and the piers during casting to separate one from another. Figure 4.9 shows the formwork of the two cross frames and the four side piers.

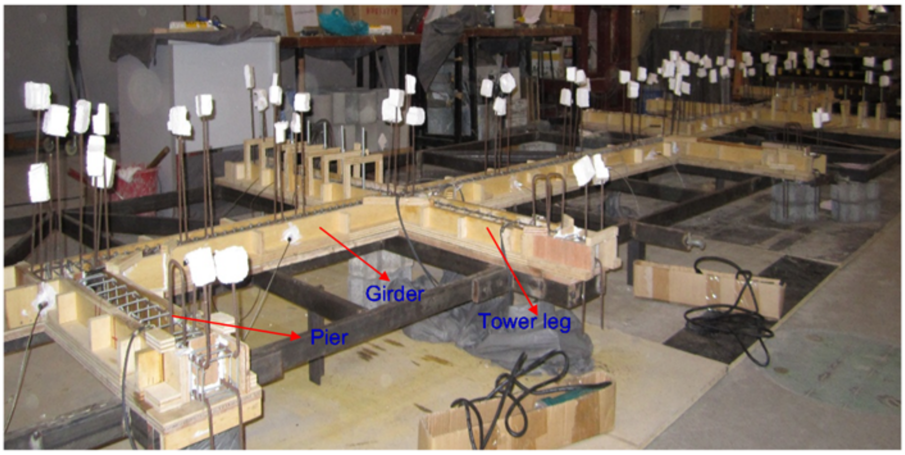

Figure 4.9 Formwork of two cross frames and four side piers

After a 28-day maintenance in moist environment, the two cross frames were elected in the vertical position, as shown in Figure 4.10. The further reinforcement works of the nine transverse beams and the five foundations were carried out. The five foundations were placed at the bottom of each east pier, each tower leg and both west piers. The two west piers shared one foundation which was made relatively large to consider the installation condition of the entire bridge model on the shake table as the length of the RC cable-stayed bridge is longer than the shake table. The transverse beams and foundations were finally assembled into a formwork and poured with concrete. Figure 4.10 shows the cross formwork of the nine transverse beams and the five foundations in the laboratory.

Figure 4.10 Formwork of nine transverse beams and five foundations

4.2.4.2 Fabrication and calibration of load cells

To indirectly measure the time-varying responses of the southeast pier and two tower legs at their bottom sections during the shaking table test, a total of 6 load cells had been designed and manufactured in the Structural Dynamics Laboratory of The Hong Kong Polytechnic University. To facilitate the installation of the bridge model on the shake table, two more dummy load cells were made to connect the foundation of the northeast pier to the shake table. The load cell was made up of a top steel plate, a bottom steel plate and an elastic steel cylinder body, as shown in Figure 4.11. In order to ensure the shear and axial stiffness of the load cell are rigid enough to sustain the RC cable-stayed bridge, two 18mm-wide steel plates and a 10mm-thick steel cylinder were welded together as the main loading body of the load cell. An appropriate electric bridge was designated by connecting 12 strain gauges to measure various reaction forces (axial force, shear force, bending moment, and torsion moment).

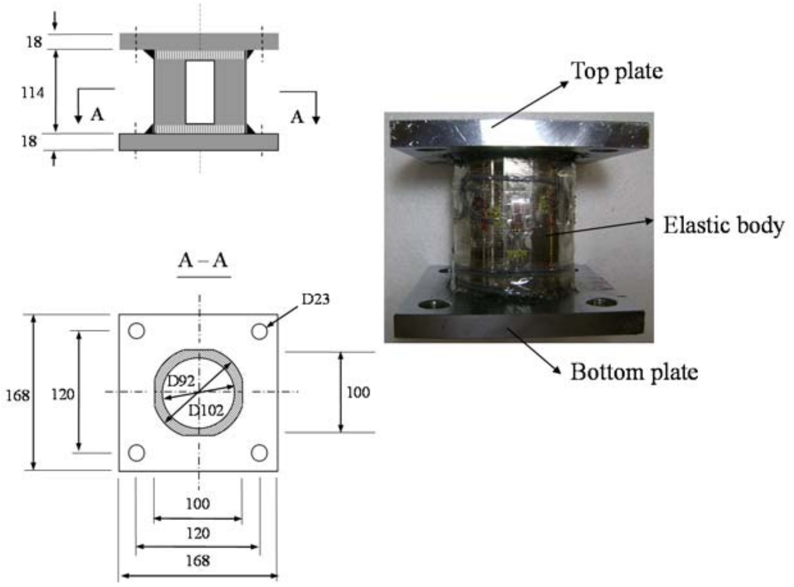

(a)

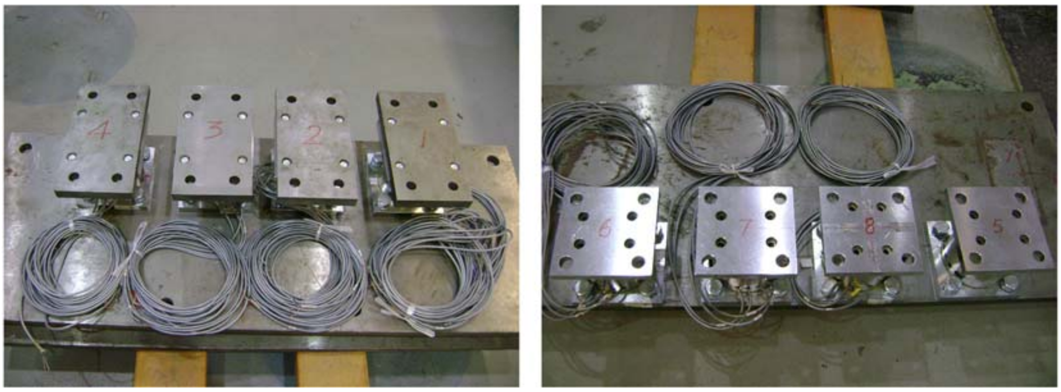

(b)

Figure 4.11 Calibration and installation of load cells

(a) Configuration of load cell (Unit: mm) (b) Installation of load cells

Six load cells were respectively calibrated before they were mounted to the foundations of the RC cable-stayed bridge. The coefficients for transforming measured strains to forces or bending moment (torsion moment) of the 6 load cells are listed in Table 4.4, respectively. The load cells of Nos.1 and 2 were placed at the bottom of the north tower leg and the load cells of Nos. 3 and 4 were placed at the bottom of the south tower leg. The load cells of Nos. 5 and 6 were placed at the bottom of the southeast pier.

Table 4.4 Transformation coefficients of load cells

Load Cell	Fx	Fy	Fz	Mx	My	Mz
No.	$\mu\varepsilon$ / kN	$\mu\varepsilon$ / kN	$\mu\varepsilon$ / kN	$\mu\varepsilon$ / kN.m	$\mu\varepsilon$ / kN.m	$\mu\varepsilon$ / kN.m
1	44.521	40.874	8.665	618.65	552.555	487.926
2	42.610	43.335	8.953		558.880	450.526
3	42.374	41.24	8.138		589.572	
4	43.303	41.712	9.580		566.158	
5	41.522	42.474	8.818		581.285	
6	44.013	42.307	9.350		577.690	

All load cells were firmly fastened with the shake table and the foundations to ensure that the foundation-load cell-shake table system can be regarded as one rigid body. As described before, the two RC tower legs are designed and expected to sustain flexure-shear failure and the RC piers are designed and expected to resist flexure failure. The internal forces on the bottom cross sections of the piers and the tower legs can be determined in terms of the measured forces (moments) from the load cells, based on the free-body diagram in Figure 4.12 and the following equations.

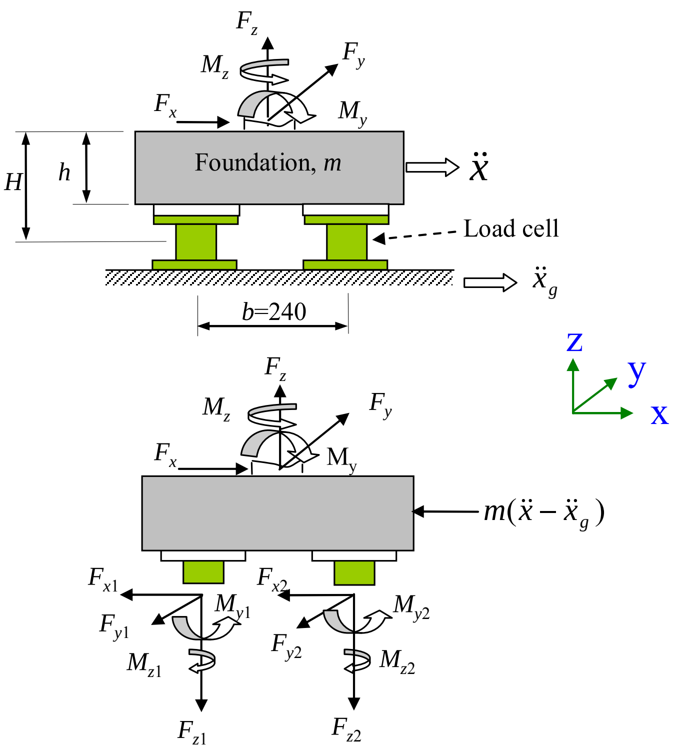

Figure 4.12 Free-body diagrams for calculating forces of columns (Unit: mm)

$$F_x = F_{x1} + F_{x2} + m(\ddot{x} - \ddot{x}_g) \tag{4.1}$$

$$F_y = F_{y1} + F_{y2} \tag{4.2}$$

$$F_z = F_{z1} + F_{z2} \tag{4.3}$$

$$M_y = M_{y1} + M_{y2} - (F_{x1} + F_{x2})H + (F_{z1} - F_{z2})b/2 - m(\ddot{x} - \ddot{x}_g)h/2 \tag{4.4}$$

$$M_z = M_{z1} + M_{z2} - (F_{y1} + F_{y2})b/2 \tag{4.5}$$

4.2.4.3 Installation of bridge model on shake table

To ensure the integrity of the entire bridge model when it is installed on the shake table, the four load cells on the two east piers were bolted to a steel plate of 25mm thick, and the four load cells on the two tower legs were bolted to another steel plate of 25mm. One more steel plate of 25mm was also fixed on the foundation of the west piers. The three steel plates were then welded to the two I-steel beams to form the completed bridge model. This completed bridge model was lifted as a whole by a crane onto the shake table. The three steel plates of the RC cable-stayed bridge model were finally bolted on the shake table, as shown in Figure 4.13. The RC cable-stayed bridge model was placed on the shake table in a longitudinal direction perpendicular to the direction of designated shaking. Figure 4.14 shows the as-built RC cable-stayed bridge model on the shake table.

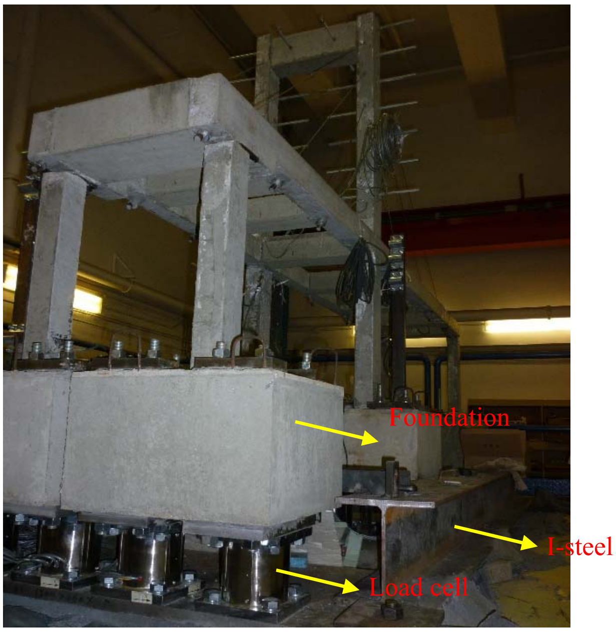

Figure 4.13 Connection details among load cells, piers and shake table

Figure 4.14 As-built RC cable-stayed bridge model on shake table

4.2.5 Supplementary lumped mass

As aforementioned, to fully satisfy the laws of similarity with respect to density, a total of 3.06 tons supplementary masses should be added and distributed on the bridge. As the space of the bridge used to put the additional mass is limited, added mass weighting about 1.51t is finally installed on the twin-girder and two tower legs, as shown in Figure 4.15. Although the 53.0% additional mass was satisfied and the seismic responses of the bridge model did not reflect the actual ones of the bridge prototype, the study on the failure modes of the failure-vulnerable RC components of the bridge model is still significant. To avoid additional stiffness contribution to the bridge structure if the mass blocks are directly fixed on the bridge, two wood blocks are placed between the added mass blocks and components of the bridge model. The total mass blocks are divided into three groups and then added to the bridge model one after another. The cable forces are also adjusted accordingly three times to distribute the additional masses on the bridge. After the stay cables are all tensioned appropriately to satisfy the targeted configuration of the bridge, the construction and installation of the scaled RC cable-stay bridge were completed.

Figure 4.15 Distribution of supplementary mass blocks

4.2.6 As-built cable forces

By adjusting the cable forces, the bridge profile under dead loads was close to the targeted configuration showed in the design drawing. The as-built cable forces can then be measured using the frequency method. The measured cable forces can be used to calculate the initial stresses of stay cables which are required in establishing the bridge FE model.

4.2.6.1 Measurement system for static cable force

The frequency method is employed to measure the as-built cable forces of stay cables. A B&K 2635 accelerometer is stuck on one cable near its end. The cable is then oscillated by external force and the cable acceleration response recorded by the accelerometer is shown on a wave displayer. The cable force can then be calculated by the following formula:

$$T = (2lf)^2 m \tag{4.6}$$

where T is the cable force, l is the length of the cable, f is the free vibration frequency of the cable, and m is the mass of the cable. The measurement system for static cable force is shown in Figure 4.16.

(a)

(b)

Figure 4.16 Measurement system for static cable forces

(a) Accelerometer and charge amplifier (b) Wave displayer

4.2.6.2 Measurement results of as-built cable forces

The cable numbers are graphed in Figure 4.17 and the as-built forces of the cables, which are calculated from the measured frequency, are listed in Table 4.5.

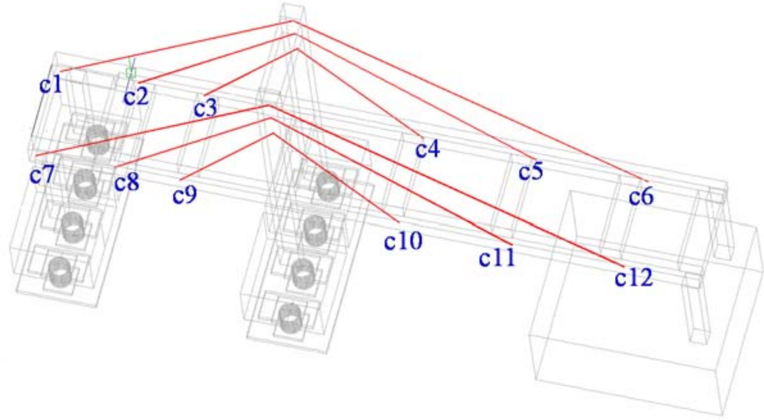

Figure 4.17 Cable number

Table 4.5 Measured as-built cable forces

Cable No.	Tension Force (N)	Cable No.	Tension Force (N)
1	501.8	7	501.8
2	563.7	8	556.5
3	487.1	9	482.5
4	531.9	10	582.9
5	418.1	11	403.3
6	245.4	12	283.5

4.3 Dynamic Characteristics Test

The dynamic characteristics of the cable-stayed bridge reflect the inherent properties of the bridge as well as the distributions of both structural stiffness and mass of the bridge. The measured frequencies, mode shapes and modal damping ratios can provide useful information for the linear model updating of the bridge in Chapter 5.

4.3.1 Measurement system for dynamic characteristics

To measure the mode shape of the cable-stayed bridge structure, a total of 29 CA-YD-109B accelerometers are installed on the bridge model to record the acceleration responses, as shown in Figure 4.18. Three charge amplifiers, B&K2692, KD 5006, and KD 5008C, are used to amplify the raw signals and increase the signal-to-noise ratio, as shown in Figure 4.19(a). A series of impulses generated by a

SINOCERA LC-04A force hammer with a rubber tip is applied on the RC bridge structure to conduct a modal test, as shown in Figure 4.19(b). The natural frequencies and mode shapes of the bridge structure are identified based on the spectral analyses of the force and acceleration responses recorded using a 32-channel data acquisition system KYOWA EDX-100A, as shown in Figure 4.19(c). The transfer function analysis is used to extract the vibration characteristics of the scaled bridge model. The real part of the transfer function is used to calculate the damping ratio corresponding to each mode shape. The imaginary part of the transfer function is used to calculate the mode shape and modal frequency. Figure 4.20 shows the measurement system for identifying the dynamic characteristics of the bridge with random excitation. The first seventh measured modal frequencies will be utilized for the linear model updating in Chapter 5.

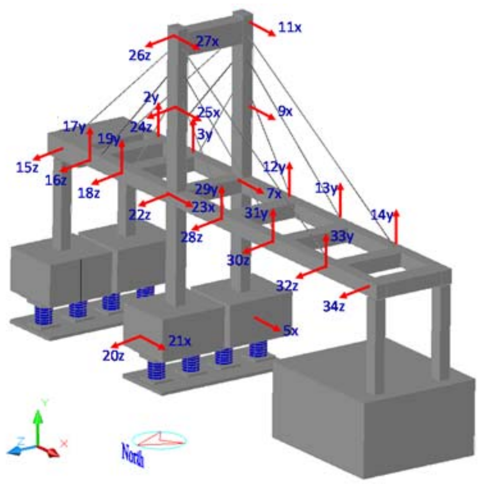

Figure 4.18 Measurement points for mode shapes

(a)

(b)

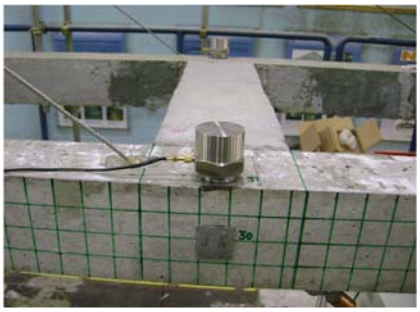

(c)

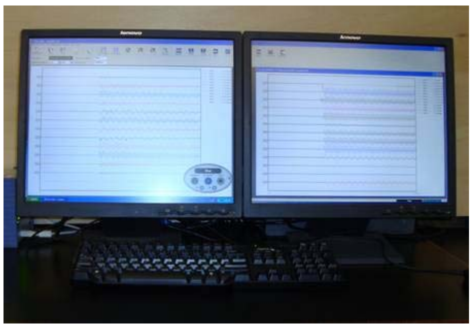

(d)

Figure 4.19 Instrumentation for measuring dynamic characteristics

(a) Impact hammer (b) KD 5006 charge amplifier (c) CA-YD-109B accelerometers (d) KYOWA EDX-100A 32 channel data acquisition system

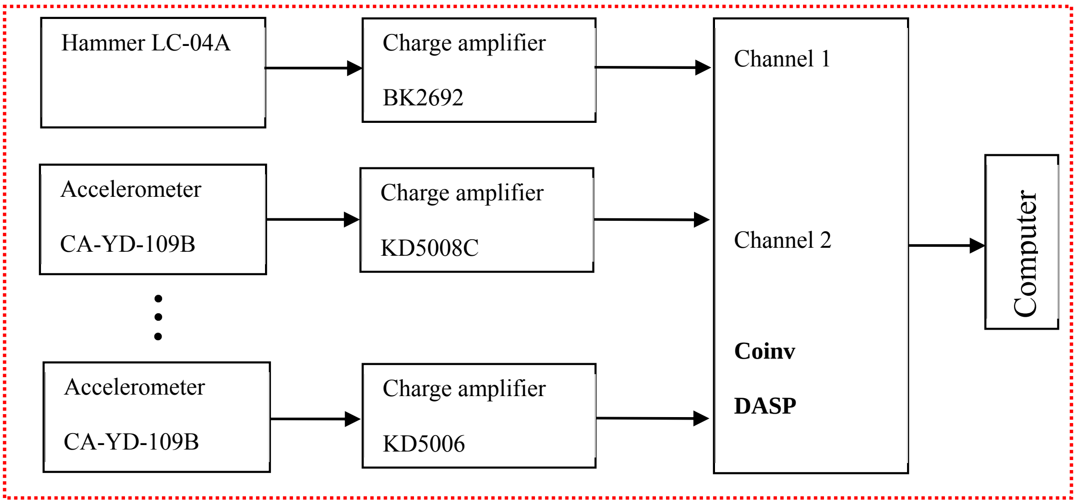

Figure 4.20 Flowchart of measurement system for dynamic characteristics

4.3.2 Measurement results of dynamic characteristics

The first seven natural frequencies and the corresponding mode shapes and damping ratios are tabulated in Table 4.6. The first seven mode shapes are separately plotted in Figure 4.21. It is noted that the oscillating direction of the shake table is along the transversal direction of the bridge model. Attention should be paid to the second, third and the fifth modes of vibration with respect to the transversal vibration of the bridge model.

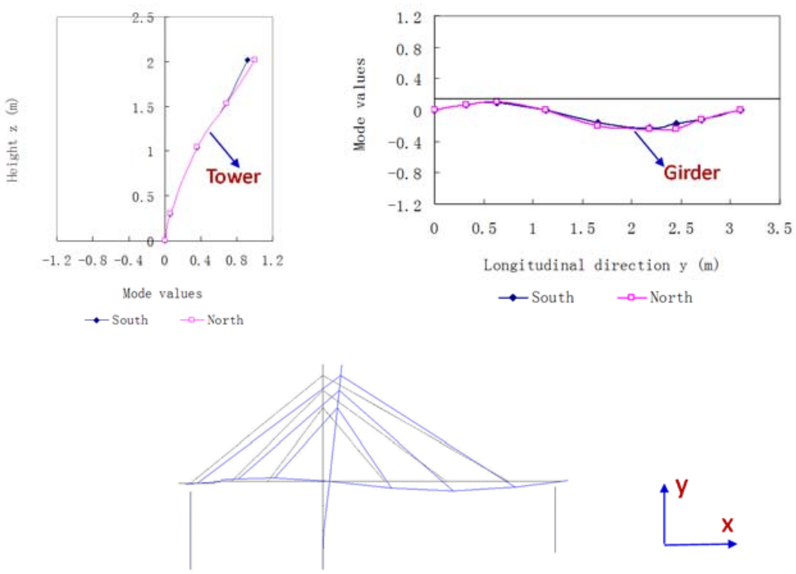

(a)

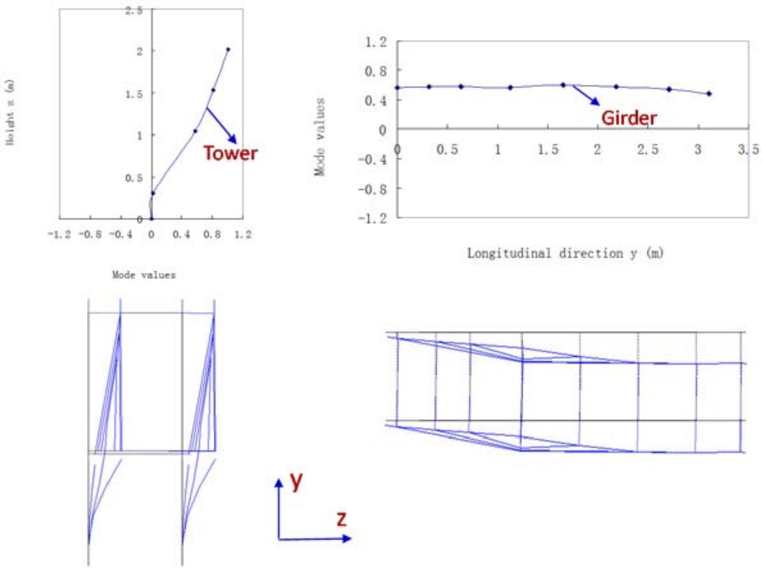
Height z (m)
Tower
Mode values
Mode values
Girder
Longitudinal direction y (m)
y
z

(b)

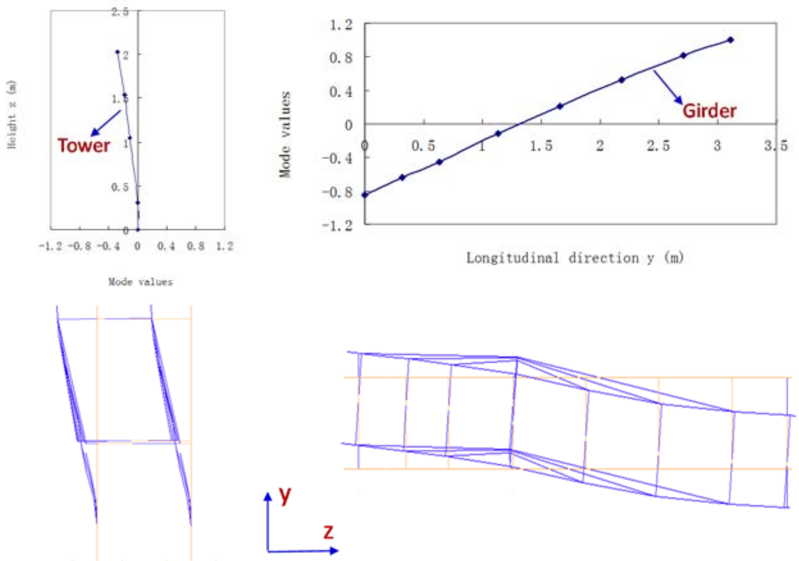
Height z (m)
Tower
Mode values
Mode values
Girder
Longitudinal direction y (m)
y
z

(c)

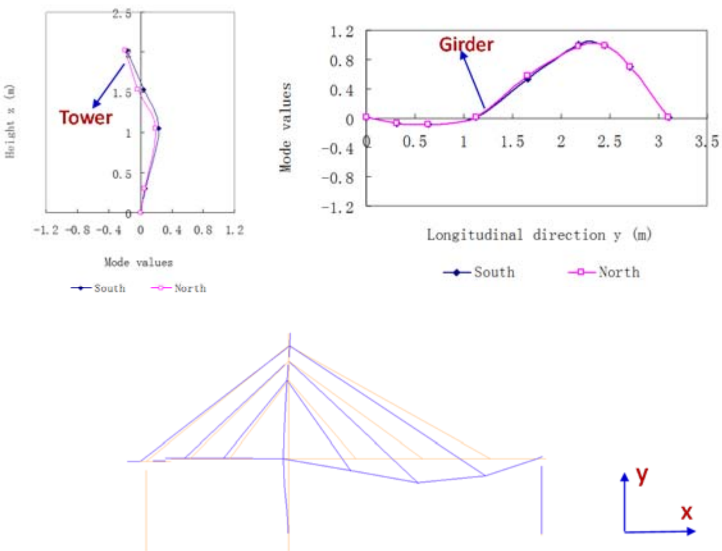
Height z (m)
Tower
Mode values
South
North
Mode values
Girder
Longitudinal direction y (m)
South
North
y
x

(d)

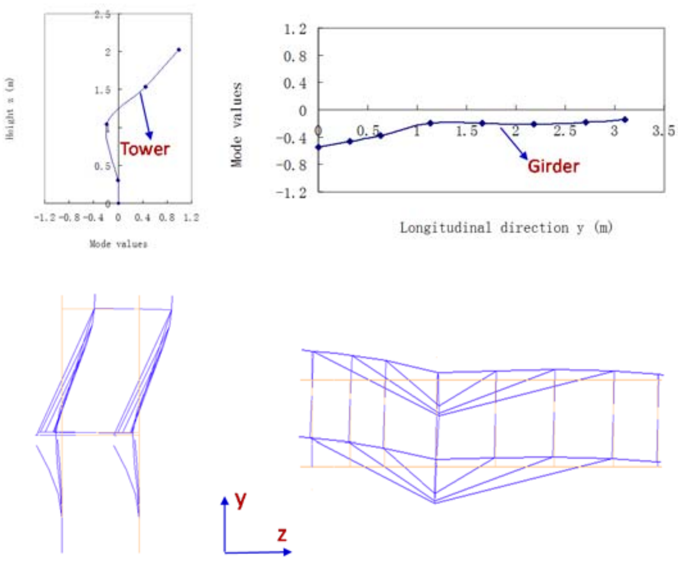
Height z (m)
Tower
Mode values
Mode values
Girder
Longitudinal direction y (m)
y
z

(e)

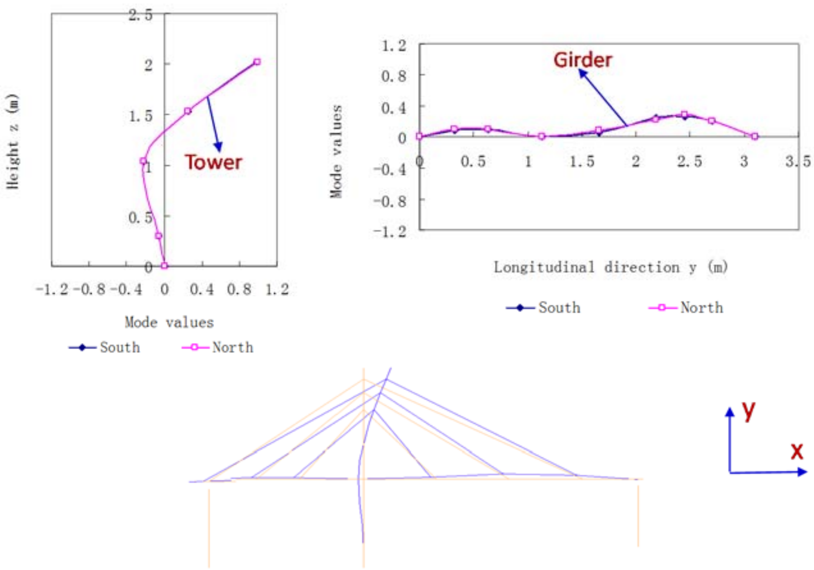

(f)

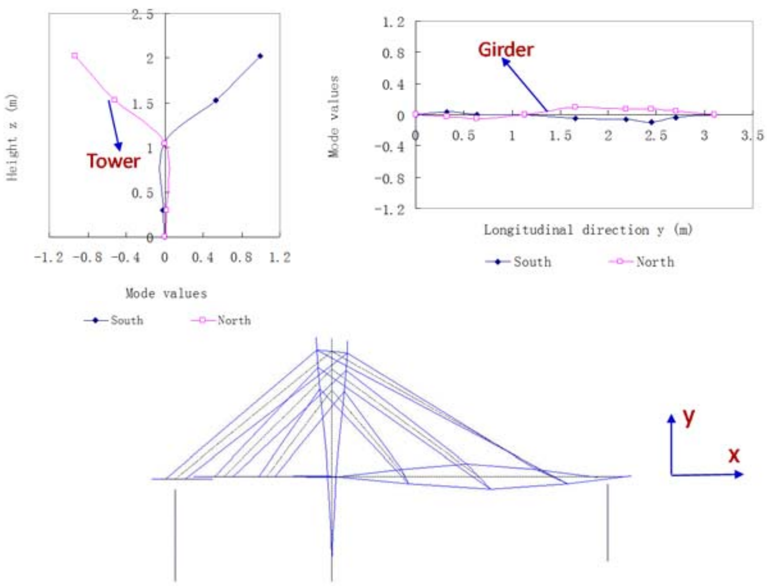

(g)

Figure 4.21 First seven mode shapes

(a) 1st mode shape (b) 2nd mode shape (c) 3rd mode shape

(d) 4th mode shape (e) 5th mode shape (f) 6th mode shape

(g) 7th mode shape

Table 4.6 Modal frequencies, mode shapes and damping ratios

Mode No.	Natural frequencies (Hz)	Mode Shape Description	Damping ratio (%)
1	10.294	1st longitudinal bending of tower	1.50
2	11.275	1st transversal bending of tower	2.23
3	14.706	1st torsional of tower	1.89
4	15.166	2nd longitudinal bending of tower	1.62
5	21.301	2nd transversal bending of tower	1.37
6	23.284	3rd longitudinal bending of tower	1.14
7	37.489	3rd transversal bending of tower	0.97

4.4 SHM System for Seismic Responses

This thesis aims to propose a SHM-based seismic collapse prognosis method for RC structures subject to earthquake excitation. To examine the feasibility and correctness of the proposed SHM-based seismic collapse analysis method, extensive tests were carried out on the scaled RC cable-stayed bridge subjected to earthquake excitation of different intensities. The measurement system, also called the SHM system hereafter, was designed and installed on the bridge model and introduced in this section in detail.

The SHM system proposed here is used to monitor the seismic collapse of the RC cable-stayed bridge model subject to earthquake excitations of different intensity levels. The acceleration responses at key locations of the bridge shall be measured to monitor the global behavior of the bridge. A total of 8 accelerometers were used to record the acceleration responses of the key locations (Figure 4.22). These locations include the tops of the tower in the longitudinal and transverse directions (A9-A11), the cross area between the tower and south girder in the transverse direction (A7), the tops of the southeast pier and southwest pier in the transversal direction (A6 and A8), and the top surface of the two girders in the vertical direction towards the west end (A12 and A13). In addition to these 8 accelerometers, 5 more accelerometers were used. The accelerometer A1 was used to record the ground acceleration generated by the shake table. To examine if the load cells are stiff enough and the four foundations (two under the two east piers and two under the two tower legs) can work together as a rigid body, the four accelerometers (A2-A5) were installed on the four foundations. The strain responses at the failure-vulnerable components are relatively large when the bridge is subject to the ground motion in the transversal direction. Therefore, the strain responses at the plastic hinge of the two tower legs and the southeast pier were measured by strain gauges as the local bridge responses for monitoring local damage which leads to global collapse. A total of 19 strain gauges (n1-n8, s1-s8, s8, and e1-e3) were uniformly mounted on the longitudinal reinforcement at the two ends of the plastic hinges of the two RC tower legs and the southeast RC pier, as shown in Figure 4.23. The measured strain responses will be used in the subsequent chapters for model updating and collapse analysis. Owing to limitation of the equipment capacity for recording measured data, the strain gauge was not stuck on the longitudinal reinforcement in the plastic hinge of the southwest pier.

As described before, six load cells were fabricated and installed on the foundations of the two tower legs and the southeast pier, as shown in Figure 4.24, to record the time-varying reaction forces (moments) during the shake table tests. These recorded reaction forces (moments) can then be used to calculate the internal forces (moments) at the bottom sections of the tower legs and the southeast pier. These internal forces (moments) will be further used in the subsequent chapters to compare with the computed ones to examine the feasibility and correctness of the proposed SHM system for collapse prognosis.

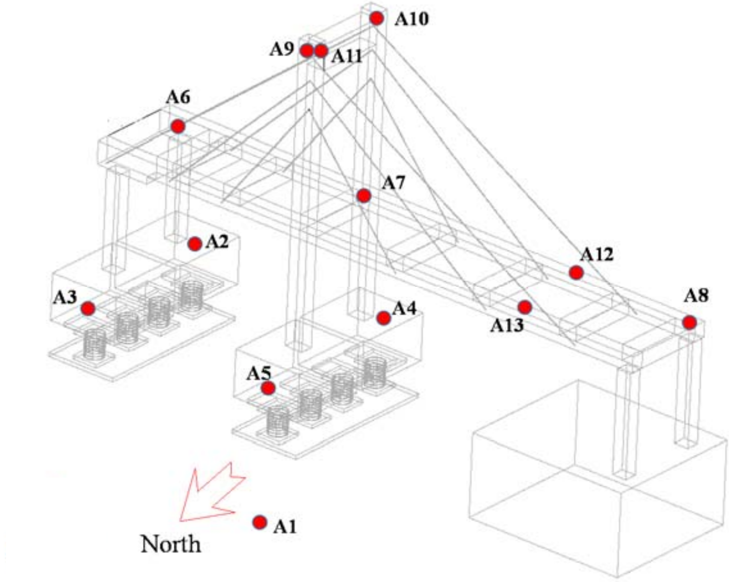

Figure 4.22 Arrangements of accelerometers

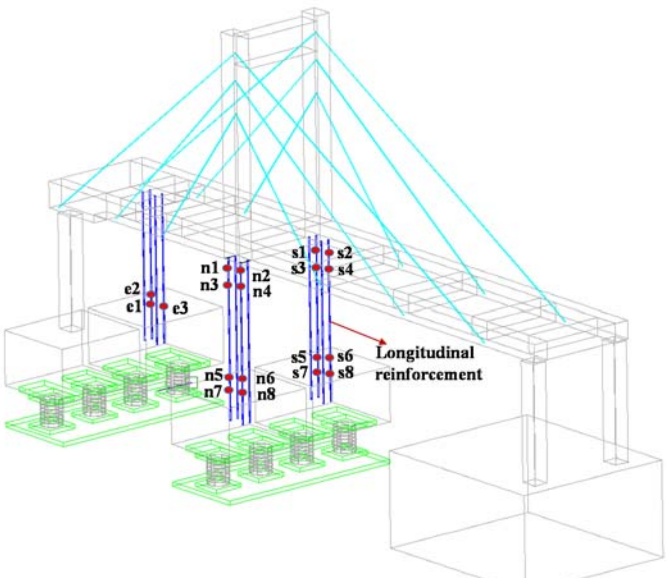

Figure 4.23 Arrangement of strain gauges on longitudinal reinforcement

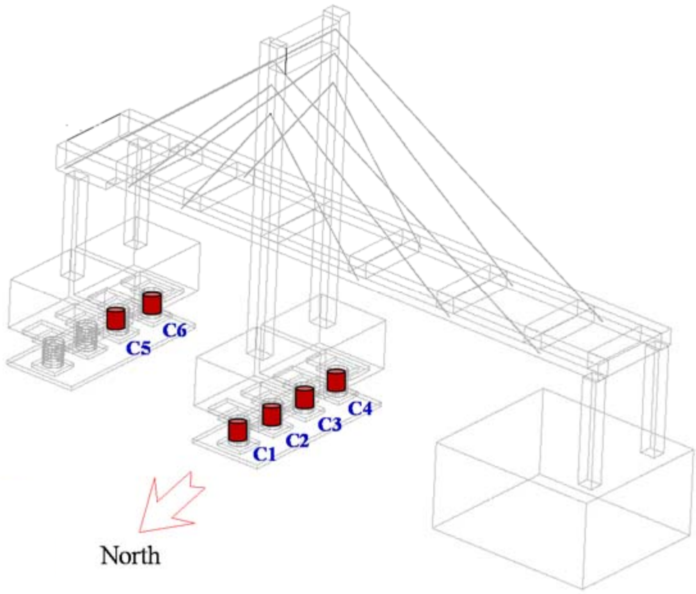

Figure 4.24 Arrangement of load cells

The accelerometers used to record acceleration responses were B&K4374, as shown in Figure 4.25 (a). The acceleration signals from the accelerometers were amplified using the charge amplifier and then transferred to the data acquisition system, as shown in Figure 4.25 (c) and (e), respectively. The strain gauges used to record strain responses are conventional electrical sensors of YFLA-2, as shown in Figure 4.25 (b). The strain signals recorded from the strain gauges were conditioned using the bridge box RXM 305D and then inputted to the data acquisition system, as shown in Figures 4.25 (d) and (e), respectively. The load cells used in this study were made of strain gauge type. The strain signals from the load cells were also conditioned using the bridge box RXM 305D and then inputted to the data acquisition system, as shown in Figures 4.25 (d) and (e), respectively. The working ranges of the accelerometers and strain gauges are listed in Table 4.7, respectively. The entire measurement system for shake table tests of the bridge is shown in Figure 4.25(f).

Table 4.7 Sensor properties

Sensor	Type	Location	Working Range
Accelerometer	B&K4374	Girder and tower	±0.03 (m/s^2)
Strain Gauge	YFLA-2	Tower and pier	±2.0%

(a)

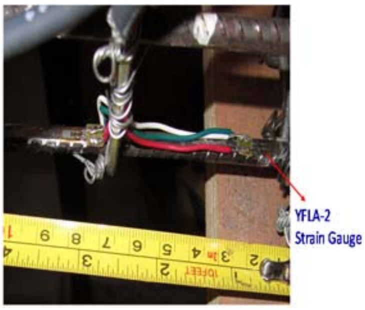

(b)

(c)

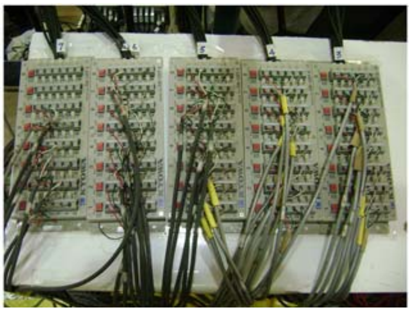

(d)

(e)

(f)

Figure 4.25 Measurement system for seismic responses of the bridge:

(a) Accelerometer (b) Strain gauge (c) Charge amplifier

(d) Bridge box (e) Data acquisition system (f) Entire measurement system

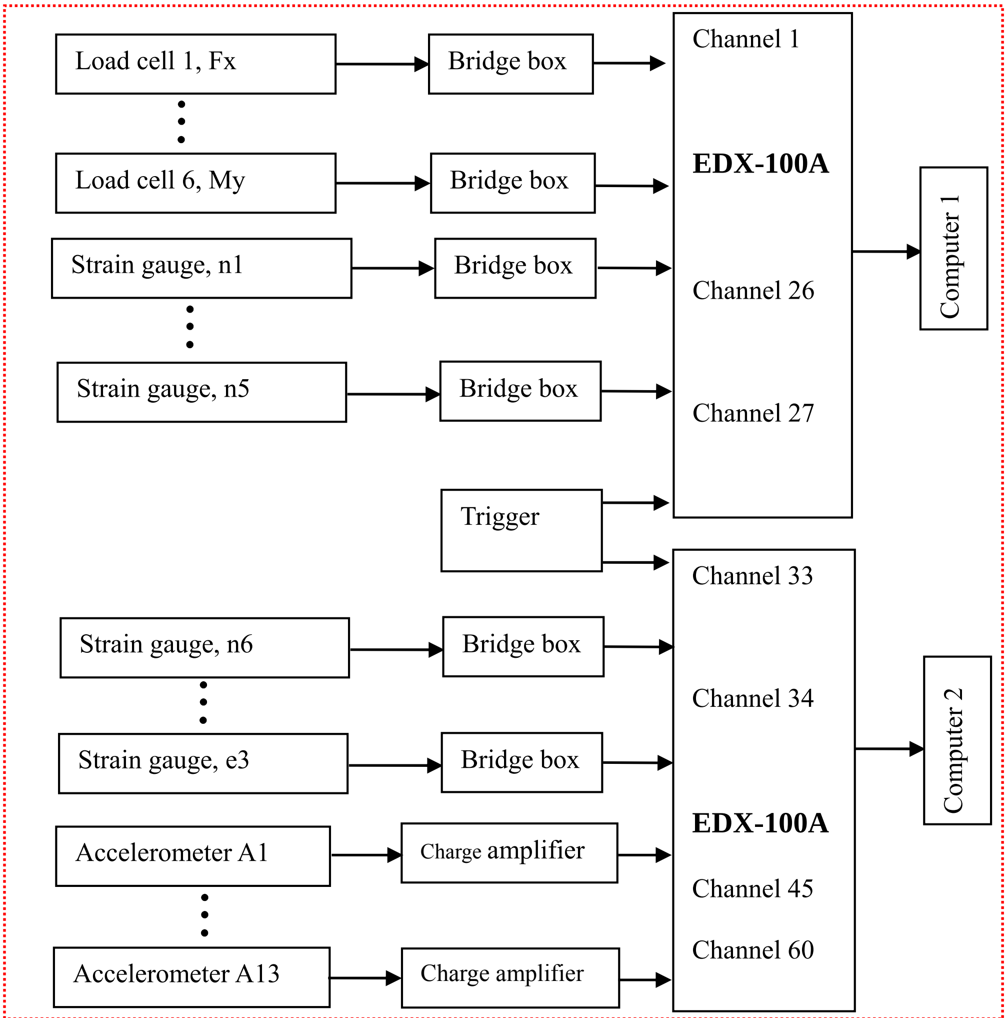

Figure 4.26 Flowchart of measurement system for seismic responses

The entire measurement system consists of 60 channels, in which 58 channels were used to record the seismic responses and 2 of them are used to keep synchronous for all sensors at the time of data collection. Among 58 channels for seismic response measurements, 26 were used for load cells, 19 for strain gauges, and 13 for accelerometers. The detailed information of the total 60 channels with respect to three types of sensors is presented in Appendix A. As there are 60 channels--two data acquisition systems, each of which has 32 channels, two computers were required. Figure 4.26 shows the flowchart of the measurement system, in which the connections of sensors, bridge boxes, charge amplifiers, data acquisition systems, and computers are clearly demonstrated.

4.5 Shaking Table Test Program and Results

4.5.1 Shaking table test program

As mentioned before, one of the main reasons for carrying out shake table tests of the 1/12 scaled RC cable-stayed bridge model is to provide test data for verifying the proposed model updating methods and seismic collapse prognosis of RC bridges. Therefore, four levels of ground motion (small earthquake, moderate earthquake, large earthquake, and collapse earthquake) were selected to conduct the seismic shaking table tests in four stages. The measurement data recorded by the sensors of the SHM system installed on the bridge model subjected to four levels of ground motions will be used in Chapters 5 and 6 for linear and nonlinear model updating and in Chapter 7 for collapse prognosis, respectively.

4.5.2 Shake table motions

According to the laws of similarity (Moncarz and Krawinkler 1981), the time durations of the small and moderate earthquake ground motion inputs were compressed according to the time ratio (time of model over time of prototype) of 1/4 to follow the similarity laws as close as possible. The time durations of the large and collapse earthquake ground motion inputs remain unchanged, that is, the time ratio of 1.0, because the bridge model was damaged to some extent after the small and moderate earthquake excitations and the dynamic characteristics of the bridge model were changed. To determine the intensity levels of small earthquake, moderate earthquake, large earthquake, and collapse earthquake for the shake table tests, a preliminary numerical analysis using the collapse analysis method presented in Chapter 3 was performed on the bridge model. It was then decided that the compressed Kobe earthquake ground motions with the PGA of 0.9573 m/s^2 and 3.548m/s^2 were used as small and moderate earthquake excitations, respectively. The duration for both the small and moderate ground excitation is 7.8 seconds and the sampling frequency of the ground excitations is 256 Hz. Strictly speaking, the compressed earthquake excitations cannot be called the Kobe earthquake ground motion. The original Kobe earthquake ground motion with the PGAs of 4.578m/s^2 and 4.633 m/s^2 were used as the large and collapse earthquake excitations, respectively. The duration for both the large and collapse ground excitation is 19.53 and 11.72 seconds, respectively. The sampling frequency of the ground excitation is also 256 Hz. It should be highlighted that after the large earthquake, the bridge model suffered from serious damage although it did not collapse and although the intensity level of the collapse earthquake is almost the same as that of the large earthquake, this earthquake caused the bridge model to collapse. The four levels of earthquake excitation were monitored by the accelerometer A1 installed on the shake table. The small, moderate, large and collapse earthquakes recorded by the accelerometer A1 are plotted in Figure 4.27, respectively. The single amplitude spectra of the recorded ground excitations are shown in Figure 4.28, respectively. The dominant frequency range of the small earthquake with the PGA of 0.9753 m/s^2 is from 5.0Hz to 12.0Hz. The dominant frequency range of the moderate earthquake with the PGA of 3.548 m/s^2 is mainly from 3.0Hz to 12.0Hz. The dominant frequency ranges of the large earthquake with the PGA of 4.758 m/s^2 and the collapse earthquake with the PGA of 4.633 m/s^2 are mainly from 1.0Hz to 3.0Hz.

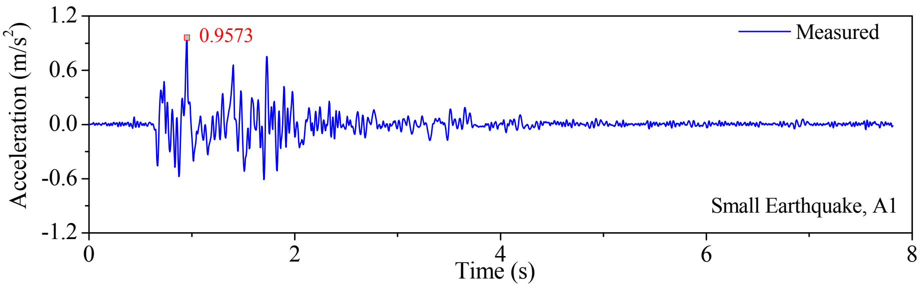

(a)

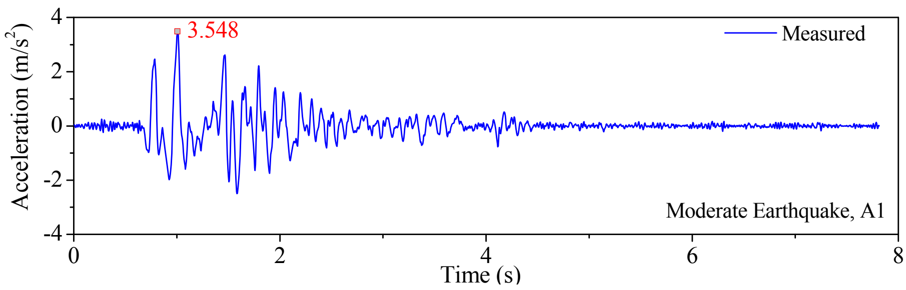

(b)

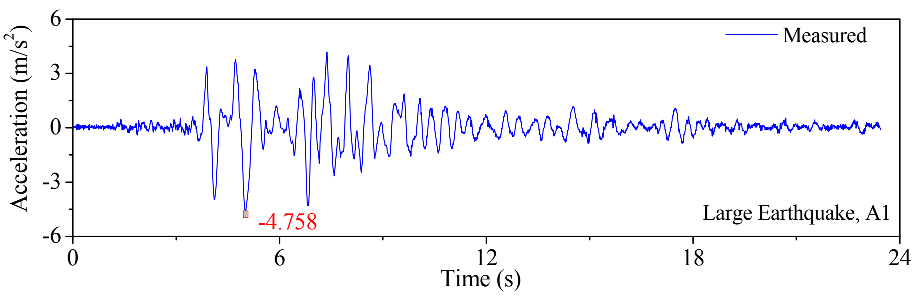

(c)

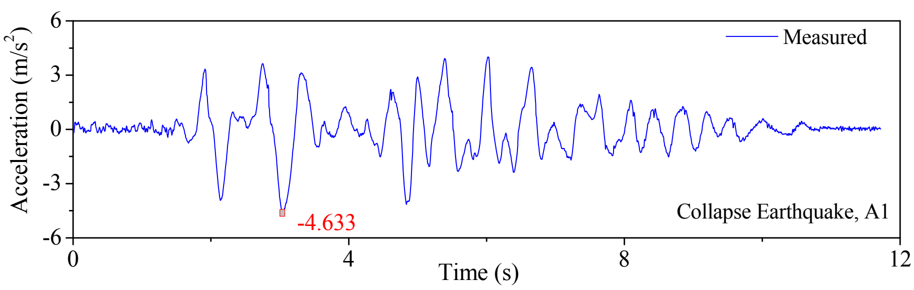

(d)

Figure 4.27 Ground acceleration recorded by accelerometer A1

(a) Small earthquake (b) Moderate earthquake

(c) Large earthquake (d) Collapse earthquake

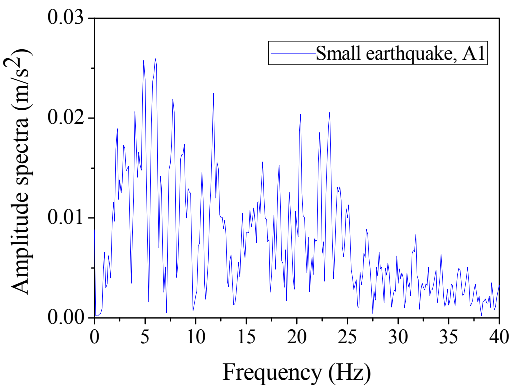

(a)

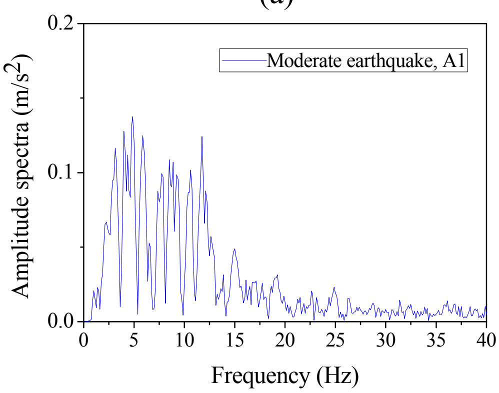

(b)

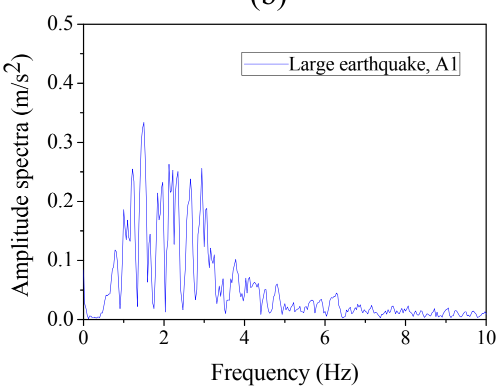

(c)

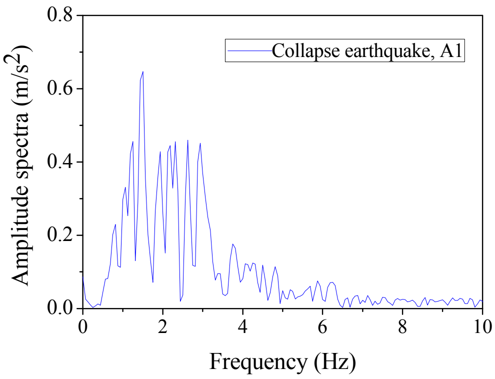

(d)

Figure 4.28 Single amplitude spectra of ground accelerations at A1

(a) Small earthquake (b) Moderate earthquake

(c) Large earthquake (d) Collapse earthquake

4.5.3 Measured seismic responses to small earthquake

Under the small earthquake excitation with peak acceleration of $0.9573 m/s^2$, the acceleration responses, strain responses and reaction forces of the bridge are expected to be small and the behavior of the bridge is expected to be linear.

4.5.3.1 Acceleration responses

The acceleration responses recorded by accelerometers A6, A7, A8 and A9 are respectively plotted in Figure 4.29. These acceleration responses are all in transverse direction of the bridge. The peak accelerations are listed in Table 4.8.

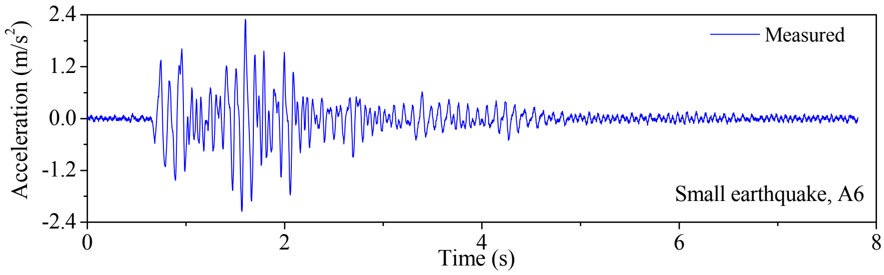

(a)

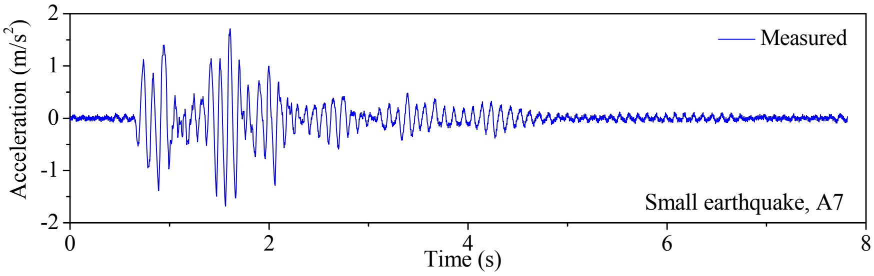

(b)

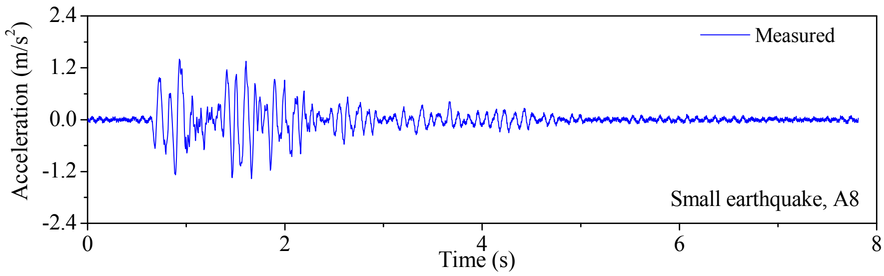

(c)

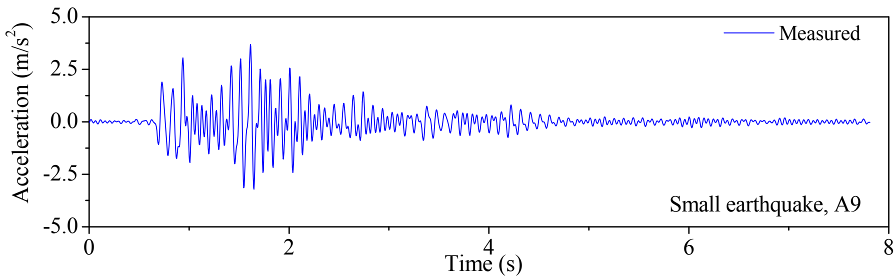

(d)

Figure 4.29 Acceleration responses of bridge

(a) A6 (b) A7 (c) A8 (d) A9

Table 4. 8 Peak acceleration responses

Accelerometer Location	Acceleration (m/s^2)
A6	2.296
A7	1.712
A8	1.402
A9	3.690

It can be seen from Table 4.8 that the maximum acceleration response was recorded by the accelerometer A9 at the top of the tower. The peak value of the acceleration response at the top of the tower is nearly 4 times as big as that of the input earthquake excitation. The acceleration response at the top of the southeast pier is more than that of the southwest pier because the southeast pier is more close to the tower than the southeast pier.

4.5.3.2 Reaction force (moment) responses

Figure 4.30 demonstrates the locations and positive directions of the reaction forces, including shear force, axial force, and bending moment. The reaction forces (moments) at the bottom of the north tower leg and the southeast pier, which are related to the transverse motion of the bridge, are respectively plotted in Figure 4.31. The peak responses of the reaction forces (moments) are listed in Table 4.9.

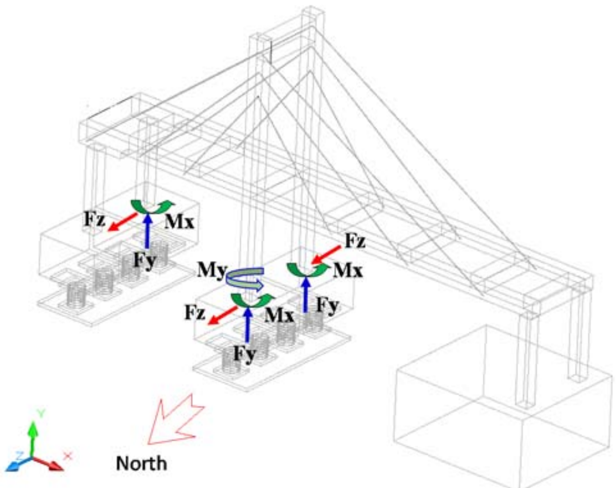

Figure 4.30 Locations for measured reaction forces (moments)

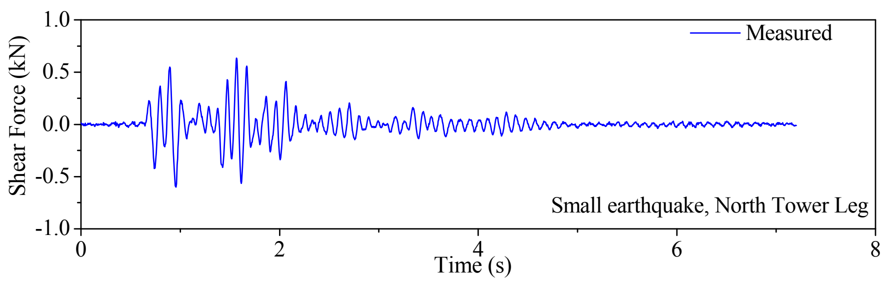

(a)

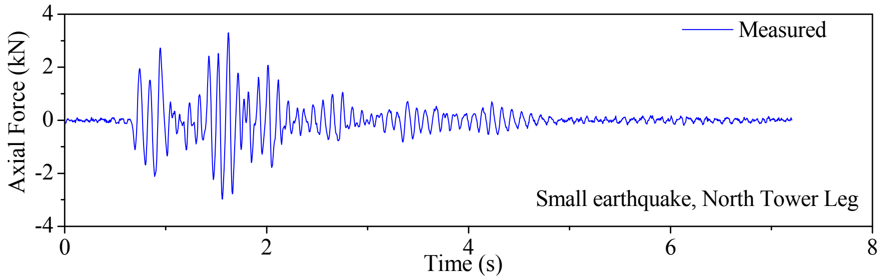
Measured
Small earthquake, North Tower Leg
Axial Force (kN)
Time (s)

(b)

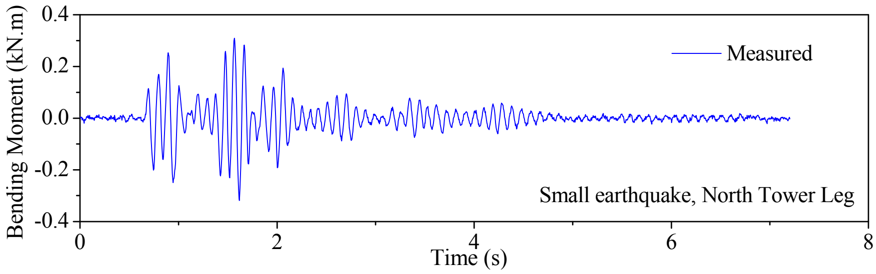
Measured
Small earthquake, North Tower Leg
Bending Moment (kN.m)
Time (s)

(c)

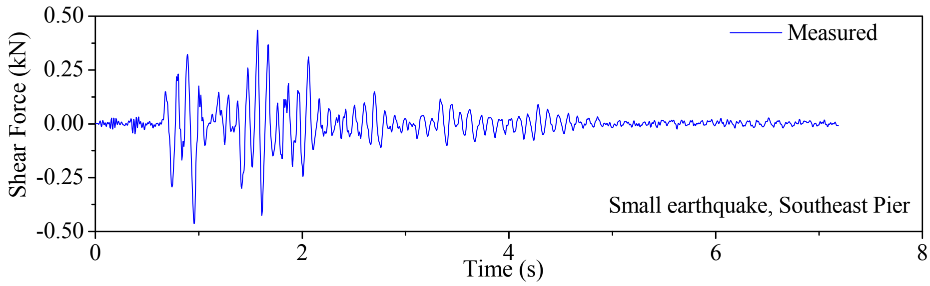
Measured
Small earthquake, Southeast Pier
Shear Force (kN)
Time (s)

(d)

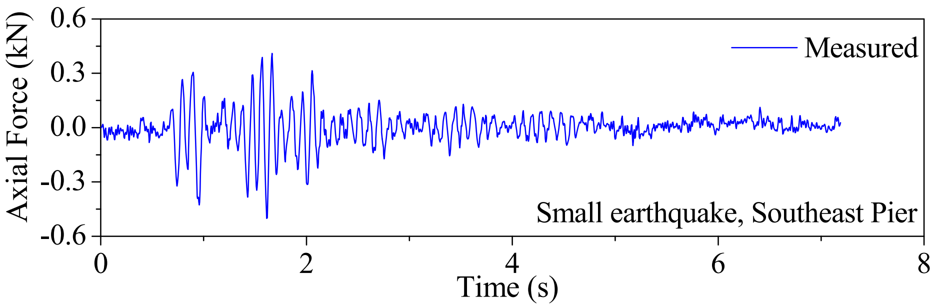
Measured
Small earthquake, Southeast Pier
Axial Force (kN)
Time (s)

(e)

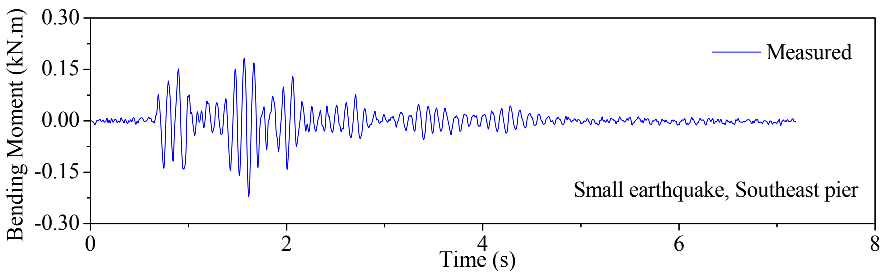

(f)

Figure 4.31 Reaction forces (moments) responses

(a) Shear force response at the bottom of the north tower leg (b) Axial force response at the bottom of the north tower leg (c) Bending moment response at the bottom of the north tower leg (d) Shear force response at the bottom of the southeast pier (e) Axial force response at the bottom of the southeast pier (f) Bending moment response at the bottom of the southeast pier

Table 4.9 Peak responses of reaction forces (moments)

Location	Force Type	Peak Forces (Moments)
North Tower Leg	Shear Force	0.634kN
	Axial Force	3.302kN
	Bending Moment	-0.318kN.m
Southeast Pier	Shear Force	-0.463kN
	Axial Force	-0.500kN
	Bending Moment	-0.222kN.m

It can be observed from Table 4.9 that the north tower leg sustains larger internal forces (shear, axial forces and bending moment) than those of the southeast pier under the small earthquake. This is because the weight of the additional mass blocks concentrated at the tower legs is larger than that at the southeast pier. The resultant inertial forces due to the additional mass blocks in the bottom of the south tower leg are larger than those at the bottom of the southeast pier.

4.5.3.3 Reinforcement strain responses

Figure 4.32 shows the measured strain responses of the reinforcement at n1, n7, s1, s2, e1 and e2. The peak reinforcement strain responses are summarized in Table 4.10.

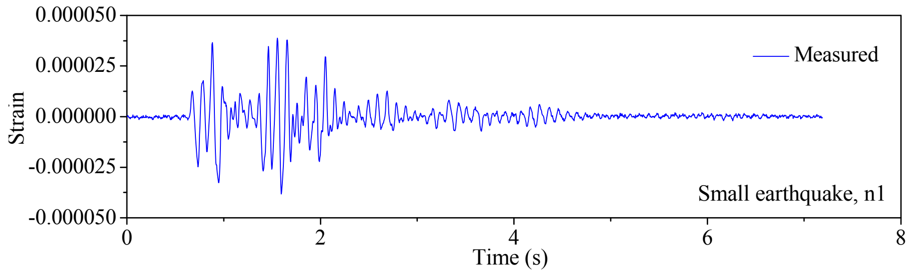

(a)

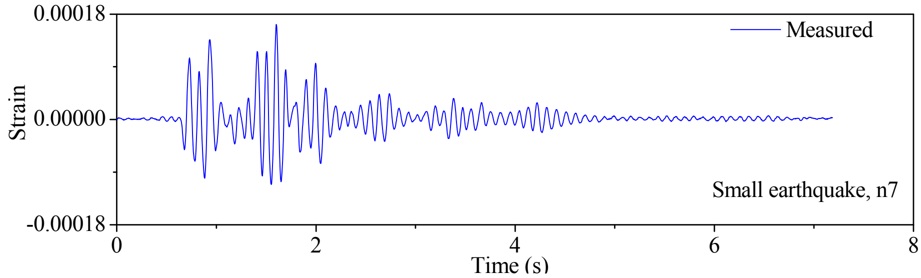

(b)

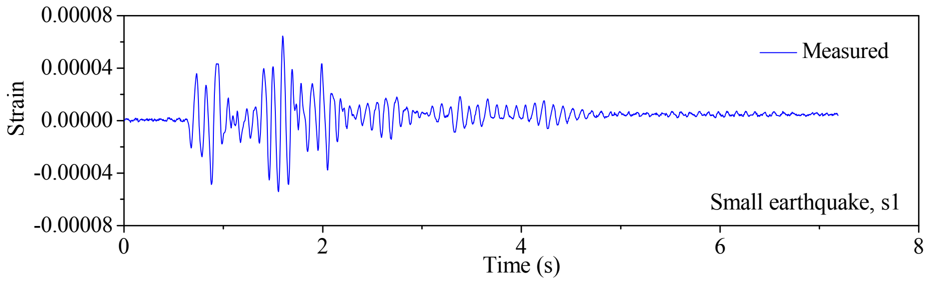

(c)

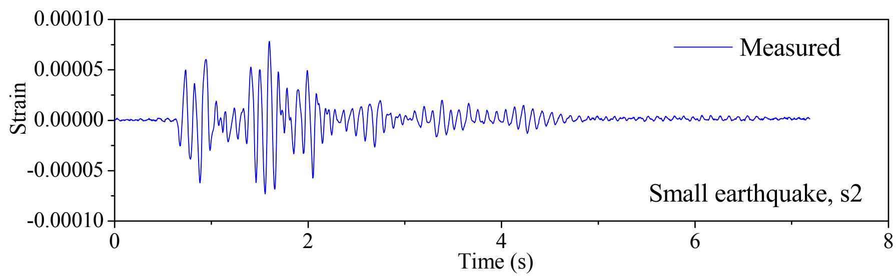

(d)

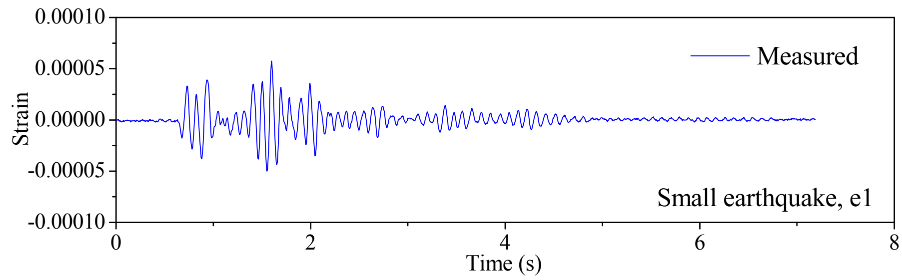

(e)

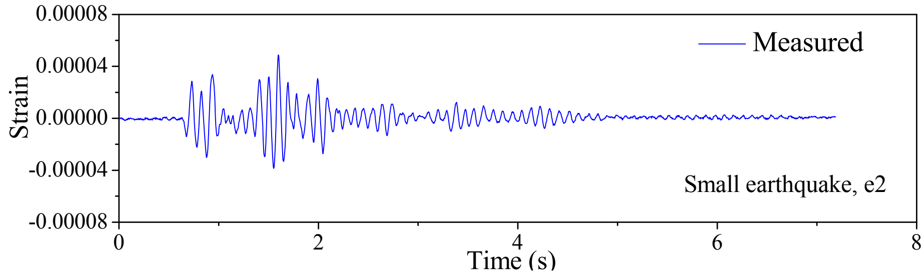

(f)

Figure 4.32 Reinforcement strain responses

(a) n1 (b) n7 (c) s1 (d) s2 (e) e1 (f) e2

Table 4.10 Peak strain responses of longitudinal reinforcement

Component	Location	Peak Reinforcement Strain
North Tower Leg	n1	3.88E-05
	n7	1.62E-04
South Tower Leg	s1	6.45E-05
	s2	7.83E-05
Southeast Pier	e1	5.75E-05
	e2	4.88E-05

It was observed that after the small earthquake, the concrete of the failure-vulnerable components did not crack. The peak strain response of the reinforcement was 0.000162 only, which is far less than the yielding strain of the reinforcement. All these indicate that the RC cable-stayed bridge performed linearly and elastically under small earthquake excitation. The acceleration and strain response information acquired from the SHM system from this test together with the measured dynamic characteristics of the bridge will be used for the linear model updating to determine the actual properties of concrete and reinforcement of the intact RC bridge in Chapter 5.

4.5.4 Measured seismic responses to moderate earthquake

Under the moderate earthquake excitation of peak acceleration of $3.548 m/s^2$, the acceleration responses, strain responses and reaction forces of the bridge are expected to be moderate and the behavior of the bridge is expected to be slightly nonlinear.

4.5.4.1 Acceleration responses

The acceleration responses recorded by accelerometers A6, A7, A8 and A9 are plotted in Figure 4.33, respectively. These acceleration responses are all in the transverse direction of the bridge. The peak acceleration responses are listed in Table 4.11.

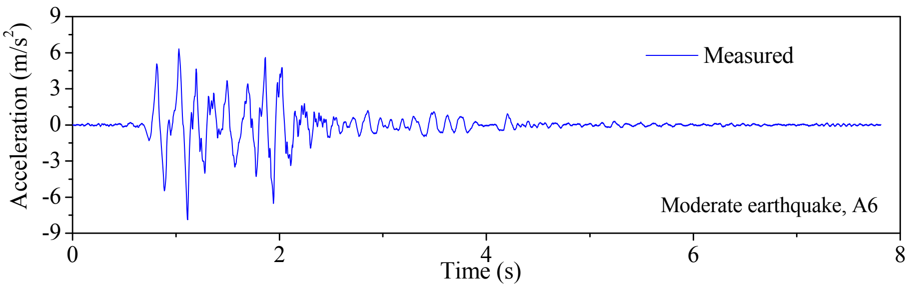

(a)

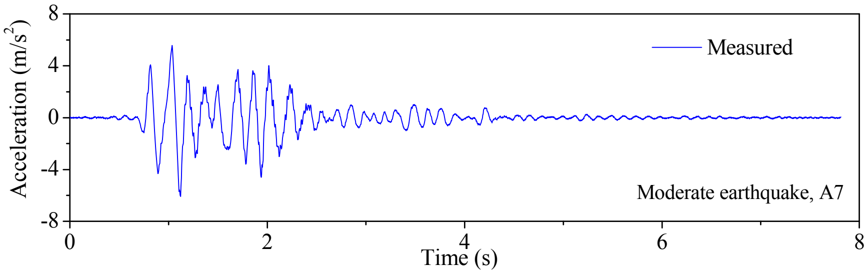

(b)

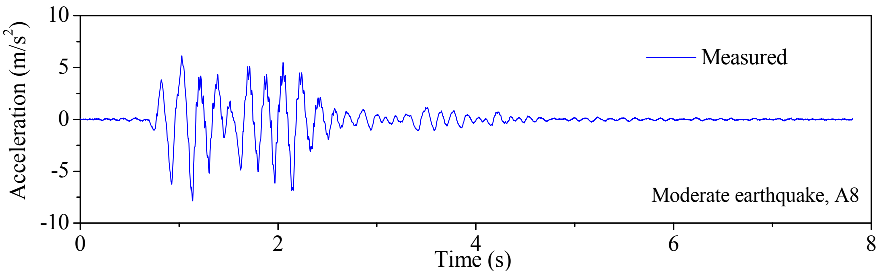

(c)

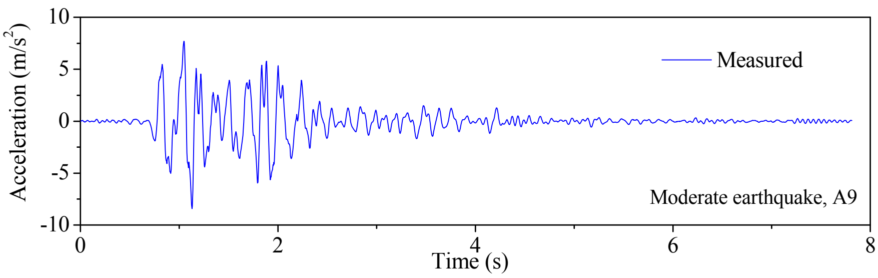

(d)

Figure 4.33 Acceleration responses

(a) A6 (b) A7 (c) A8 (d) A9

Table 4.11 Peak acceleration responses

Accelerometer No.	Acceleration (m/s^2)
A6	7.872
A7	6.078
A8	7.860
A9	8.419

It can be seen from Table 4.11 that the maximum acceleration response was recorded by the accelerometer A9 at the top of the tower. The peak value of the acceleration response at the top of the tower is nearly 2.4 times as big as that of the input earthquake excitation. The acceleration response at the top of the southeast pier is similar to that of the southwest pier. The acceleration response at the cross area between the tower and the girder is the smallest.

4.5.4.2 Reaction force (moment) responses

Figure 4.30 demonstrates the locations and positive directions of the reaction forces (moments), i.e. shear force, axial force, bending moment, and torsion moment. The reaction forces (moments) at the bottom of two tower legs and southeast pier are plotted in Figure 4.34. The peak reaction forces (moments) responses are listed in Table 4.12.

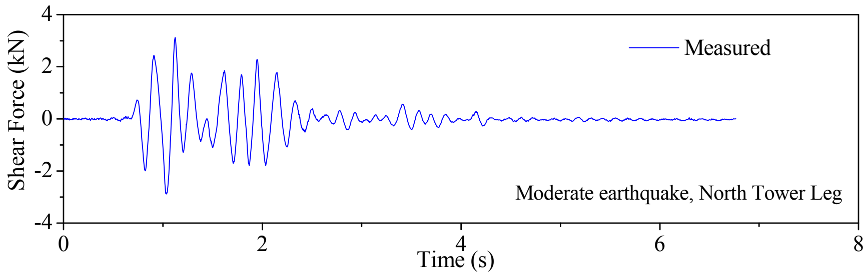

(a)

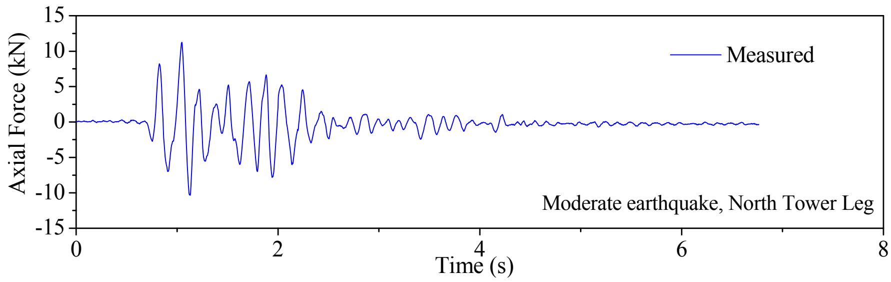

(b)

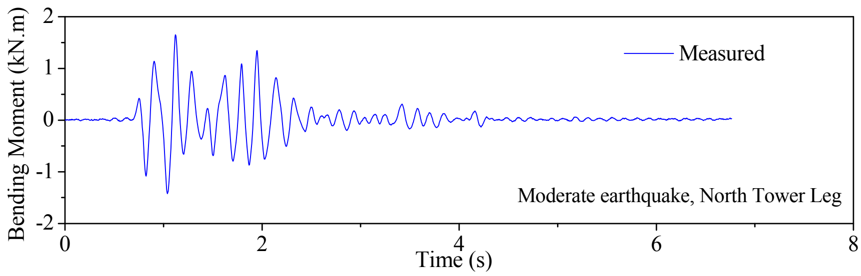

(c)

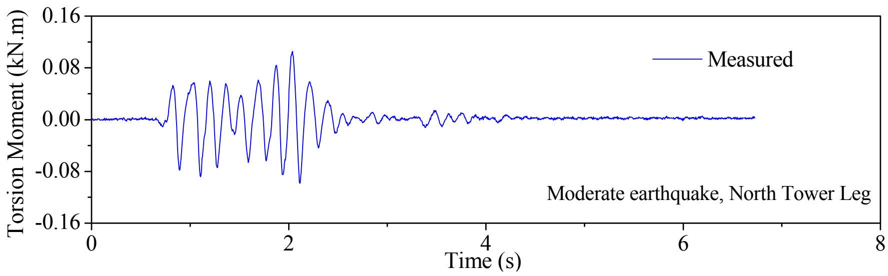

(d)

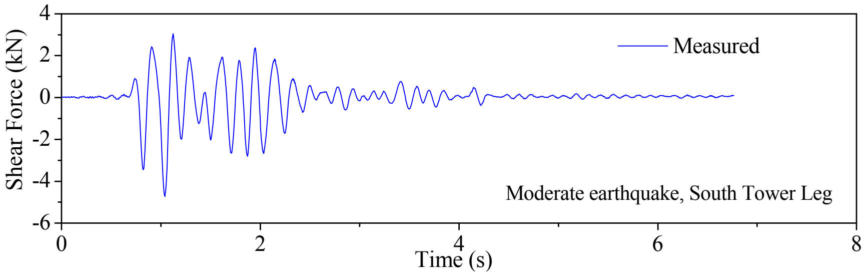
Shear Force (kN)
Time (s)
Measured
Moderate earthquake, South Tower Leg

(e)

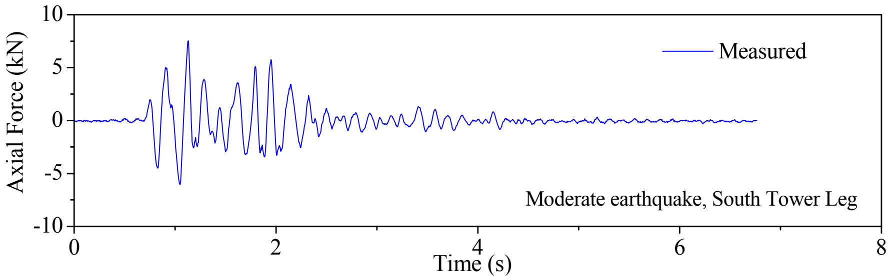
Axial Force (kN)
Time (s)
Measured
Moderate earthquake, South Tower Leg

(f)

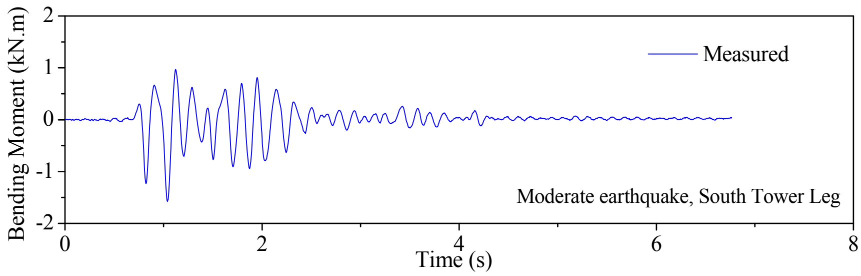
Bending Moment (kN.m)
Time (s)
Measured
Moderate earthquake, South Tower Leg

(g)

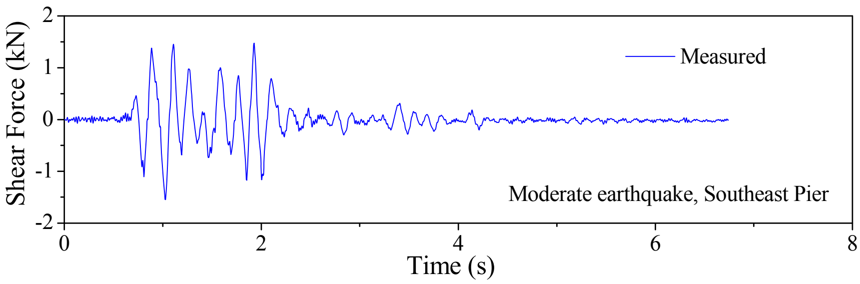
Shear Force (kN)
Time (s)
Measured
Moderate earthquake, Southeast Pier

(h)

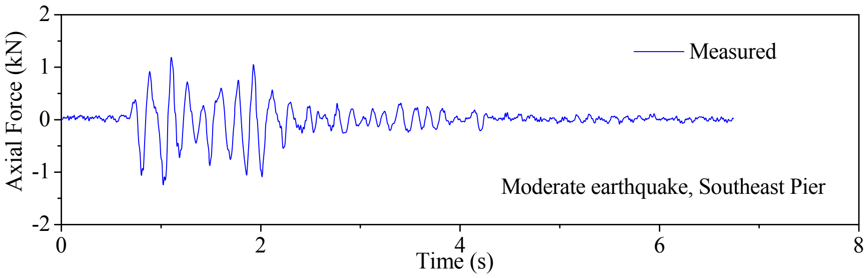
Axial Force (kN)
Time (s)
Measured
Moderate earthquake, Southeast Pier

(i)

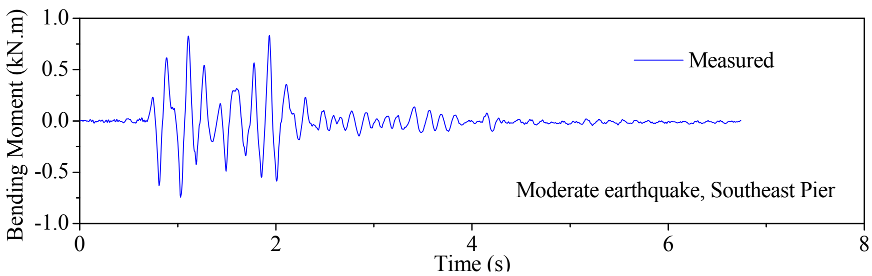

(j)

Figure 4. 34 Reaction forces (moments) responses

(a) Shear force response at the bottom of the north tower leg (b) Axial force response at the bottom of the north tower leg (c) Bending moment response at the bottom of the north tower leg (d) Torsion moment response at the bottom of the north tower leg (e) Shear force response at the bottom of the southeast pier (f) Axial force response at the bottom of the southeast pier (g) Bending moment response at the bottom of the southeast pier (h) Shear force response at the bottom of the southeast pier (i) Axial force response at the bottom of the southeast pier (j) Bending moment response at the bottom of the southeast pier

Table 4.12 Peak responses of reaction forces (moments)

Location	Force Type	Peak Forces (Moments)
North Tower Leg	Shear Force	3.106kN
	Axial Force	11.231kN
	Bending Moment	1.652kN.m
	Torsion Moment	0.105kN.m
South Tower Leg	Shear Force	4.726kN
	Axial Force	7.552kN
	Bending Moment	1.577kN.m
Southeast Pier	Shear Force	1.537kN
	Axial Force	1.301kN
	Bending Moment	0.835kN.m

It can be observed from Table 4.12 that the south tower leg sustains larger shear forces but smaller bending moment than those of the north tower leg under the moderate earthquake. This may be because of different connections between the piers and the girders on the south side and the north side: the two south piers were fixed to the south girder in the transverse direction while the two north piers were not fixed to the north girder in the transverse direction. The reaction forces in the southeast pier were all smaller than those of the two tower legs, because the side pier sustained less weight of the additional mass blocks than those borne by each tower leg.

4.5.4.3 Reinforcement strain responses

Figure 4.35 shows the measured strain responses of the reinforcement at n1, n7, s2, s7, e1 and e2. The peak reinforcement strain responses are summarized in Table 4.13.

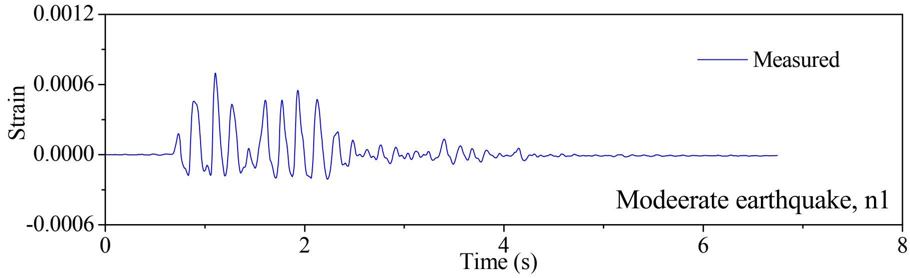

(a)

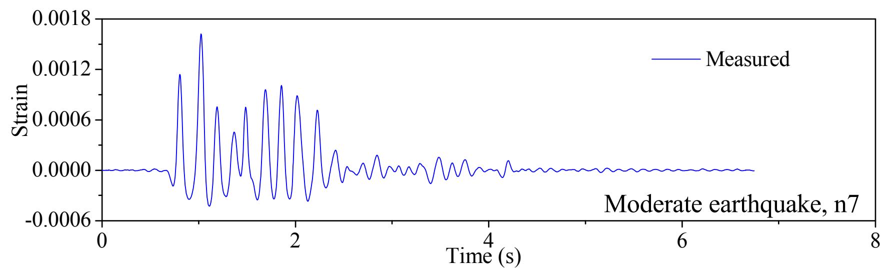

(b)

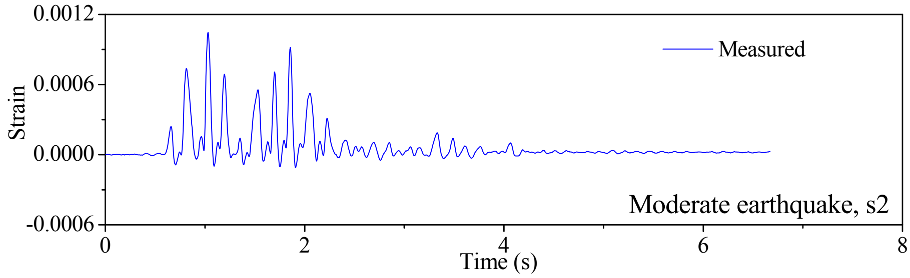

(c)

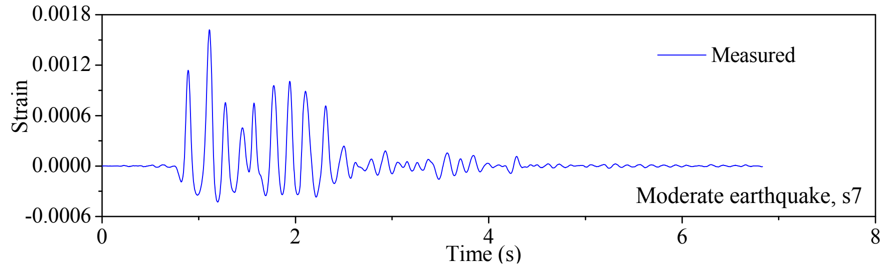

(d)

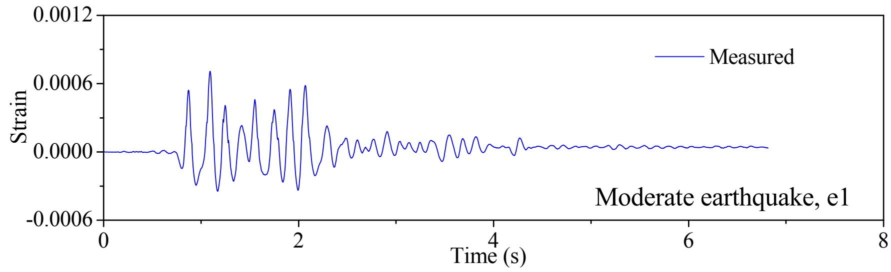

(e)

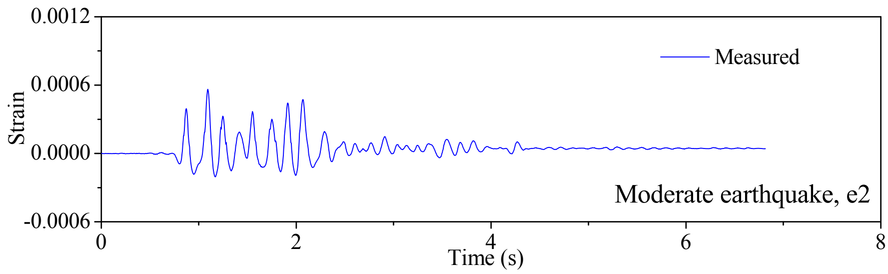

(f)

Figure 4.35 Reinforcement strain responses

(a) n1 (b) n7 (c) s2 (d) s7 (e) e1 (f) e2

Table 4.13 Peak strain responses of longitudinal reinforcement

Component	Location	Peak Reinforcement Strain
North Tower Leg	n1	6.97E-04
	n7	1.60E-03
South Tower Leg	S2	1.00E-03
	S7	1.60E-03
Southeast Pier	e1	7.08E-04
	e2	5.64E-04

It was observed that after the moderate earthquake, the concrete of the failure-vulnerable components cracked slightly. The peak strain response of the reinforcement was 0.0016, which is near the yielding strain of the reinforcement. It is of interest that the peak tensile strain was larger than the peak compressive strain, because the reinforcement sustained all the tension force yet the concrete did not bear tension force. All these indicate that the RC cable-stayed bridge performed slightly nonlinearly and plastically under the moderate earthquake excitation. The acceleration and strain response information acquired from the SHM system in this test of the bridge will be used for the nonlinear model updating to determine the actual properties of concrete and reinforcement of the slightly damaged RC bridge in Chapter 6.

4.5.5 Measured seismic responses to large earthquake

For the bridge with slight damage and under the large earthquake excitation of peak acceleration of 4.578m/s^2, the acceleration responses, strain responses and reaction forces of the bridge are expected to be large and the behavior of the bridge is expected to be severely nonlinear. Actually, during the shake table test at this stage the strain gauges at n7 and s2 were damaged.

4.5.5.1 Acceleration responses

The acceleration responses recorded by accelerometers A6, A7, A8 and A9 are plotted in Figure 4.36, respectively. These acceleration responses are all in the transverse direction of the bridge. The peak accelerations are listed in Table 4.14.

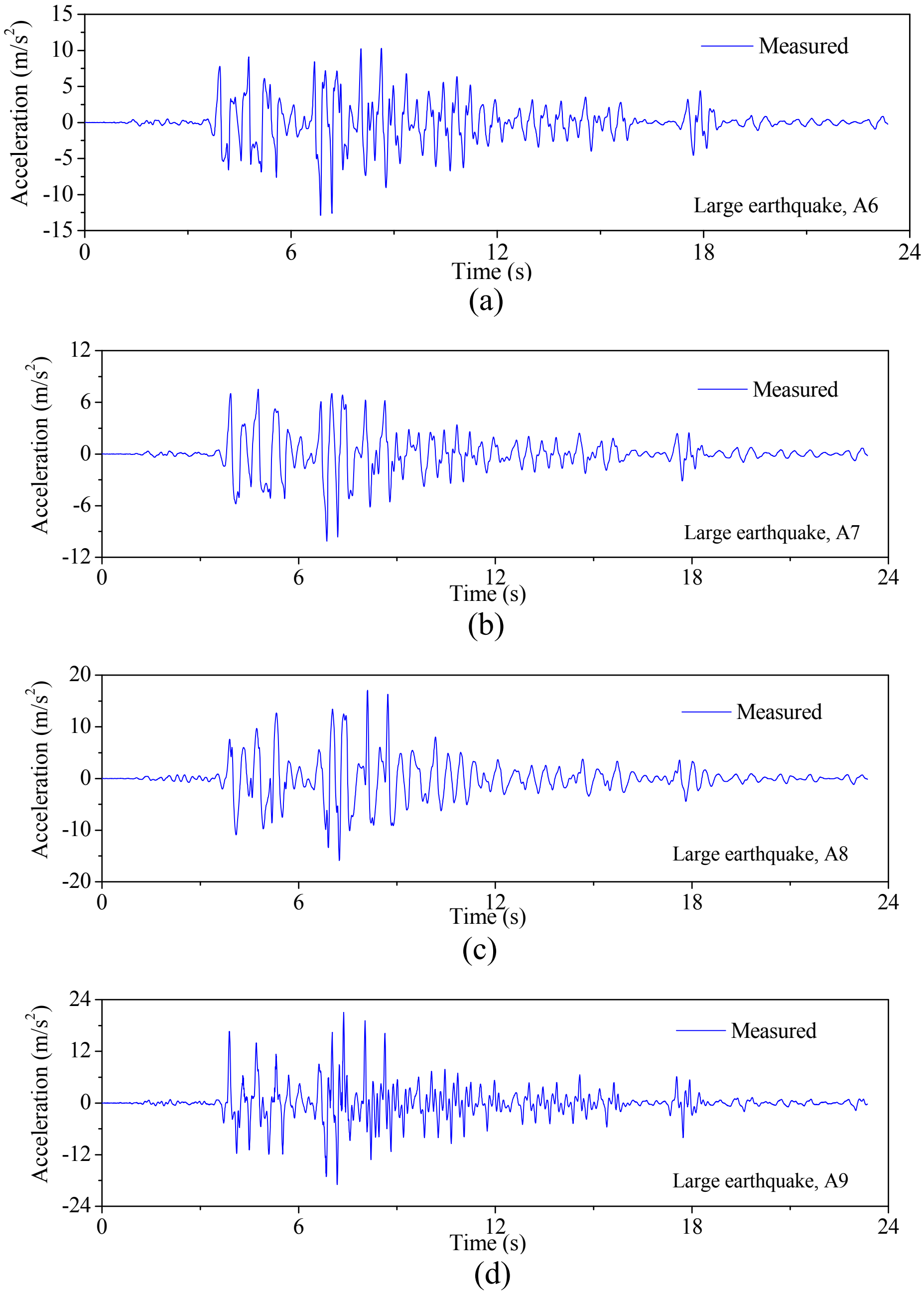

Figure 4.36 Acceleration responses

(a) A6 (b) A7 (c) A8 (d) A9

Table 4.14 Peak acceleration responses

Accelerometer No.	Acceleration (m/s^2)
A6	12.875
A7	10.137
A8	17.048
A9	21.047

It can be seen from Table 4.14 that the maximum acceleration response was recorded by the accelerometer A9 at the top of the tower. The peak value of the acceleration response at the top of the tower is nearly 4.4 times as big as that of the input earthquake excitation. The acceleration response at the top of the southeast pier is smaller than that of the southwest pier, because the southwest pier experienced severe damage and its flexural stiffness degraded sharply.

4.5.5.2 Reaction force (moment) responses

Figure 4.30 demonstrates the locations and positive directions of the reaction forces (moments), i.e. shear force, axial force, bending moment, and torsion moment. The reaction forces (moments) at the bottom of two tower legs and southeast pier are plotted in Figure 4.37. The peak reaction forces (moments) responses are listed in Table 4.15.

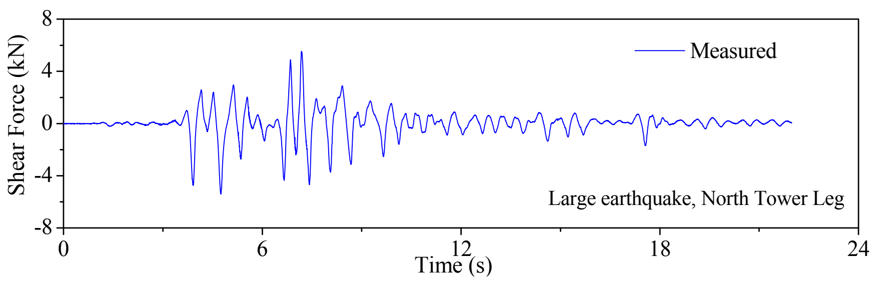

(a)

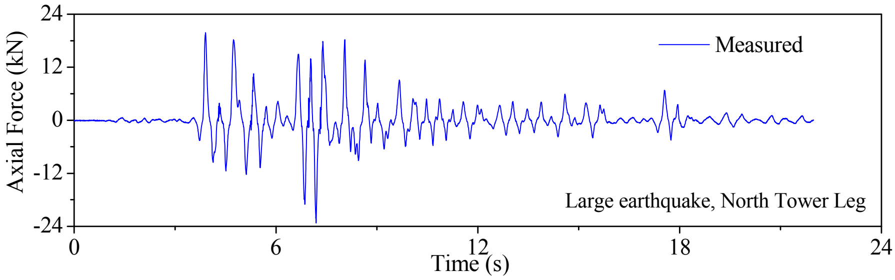

Axial Force (kN)
24
12
0
-12
-24
0
6
12
18
24
Time (s)
Measured
Large earthquake, North Tower Leg

(b)

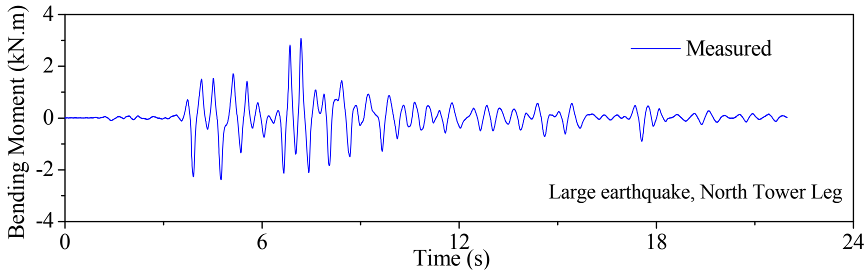

Bending Moment (kN.m)
4
2
0
-2
-4
0
6
12
18
24
Time (s)
Measured
Large earthquake, North Tower Leg

(c)

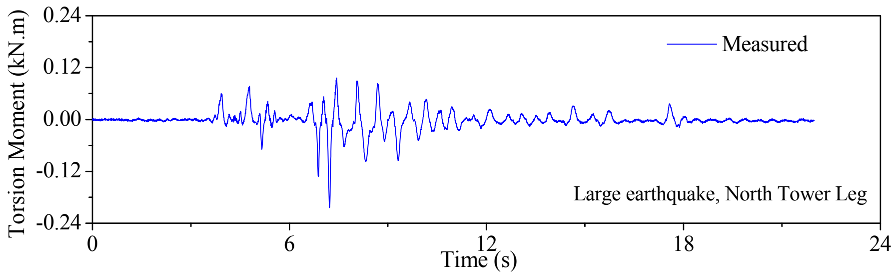

Torsion Moment (kN.m)
0.24
0.12
0.00
-0.12
-0.24
0
6
12
18
24
Time (s)
Measured
Large earthquake, North Tower Leg

(d)

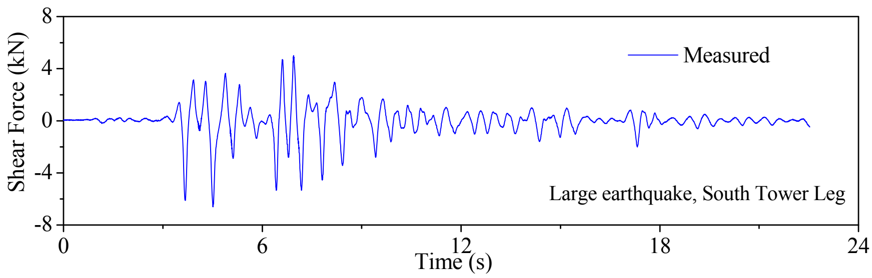

Shear Force (kN)
8
4
0
-4
-8
0
6
12
18
24
Time (s)
Measured
Large earthquake, South Tower Leg

(e)

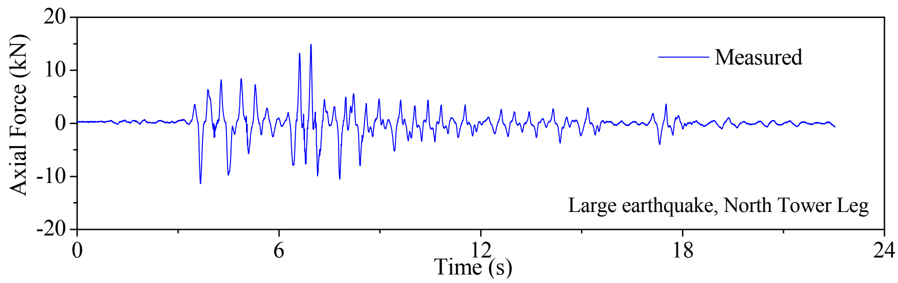

Axial Force (kN)
20
10
0
-10
-20
0
6
12
18
24
Time (s)
Measured
Large earthquake, North Tower Leg

(f)

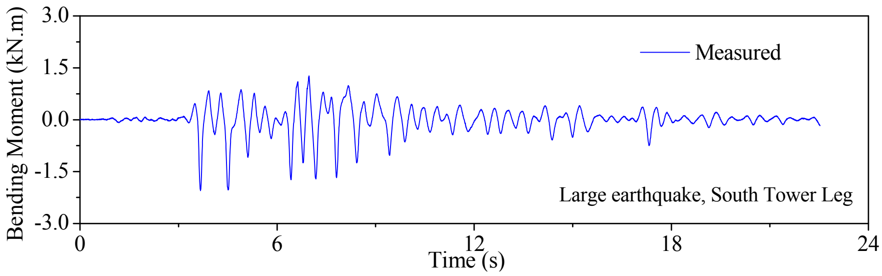

(g)

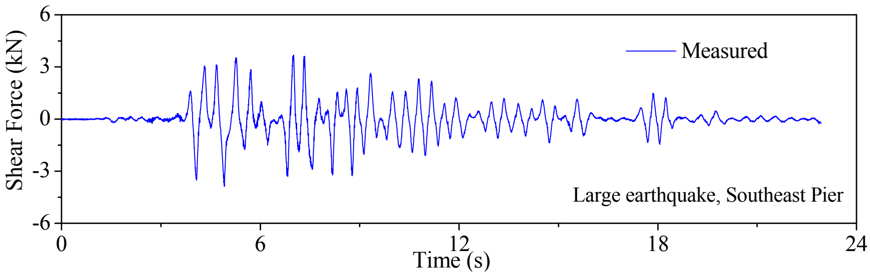

(h)

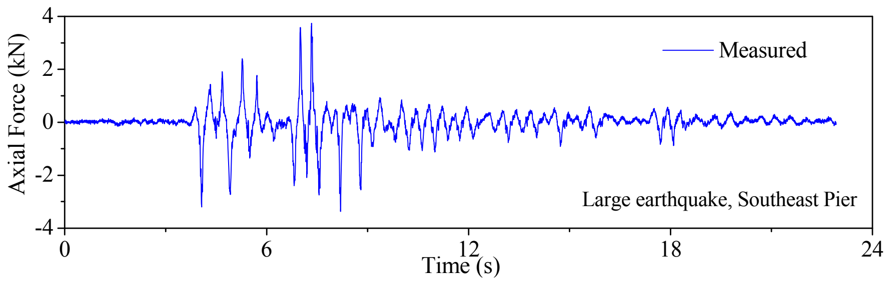

(i)

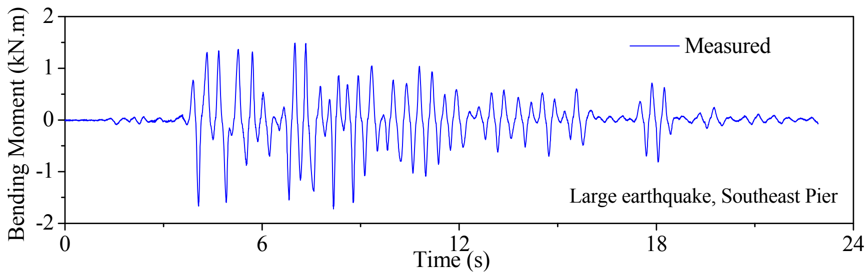

(j)

Figure 4.37 Reaction forces (moments) responses

(a) Shear force response at the bottom of the north tower leg (b) Axial force response at the bottom of the north tower leg (c) Bending moment response at the bottom of the north tower leg (d) Torsion moment response at the bottom of the north tower leg (e) Shear force response at the bottom of the southeast pier (f)

Axial force response at the bottom of the southeast pier (g) Bending moment response at the bottom of the southeast pier (h) Shear force response at the bottom of the southeast pier (i) Axial force response at the bottom of the southeast pier (j) Bending moment response at the bottom of the southeast pier

Table 4.15 Peak responses of reaction forces (moments)

Location	Force Type	Peak Forces
North Tower Leg	Shear Force	5.532kN
	Axial Force	23.229kN
	Bending Moment	3.075kN.m
	Torsion Moment	0.204kN.m
South Tower Leg	Shear Force	6.600kN
	Axial Force	14.912kN
	Bending Moment	2.055kN.m
Southeast Pier	Shear Force	3.873kN
	Axial Force	3.738kN
	Bending Moment	1.721kN.m

It can be observed from Table 4.15 that the south tower leg sustained larger shear forces but smaller bending moment than those of the north tower leg under the moderate earthquake. This is because the two south piers were fixed to the south girder in the transverse direction while the two north piers were not fixed to the north girder in the transverse direction. The reaction forces in the southeast pier were all smaller than those of the two tower legs, because the side pier sustained less weight of the additional mass blocks than those borne by each tower leg.

4.5.5.3 Reinforcement strain responses

Figure 4.38 shows the measured strain responses of the reinforcement at n4, n8, s5, s8, and e1. The peak reinforcement strain responses are summarized in Table 4.16.

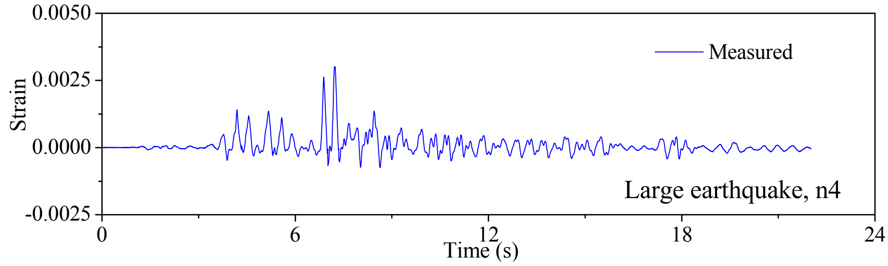

(a)

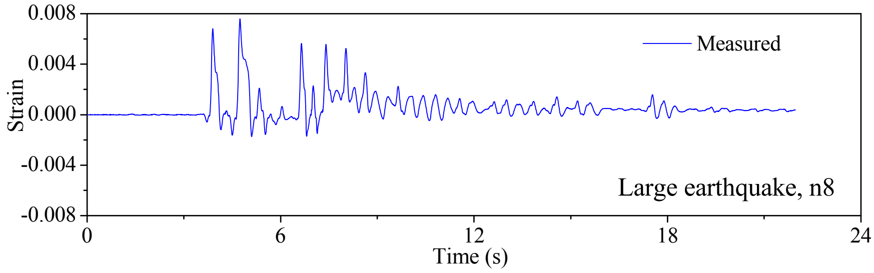

(b)

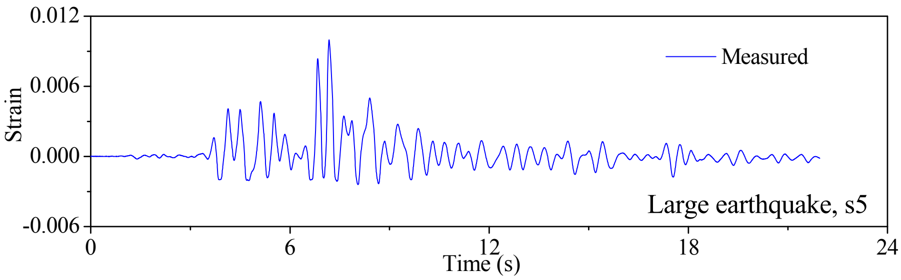

(c)

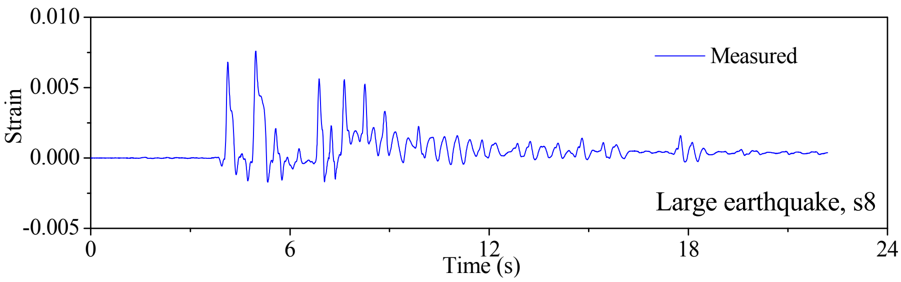

(d)

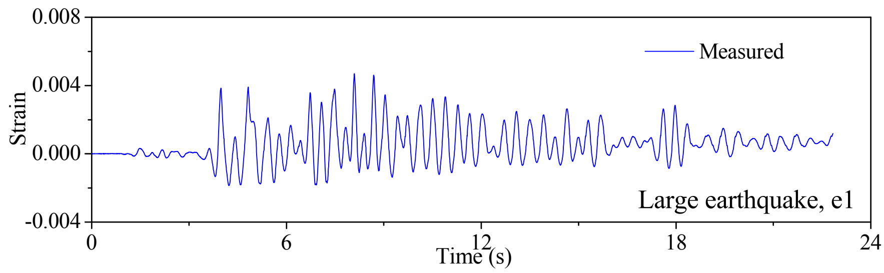

(e)

Figure 4.38 Reinforcement strain responses

(a) n4 (b) n8 (c) s5 (d) s8 (e) e1

Table 4.16 Peak strain responses of longitudinal reinforcement

Component	Location	Peak Reinforcement Strain
North Tower Leg	n4	0.0030
	n8	0.0076
South Tower Leg	s5	0.0100
	s8	0.0076
Southeast Pier	e1	0.0047

It was observed that after the large earthquake, the concrete of the failure-vulnerable components crushed. The peak strain response of the reinforcement was 0.01, which is significantly larger than the yielding strain of the reinforcement. It is also observed that the peak tensile strain was much larger than the peak compressive strain, because the reinforcement sustained all the tension force yet the concrete did not bear any tension force. All these indicate that the RC cable-stayed bridge performed severely nonlinearly and plastically under the large earthquake excitation. The acceleration and strain response information acquired from the SHM system from this test of the bridge will be used for the nonlinear model updating to determine the actual properties of concrete and reinforcement of the severely damaged RC bridge for the further collapse prognosis in Chapter 7.

4.5.6 Measured seismic responses to collapse earthquake

For the bridge with significant damage and now under the collapse earthquake excitation of peak acceleration of 4.633m/s^2, the acceleration responses, strain responses and reaction forces of the bridge are expected to be significantly large and the bridge is expected to collapse.

4.5.6.1 Acceleration responses

The acceleration responses recorded by accelerometers A6, A7, A8 and A9 are respectively plotted in Figure 4.39. These acceleration responses are all in the transverse direction of the bridge. The peak accelerations are listed in Table 4.17.

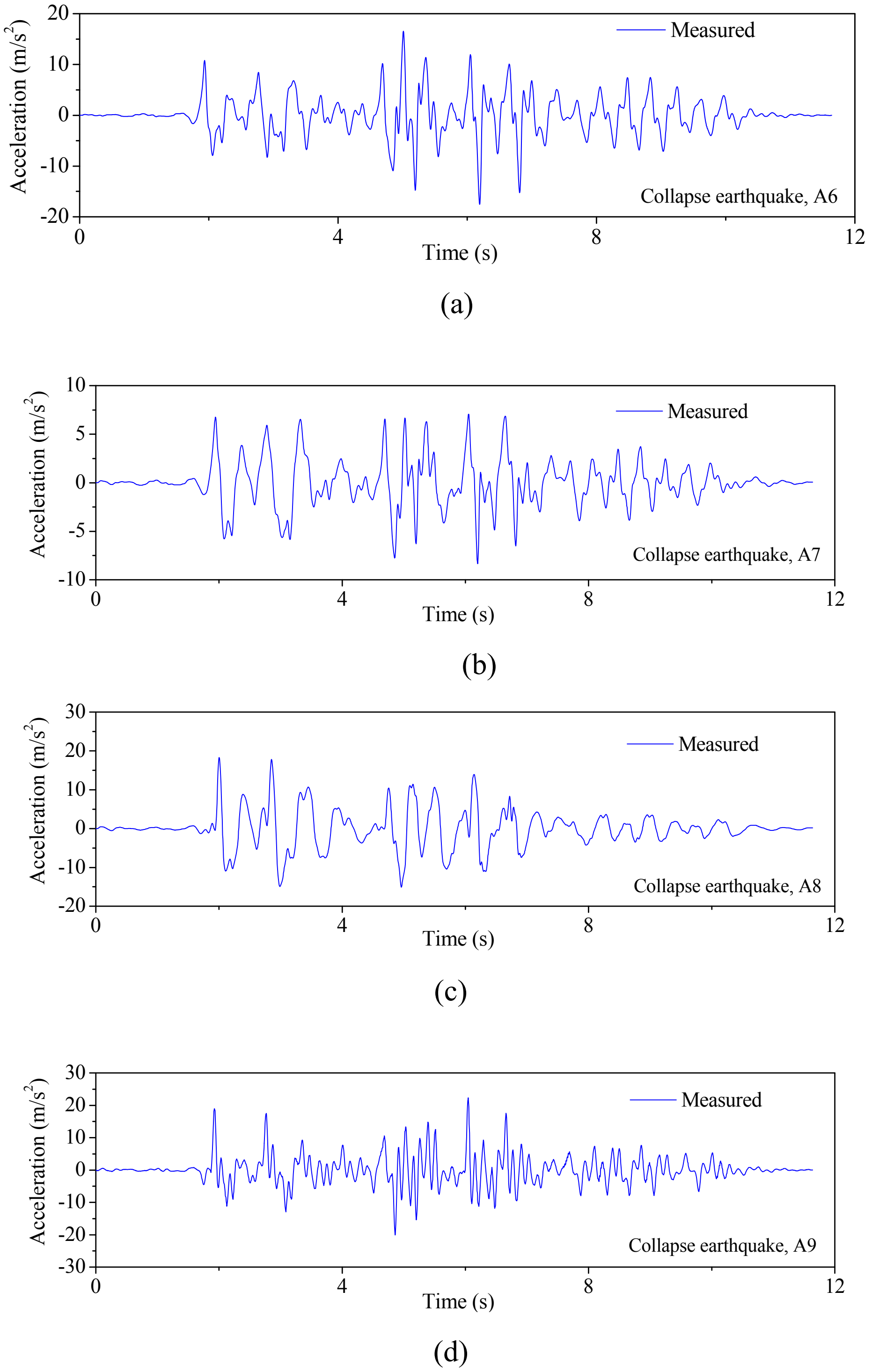

Figure 4.39 Acceleration responses

(a) A6 (b) A7 (c) A8 (d) A9

Table 4.17 Peak acceleration responses

Accelerometer No.	Acceleration (m/s^2)
A6	17.546
A7	8.351
A8	18.316
A9	22.298

It can be seen from Table 4.17 that the maximum acceleration response was recorded by the accelerometer A9 at the top of the tower. The peak value of the acceleration response at the top of the tower is nearly 4.8 times as big as that of the input earthquake excitation. The acceleration response at the top of the southeast pier is smaller than that of the southwest pier, because the southwest pier experienced severe damage and its flexural stiffness degraded sharply.

4.5.6.2 Reaction force (moment) responses

Figure 4.30 demonstrates the locations and positive directions of the reaction forces (moments), i.e. shear force, axial force, bending moment, and torsion moment. The reaction forces (moments) at the bottom of two tower legs and southeast pier are plotted in Figure 4.40. The peak reaction forces (moments) responses are listed in Table 4.18.

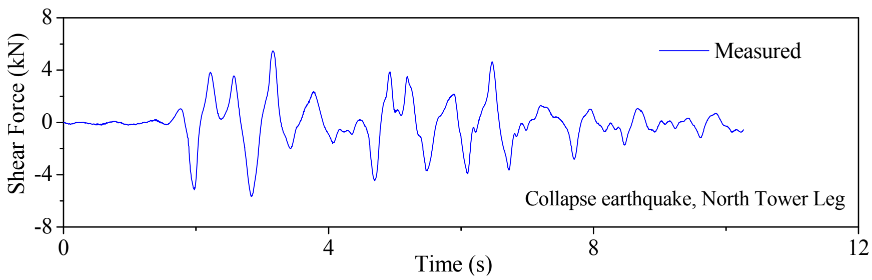

(a)

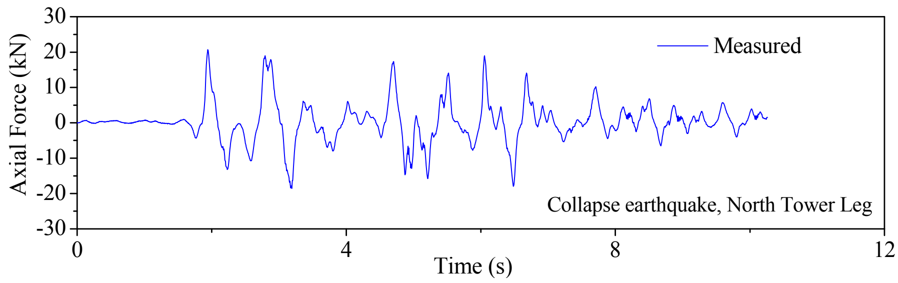
Measured
Collapse earthquake, North Tower Leg
Axial Force (kN)
Time (s)
30
20
10
0
-10
-20
-30
0
4
8
12

(b)

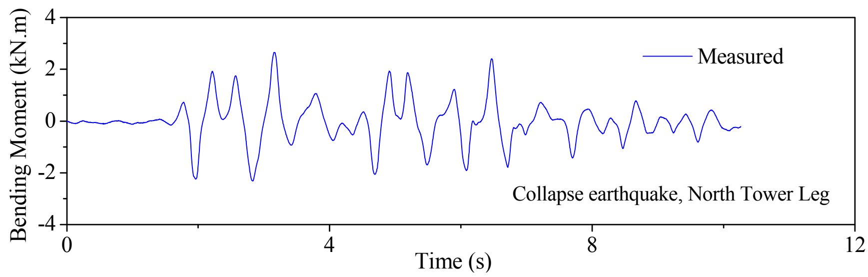
Measured
Collapse earthquake, North Tower Leg
Bending Moment (kN.m)
Time (s)
4
2
0
-2
-4
0
4
8
12

(c)

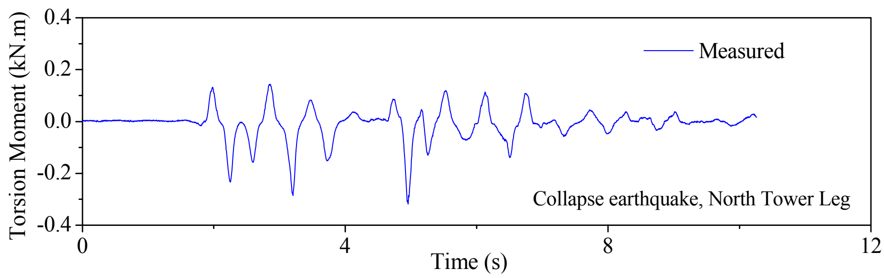
Measured
Collapse earthquake, North Tower Leg
Torsion Moment (kN.m)
Time (s)
0.4
0.2
0.0
-0.2
-0.4
0
4
8
12

(d)

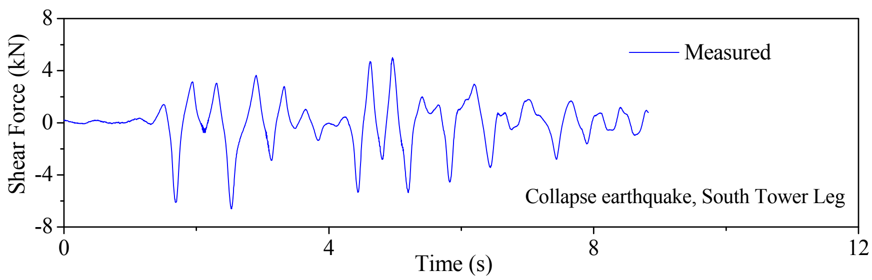
Measured
Collapse earthquake, South Tower Leg
Shear Force (kN)
Time (s)
8
4
0
-4
-8
0
4
8
12

(e)

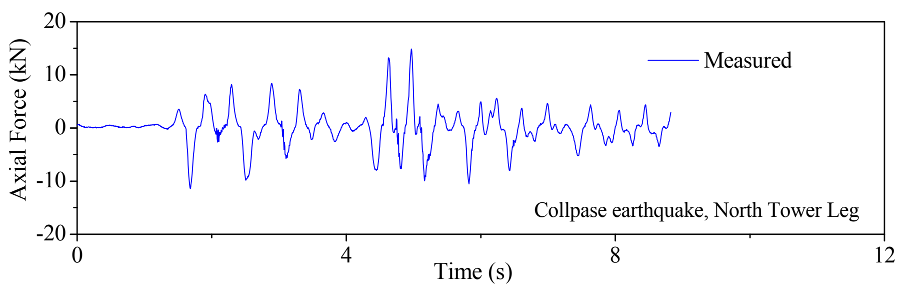
Measured
Collpase earthquake, North Tower Leg
Axial Force (kN)
Time (s)
20
10
0
-10
-20
0
4
8
12

(f)

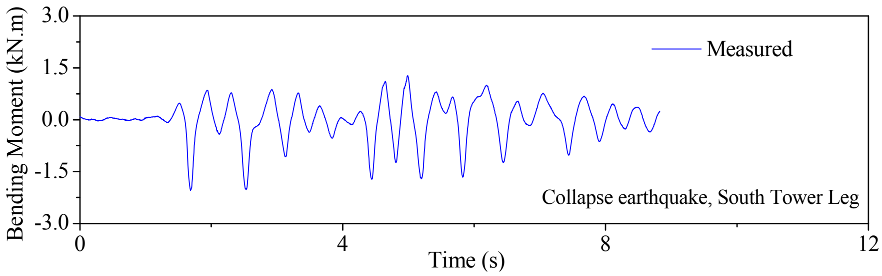

(g)

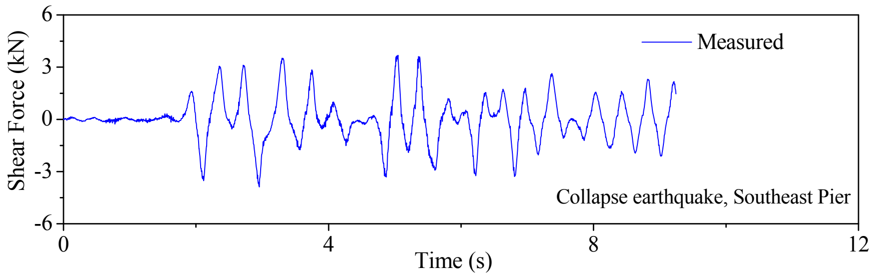

(h)

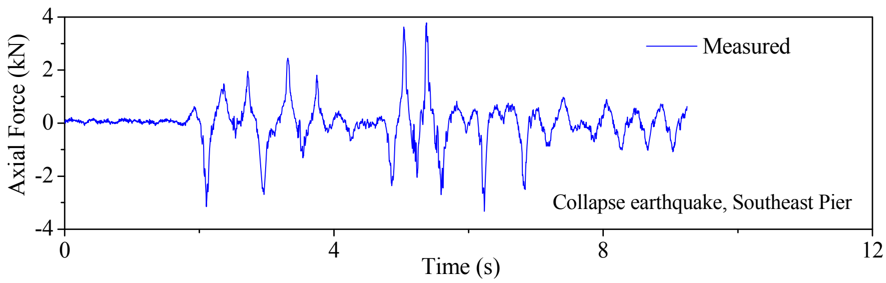

(i)

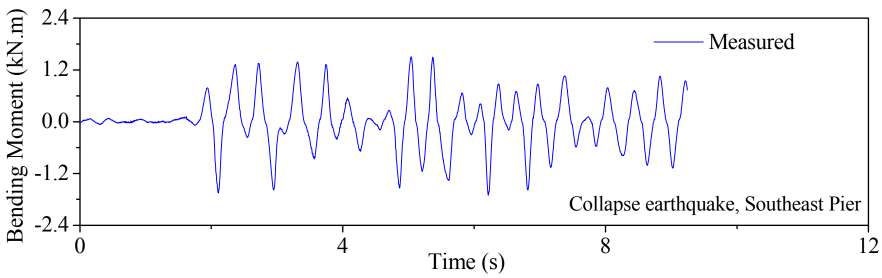

(j)

Figure 4.40 Reaction forces (moments) responses

(a) Shear force response at the bottom of the north tower leg (b) Axial force response at the bottom of the north tower leg (c) Bending moment response at the bottom of the north tower leg (d) Torsion moment response at the bottom of the north tower leg (e) Shear force response at the bottom of the southeast pier (f)

Axial force response at the bottom of the southeast pier (g) Bending moment response at the bottom of the southeast pier (h) Shear force response at the bottom of the southeast pier (i) Axial force response at the bottom of the southeast pier (j) Bending moment response at the bottom of the southeast pier

Table 4.18 Peak responses of reaction forces (moments)

Location	Force Type	Peak Forces
North Tower Leg	Shear Force	5.651kN
	Axial Force	20.712kN
	Bending Moment	2.657kN.m
	Torsion Moment	0.319kN.m
South Tower Leg	Shear Force	6.602kN
	Axial Force	14.893kN
	Bending Moment	2.046kN.m
Southeast Pier	Shear Force	3.882kN
	Axial Force	3.782kN
	Bending Moment	1.704kN.m

It can be observed from Table 4.18 that the south tower leg sustained larger shear forces but smaller bending moment than those of the north tower leg under the moderate earthquake. Again, this is because the two south piers were fixed to the south girder in the transverse direction while the two north piers were not fixed to the north girder in the transverse direction. The reaction forces in the southeast pier were all smaller than those of the two tower legs, because the side pier sustained less weight of the additional mass blocks than those born by each tower leg.

4.5.6.3 Reinforcement strain responses

Figure 4.41 shows the measured strain responses of the reinforcement at n4, n8, s5, s8, and e1. The peak reinforcement strain responses are summarized in Table 4.19.

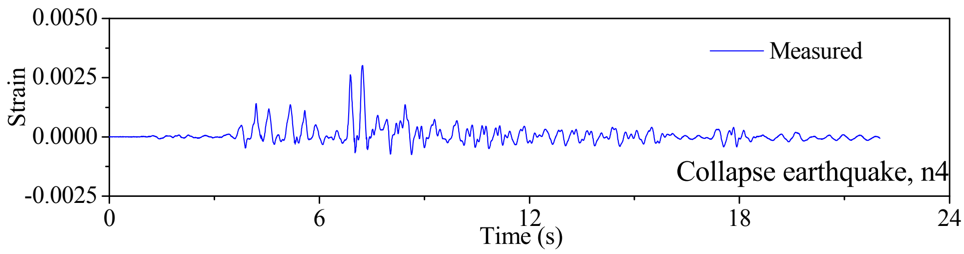

Measured
Collapse earthquake, n4
Strain
0.0050
0.0025
0.0000
-0.0025
0
6
12
18
24
Time (s)

(a)

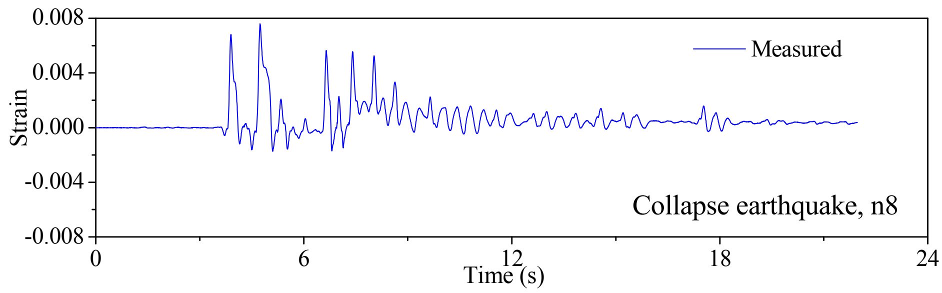

Measured
Collapse earthquake, n8
Strain
0.008
0.004
0.000
-0.004
-0.008
0
6
12
18
24
Time (s)

(b)

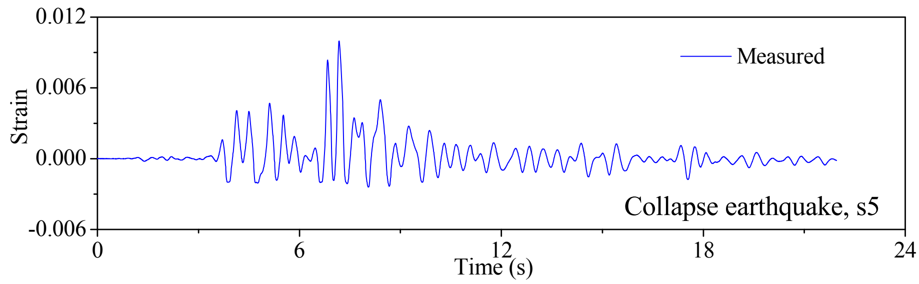

Measured
Collapse earthquake, s5
Strain
0.012
0.006
0.000
-0.006
0
6
12
18
24
Time (s)

(c)

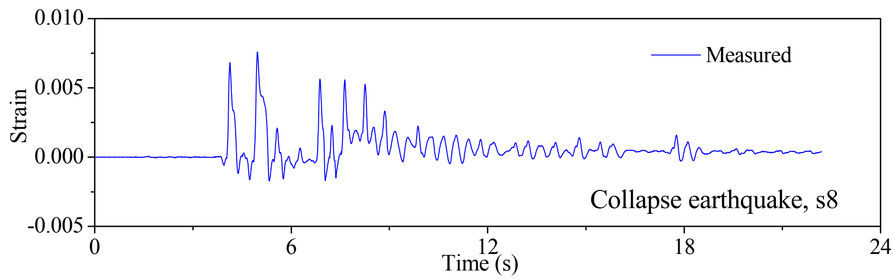

Measured
Collapse earthquake, s8
Strain
0.010
0.005
0.000
-0.005
0
6
12
18
24
Time (s)

(d)

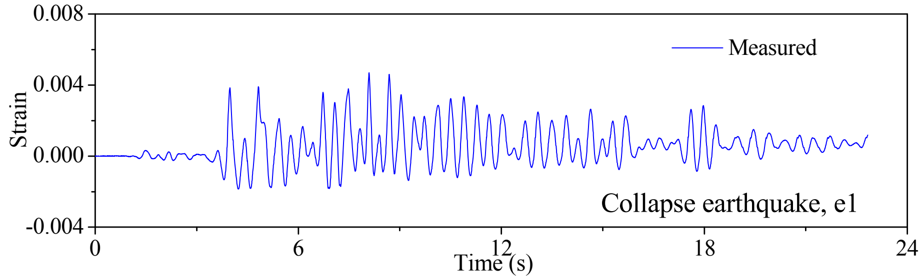

(e)

Figure 4.41 Reinforcement strain responses

(a) n4 (b) n8 (c) s5 (d) s8 (e) e1

Table 4.19 Peak strain responses of longitudinal reinforcement

Component	Location	Peak Reinforcement Strain
North Tower Leg	n4	0.0030
	n8	0.0076
South Tower Leg	s5	0.0100
	s8	0.0076
Southeast Pier	e1	0.0047

It was observed that after the collapse earthquake, the concrete of the failure-vulnerable components crushed severely. The peak strain response of the reinforcement was 0.01, which is significantly larger than the yielding strain of the reinforcement. It is of interest that the peak tensile strain was much larger than the peak compressive strain, because the reinforcement sustained all the tension force yet the concrete did not bear any tension force. All these indicate that the RC cable-stayed bridge partially collapsed under the collapse earthquake excitation. The partial collapse process of the bridge under the collapse earthquake is described in the following section. The acceleration and strain response information acquired from the SHM system in this test of the bridge will be used for the comparison with the numerical simulation for collapse prognosis in Chapter 7.

4.5.6.4 Partial collapse process

The RC cable-stayed bridge experienced partial collapse under the collapse earthquake as shown in Figure 4.42. The southeast RC pier experienced significant flexure deformation and plastic hinge but it was still attached to the girder. The southwest RC pier experienced flexure failure (see Figure 4.42 (b)): the concrete at the plastic hinge crushed, the longitudinal reinforcement yielded, the stirrup at plastic hinge fractured, and the top of the pier was separated from the girder. Although the two tower legs experienced flexure-shear damage with the concrete cracked, they survived without collapse during the collapse earthquake, as shown in Figure 4.42 (c).

(a)

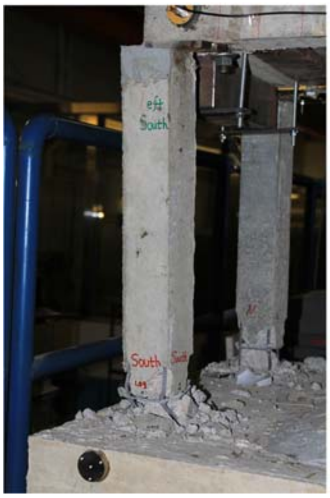

(b)

(c)

Figure 4.42 Partial collapse of the RC cable-stayed bridge

(a) Entire ridge (b) West side piers (c) Two tower legs

4.6 Summary

In this chapter, a 1:12 scaled RC cable-stayed bridge model was elaborately designed and constructed to have an experimental study of the seismic collapse of a RC bridge that was not designed with the seismic resistance. A comprehensive measurement (SHM) system was designed and installed on the RC bridge to record both the global responses and local responses of the bridge.

Before the shaking table tests, each cable force of the as-built RC bridge was measured by the frequency method to ensure that the bridge configuration meets the design requirements. The dynamic characteristic test was then conducted to gain an insight of the properties of the bridge. Finally, a series of earthquake tests, which include small earthquake, moderate earthquake, large earthquake, and collapse earthquake in terms of the PGA and spectrum, were conducted. It was observed from the four shake table tests that: (1) the RC bridge performed linearly and elastically under the small earthquake excitation and the RC bridge kept intact conditions after the small earthquake excitation; (2) the RC bridge performed slightly nonlinearly and plastically under the moderate earthquake excitation. The concrete in the failure-vulnerable components cracked slightly; (3) the RC bridge performed severely nonlinearly and plastically under the large earthquake excitation. The concrete in the failure-vulnerable components crushed severely and the reinforcement in the failure-vulnerable components yielded severely; and (4) the RC bridge partially collapsed under the collapse earthquake excitation. The concrete in the failure-vulnerable components crushed severely and the reinforcement in the failure-vulnerable components yielded severely. The measured data acquired from the SHM system together with the dynamic characteristics provide plentiful information for the linear model updating of the intact bridge in Chapter 5, nonlinear model updating of the damaged bridge in Chapter 6, and collapse prognosis for the damaged bridge in Chapter 7, respectively.

CHAPTER 5

FINITE ELEMENT MODELING AND LINEAR MODEL UPDATING OF A BRIDGE STRUCTURE FOR COLLAPSE ANALYSIS

5.1 Introduction

As reviewed in Chapter 2, numerous investigations have been made on collapse of reinforced concrete (RC) building structures, but seismic collapse analysis on RC bridge structures has been rarely conducted. With the rapid development of economy and urbanization, more and more RC viaducts and foot bridges have been constructed in metropolis around the world to reduce traffic jam. If these viaducts and foot bridges are located in earthquake-prone zones, the collapse of these bridge structures during earthquake events will cause heavy casualties and property losses. Therefore, the earthquake-induced collapse mechanism of RC bridge structures should be carefully investigated. Moreover, the structural properties of RC bridge structures are different from those of the RC building structures. For one example, the ratio of axial force to compressive capacity of a RC pier or a RC tower of a cable-stayed bridge structure on the foundation is always lower than that of a RC column of a high-rise building at bottom floors. Consequently, the flexure-shear failure often occurs for RC piers or towers of cable-stayed bridge structures with light hoop arrangement rather than the flexure-shear-axial failure commonly found in RC columns of high-building structures. For another, if the relative displacement between the pier and the girder is too large during earthquakes, it may cause the girder to drop from the piers, whereas this is not an issue for building structures. All of these differences make the collapse modes of RC bridge structures remarkably different from those of RC building structures under earthquake attach. Therefore, it is important to know how to establish appropriate finite element (FE) models for RC bridge structures for seismic collapse analysis. Furthermore, the current investigations on earthquake-induced collapse of RC building structures do not pay enough attention to the qualities of the FE models for collapse analysis. Actually, there are more uncertainties involved in collapse analysis than linear or nonlinear analysis of a building structure or a bridge structure because the collapse analysis is built on the linear and nonlinear analysis. Therefore, if the FE models used to perform collapse analyses are not updated based on their present conditions, the collapse analysis will be inaccurate. This is because the collapse analysis is performed after a linear and nonlinear analysis when both the linear model updating and nonlinear model updating are required for a collapse analysis. Fortunately, more and more structural health monitoring (SHM) systems have been installed in important RC structures, which make the model updating of these important RC structure realistic. Armed with SHM system, the laboratory tests of a RC bridge structure subjected to earthquake excitation, as conducted in Chapter 4, actually provide extensive measurement data for verifying the subsequent linear model updating, nonlinear model updating, and collapse prognosis of the RC bridge structure.

In view of the above, this chapter aims to establish an accurate FE model and conduct a linear model updating of the RC cable-stayed bridge, as investigated experimentally in Chapter 4, for seismic collapse analysis in OpenSees (McKenna et al. 2007). The characteristic FE model of the RC bridge structure for progressive collapse analysis is elaborately established accounting for not only material nonlinearity but also geometric nonlinearity. Besides, the zero-length elements with appropriate failure criteria are assigned at failure-vulnerable locations in the FE model to detect the potential failures. To ensure the accuracy of the FE model of the bridge structure, a two-stage model updating method (linear model updating and nonlinear model updating) are proposed in this study. The most recent linear model updating of RC structures is performed in the frequency domain, but in this study the linear model updating will be performed in both the frequency and time domains considering the subsequent nonlinear model updating. The linear model updating will be discussed in this chapter and the nonlinear model updating will be discussed in Chapter 6. In the linear model updating stage, twelve parameters are selected through sensitivity-based FE analyses and two different optimization objective functions are used. Measurement data acquired from the SHM system installed in the cable-stayed bridge model subject to small ground motion, as presented in Chapter 4, are utilized for the linear model updating and for the validation of the proposed model updating method.

5.2 FE Model for Seismic Collapse Analysis

The well-known open-source soft package of OpenSees (McKenna et al. 2007), powerful for nonlinear seismic analysis for RC structures, is taken as the platform for seismic collapse analysis in this study. As aforementioned, the most distinguished difference between the FE model for seismic collapse analysis and the traditional FE model for nonlinear analysis is that the FE model for collapse analysis must include the zero-length elements, which are inserted into appropriate locations and assigned with failure criteria for detecting the potential failures and releasing the zero-length springs automatically. The material nonlinearities of concrete and reinforcement are considered by fiber elements provided by OpenSees (McKenna et al. 2007). For a given section of fiber element, an appropriate number of fibers that respectively represent concrete and reinforcement should be divided first. If the fibers are located in confined concrete zone, they are assigned with the constitutive laws of confined concrete. If the fibers are located in unconfined concrete zone, they are assigned with the constitutive laws of unconfined concrete. The fibers that represent reinforcing steels are assigned with the constitutive laws of the reinforcement. Thus, the fiber elements that consist of various material fibers can take the various material nonlinearities into consideration. The geometric nonlinearity of the FE bridge model is considered by co-rotational transformation algorithm (Crisfield 1990). Until now, the material and geometric nonlinearities and the zero-length elements all have been introduced and involved in the FE model for collapse analysis.

In reality, the main materials of a physical RC cable-stayed bridge include concrete, reinforcement, and stainless wires for stay cables. Therefore, the numerical material constitutive laws for the concrete, reinforcement and stainless wire are introduced first, respectively, before the FE model is constructed.

5.2.1 Concrete material model

The concrete is modeled by a uniaxial material of Concrete01, and the Concrete01 model uses a uniaxial Kent-Scott-Park concrete material model with degrading linear unloading/reloading stiffness according to the references (Kent and Park 1971). The tensile capacity is not involved in the Concrete01 model. The constitutive law of the Concrete01 model includes an envelope curve and unloading/reloading rules, as demonstrated in Figure 5.1. The three regions on the envelop curve are expressed as:

Region OA: $\varepsilon \le \varepsilon_{c0} \quad \sigma = Kf_c' \left[2\left(\frac{\varepsilon}{\varepsilon_{c0}} \right) - \left(\frac{\varepsilon}{\varepsilon_{c0}} \right)^2 \right]$ (5.1)

Region AB: $\varepsilon_{c0} < \varepsilon \le \varepsilon_{cu} \quad \sigma = Kf_c' \left[1 - Z(\varepsilon - \varepsilon_{c0}) \right]$ (5.2)

Region BC: $\varepsilon > \varepsilon_{cu} \quad \sigma = f_{cu}$ (5.3)

where K is a factor accounting for the strength increase due to confinement, f_c' is the compressive strength of concrete at 28 days, ε_{c0} is the strain at maximum compressive strength, f_{cu} is the crushing strength, and ε_{cu} is the strain at the crushing strength. The initial slope for the model is noted by $E_0 = 2Kf_c' / \varepsilon_{c0}$, which is an important parameter affecting the linear performance of RC structures. The unloading/reloading stiffness λE_0 of the Concrete01 is identical and can be determined experimentally, as shown in Figure 5.1. The parameters of ε_r and f_r can be determined and expressed:

$$\varepsilon_r = \frac{\lambda E_0 \varepsilon_{cu} - f_{cu}}{(1-\lambda)E_0} \tag{5.4}$$

$$f_r = E_0 \varepsilon_r \tag{5.5}$$

After obtaining the values of parameters of ε_r and f_r, the point R can be determined. The unloading path always points to point R. For example, if unloading event occurs at point D on the envelop curve, the unloading path will be DD' pointing to R. The reloading path coincides with the unloading path.

It should be emphasized that only the point A on the envelop curve of Concrete01 model should be identified in linear model updating stage and the other points of B and C will be determined in the nonlinear model updating stage.

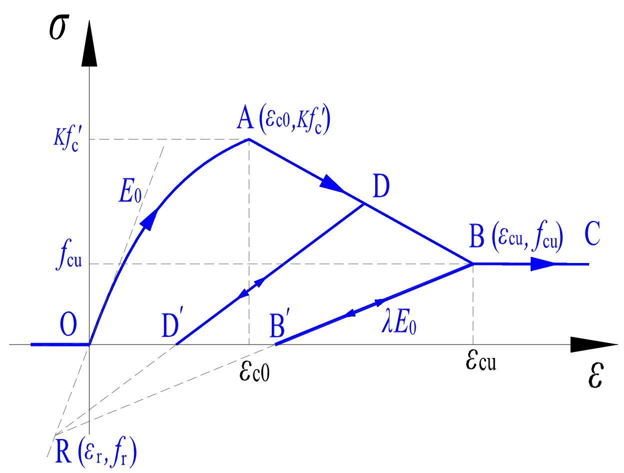

Figure 5.1 Constitutive laws of Concrete01

5.2.2 Reinforcement material model

The reinforcement is modeled by a uniaxial material of hysteretic model in OpenSees (McKenna et al. 2007). The constitutive laws of the hysteretic model include an envelope curve and unloading/reloading rules, as demonstrated in Figure 5.2. In Figure 5.2, f_y is the yielding strength, ε_y is the strain at yielding strength, f_u is the ultimate compressive strength, ε_u is the strain at ultimate compressive strength, f_r is the residual compressive strength, and ε_r is the strain at residual compressive strength. The tensile properties of the reinforcement are assumed to be the same as the compressive ones. The parameters of ε_{ni} and ε_{pi} are the last zero-load crossing strains at the compression and tension regions, respectively. The initial slope for the model is expressed by $E_0 = f_y / \varepsilon_y$, which is an important parameter affecting the linear performance of RC structures. The envelop curve consists of OABCE and OA'B'C'E', as shown in Figure 5.2. The unloading/reloading rules on both the envelope curve and inner envelope curve are shown by arrowed lines in Figure 5.2. The loading path coincides with the reloading path to give a uniform zero-load crossing instantaneous stiffness. The unloading/reloading stiffness is decreasing as the maximum (or minimum for compression region) strain increases. The relationship is expressed as:

$$E_{ti} = \mu_t^{\beta} E_0, \mu_t = \min(\varepsilon_y / \varepsilon_{max}, 1) \tag{5.6}$$

and for the compression region, the relationship is expressed as:

$$E_{ci} = \mu_c^{\beta} E_0, \mu_c = \min(-\varepsilon_y / \varepsilon_{min}, 1) \tag{5.7}$$

where ε_{max} and ε_{min} are the maximum and minimum strains that the model has ever experienced and β is a material constant.

It should be emphasized that only the two points A and A' on the envelop curve of hysteretic material model are determined in the linear model updating stage, and the other points B, B', C, C', E and E' on the envelop curve will be determined in the nonlinear model updating stage.

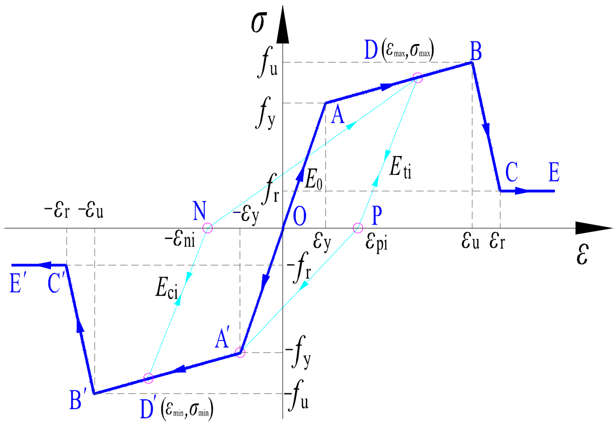

Figure 5.2 Constitutive laws of reinforcement material

5.2.3 Tension-only uniaxial material model

To accurately simulate stay cable performance, a uniaxial elastic tension-only material with initial stress is used for a stay cable, which has been implemented into the source code of OpenSees (McKenna et al. 2007). The constitutive law of the material is shown in Figure 5.3, where E is the elastic modulus and σ_0 is the initial compressive stress applied, used for simulating the initial tendon of a stay cable, ε_0 is the compressive strain of the material corresponding to zero stress, ε_1 is the designated compressive strain that can cover the working range of a stay cable, ε_2 and σ_2 are respectively the designated tensile strain and stress that can cover the working range of a stay cable. The elastic modulus and the as-built compressive stress in a stay cable can be determined through the material test and the cable vibration test, respectively.

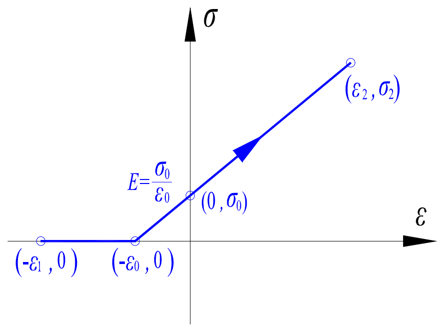

Figure 5.3 Constitutive laws of tension-only material with initial stress

5.3 A 3-D Finite Element Model

Although this chapter concerns only linear model updating, the FE model established in this chapter will also consider nonlinear model updating which will be carried out in Chapter 6, and eventually, seismic collapse analysis will be conducted in Chapter 7. Previous studies already demonstrated that FE analysis is a powerful tool in evaluating and predicting the nonlinear behavior of structures. However, the FE model for nonlinear analysis is essential but not adequate for conducting a seismic collapse analysis. The characteristic FE model for collapse analysis should not only predict the global response of a structure but also predict the local response, not only involve material nonlinearity but also geometric nonlinearity, not only include zero-length elements with appropriate criteria but also detect damage and release zero-length spring automatically. To establish such a FE model for the physical bridge as described in Chapter 4 for seismic collapse analysis, the FE model should simulate all the components of the actual physical bridge in the laboratory and all the components as well as their detail information will be simulated accurately so that the global and local responses can be predicted confidently. In this regard, the main components of the physical bridge described in Chapter 4 include the twin-girder, the transverse beams, the tower, the piers, the foundations, the load cells, the stay cables, the failure elements, and the connection conditions, and all of them will be carefully considered and modeled in the subsequent sections for seismic collapse analysis. It should be emphasized that the element meshing should account for the monitoring stations of multiple sensors in the SHM system installed in the physical bridge, as described in Chapter 4.

5.3.1 Modeling of RC twin-girder and transverse beam

The RC cable-stayed bridge tested in Chapter 4 consists of two separated longitudinal girders of rectangular cross sections which are linked by 8 transverse beams. To balance the dead loads of the side span and main span with different lengths, a length of 300mm heighten twin-girder is designed at the end of the side span. The heights of the normal girder and the heighten girder are 83mm and 120mm respectively, as shown in Figure 5.4. The twin-girder and the transverse beam are simulated by nonlinear fiber beam-column element that can respectively account for material nonlinearities of both concrete and reinforcement. The cross sections of the twin-girder and the transverse beam are all discretized using a layered mesh of 10×10 confined concrete fiber for the core concrete and one layer of fiber in each direction for the cover concrete, as shown in Figure 5.4. The Concrete01 material model is used to simulate the concrete in both linear and nonlinear analyses. The hysteretic material model is used to model the longitudinal reinforcement. Each single RC girder is divided into nine nonlinear fiber elements. Each RC transverse beam is divided into two nonlinear fiber elements. There are a total of 36 nonlinear fiber elements in the main girders and transverse beams.

There is a series of additional mass blocks mounted on the twin-girder of the bridge tested in the laboratory. To ensure no additional stiffness introduced to the bridge by the installation of additional mass blocks, two pieces of steel plate are inserted between the mass block and the girder. Correspondingly, in the FE modeling the densities of the 2 girders and 8 transverse beams are increased to consider the additional mass blocks mounted on them, but no additional stiffness is applied to the girders and transverse beams.

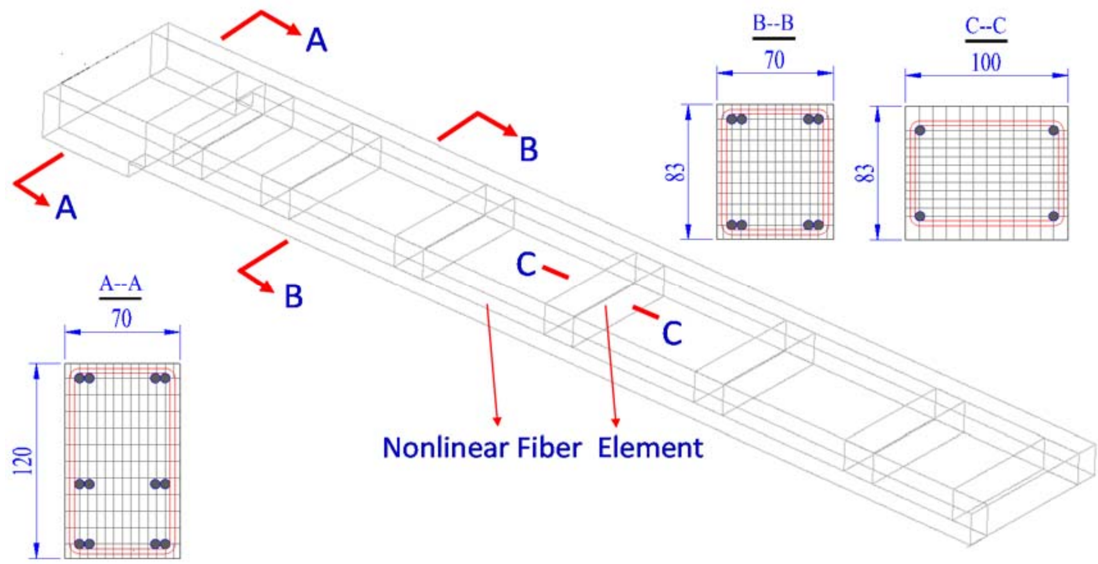

Figure 5.4 FE model of twin-girder and transverse beams (Unit: mm)

5.3.2 Modeling of tower, pier, foundation and load cell

There are four RC piers in the cable-stayed bridge located at the two ends of the bridge. The single RC tower is rigidly connected with the twin-girder (see Figure 5.5). The two tower legs and four piers are modeled by nonlinear fiber beam-column elements, the cross section of which is then discretized using a layered mesh of 10×10 confined concrete fiber for the core concrete and one layer of fiber in each direction for the cover concrete, as shown in Figure 5.5. The Concrete01 material model is used to simulate the concrete in both linear and nonlinear analyses. The hysteretic material model is used to model the reinforcement. The transverse beam at the top of the tower is modeled by 2 nonlinear fiber beam-column elements. Each pier and each tower leg are respectively divided into 3 and 11 nonlinear fiber elements. To avoid extensive computational cost and ensure enough accuracy during model updating process, force interpolation shape function other than displacement interpolation shape function is chosen (Spacone et al. 1996). Furthermore, the densities of the tower leg and the transverse beam are increased appropriately to account for the additional mass blocks mounted on them, but no additional stiffness is considered. The foundation of each pier and each tower leg is modeled by 16 elastic solid brick isoparametric elements with eight nodes, as shown in Figure 5.5. The load cell installed beneath the foundations is mainly composed of elastic steel cylinder body to sustain external forces and at the same time to measure forces. Each load cell is simulated by two elastic beam-column elements, as shown in Figure 5.5.

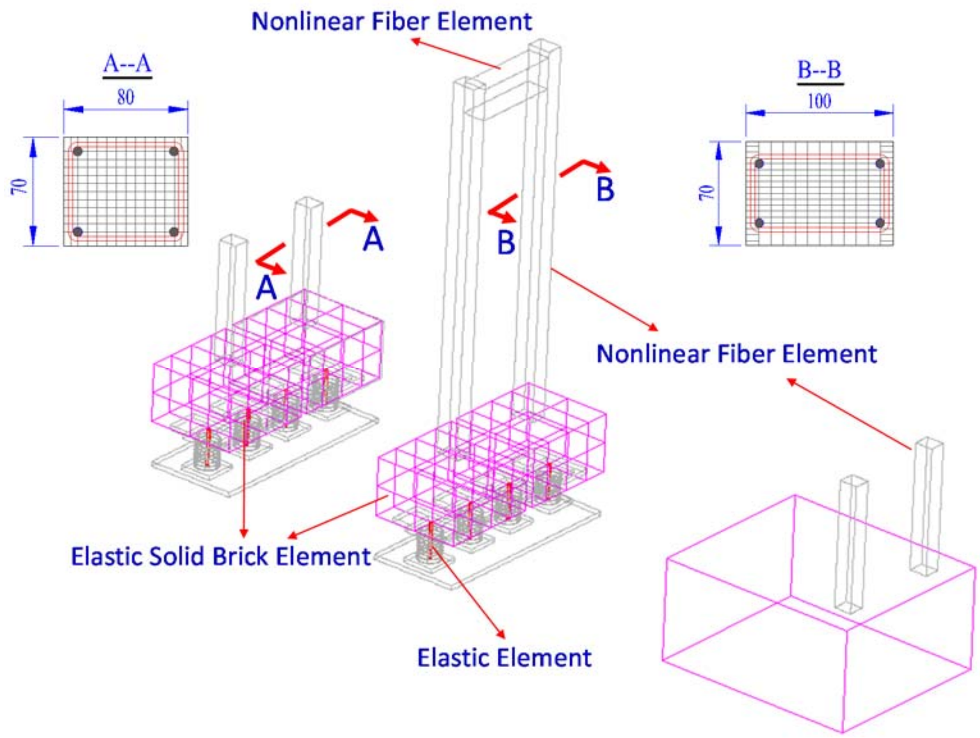

Figure 5.5 FE model of tower, pier, foundation and load cell (Unit: mm)

5.3.3 Modeling of stay cables

The cable system of the physical bridge consists of 6 pairs of stay cables. The stay cables are composed of identical numbers of stainless wires. Each stay cable is modeled by one tension-only truss element. In the laboratory tests, the as-built cable forces were measured and the initial stresses in the cables were then determined through iterative analysis. The initial stresses determined are assigned to the cables in the FE analysis. The sag effect of each cable element is considered by using the equivalent elastic modulus to replace the actual modulus of the cable. The equivalent elastic modulus is determined by the following equation:

$$E_{\mathrm{eq}} = \frac{E}{1 + \dfrac{(\rho A g \bar{l})^2 AE}{12T^3}} \tag{5.8}$$

where E_{eq} is the equivalent modulus of elasticity, E is the effective modulus of elasticity of cable, ρ is the effective density, g is the gravity acceleration, $\bar{l}$ is the horizontal projected length of the cable, A is the effective cross section area, and T is the cable tension. In this study, the elastic modulus of a cable is calculated by Eq. (5.8) using the measured force T.

5.3.4 Modeling boundary conditions and connections

There is a total of 8 load cells mounted between the shaking table and the foundations of the two piers on east side and the two tower legs to measure seismic forces transferred to the bridge from the motion of the shaking table. The bases of load cells are modeled as the fixed supports, i.e. all DOFs are restrained on the shaking table. The bases of the piers at the end of the long span are directly modeled as the fixed supports and their big foundation is not included in the FE model. Stay cables are connected to the twin-girders and the tower legs by sharing the same nodes. The connection of the twin-girder at the location, where the size of the girder cross section changes sharply, is modeled by master-slavery DOFs approach. The bearing conditions between the piers and the girders are summarized in Table 5.1, in which the numbers 0 and 1 denote free and constrained DOFs in the global coordinate system, respectively, as shown in Figure 5.6.

Table 5.1 Bearing conditions

Bearing Location	X	Y	Z	ROTX	ROTY	ROTZ
Northwest	0	1	1	0	1	0
Northeast	0	1	1	0	1	0
Southwest	0	1	0	0	1	0
Southeast	0	1	0	0	1	0

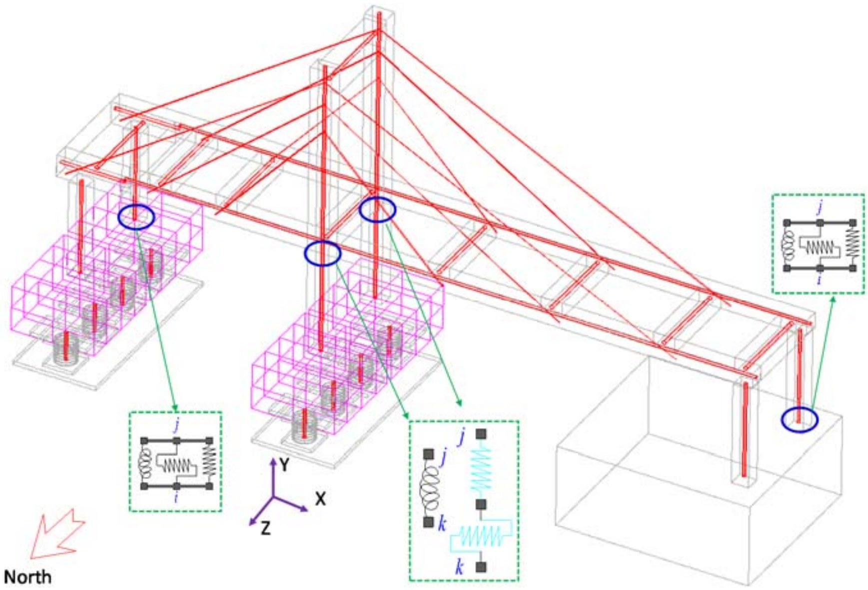

Figure 5.6 Locations of zero-length elements

5.3.5 Modeling element failure

Based on the aforementioned modeling work, a 3-D nonlinear FE model of the RC bridge is established in OpenSees (McKenna et al. 2007), which is composed of 72 nonlinear fiber beam-column elements, 16 elastic beam-column elements, 12 truss elements and 64 isoparametric solid brick elements. As described in Chapter 3, RC columns and RC beams have different failure modes. For the RC cable-stayed bridge, the main failure locations and failure modes are predicted by the principles presented in Chapter 3. In this regard, a nonlinear dynamic analysis of the FE model is conducted. The input ground excitation should be strong enough to make the bridge structure experience the yielding states at its damage-vulnerable locations and the intensity of the ground excitation is decided with reference to the test results presented in Chapter 4. The nonlinear analysis results showed that the RC tower legs would experience flexure-shear-axial failure at the locations below the tower-girder joints. The two RC piers on the south side of the bridge would suffer from flexure failure at the bottom due to the connection condition as described in Section 5.3.4. As a result, each of the two zero-length elements to detect potential flexure failure is inserted into the bottom of one side pier, and each of the two zero-length elements is inserted into the section of one tower leg under the tower-girder joint to detect flexure-shear-axial failure, as shown in Figure 5.6. The two nodes of the zero-length element *i* and *j* share the identical coordinates. It should be noted that the earthquake excitations are input along the transverse direction (Z axis). The zero-length elements linking the nodes *i* and *j* only include the three DOFs corresponding to Y, Z and ROTX, respectively. The other three DOFs (i.e., X, ROTY and ROTZ) between nodes *i* and *j* are connected by rigid zero-length springs, respectively. The parameters and failure criteria used in the zero-length elements are referred to in Chapter 3. It is worth noting that the zero-length elements in the FE model of the RC cable-stayed bridge are always far below the failure thresholds when the bridge structure is subjected to small earthquakes. Therefore, it is not an essential issue in this chapter to determine the parameters of the zero-length elements.

5.4 Linear Model Updating and Results

A 3-D FE model of the RC bridge with 4 zero-length elements for collapse analysis has been established in Section 5.3. The dynamic characteristics and linear dynamic analysis of the bridge are carried out using the established 3-D FE model, and the computed results are presented in the subsequent sections and compared with the measured ones presented in Chapter 4. The comparative results show that there are some differences between the computed and measured results. This is because the FE model can never be exactly the same as the physical structure and because there are many uncertainties in the FE modeling such as initial stresses in stay cables, material properties of concrete and reinforcement, connections, and others. Therefore, the linear model updating is necessary. The linear model updating in this study involves three basic steps. The first step is the set-up of two types of objective function: (1) the objective function is the function of natural frequencies as it is widely used at present for large civil structures; (2) the objective function is the function of time-varying responses, such as acceleration and strain responses, in consideration of the nonlinear model updating in Chapter 6. The second step is the selection of key parameters through a sensitivity study and the updating of the key parameters based on the first type of objective function so that the updating model is more close to the real one. The third step is to select key sensor locations and further update the key parameters based on the second type of objective function.

5.4.1 Two objective functions

The objective functions usually comprise the difference between the measured quantities and the model predictions. For a linear structure, the natural frequencies can be measured with a high accuracy. Natural frequencies and mode shapes are often selected as the quantities to form objective functions. However, the mode shapes of a real bridge structure cannot be measured accurately because of a limited number of sensors used in the measurement. Therefore, only the measured natural frequencies are selected in this study as the first type of objective function, whose mathematical formula is expressed as:

$$Min(J(\mathbf{r})) = Min\left(w_i \sum_{i=1}^{N} \left(\frac{f_i^a(\mathbf{DV}) - f_i^e}{f_i^e} \right)^2 \right) \tag{5.9}$$

subject to $\left|1 - r_k^a / r_k^e\right| \le 60\%$, k=1, 2, …, n_p

where w_i denotes the weighting factor. The weighting factors in Eq. (5.9) are all equal to 1.0 used in this study, which means that the contribution of each mode shape to the objective function is the same. N is the number of the natural frequencies, $f_i^a(\mathbf{DV})$ and f_i^e represent the ith analyzed and measured natural frequencies, respectively, **DV** is the vector of key parameters to be updated, r_k^a and r_k^e represent the kth updated and initial values of key parameter, respectively, and n_p denotes the number of the key parameters to be updated. In this study, the same weight factor is applied to the concerned natural frequencies. The varying range of each key parameter is set to be 60% of the initial value in order to maintain the physical meaning of the parameters in the updating process.

It should be pointed out that the FE model of the RC cable-stayed bridge structure established in this study is for seismic collapse analysis. For the RC bridge structures located in earthquake-prone zeros, they will experience concrete crack, reinforcement yielding, local damage and partial collapse during strong earthquake. The use of natural frequencies as quantities in the objective function for a nonlinear structure is no longer valid. The nonlinear model updating will be conducted using time-domain objective functions as discussed in Chapter 6. To be consistent with nonlinear model updating, this chapter also considers the objective function in the time domain. The updated results are then compared with those using the natural frequencies as the objective function to see if and how the time domain objective functions can be used for model updating. In this regards, the global responses such as acceleration, and local response, such as reinforcement strain, in the time domain are selected as objective function for model updating.

$$Min(J(\mathbf{r})) = Min(w_1 J^1 + w_2 J^2) \tag{5.10}$$

subject to $\left|1 - r_k^a / r_k^e\right| \le 60\%$, k=1, 2, …, n_p

where the weighting factors for the objective function are set as $w_1 = w_2 = 0.5$, J^1 and J^2 are the functions associated with acceleration and reinforcement strain responses, respectively.

$$J^1 = \sum_{i=1}^{N_a} \left(\frac{\sum_{n=1}^{N_t} \left(\ddot{u}_i^a(t_n, \mathbf{DV}) - \ddot{u}_i^e(t_n) \right)^2}{\sum_{n=1}^{N_t} \left(\ddot{u}_i^e(t_n) \right)^2} \right) \tag{5.11}$$

$$J^2 = \sum_{i=1}^{N_s} \left(\frac{\sum_{n=1}^{N_t} \left(\varepsilon_i^a(t_n, \mathbf{DV}) - \varepsilon_i^e(t_n) \right)^2}{\sum_{n=1}^{N_t} \left(\varepsilon_i^e(t_n) \right)^2} \right) \tag{5.12}$$

where N_a denotes the number of the accelerometers to measure acceleration responses, N_t denotes the time steps in the response time history used for optimization, $\ddot{u}_i^a(t_n, \mathbf{DV})$ is the computed acceleration response at the location of the ith accelerometer at the time t_n with respect to the key parameter vector **DV**, $\ddot{u}_i^e(t_n)$ is the measured acceleration response from the ith accelerometer at the time t_n, Ns is the number of the strain gauges, and $\varepsilon_i^a(t_n, \mathbf{DV})$ and $\varepsilon_i^e(t_n)$ are the ith computed and measured reinforcement strains at the time t_n, respectively.

Both Eq. (5.9) and Eq. (5.10) can be solved using the sparse nonlinear optimization technique (SNOPT) (Gill et al. 2002) implemented in OpenSees (Gu et al. 2011) but the accuracy of the solution of key parameters depends on their initial values. A multi-start method is employed in this study to run the updating algorithm with numerous initial conditions within the pre-set domain. To get convergence, the values of the objective function at each iteration step are recorded and plotted against the number of the iteration step during the model updating. Once the decrease trend (slope) is smaller than the designated value, the iteration stops and the updated parameters are determined. The corresponding key parameters can be regarded as the global solution.

5.4.2 Selection and updating of key parameters

As the geometric dimension and mass of the physical bridge tested in the laboratory can be measured with relative accuracy, the parameters of geometric dimension and density of the bridge components are excluded from the parameters to be updated. The tension forces in stay cables in the FE model of the bridge were determined through an iterative analysis to match the measured forces of as-built cables in the physical bridge. Therefore, the tension force of each cable is not taken as a parameter to be updated, but it will vary when the key parameters are updated. The load cells are made so stiff, compared with other parts of the bridge, that small change in stiffness of the load cells will not cause any change in the natural frequencies of the bridge. Therefore, the parameters of the load cells will not be selected as ones to be updated. The first key points on the envelope curves of confined and unconfined concretes, which signify the compressive strength (the first critical stress and the first critical strain), and the first key point on the envelop of constitutive law of reinforcement, which denotes the yielding stress and the yielding strain (equivalent to the yielding stress and the module), are selected as the parameters to be updated in the linear model updating. As the tower, girders, transverse beams, piers, and foundations of the physical bridge were made of concrete of different strengths at different casting time with different spacing of hoops, the first key point (the first critical stress and the first critical strain) on the envelope curve will be taken as different parameters for the tower, transverse beams, girders and foundation. As a result, a total of 16 material parameters will be considered as candidate parameters. However, although all the candidate parameters are important in the linear model updating, whether or not they are taken as key parameters to be updated depends on their sensitivity to the natural frequencies. In such a way, only key parameters are selected for updating so that computation efforts can be reduced to a minimum to make the model updating possible and the updated results accurate.

The direct differentiation method (DDM) and finite differentiation method (FDM) for the sensitivity analysis of geometrically nonlinear structures by virtue of total Lagrangian formulation was proposed (Imai and Frangopol 2000; Liu and Kiureghian 1991). The FDM is employed in this chapter to calculate the sensitivities of the natural frequency to the candidate parameters so as to find the key parameters for the subsequent model updating.

The procedure for selecting key parameters using FDM is described as follows:

- Step 1: Compute the structural natural frequencies using the initial values of the parameters ($\mathbf{r}_{\mathrm{a}}^{0} = \{r_{\mathrm{k,a}}^{0}, \mathrm{k} = 1, 2, ..., n_{\mathrm{p}}\}^{\mathrm{T}}$), where n_{p} is the total number of the parameters to be considered;
- Step 2: Perturb one of the parameters with a small increment $r_{\mathrm{k,a}}^{0} + \Delta r_{\mathrm{k,a}}$ and re-compute the natural frequencies;
- Step 3: Calculate the sensitivities of the natural frequencies ($\mathbf{f}$) and their partial derivatives ($\dfrac{\partial \mathbf{f}}{\partial r_{\mathrm{k,a}}}$) with respect to the designated variable by the FDM;
- Step 4: Repeat Step 2 and Step 3 until the sensitivities of the natural frequencies to all the candidate parameters are acquired.
- Step 5: Select the key parameters from the candidate parameters, to which the natural frequencies are most sensitive.

The above procedure is applied to the FE model of the RC bridge with respect to a total of 16 candidate parameters. Based on the results from the sensitivity study, a total of 12 key parameters is finally selected with respect to the first three natural frequencies in the Z-direction and the first torsional frequency of the bridge. The 4 candidate parameters associated with the RC foundation are not selected as key parameters.

The updated values of the 12 key parameters can be obtained through optimization analyses based on the first objective function and they are tabulated in Table 5.2. The parameter that has the greatest change among all the updated parameters is the first critical stress of the confined concrete of tower, girder and pier, increasing from 36.7MPa to 54.0MPa. The increase of the first critical stress is reasonable because 36.7MPa is the critical stress measured from the unconfined concrete samples and when the concrete is confined by hoops, the first critical stress will increase. For similar reasons, all the updated parameters listed in Table 5.2 are acceptable.

Table 5.2 Updated key parameters

Parameter No.	Description	Before Updating	Updated 1
1	First critical stress of confined concrete of tower and pier (MPa)	-36.7	-54.0
2	First critical strain of confined concrete of tower and pier	-0.0022	-0.0020
3	First critical stress of cover concrete of tower, girder and pier (MPa)	-36.7	-53.7
4	First critical strain of cover concrete of tower, girder and pier	-0.0022	-0.0030
5	First critical stress of confined concrete of transverse beam (MPa)	-42.9	-61.4
6	First critical strain of confined concrete of transverse beam	-0.0023	-0.0027
7	First critical stress of cover concrete of transverse beam (MPa)	-42.9	-47.0
8	First critical strain of cover concrete of transverse beam	-0.0023	-0.0027
9	First critical strain of confined concrete of girder (MPa)	-36.7	-51.2
10	First critical strain of confined concrete of girder	-0.0022	-0.0025
11	Yielding strength of reinforcement in tower, girder and pier (MPa)	460.0	626.9
12	Yielding strain of reinforcement in tower, girder and pier	0.0020	0.0019

The first 7 natural frequencies of the bridge structure using the updated parameters are presented in Table 5.3. The difference in natural frequencies presented in Table 5.3 is defined as the measured frequency minus the calculated one and then divided by the measured frequency. The mean value is defined as the sum of all the absolute differences and then divided by seven. The results listed in Table 5.3 show that before the model updating, the differences in the first and seventh natural frequencies reach 23% and 21%, respectively. After the model updating, the two differences are reduced to 14% and 13%, respectively. The differences in other 5 natural frequencies are all less than 10% after the model updating. The quality of the updated FE model is significantly improved and the updated model is more close to the real bridge. Furthermore, the computed first seven mode shapes after the model updating are similar to the measured ones and the characteristics of the first seven mode shapes are described in Table 5.4. In consideration that the physical bridge was tested under the ground motion in the Z-direction (see Chapter 4), the first three natural frequencies and model shapes in the Z-direction and the first torsional natural frequency and mode shape are the most important dynamic characteristics of the bridge.

Table 5.3 Comparison of natural frequencies (Unit: Hz)

Mode No.	Measured	Before Updating	Diff 0	Updated 1	Diff 1
1	10.294	7.931	23.0%	8.832	14.2%
2	11.275	9.651	14.4%	10.706	5.0%
3	14.706	14.204	3.4%	15.743	-7.0%
4	15.166	14.704	3.0%	16.482	-8.7%
5	21.301	18.100	15.0%	19.881	6.7%
6	23.284	23.422	-0.6%	24.698	-6.1%
7	37.489	29.731	20.7%	32.563	13.1%
Mean			11.4%		8.7%

Table 5.4 First seventh mode shapes

Mode Shape No.	Mode Shape Description
1	1st longitudinal bending of tower
2	1st transversal bending of tower
3	1st torsional of tower
4	2nd longitudinal bending of tower
5	2nd transversal bending of tower
6	3rd longitudinal bending of tower
7	3rd transversal bending of tower

5.4.3 Selection of key sensors and further updating of key parameters

As described in Chapter 4, a total of 66 sensors classified into 4 types was installed in the RC cable-stayed bridge: 9 strain gauges were respectively installed on 9 stay cables; 19 strain gauges were installed in the longitudinal reinforcement in two tower legs and two side piers; 13 accelerometers were installed on the tower legs, twin-girder, foundations and shaking table; and 6 load cells were installed beneath the two tower leg and the southeast pier foundations, respectively. The information of natural frequencies is commonly employed to conduct model updating for linear structures. However, the natural frequencies as the quantities in the objective function for nonlinear model updating is no longer valid. For the nonlinear model updating, it is better for it to be conducted in the time domain so that the structural responses can be directly used. Nevertheless, it will be very difficult, if not impossible, to use the responses from all the sensors for model updating. Considering that the acceleration responses can provide useful global information for dynamic characteristics of a structure, they will be used for nonlinear model updating in the time domain. A total of 8 accelerometers was installed in the tower, twin-girder and foundations to record the acceleration responses of the bridge in the Z-direction. The relative acceleration responses from the 4 accelerometers installed in the four foundations are too small to provide useful information for model updating. The accelerometers at A6, A8 and A9 are close to the four failure-vulnerable components, respectively, and the acceleration responses recorded by these three accelerometers are relatively large and associated with the first three natural frequencies and mode shapes in the Z-direction and the first torsional natural frequency and mode shape. Therefore, the accelerometers at A6, A8 and A9 are selected as the key sensor locations and their acceleration responses are considered in the second objective function. The accelerometer at A7 is used to validate the effectiveness of the second objective function proposed in this study. Moreover, the local seismic responses of failure-vulnerable components should be considered in the nonlinear model updating for seismic collapse analysis. Therefore, they will be considered in the linear model updating using the second objective function. A total of 19 strain gauges installed in the longitudinal reinforcement in three of the four failure-vulnerable components can be used to provide useful local information in the time domain for model updating. The four failure-vulnerable components are the two RC tower legs and two RC side piers (i.e., the southeast and southwest piers). Therefore, 3 strain gauges, respectively mounted on the longitudinal reinforcement at the bottom of the north tower leg, the south tower leg close to the girder, and the bottom of the southeast pier, are selected as the key sensors. These 3 strain gauges also record the maximum seismic responses which are considered in the second objective function. As no strain gauges were mounted on the longitudinal reinforcement in the southwest pier, the local strain information could not be provided for model updating. Other sensors, such as displacement sensors and load cells, are not considered in the model updating in the time domain.

In summary, the accelerometers at the locations A6, A8 and A9 and the strain gauges at the locations n7, s2 and e1 are selected as the key sensors for model updating in the time domain using the second type of objective function, as shown in Figure 5.7.

The acceleration response recorded by the accelerometer at A7 and the strain responses recorded by the strain gauges at n1, s7 and e2 are used to examine the feasibility and accuracy of the linear model updating method in the time domain.

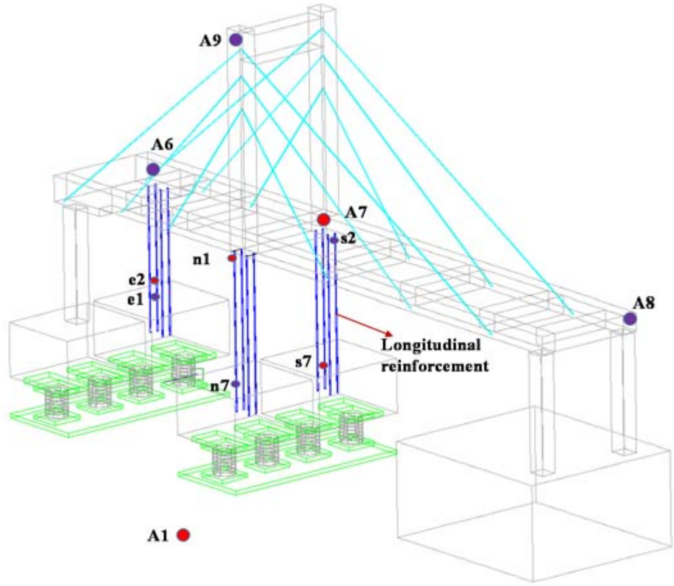

Figure 5.7 Key sensor locations for linear model updating

The further updated values of the 12 key parameters can be obtained through optimization analyses using the second type of objective function as tabulated in Table 5.5. It is worth noting that the initial values of the 12 key parameters using in the second type of objective function are the updated 12 key parameters using the first type of objective function. It can be seen that the second updated parameters are very close to the first updated parameters. Furthermore, Table 5.6 shows the measured natural frequencies, the first updated natural frequencies, and the second updated natural frequencies. It can be seen from Table 5.6 that the second updated natural frequencies are also very close to the first updated natural frequencies. All the comparative results discussed above indicate that the qualities of the two updated FE models using two different types of objective functions are very similar in terms of natural frequencies or dynamic characteristics of the bridge. It is feasible to take the second type of objective function for model dating in the time domain.

Table 5.5 Updated key parameters

Parameter No.	Description	Updated 1	Updated 2
1	First critical stress of confined concrete of tower and pier (MPa)	-54.0	-58.7
2	First critical strain of confined concrete of tower and pier	-0.0020	-0.0023
3	First critical stress of cover concrete of tower, girder and pier (MPa)	-53.7	-52.6
4	First critical strain of cover concrete of tower, girder and pier	-0.0030	-0.0033
5	First critical stress of confined concrete of transverse beam (MPa)	-61.4	-62.8
6	First critical strain of confined concrete of transverse beam	-0.0027	-0.0026
7	First critical stress of cover concrete of transverse beam (MPa)	-47.0	-46.4
8	First critical strain of cover concrete of transverse beam	-0.0027	-0.0029
9	First critical strain of confined concrete of girder (MPa)	-51.2	-52.8
10	First critical strain of confined concrete of girder	-0.0025	-0.0024
11	Yielding strength of reinforcement in tower, girder and pier (MPa)	626.9	589.9
12	Yielding strain of reinforcement in tower, girder and pier	0.0019	0.0019

Table 5.6 Comparison of natural frequencies (Unit: Hz)

Mode No.	Measured	Updated 1	Diff 1	Updated 2	Diff 2
1	10.294	8.832	14.2%	8.899	13.5%
2	11.275	10.706	5.0%	10.594	6.0%
3	14.706	15.743	-7.0%	15.613	-6.2%
4	15.166	16.482	-8.7%	16.609	-9.5%
5	21.301	19.881	6.7%	19.779	7.1%
6	23.284	24.698	-6.1%	24.781	-6.4%
7	37.489	32.563	13.1%	32.679	12.8%
	Mean		8.7%		8.9%

To have a further comparison between the two model updating methods, seismic responses of the bridge that is obtained from the FE model without model updating, the FE model updated with the first type of objective function, and the FE model updated with the second type of objective function are compared with each other. The ground excitation recorded by the accelerometer A1 is taken as the input into all the three models and is plotted in Figure 5.9. The peak acceleration and duration of the ground excitation are 0.9573m/s^2 and 7.8 seconds, respectively. The sampling frequency of the ground excitation is 256 Hz.

The acceleration responses of the bridge at the sensor locations A6, A8 and A9 are plotted in Figure 5.8. The peak acceleration responses are summarized in Table 5.7. It can be seen that the acceleration responses predicted from the first updated FE model are similar to those from the second updated FE model. To facilitate the fine comparison, an index J is further introduced as:

$$J = \frac{\sum_{n=1}^{N_t}\left(Mea(t_n) - Ana(t_n)\right)^2}{\sum_{n=1}^{N_t}\left(Mea(t_n)\right)^2} \tag{5.13}$$

where *Mea* and *A*na denote the measured and computed responses, respectively. The indexes $J(0)$, $J(1)$ and $J(2)$, which reflect the average errors of the responses predicted using the FE model without model updating, the first updated FE model, and the second updated FE model, are also listed in Table 5.8. It can be seen that the differences between the measured and computed accelerations are reduced after the model updating. As the index $J(2)$ is smaller than the index $J(1)$, the quality of the second model updating method is better than that of the first model updating method.

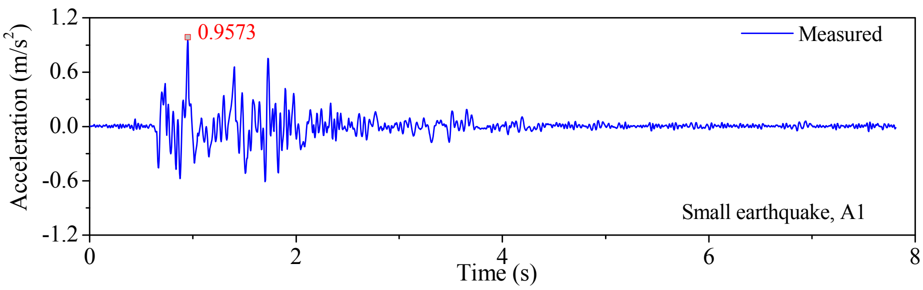

Figure 5.8 Acceleration recorded at station A1

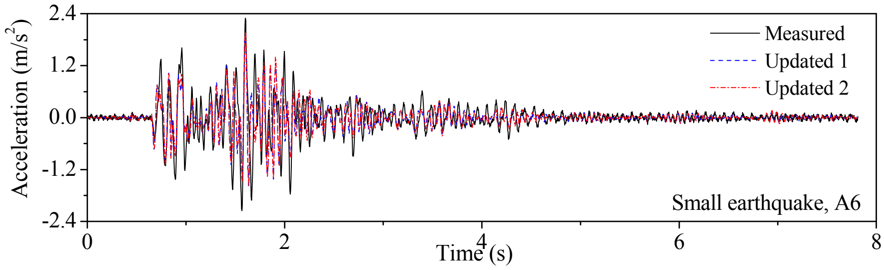

(a)

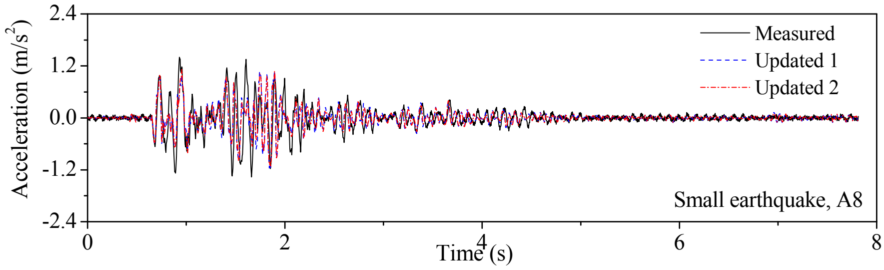

(b)

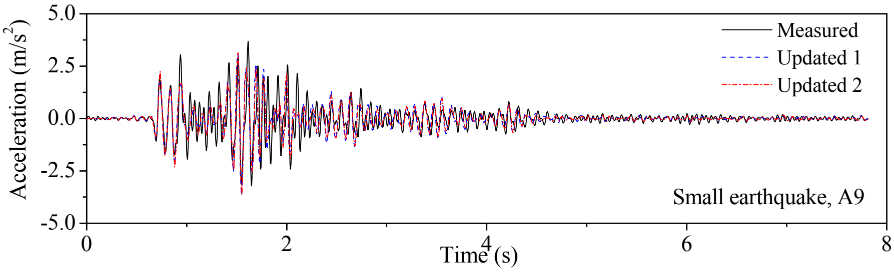

(c)

Figure 5.9 Comparison of acceleration time histories (a) A6 (b) A8 (c) A9

Table 5.7 Comparison of acceleration responses

Station No.	Peak Acceleration (m/s^2)				$J(0)$	$J(1)$	$J(2)$
	Measured	Initial	Updated 1	Updated 2			
A6	2.296	2.119	1.934	1.987	1.116	0.939	0.893
A8	1.402	1.591	1.162	1.136	1.267	0.905	0.786
A9	3.690	3.185	3.645	3.649	1.157	0.743	0.609
	Mean				1.180	0.862	0.763

Figure 5.10 shows the strain responses of the reinforcement at the bottom of north tower leg, the south tower leg close to the girder, and the bottom of the southeast pier from the three FE models, and the measured ones are also plotted in Figure 5.10. The measured and computed strain response time histories are similar. The peak reinforcement strain responses and the average errors of strain responses are summarized in Table 5.8. It shows that the average errors are significantly reduced after the model updating. The average errors from the second FE model updating method are smaller than those from the first FE model updating method. The second updating method is thus better than the first updating method with respect to strain

responses. It is noted that strain responses can be regarded as local responses while acceleration responses can be regarded as global responses. It is also noted that the computed peak strain responses are different from the measured ones, indicating that the updating of local responses is more difficult than the updating of global responses.

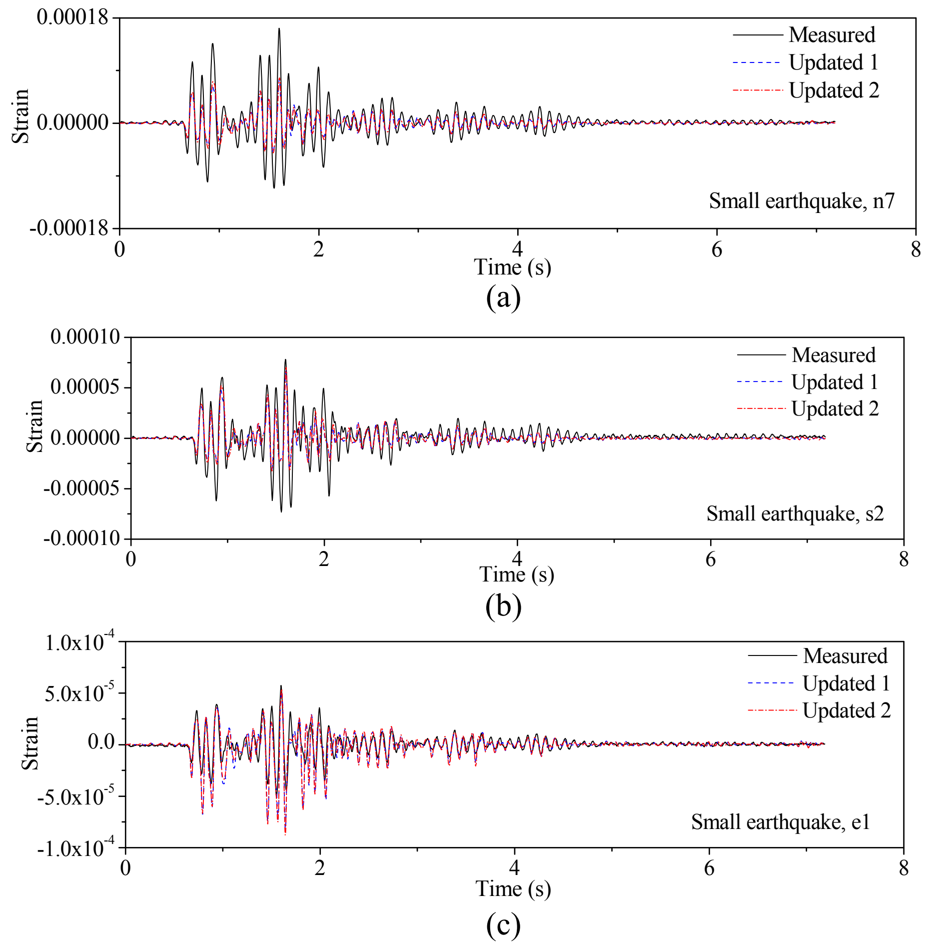

Figure 5.10 Comparison of reinforcement strain time histories (a) n7 (b) s2 (c) e1

Table 5.8 Comparison of reinforcement strains

Component	Location	Peak Reinforcement Strain				$J(0)$	$J(1)$	$J(2)$
		Measured	Initial	Updated 1	Updated 2			
North Tower Leg	n7	1.62E-04	1.13E-04	7.47E-05	7.81E-05	0.847	0.426	0.362
South Tower Leg	s2	7.83E-05	8.22E-05	6.69E-05	7.03E-05	0.956	0.434	0.367
Southeast Pier	e1	5.75E-05	9.76E-05	8.60E-05	8.79E-05	2.883	0.721	0.718
Mean						1.562	0.527	0.482

5.5 Validation

To validate the two model updating methods, one acceleration response, 6 reaction forces and 3 reinforcement strain responses, which are not used in the model updating, are employed to compare with the corresponding measurement results in the following sections.

5.5.1 Comparison of acceleration responses

The acceleration responses of A7 computed from the two updated FE models are plotted in Figure 5.11 together with the measured one. The acceleration responses computed from the two updated FE models are similar to the measured one. The peak acceleration responses and the average errors are tabulated in Table 5.9. The average errors of the responses after model updating are reduced, compared with the FE model without model updating. The average error from the second FE model updating method is smaller than that from the first FE model updating method. The second updating method is again better than the first updating method with respect to acceleration responses.

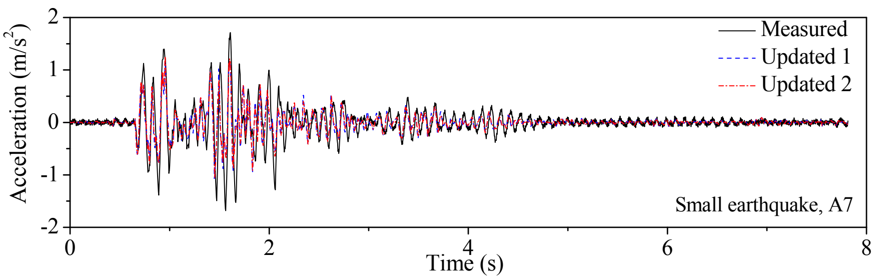

Figure 5.11 Comparison of acceleration response time histories at A7

Table 5.9 Comparison of acceleration responses

Station No.	Peak Acceleration (m/s^2)				Diff 0	Diff 1	Diff 2
	Measured	Initial	Updated 1	Updated 2			
A7	1.712	1.407	1.179	1.262	0.854	0.694	0.576
Mean					0.854	0.694	0.576

5.5.2 Comparison of reaction forces

Figure 5.12 demonstrates the locations and positive directions of the reaction forces (shear force, axial force and bending moment). The reaction forces at the north tower leg and the southeast pier predicted from the two updated FE models are plotted in Figure 5.13 and Figure 5.14, respectively, together with the measured one. The peak reaction force responses and the average errors are tabulated in Table 5.10. The average errors of the reaction forces after the second model updating are reduced, compared with the FE model without model updating. However, the average errors of the reaction forces after the first model updating are increased, compared with the FE model without model updating. The average errors from the second FE model updating method are smaller than those from the first FE model updating method. The second updating method is thus better than the first updating method with respect to reaction forces.

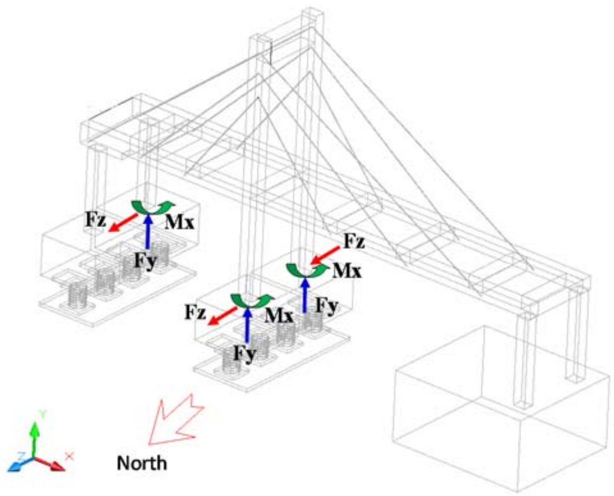

Figure 5.12 Locations for measured reaction forces

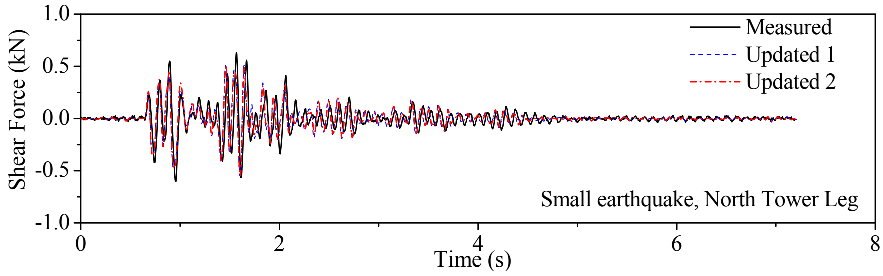

(a)

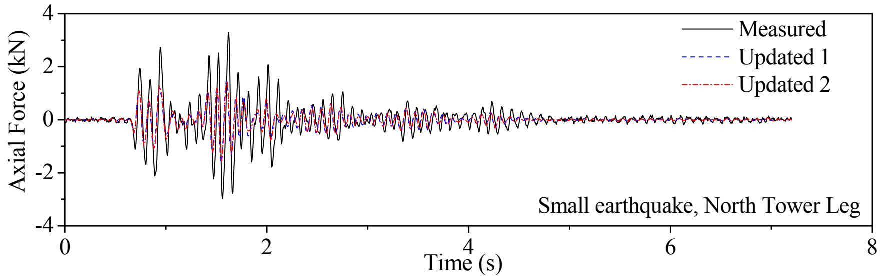

(b)

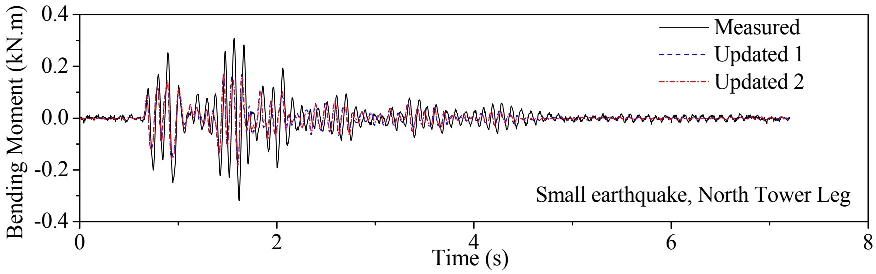

(c)

Figure 5.13 Comparison of reaction forces at the bottom of the north tower leg

(a) Shear force (b) Axial force (c) Bending moment

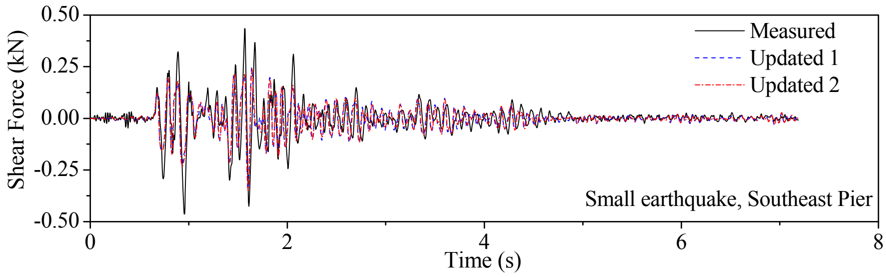

(a)

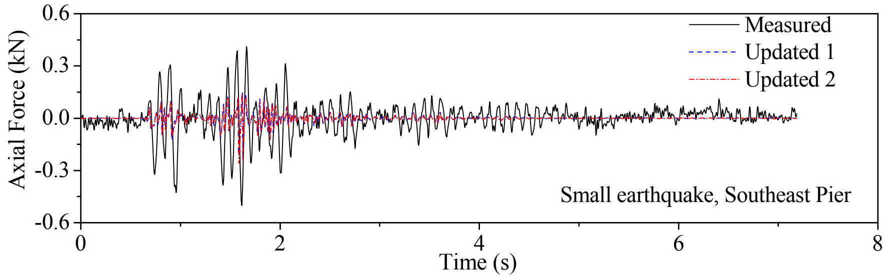

(b)

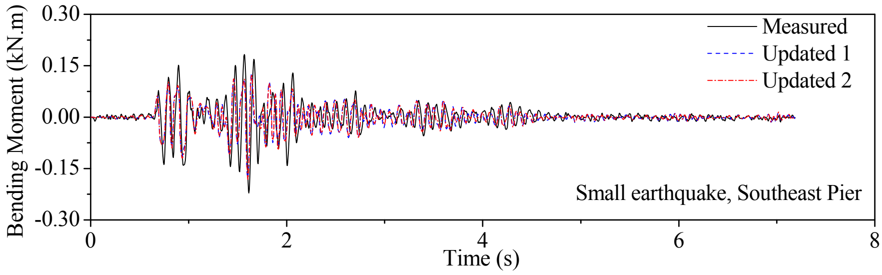

(c)

Figure 5.14 Comparison of reaction forces at the bottom of the southeast pier

(a) Shear force (b) Axial force (c) Bending moment

Table 5.10 Comparison of reaction forces

Location	Force Type	Peak Forces (kN, m)				$J(0)$	$J(1)$	$J(2)$
		Measured	Initial	Updated 1	Updated 2			
North Tower Leg	Shear Force	0.634	0.702	0.548	0.551	0.941	1.000	0.744
	Axial Force	3.302	1.532	1.616	1.564	0.655	0.819	0.662
	Bending Moment	0.318	0.233	0.183	0.184	0.769	0.882	0.698
Southeast Pier	Shear Force	0.463	0.276	0.346	0.350	0.684	0.858	0.675
	Axial Force	0.500	0.196	0.235	0.258	0.912	0.977	0.928
	Bending Moment	0.222	0.143	0.179	0.182	0.824	1.027	0.815
Mean						0.798	0.927	0.754

5.5.3 Comparison of reinforcement strains

Figure 5.15 shows the strain responses of the reinforcement at the north tower leg close to the girder, the south tower leg close to the girder, and the bottom of the southeast pier from the two updated FE models, and the measured ones are also plotted in Figure 5.15. The measured and computed strain response time histories are similar. The peak reinforcement strain responses and the average errors of strain responses are summarized in Table 5.11. It shows that the average errors are significantly reduced after the model updating. The average errors from the second FE model updating method are smaller than those from the first FE model updating method. The second updating method is thus better than the first updating method with respect to strain responses.

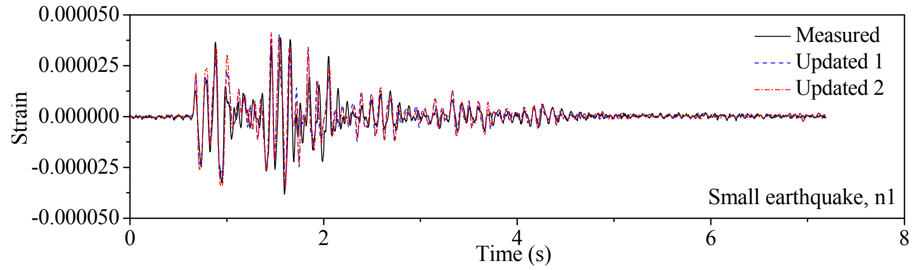

(a)

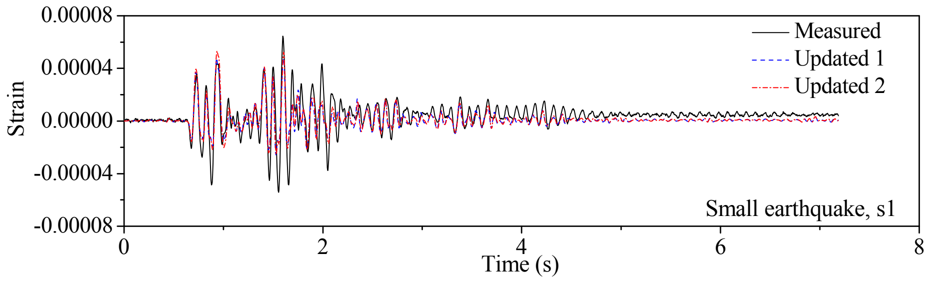

(b)

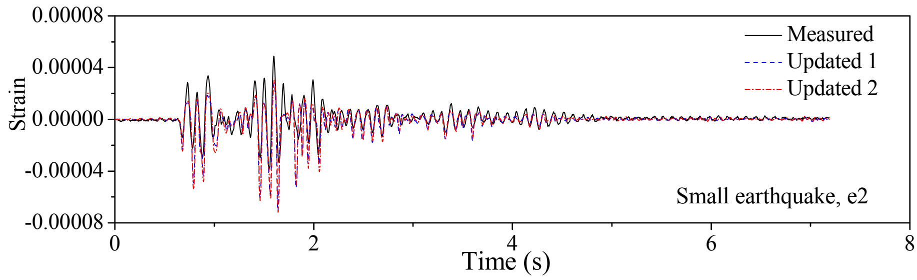

(c)

Figure 5.15 Comparison of reinforcement strain time histories (a) n1 (b) e1 (c) e2

Table 5.11 Comparison of reinforcement strains

Component	Location	Peak Strain				$J(0)$	$J(1)$	$J(2)$
		Measured	Initial	Updated 1	Updated 2			
North Tower Leg	n1	3.88E-05	8.06E-05	4.06E-05	4.14E-05	2.108	0.488	0.392
South Tower Leg	s1	6.45E-05	8.54E-05	4.79E-05	5.35E-05	1.160	0.496	0.430
Southeast Pier	e2	4.88E-05	8.10E-05	7.13E-05	7.19E-05	2.638	0.817	0.820
Mean						1.969	0.600	0.547

5.6 Summary

This chapter illustrates how to establish a 3-D FE model of the physical RC cable-stayed bridge tested in Chapter 4 for conducting a seismic collapse analysis complying with the framework depicted in Chapter 3. This chapter also proposes a two-stage model updating strategy (linear model updating and nonlinear model updating) and details of the linear model updating of the FE model using two types of objective functions: the objective function based on natural frequencies and the objective function based on acceleration and strain responses. A total of 12 key parameters is identified by virtue of sensitivity-based FE model analysis and updating using natural frequencies as the objective function. The 3 accelerometers at A6, A8 and A9 and 3 strain gauges at n7, s2 and e1 are selected as the key sensor locations and their responses are used for the further model updating in the time domain. Various seismic response time histories computed using the two different updating methods are compared with the measured responses. The comparison results indicate that both of the two objective functions can improve the quality of the FE model. The second objective function can not only be used as an alternate of the first one for nonlinear model updating but also provide better updating results than the first objective function.

As this chapter demonstrates the success of the linear updating of the 3-D FE model using acceleration and reinforcement strain responses in the time domain, the second objective function presented in this chapter will be used in the next chapter elaborating on the nonlinear model updating.

CHAPTER 6
NONLINEAR MODEL UPDATING OF A RC BRIDGE STRUCTURE FOR SEISMIC COLLAPSE ANALYSIS

6.1 Introduction

During the service life of a RC cable-stayed bridge, it mainly sustains low-level vibrations caused by traffic loads, wind loads, and small earthquakes. Under such dynamic loadings, the structural responses of the entire RC bridge are basically linear and may not lead to any structural damage. However, during moderate earthquake, some of structural components may experience damage and their materials are no longer linear and elastic, although the bridge does not collapse and other structural components still remain linear and elastic. Therefore, when a RC bridge is subjected to moderate earthquakes, some components become nonlinear while some components are intact. The linear model updating method presented in Chapter 5 does provide a useful tool to update the key parameters of the entirely intact RC structure or the intact components of the damaged RC structure, but it is not clear how to update nonlinear components of the damaged RC structure so that an updated nonlinear FE model can best represent the actual damaged RC structure.

As reviewed in Chapter 2, the material properties of a damaged RC component are nonlinear and time-dependent. Both concrete and reinforcement materials of the damaged RC component will experience successive strength and stiffness degradations under reversed cyclic loading. The strength degradation of the material can be accomplished by the evolution of the envelop curve of the material while the stiffness degradation can be considered in terms of reloading and unloading rules. The complex nonlinear behaviors of the reinforced concrete clearly present challenges to the nonlinear model updating task. The most recent nonlinear model updating for a RC structure aims to update stiffness degradation using the measured dynamic characteristics of the RC shear wall (Song et al. 2012) based on the assumption that there is no evolution of the envelop curves of both concrete and reinforcement. Therefore, their nonlinear updating method could not consider the strength degradation of concrete and reinforcement appropriately when the earthquake loading history is unknown. However, for dynamic collapse analysis of RC structures without knowing earthquake loading history, the strength degradation of the materials must be considered. Thus, a new nonlinear model updating method is required to account for both strength and stiffness degradations. The new nonlinear model updating method proposed in this study is to update the strength degradation of both concrete and reinforcement in the time domain using the acceleration and strain responses as the optimization objectives. The envelop curves of the materials are then reconstructed and used to calculate the structural responses together with the unloading and reloading rules until the key parameters controlling the strength degradation are finalized. It is worth noting that the nonlinear model updating method proposed in this chapter is to update the strength degradation of the materials at a given time (at the end time of the measured responses used). Therefore, the method does not need the entire loading history of a RC bridge and only the time histories of loading information and seismic responses of a certain period at critical locations of a RC bridge are needed. In such a way, the uncertainties in the confining effect on the concrete due to the stirrups and the strengthening effect on the reinforcement due to the surrounding concrete can be partially quantified through the nonlinear model updating method proposed in this study.

In brief, this chapter will first discuss the evolution principles for the envelop curves of both concrete and reinforcement together with the degradation rules of stiffness. The preliminary nonlinear seismic analysis of a RC bridge subject to moderate earthquake will then be carried out using the updated linear FE model obtained in Chapter 5 as well as the initial envelop curves of the materials and the degradation rules of stiffness. Based on the calculated response magnitudes, the configurations and locations of the structural members, all the members are classified into five groups. Except for the group of linear members whose key parameters have been updated using the linear model updating method in Chapter 5, the key parameters of other groups of nonlinear members will be identified and updated. The nonlinear model updating will then be conducted using the acceleration and strain responses at the critical locations decided in Chapter 5 as the optimization objectives to update the key parameters of the nonlinear elements. To confirm the correctness of the updated key parameters, the calculated seismic responses are compared with the so-called measured responses which are used in the model updating. Furthermore, the feasibility and accuracy of the proposed nonlinear model updating method is finally verified through the comparison between the predicted responses and the measured responses which are not used in the model updating.

6.2 Evolution of Envelop Curves

The nonlinear model updating of the FE model for a RC bridge structure must involve material nonlinearities of both concrete and reinforcement that possess characteristics of degradations of both strength and stiffness. These characteristics actually vary with time when a RC bridge is subjected to moderate or strong earthquakes. Therefore, it is crucial to comprehend the evolution of the envelop curves of both concrete and reinforcement under reversed cyclic loading, which involves unloading stiffness degradation, reloading stiffness degradation, and strength degradation (Mitra and Lowes 2007).

6.2.1 Envelop curve evolution for concrete material

Figure 6.1 shows the envelop curve M-O-A-B-N provided in OpenSees (McKenna et al. 2007) for Concrete01 without tensile capacity. There are three regions in the envelop curve in the coordinate system ($\sigma_c O \varepsilon_c$):

Region OA: $\varepsilon_c \le \varepsilon_{c0}$ $$\sigma_c = Kf_c^{'}\left[2\left(\frac{\varepsilon_c}{\varepsilon_{c0}}\right)-\left(\frac{\varepsilon_c}{\varepsilon_{c0}}\right)^2\right] \tag{6.1}$$

Region AB: $\varepsilon_{c0} < \varepsilon_c \le \varepsilon_{cu}$ $$\sigma_c = Kf_c^{'}\left[1 - Z(\varepsilon_c - \varepsilon_{c0})\right] \tag{6.2}$$

Region BC: $\varepsilon_c > \varepsilon_{cu}$ $$\sigma_c = f_{cu} \tag{6.3}$$

where ε_c is the compressive stress of concrete, K is a factor which accounts for the strength increase due to confinement, $f_c^{'}$ is the concrete cylinder compressive strength, ε_{c0} is the strain at the maximum compressive stress ($Kf_c^{'}$), Z is the strain softening slope, f_{cu} is the crushing strength, and ε_{cu} is the strain at the crushing strength. The initial slope for the model is noted by $E_{c0} = 2Kf_c^{'} / \varepsilon_{c0}$, which is the important parameter affecting the linear performance of RC structures. Figure 6.1 also shows the unloading and reloading rules used in OpenSees (McKenna et al. 2007). For example, the unloading line CO' coincides with the reloading line O'C and both lines are converged to a common point R. The point R is determined by the intersection of the tangent line to the envelop curve at the original point O and the unloading line starting from the point B with slope λE_{c0}, in which λ is a reduction factor determined by experiments. The values of strain and stress at the point R are respectively expressed as:

$$\varepsilon_{cr} = \frac{f_{cu} - \lambda E_{c0}\varepsilon_{cu}}{E_{c0} - \lambda E_{c0}} \tag{6.4}$$

$$\sigma_{cr} = E_{c0}\varepsilon_{cr} \tag{6.5}$$

where f_{cu} and ε_{cu} represent the ultimate compressive stress and strain at the point B, respectively, and E_{c0} represents the concrete elastic modulus at the original point O.

This study concerns the nonlinear model updating of a RC structure, and the materials of some components of the structure already experience both the strength and stiffness degradations under previous moderate earthquakes. Let ε_{max} and f_{max} be the minimum compressive strain and stress on the envelop curve for the concrete material in its history, and they are also denoted as the maximum compressive strain and stress on the envelop curve for the concrete material in the nonlinear model updating of the structure subject to the current earthquake. These two parameters actually represent the strength degradation due to the previous earthquakes and are taken as the key parameters to be determined through the nonlinear model updating in this study. In the nonlinear model updating, the unloading stiffness of the material in its history can be computed by:

$$E_r = \frac{f_{max} - f_{cr}}{\varepsilon_{max} - \varepsilon_{cr}} \tag{6.6}$$

The stress of the concrete is supposed to reduce to zero at the point O’ along the line CO’. In the nonlinear model updating of the structure under the current earthquake, the envelop curve of the concrete material with its strength degradation will be the curve M’-O’-C-B-N in the new coordinate system ($\sigma_c^{'}O^{'}\varepsilon_c^{'}$). The three new regions on the new envelop curve in the new coordinate system are expressed as:

Region O’C: $\varepsilon_c^{'} \le \varepsilon_{max}$ $\qquad \sigma_c^{'} = f_{max}\left[2\left(\frac{\varepsilon_c^{'}}{\varepsilon_{max}}\right) - \left(\frac{\varepsilon_c^{'}}{\varepsilon_{max}}\right)^2\right]$ (6.7)

Region CB: $\varepsilon_{\max} < \varepsilon_{\mathrm{c}}^{'} \le \varepsilon_{\mathrm{cu}}$ $\quad \sigma_{\mathrm{c}}^{'} = f_{\max}\left[1 - Z(\varepsilon_{\mathrm{c}}^{'} - \varepsilon_{\max})\right]$ (6.8)

Region BN: $\varepsilon_{\mathrm{c}}^{'} > \varepsilon_{\mathrm{cu}}$ $\quad \sigma_{\mathrm{c}}^{'} = f_{\mathrm{cu}}$ (6.9)

where $\varepsilon_{\mathrm{c}}^{'}$ is the compressive stress of concrete in the new coordinate system ($\sigma_{\mathrm{c}}^{'}\mathrm{O}^{'}\varepsilon_{\mathrm{c}}^{'}$), $f_{\max}$ is the maximum compressive stress on the new envelop curve, and $\varepsilon_{\max}$ is the strain at the maximum compressive stress. The initial slope for the new envelop curve at the point O' is determined by $E_{c0}^{'} = 2 f_{\max} / \varepsilon_{\max}$.

Now let us discuss the unloading and reloading rules for the concrete material used in the nonlinear model updating. The unloading line C'O" coincides with the reloading line O"C' and both lines are converged to a common point R'. The point R' is determined by the intersection of the new tangent line to the new envelop curve at the point O' and the unloading line starting from the point B with slope λE_{c0}. With the crushing strain ($\varepsilon_{\mathrm{cu}}$), the crushing strength (f_{cu}) and the stiffness (λE_{c0}), the strain and stress at the point R' are respectively expressed as:

$$\varepsilon_{\mathrm{cr}}^{'} = \frac{f_{\mathrm{cu}} - \lambda E_{\mathrm{c0}}\varepsilon_{\mathrm{cu}}}{E_{\mathrm{c0}}^{'} - \lambda E_{\mathrm{c0}}} \tag{6.10}$$

$$f_{\mathrm{cr}}^{'} = E_{\mathrm{c0}}^{'}\varepsilon_{\mathrm{cr}}^{'} \tag{6.11}$$

The reloading/unloading stiffness can then be computed by

$$E_{\mathrm{r}}^{'} = \frac{\sigma_{c}^{'} - f_{\mathrm{cr}}^{'}}{\varepsilon_{c}^{'} - \varepsilon_{\mathrm{cr}}^{'}} \tag{6.12}$$

where $\varepsilon_{c}^{'}$ and $\sigma_{c}^{'}$ are the strain and stress of the concrete material, respectively, on the new envelope curve in the current seismic analysis for the nonlinear model updating.

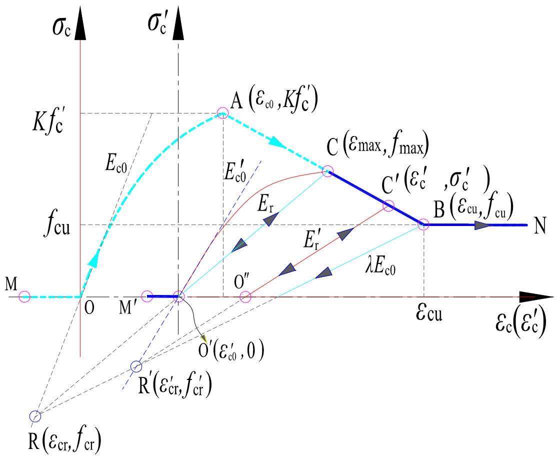

Figure 6.1 Envelop curve evolution of concrete material

In summary, the strength degradation of the concrete material due to the previous earthquakes is considered by the evolution of the envelop curve and determined through the nonlinear model updating. In the nonlinear model updating of the structure under the current earthquake, the stiffness degradation of the concrete material is considered by using the same reloading/unloading rules as those used in OpenSees (McKenna et al. 2007) for Concrete01.

6.2.2 Envelop curve evolution for reinforcement material

To model the seismic performance of reinforcement, the hysteretic material model is used in OpenSees (McKenna et al. 2007). The hysteretic model involves three kinds of degradation: unloading stiffness degradation, strength degradation, and reloading stiffness degradation, as shown in Figures 6.2(a)-(c), respectively, for the reinforcement without considering pinching effect. The initial envelop curve shown in Figure 6.2 often refers to the intact structural material. This study concerns the nonlinear model updating of a RC structure, and the materials of some components of the structure already experience both the strength and stiffness degradations due to previous earthquakes. However, the envelop curve of the damaged material is not known due to the unknown previous load history. To predict the further performance of the damaged structure after the current earthquake, the envelop curve of the damaged material in the damaged structure due to previous earthquakes will be identified. Let us assume that the envelop curve shown in Figure 6.2 is one of the damaged material due to previous earthquakes and will be identified through the nonlinear model updating of the structure under the current earthquake. This envelop curve can be determined by 6 key points (C1, B1, A1, A'', B'' and C''). If the tension properties of the reinforcement are the same as the compressive ones, then only 3 key points or 6 key parameters need to be identified in the nonlinear model updating. If the 6 key parameters and the envelop curve are identified, the hysteretic material model that includes the principles of unloading, reloading and strength degradation together with the three damage rules can be used for the subsequent seismic analysis of the structure under the current earthquake.

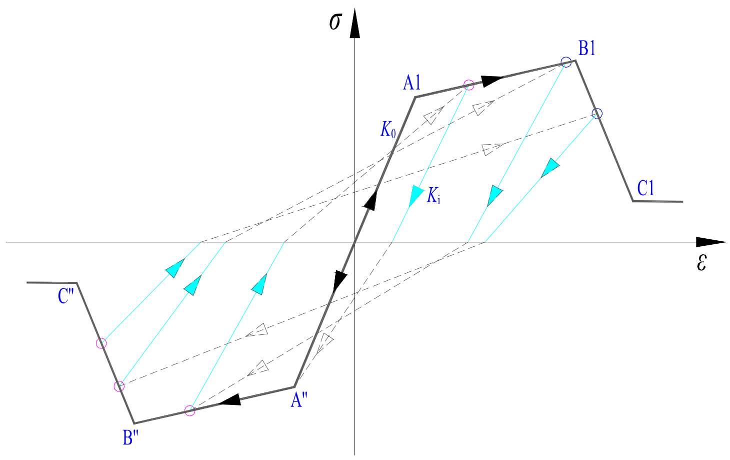

(a)

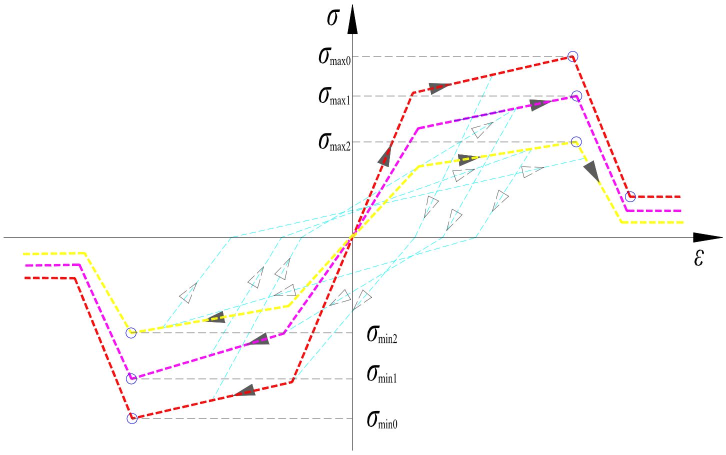

(b)

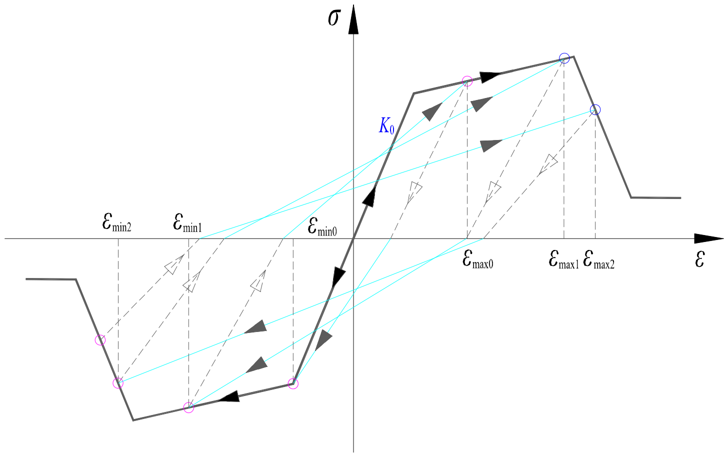

(c)

Figure 6.2 Envelop curve evolution of reinforcement material (a) Unloading stiffness degradation (b) Strength degradation (c) Reloading stiffness degradation

The three damage rules associated with the three degradations define the evolution of response envelop curve and the unloading/reloading path. The form of each damage rule remains the same. The damage index (Park and Ang 1985) is used in OpenSees (McKenna et al. 2007) as the damage index to quantify the three deteriorations:

$$\delta_i = \left(\alpha_1 \left(\tilde{\varepsilon}_{\max} \right)^{\alpha_3} + \alpha_2 \left(\frac{E_i}{E_{\text{monotonic}}} \right)^{\alpha_4} \right) \tag{6.13}$$

$$\tilde{\varepsilon}_{\max} = max\left[\frac{\varepsilon_{\mathrm{maxi}}}{\varepsilon_{\max}}, \frac{\varepsilon_{\mathrm{mini}}}{\varepsilon_{\min}}\right] \tag{6.14}$$

$$E_{\mathrm{i}} = \int_{stress\ \ history} dE \tag{6.15}$$

where i represents the current strain increment, δ_{i} is the damage index (δ_{i} equal to 0 means an intact state of no damage and δ_{i} being 1.0 means the failure), $\alpha_1 - \alpha_4$ represent the parameters which are used to fit the damage rules to test data, E_{i} is the current absorbed hysteretic energy increment, $E_{\mathrm{monotonic}}$ represents the energy required to achieve under monotonic loading the strain that defines failure, $\varepsilon_{\max}$ and $\varepsilon_{\min}$ represent the ultimate positive and negative strains, and $\varepsilon_{\mathrm{maxi}}$ and $\varepsilon_{\mathrm{mini}}$ are the maximum and minimum historic strain demands.

For the case of stiffness degradation:

$$K_{\mathrm{i}} = K_0(1-\delta K_{\mathrm{i}}) \tag{6.16}$$

where K_{i} is the current unloading stiffness (see Figure 6.2 (a)), K_0 represents the initial linear unloading stiffness (see Figure 6.2 (a)), and δK_{i} indicates the current value of the stiffness damage index which can be calculated using Eqs.6.13-6.15.

The strength degradation is acquired in the same way:

$$\sigma_{\max \mathrm{i}} = \sigma_{\max 0}(1-\delta\sigma_{\mathrm{i}}) \tag{6.17}$$

where $\sigma_{\max \mathrm{i}}$ denotes the current envelop maximum stress (see Figure 6.2 (b)), $\sigma_{\max 0}$ represents the initial envelop maximum stress (see Figure 6.2 (b)), and $\delta\sigma_{\mathrm{i}}$ is the current value of the stress damage index which can also be calculated using Eqs. (6-13)-(6.15).

The reduction in strength that is observed on reloading is modeled by employing the damage rules to decide an increase in the maximum historic strain (decrease in the minimum):

$$\varepsilon_{\max i} = \varepsilon_{\max 0}(1+\delta\varepsilon_{i}) \tag{6.18}$$

where $\varepsilon_{\max i}$ represents the current strain that decides the end of the reload cycle for increasing strain demand (see Figure 6.2 (c)), $\varepsilon_{\max 0}$ is the maximum historic strain demand (see Figure 6.2 (c)), and $\delta\varepsilon_{i}$ is the current value of the reloading strain damage index which can also be calculated using Eqs. (6.13)-(6.15).

In summary, the envelop curve of the damaged reinforcement material due to previous earthquakes is determined through the nonlinear model updating. In the nonlinear model updating of the structure under the current earthquake, the strength degradation and the stiffness degradation of the reinforcement material is considered by using the same strength degradation and reloading/unloading rules as those used in the hysteretic material model provided by OpenSees (McKenna et al. 2007).

6.3 Selection of Key Parameters to Be Updated

In the nonlinear model updating of a RC bridge subject to the current earthquake, the envelop curve controlled by key parameters due to previous earthquakes should be updated ideally for each of nonlinear fiber elements of the bridge whereas all linear performance fiber elements of the bridge need not to be updated because their parameters were linearly updated in Chapter 5. However, the nonlinear model updating is time-consuming and difficult to have a convergence solution if the updated parameters are numerous because of many uncertainties associated with the hysteretic materials model and others. To reduce the number of updated key parameters in the nonlinear model updating, all the fiber elements in the RC bridge are classified into five groups according to the calculated response magnitudes, the configurations and locations of the structural members. The response magnitudes are determined through a nonlinear seismic analysis using the linearly updated FE model of the bridge established in Chapter 5 and subjected to the current earthquake. The five groups of the fiber elements are (1) all the fiber elements in the transverse beams, twin-girder, and north side piers; (2) the failure-vulnerable fiber elements in the two tower legs (see Figure 6.3); (3) the failure-vulnerable fiber elements in the southeast pier (see Figure 6.3); (4) the failure-vulnerable fiber elements in the southwest pier (see Figure 6.3); (5) all the other fiber elements in the tower legs and the southwest and southeast piers except for their failure-vulnerable elements. The fiber elements in the first group are in linear states and their key parameters have been identified in Chapter 5 using the linear updating method. The calculated stress response magnitudes of the fiber elements in the second group are more than 8.0MPa and they are assumed to suffer from similar damage. The failure-vulnerable fiber elements in the southeast and southwest piers are subjected to different damaging conditions, although their stress responses are more than 8.0MPa, and accordingly they are classified into the two different groups, i.e. the third and fourth groups. The maximum stress responses of the fiber elements in the fifth group are less than 8.0MPa, and they are thus assumed to have similar but small damage. As a result, for each of the four groups of nonlinear fiber elements, there is total of 14 key parameters: 6 parameters for reinforcement; 4 parameters for the confined concrete; and 4 parameters for the unconfined concrete. For the entire structure, there is a total of 56 key parameters to be updated. In addition, the two Rayleigh damping coefficients for determining the damping matrix for the bridge need to be updated. Therefore, a total of 58 key parameters of the damaged RC bridge needs to be updated through the nonlinear model updating of the bridge subject to the current earthquake.

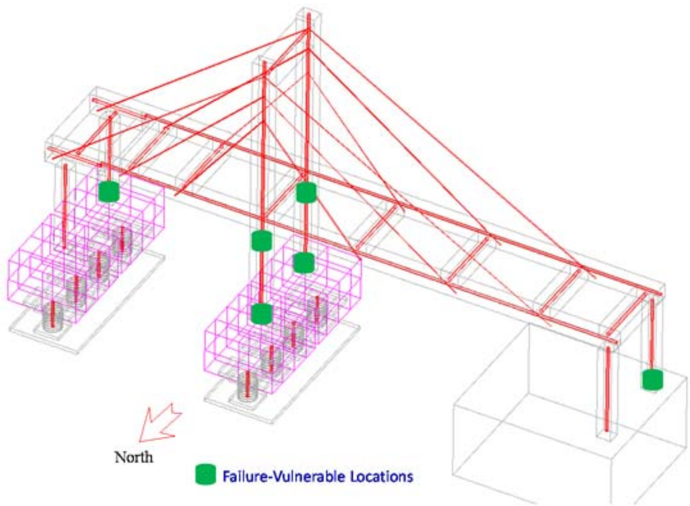

Figure 6.3 Failure-vulnerable locations

6.4 Nonlinear Model Updating and Results

It is assumed that due to previous earthquakes, some components of the RC bridge already experience damage and some still remain linear and elastic. We would like to know the envelop curves of the materials of the damaged components due to the previous earthquakes through the nonlinear model updating. For the sake of convenience, the nonlinear model updating will be conducted in the time domain so that both the damaged and undamaged components can be considered at the same time. Therefore, the optimization objective functions proposed in Chapter 5 in the time domain are used in this chapter for the nonlinear model updating. Furthermore, in the model updating the computed structural responses with the key parameters to be updated will be compared with the measurement results recorded by the sensors of the structural health monitoring (SHM) system installed in the bridge. Therefore, the sensors selected in the liner model updating are also used in the nonlinear model updating. The identification of the envelop curves of the concrete and reinforcement due to previous earthquakes can be achieved.

6.4.1 Optimization objective function

The optimization objective function used in the nonlinear model updating is the same as the one proposed for the liner model updating in the time domain as described in Chapter 5. The accelerometers at the sensor locations A6, A8 and A9 and the strain gauges at the sensor locations n7, s2 and e1, which are used in the linear model updating in Chapter 5, are also used in this chapter as the key sensor locations for the nonlinear model updating in the time domain, as shown in Figure 6.4. The objective function is expressed as:

$$Min(J(\mathbf{r})) = Min(w_1 J^1 + w_2 J^2) \tag{6.19}$$

subject to $\left|1 - r_{\mathrm{k}}^{\mathrm{a}} / r_{\mathrm{k}}^{\mathrm{e}}\right| \le 60\%$, k=1, 2, …, n_{p}

where the weighting factors for the objective function are set as $w_1 = w_2 = 0.5$, and J^1 and J^2 are the functions associated with acceleration and reinforcement strain responses, respectively.

$$J^1 = \sum_{\mathrm{i}=1}^{3}\left(\frac{\sum_{\mathrm{n}=1}^{\mathrm{N_t}}\left(\ddot{u}_{\mathrm{i}}^{\mathrm{a}}(t_{\mathrm{n}},\mathbf{DV}) - \ddot{u}_{\mathrm{i}}^{\mathrm{e}}(t_{\mathrm{n}})\right)^2}{\sum_{\mathrm{n}=1}^{N_{\mathrm{t}}}\left(\ddot{u}_{\mathrm{i}}^{\mathrm{e}}(t_{\mathrm{n}})\right)^2}\right) \tag{6.20}$$

$$J^2 = \sum_{\mathrm{i}=1}^{3}\left(\frac{\sum_{\mathrm{n}=1}^{\mathrm{N_t}}\left(\varepsilon_{\mathrm{i}}^{\mathrm{a}}(t_{\mathrm{n}},\mathbf{DV}) - \varepsilon_{\mathrm{i}}^{\mathrm{e}}(t_{\mathrm{n}})\right)^2}{\sum_{\mathrm{n}=1}^{N_{\mathrm{t}}}\left(\varepsilon_{\mathrm{i}}^{\mathrm{e}}(t_{\mathrm{n}})\right)^2}\right) \tag{6.21}$$

where $\mathrm{N_t}$ denotes the time steps in the response time history used for optimization, $\ddot{u}_{\mathrm{i}}^{\mathrm{a}}(t_{\mathrm{n}},\mathbf{DV})$ is the computed acceleration response at the location of the i^th^ accelerometer at the time t_{n} with respect to the key parameter vector **DV,** $\ddot{u}_{\mathrm{i}}^{\mathrm{e}}(t_{\mathrm{n}})$ is the measured acceleration response from the i^th^ accelerometer at the time t_{n}, and $\varepsilon_{\mathrm{i}}^{\mathrm{a}}(t_{\mathrm{n}},\mathbf{DV})$ and $\varepsilon_{\mathrm{i}}^{\mathrm{e}}(t_{\mathrm{n}})$ are the i^th^ computed and measured reinforcement strains at the time t_n, respectively.

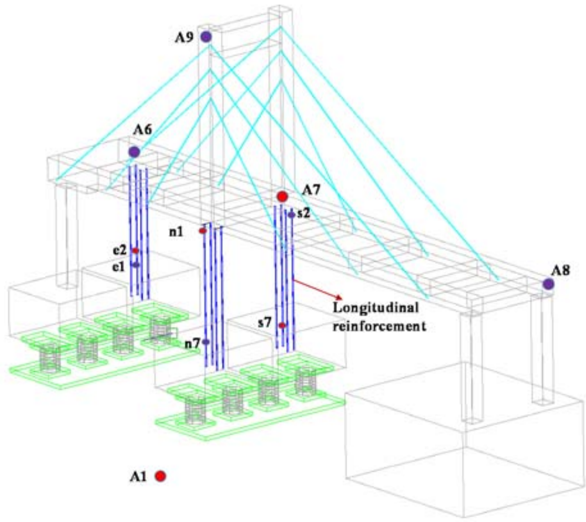

Figure 6.4 Key sensor locations for model updating

6.4.2 Optimization procedure

The optimization function expressed by Eq. 6.19 can be solved using the sparse nonlinear optimization technique (SNOPT) (Gill et al. 2002)implemented in OpenSees (Gu et al. 2011). The SNOPT (Gill et al. 2002) is a local optimization method and dependent of initial values of the key parameters to be updated. A multi-start method is employed in this study to run the updating algorithm with many sets of initial values within the pre-set domain. If one initial guess yields the achievable minimum value of the objective function, the corresponding key parameters can be regarded as the global solution. The detailed optimization procedure is summarized as:

- Step 1: Provide a set of initial values for the 58 key parameters to be updated and a tolerance for the objective function;
- Step 2: Call the SNOPT (Gill et al. 2002) module in the OpenSees (Gu et al. 2011) to perform the nonlinear seismic analysis of the FE model of the bridge established in Chapter 5 subject to the current moderate earthquake. The

acceleration responses at A6, A8 and A9 as well as the strain responses at n7, s2 and e1 are computed. These calculated responses and the directly measured responses at the key sensor locations are then inputted into the objective function expressed by Eq. 6.19. If the result obtained from Eq. 6.19 is less than the designated tolerance, the values initially assigned to the 58 key parameters are the right solution. Otherwise, another set of initial values for the 58 key parameters are selected using the gradient search method implemented in the SNOPT(Gill et al. 2002). The new set of values for the 58 key parameters is then assigned to the FE model of the bridge;

- Step 3: Repeat step 2 until a set of values for the 58 key parameters satisfies the designated tolerance. The optimization process then stops and the latest set of values are regarded as the global optimization solution.

6.4.3 Updated results of key parameters

Figure 6.5 shows the current moderate earthquake applied to the bridge structure for the nonlinear model updating. The peak acceleration and duration of the moderate earthquake are 3.548m/s^2 and 7.8 seconds, respectively. The sampling frequency of the moderate earthquake ground excitation is 256 Hz. The updated results of the 56 key parameters for the envelop curves of the materials of the damaged RC bridge due to the previous earthquakes are tabulated in Table 6.1, in which the alphabet A, A1, B1 and C1 represent the key points on the envelop curves shown in Figure 6.6 (a) and Figure 6.6 (b). Table 6.2 lists the updated two Rayleigh damping coefficients. From Table 6.1, it can be seen that the compressive strengths of the concrete and the yielding strength of the reinforcement of the failure-vulnerable fiber elements in the second, third and fourth groups decrease sharply due to the damage caused by previous earthquakes, whereas those of the fiber elements in the fifth group decrease slightly.

These changes are attributed to the strength degradations of both concrete and reinforcement. In Figure 6.6 (a) and Figure 6.6 (b), the envelop curves OA and AA' for concrete and reinforcement are for the undamaged southwest pier and they are determined through the linear model updating conducted in Chapter 5. The envelop curves A'OA and D"C"B"A"OABCD for concrete and reinforcement are for the damaged southwest pier and they are determined through the nonlinear model updating in this chapter. It can be seen that the envelop curves of the confined concrete and the reinforcement in the undamaged southwest pier are significantly different from those of the damaged southwest pier due to previous earthquakes. The envelop curves evolve clearly. The maximum compressive strength of the confined concrete sharply decreases from 58.7MPa to 25.8MPa. The compressive strength 25.8MPa is actually the residual strength of the concrete that experiences all the previous earthquakes. For reinforcement, although the yielding strength of the reinforcement slightly increases from 589.9MPa to 605.7MPa, the modulus of the reinforcement substantially decreases from 3.17×10^5 MPa to 1.40×10^5 MPa. It is interesting to know from Table 6.2 that the updated Rayleigh damping coefficients for the damaged structure are larger than those of the undamaged structure.

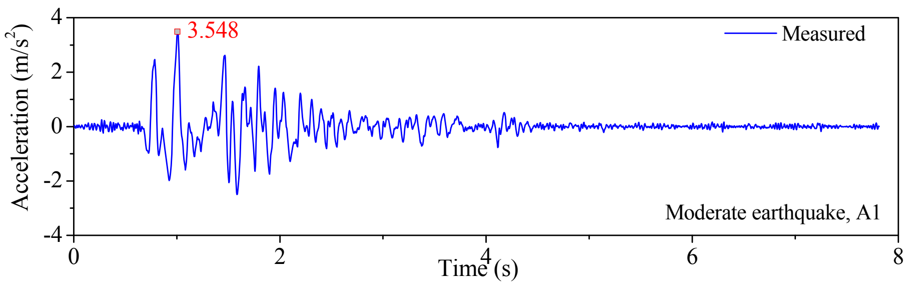

Figure 6.5 Acceleration recorded at station A1

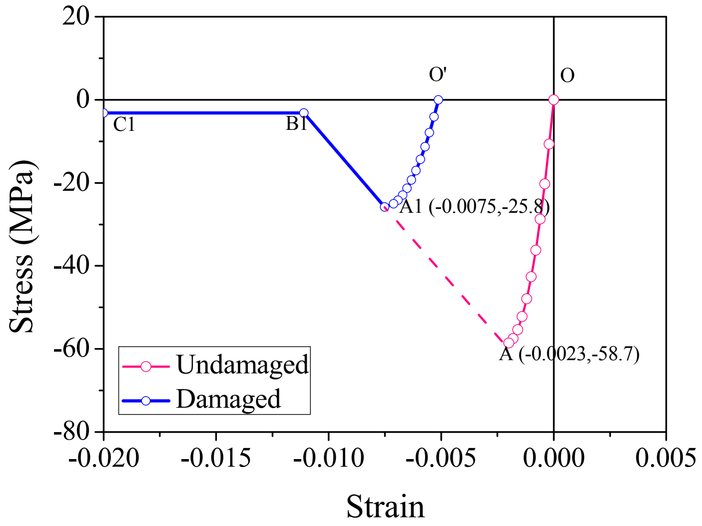

(a)

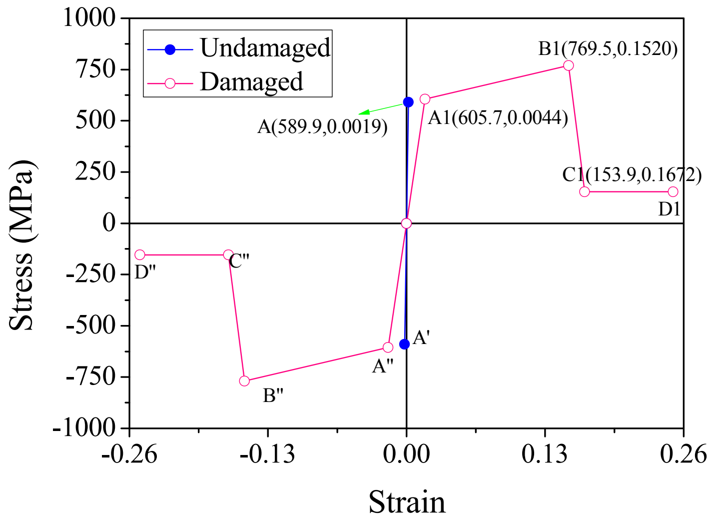

(b)

Figure 6.6 Evolution of envelop curves (a) Confined concrete (b) Reinforcement

Table 6.1 Updated key parameters

Parameter No.	Description	Linear model updating	Nonlinear model updating		
		A	A1	B1	C1
1-2	Confined concrete compressive stress of the slightly damaged tower and pier (MPa)	-58.7	-51.9	-3.2	
3-4	Confined concrete compressive strain of the slightly damaged tower and pier	-0.0023	-0.0021	-0.0108	
5-6	Cover concrete compressive stress of the slightly damaged tower and pier (MPa)	-52.6	-51.1	0.0	
7-8	Cover concrete compressive strain of the slightly damaged tower and pier	-0.0033	-0.0027	-0.0069	
9-10	Confined concrete compressive stress of the southeast damaged pier (MPa)	-58.7	-29.7	-3.2	
11-12	Confined concrete compressive strain of the southeast damaged pier	-0.0023	-0.0024	-0.0111	
13-14	Cover concrete compressive stress of the southeast damaged pier (MPa)	-52.6	-25.7	0.0	
15-16	Cover concrete compressive strain of the southeast damaged pier	-0.0033	-0.0024	-0.0328	
17-18	Confined concrete compressive stress of the damaged tower (MPa)	-58.7	-28.0	-3.2	
19-20	Confined concrete compressive strain of the damaged tower	-0.0023	-0.0024	-0.0105	
21-22	Cover concrete compressive stress of the damaged tower (MPa)	-52.6	-25.6	0.0	
23-24	Cover concrete compressive strain of the damaged tower	-0.0033	-0.0025	-0.0637	
25-26	Confined concrete compressive stress of the southwest damaged pier (MPa)	-58.7	-25.8	-3.2	
27-28	Confined concrete compressive strain of the southwest damaged pier	-0.0023	-0.0024	-0.0111	
29-30	Cover concrete compressive stress of the southwest damaged pier (MPa)	-52.6	-25.7	0.0	
31-32	Cover concrete compressive strain of the southwest damaged pier	-0.0033	-0.0020	-0.0337	
33-35	Yielding stress of reinforcement in the slightly damaged tower and pier (MPa)	589.9	600.4	916.0	183.2
36-38	Yielding strain of reinforcement in the slightly damaged tower and pier	0.0019	0.0023	0.1520	0.1672
39-41	Yielding stress of reinforcement in the damaged southeast pier (MPa)	589.9	605.6	770.9	154.2
42-44	Yielding strain of reinforcement in the damaged southeast pier	0.0019	0.0043	0.1520	0.1672
45-47	Yielding stress of reinforcement in the damaged tower (MPa)	589.9	605.0	780.4	156.1
48-50	Yielding strain of reinforcement in the damaged tower	0.0019	0.0041	0.1520	0.1672
51-53	Yielding stress of reinforcement in the damaged southwest pier (MPa)	589.9	605.7	769.5	153.9
54-56	Yielding strain of reinforcement in the damaged southwest pier	0.0019	0.0044	0.1520	0.1672

Table 6.2 Updated key parameters

Parameter No.	Description	Linear model updating	Nonlinear model updating
57	Rayleigh damping coefficient of mass	1.921 (rad/s)	4.647 (s/rad)
58	Rayleigh damping coefficient of stiffness	0.00018 (rad/s)	0.00030 (s/rad)

6.4.3 Confirmation of nonlinear model updating results

As mentioned before, the multi-start method is employed in this study to find the nonlinear model updating solution. With many sets of initial values within the pre-set domain, only one set yielding the achievable minimum value of the objective function is regarded as the global solution. To confirm the correctness of the model updating solution obtained above, the calculated seismic responses are compared with the so-called measured responses. There are 3 measured acceleration responses at the sensor locations A6, A8 and A9 and 3 measured reinforcement strain responses at the sensor locations n7, s2 and e1. To quantify the difference between the computed and measured responses, the following index is proposed.

$$J = \frac{\sum_{\mathrm{n}=1}^{N_{\mathrm{t}}} \left(Mea(t_{\mathrm{n}}) - Ana(t_{\mathrm{n}}) \right)^2}{\sum_{\mathrm{n}=1}^{N_{\mathrm{t}}} \left(Mea(t_{\mathrm{n}}) \right)^2} \tag{6.22}$$

where *Mea* and *A*na denote the measured and the calculated results, respectively and the index *J* actually represents the relative average error of the computed response. The calculated acceleration responses based on the updated nonlinear FE model of the bridge and the measured acceleration responses recorded by the accelerometers at sensor locations A6, A8 and A9 are plotted in Figure 6.7 for comparison. It can be seen that the computed acceleration responses at A6, A8 and A9 match reasonably well with the measured results in consideration of the complex nature of the problem. The peak acceleration responses of the bridge and the index *J* at the sensor locations A6, A8 and A9 are presented in Table 6.3. The mean value in Table 6.3 is defined as the sum of the three relative average errors and then divided by three. It can be seen that the differences in the peak acceleration are small and the relative average errors are also small.

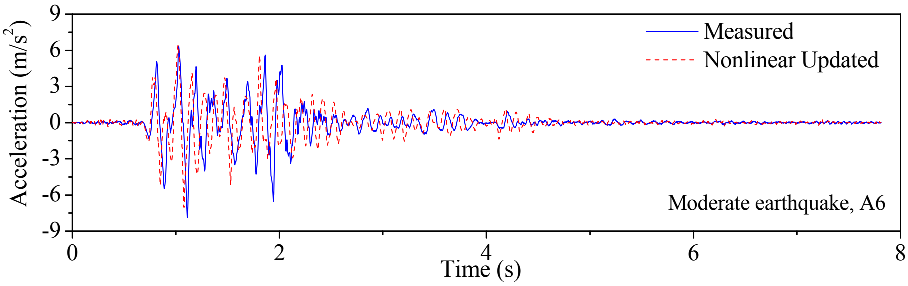

(a)

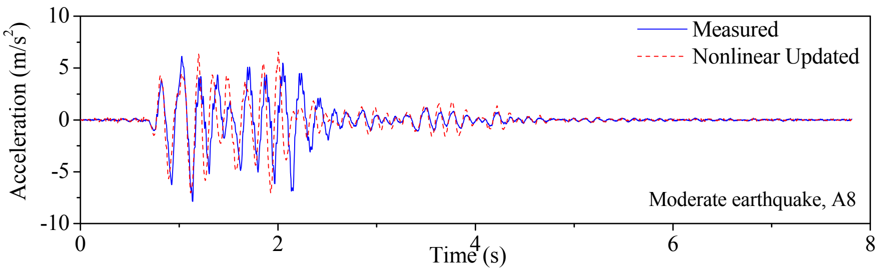

(b)

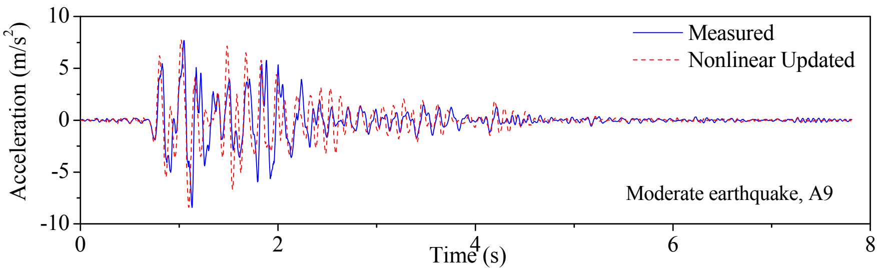

(c)

Figure 6.7 Comparison of acceleration time histories (a) A6 (b) A8 (c) A9

Table 6.3 Comparison of acceleration responses

Station No.	Peak Acceleration (m/s^2)		J
	Measured	Nonlinear Updated	
A6	7.872	7.044	1.379
A8	7.860	7.073	0.894
A9	8.419	8.398	0.778
	Mean		1.017

Figure 6.8 shows the strain responses of the reinforcement at the bottom of the north tower leg, at the south tower leg close to the girder, and at the bottom of the southeast pier calculated from the updated nonlinear FE model of the bridge. The

corresponding measured responses are also plotted in Figure 6.8. The measured and computed strain response time histories are similar in pattern. The peak reinforcement strain responses and the average errors of strain responses are summarized in Table 6.4. From Table 6.4, it can be seen that the average error associated with the strain response at n7 is the smallest, and the average error associated with the strain response at e1 is the largest. The maximum average error associated with the acceleration response is larger than that associated with the strain response. The measured maximum reinforcement strain response is 0.0016 at the sensor location n7, indicating that the deformation of the reinforcement at the location n7 is the largest among the three locations. It is of interest that the peak absolute tensile strain is larger than the peak absolute compressive strain because the reinforcement sustains all the tension force yet the concrete does not bear tension force.

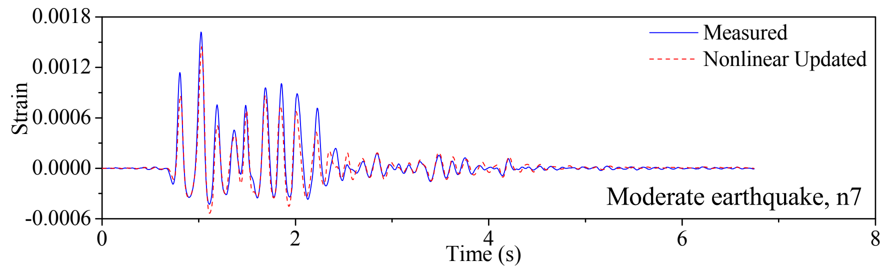

(a)

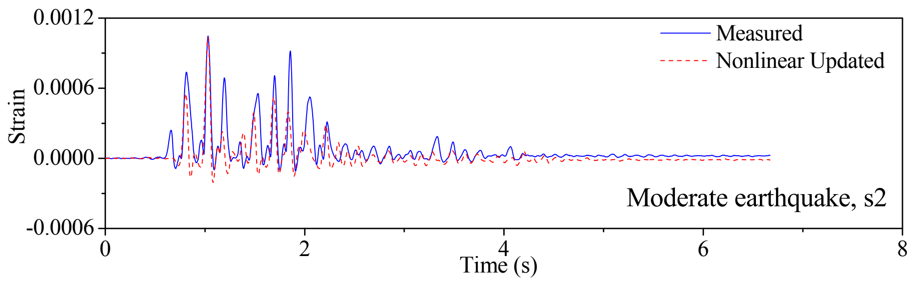

(b)

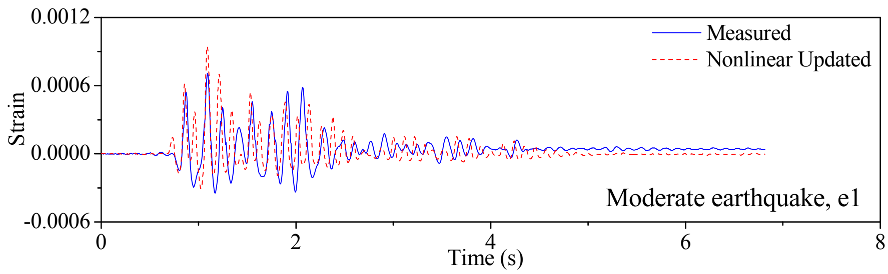

(c)

Figure 6.8 Comparison of reinforcement strain time histories (a) n7 (b) s2 (c) e1

Table 6.4 Comparison of reinforcement strains

Component	Location	Peak Strain		*J*
		Measured	Nonlinear Updated	
North Tower Leg	n7	1.60E-03	1.40E-03	0.117
South Tower Leg	s2	1.00E-03	1.00E-03	0.545
Southeast Pier	e1	7.08E-04	9.44E-04	1.331
	Mean			0.664

6.5 Validation

To further confirm the correctness of the nonlinear model updating results, the calculated seismic responses are compared with the measured responses which are not used in the model updating. One acceleration response at A7, 10 reaction forces and 3 reinforcement strain responses at n1, s7 and e2, which are not used in the optimization objective function, are employed for the comparison.

6.5.1 Comparison of acceleration responses

The acceleration response of A7 computed from the updated nonlinear FE model of the bridge is plotted in Figure 6.9 together with the measured one. The computed acceleration response matches well with the measured one. The peak acceleration responses and the average errors are presented in Table 6.5. The difference in the peak acceleration response and the index *J* are small.

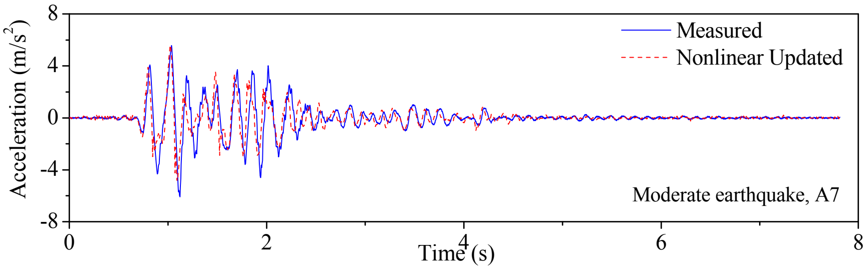

Figure 6.9 Comparison of acceleration response time histories at A7

Table 6.5 Comparison of acceleration responses

Station No.	Peak Acceleration (m/s^2)		J
	Measured	Nonlinear Updated	
A7	6.078	5.613	0.548
	Mean		0.548

6.5.2 Comparison of reaction forces

Figure 6.10 demonstrates the locations and positive directions of the reaction forces (i.e., shear force, axial force, bending moment and torsion moment). The reaction forces at the north and south tower legs and the southeast pier calculated from the updated nonlinear FE model of the bridge are plotted in Figures 6.11, 6.13 and 6.15, respectively, together with the measured ones. The peak reaction forces and the average errors are summarized in Table 6.6. The computed reaction force time-histories are in good agreement with the measured ones. The calculated peak reaction forces also match with measured ones in general and the maximum error occurs in the axial force of the north tower leg. The hysteretic responses of the computed bending moment versus the curvature at the bottom of the two tower legs, the southeast pier and southwest pier are plotted in Figures 6.12, 6.14, 6.16 and 6.17, respectively. It can be clearly seen that the two RC tower legs and the two south RC piers all experience material nonlinearity and exhibit hysteretic loops during the moderate earthquake. The hysteretic loops in Figure 6.16 or 6.17 indeed are very narrow. This is because the reinforcement is only slightly damaged in these cases. The

Young's modulus of reinforcement is about 6 times of the one of concrete so that the hysteretic loops depend mainly on the properties of reinforcement even though the concrete is severely damaged. In this regards, the degradations of both stiffness and strength should be considered in the nonlinear model updating.

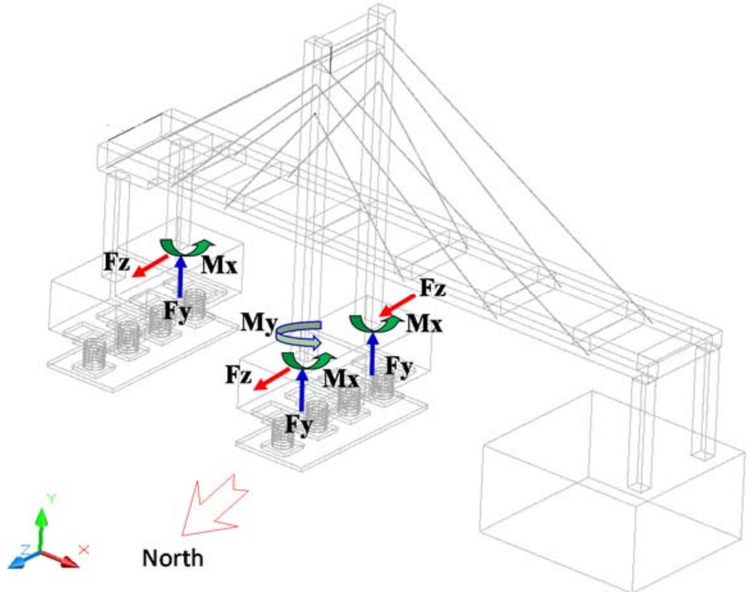

Figure 6.10 Locations for recorded reaction forces

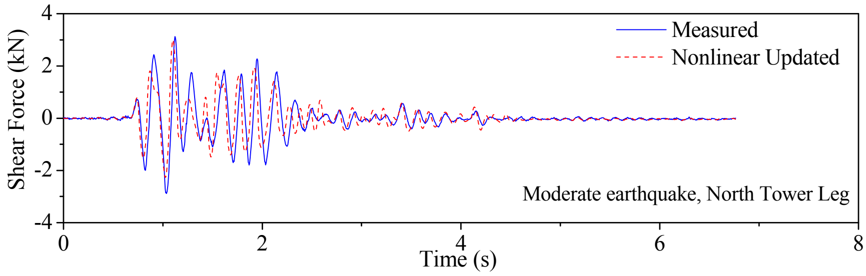

(a)

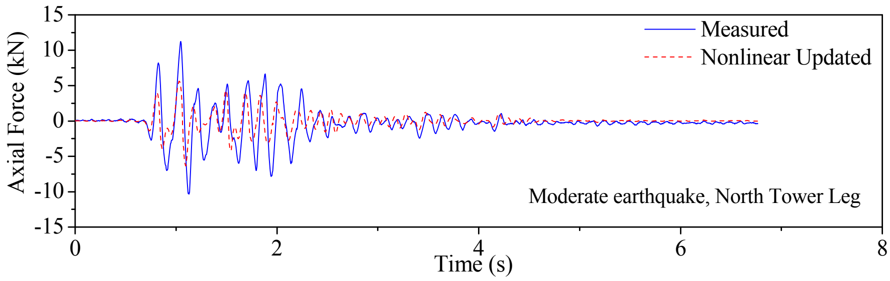

(b)

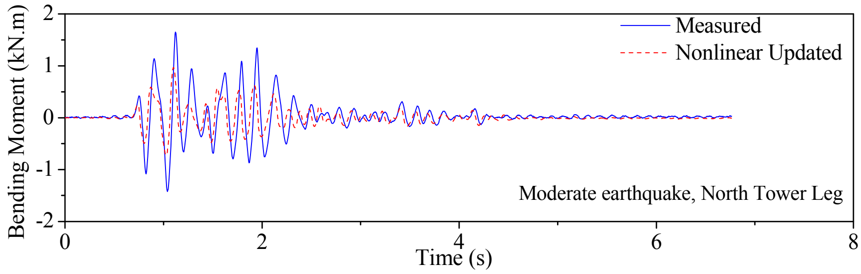

(c)

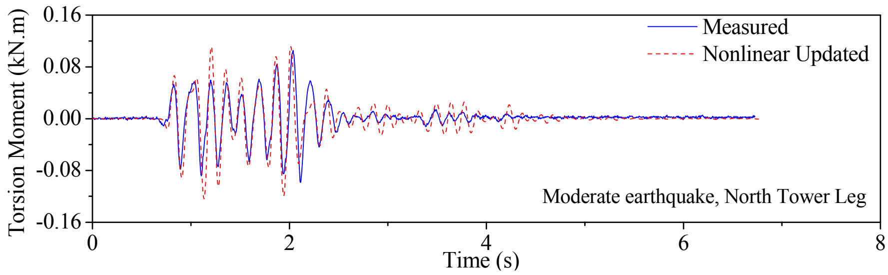

(d)

Figure 6.11 Comparison of reaction forces at the bottom of the north tower leg

(a) Shear force (b) Axial force (c) Bending moment (d) Torsion moment

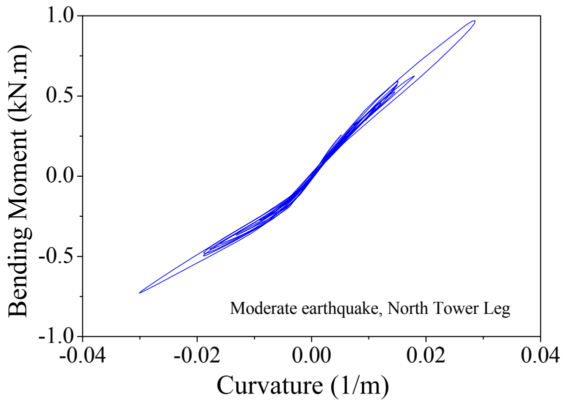

Figure 6.12 Hysteretic response of the bending moment vs. curvature

at the bottom of the north tower leg

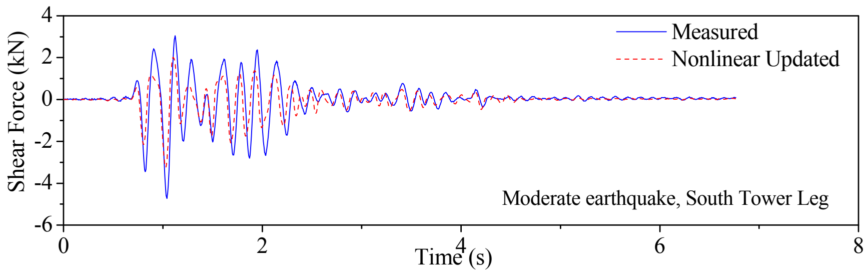

(a)

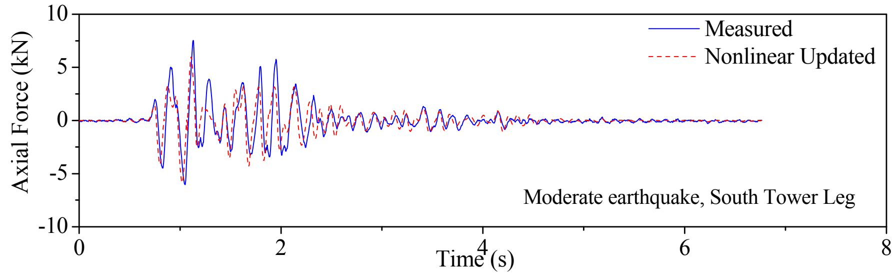

(b)

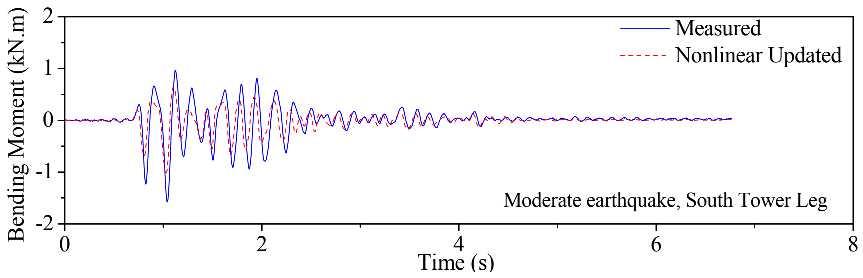

(c)

Figure 6.13 Comparison of reaction forces at the bottom of the south tower leg

(a) Shear force (b) Axial force (c) Bending moment

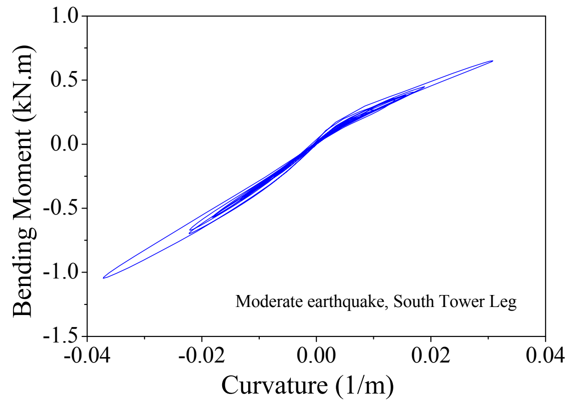

Figure 6.14 Hysteretic response of bending moment vs. curvature

at the bottom of the south tower leg

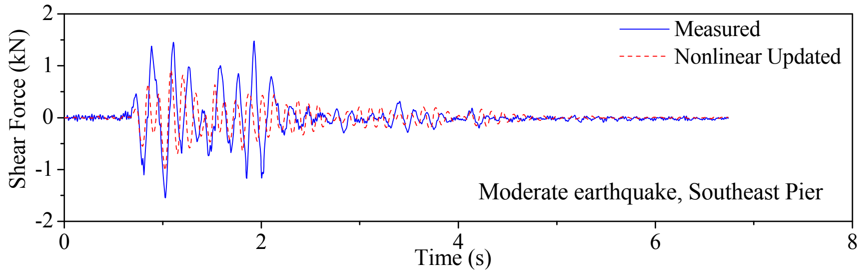

(a)

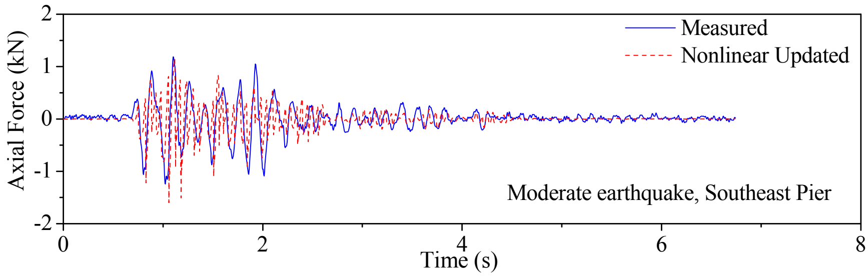

(b)

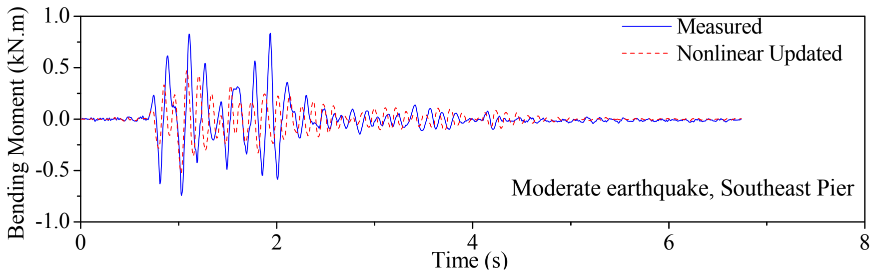

(c)

Figure 6.15 Comparison of reaction forces at the bottom of the southeast pier:

(a) Shear force (b) Axial force (c) Bending moment

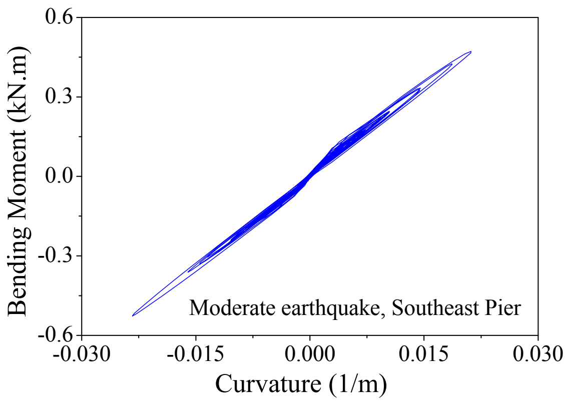

Figure 6.16 Hysteretic response of bending moment vs. curvature

at the bottom of the southeast pier

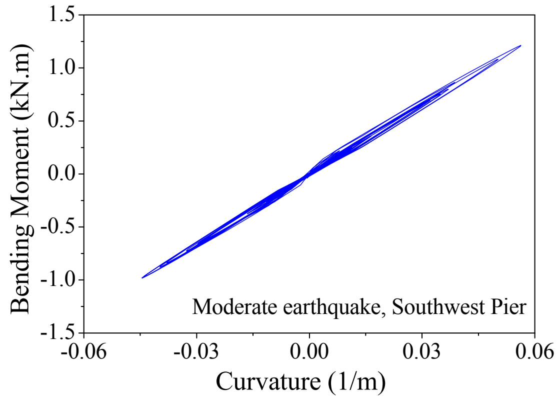

Figure 6.17 Hysteretic response of the bending moment vs. curvature at the bottom of the southwest pier

Table 6.6 Comparison of reaction forces

Location	Force Type	Peak Forces		*J*
		Measured	Nonlinear Updated	
North Tower Leg	Shear Force	3.106kN	2.996kN	0.761
	Axial Force	11.231kN	6.366kN	0.736
	Bending Moment	1.652kN.m	0.971kN.m	0.688
	Torsion Moment	0.105kN.m	0.112kN.m	0.465
South Tower Leg	Shear Force	4.726kN	3.255kN	0.483
	Axial Force	7.552kN	5.997kN	0.612
	Bending Moment	1.577kN	1.051kN	0.562
Southeast Pier	Shear Force	1.537kN	1.019kN	1.199
	Axial Force	1.301kN	1.599kN	1.031
	Bending Moment	0.835kN.m	0.527kN.m	1.304
Mean				0.784

6.5.3 Comparison of reinforcement strains

Figure 6.18 shows the strain responses of the reinforcement at the north tower leg close to the girder, at the bottom of the south tower leg, and at the bottom of the southeast pier calculated from the updated nonlinear FE model of the bridge. The corresponding measured strain responses are also plotted in Figure 6.18. The measured and computed strain response time histories are similar in pattern. The peak reinforcement strain responses and the average errors of strain responses are summarized in Table 6.7. It can be seen in Table 6.7 that the average error associated with the strain response at s7 is the smallest and the average error associated with the strain response at e2 is the largest with the *J* index of 1.314. The measured maximum reinforcement strain response is 0.0016 at the sensor location s7, indicating that the deformation of the reinforcement at the location s7 is the largest among the three locations. It is of interest that the absolute tensile peak strain is larger than the absolute compressive peak strain because the reinforcement sustains all the tension force yet the concrete does not bear tension force.

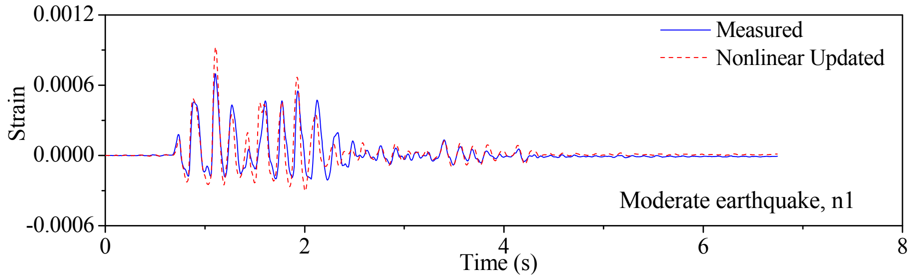

(a)

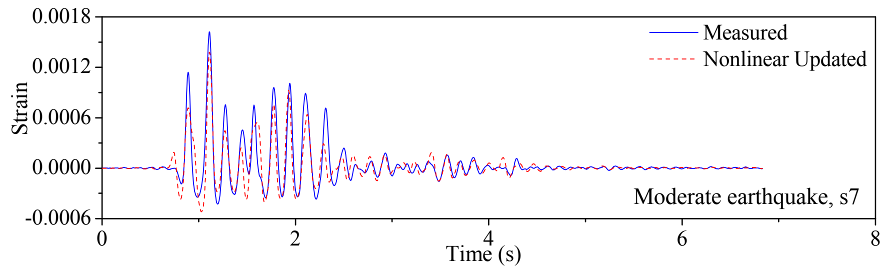

(b)

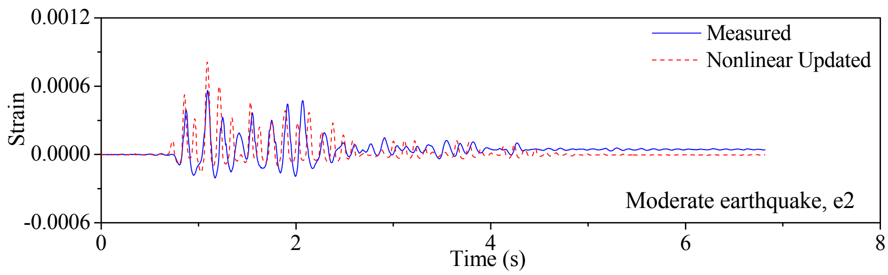

(c)

Figure 6.18 Comparison of reinforcement strain time histories (a) n1 (b) e1 (c) e2

Table 6.7 Comparison of reinforcement strains

Component	Location	Peak Strain		J
		Measured	Nonlinear Updated	
North Tower Leg	n1	6.97E-04	9.26E-04	0.396
South Tower Leg	S7	1.60E-03	1.40E-03	0.280
Southeast Pier	e2	5.64E-04	8.14E-04	1.314
Mean				0.663

6.6 Summary

This chapter presents a nonlinear model updating method by using the measured responses of acceleration and strain of reinforcement of a RC cable-stayed bridge in the time domain to update the envelop curves of the materials of the bridge without knowing its previous loading history. In the nonlinear model updating, the degradations of both unloading stiffness and reloading stiffness are accomplished in addition to the strength degradation by using the rules of the Concrete01 and the hysteretic material model provided in OpenSees (McKenna et al. 2007). A total of 58 key parameters divided into five groups are introduced for updating. The optimization objective function used in the time domain is the same as the one presented for the linear model updating. The 3 accelerometers at the locations A6, A8 and A9 and the 3 strain gauges at the locations n7, s2 and e1 are selected as the key sensor locations and their responses are used for the nonlinear model updating. The updated 58 key parameters are used to configure the envelop curves of the materials of the bridge due to the previous earthquakes and these curves are then used to calculate the seismic responses of the bridge subject to current earthquake excitation. Various seismic response time histories computed using the nonlinear updated results are compared with the measured responses. The comparison results indicate that the updated results of the key parameters are correct and the nonlinear model updating method is feasible.

As this chapter demonstrates the success of the nonlinear model updating of the

3-D nonlinear FE model by using acceleration and reinforcement strain responses in the time domain, it can be used as a useful tool for the further seismic collapse analysis presented in the next chapter.

CHAPTER 7
SHM-BASED SEISMIC COLLAPSE ANALYSIS OF A RC CABLE-STAYED BRIDGE

7.1 Introduction

The seismic collapse of RC building structures has been investigated extensively, as highlighted in Chapter 2. The seismic collapse analysis of a RC building structure is performed mainly based on its finite element (FE) model, as demonstrated in Chapter 3. However, the FE model used for collapse analysis is established based on a series of assumptions. For example, the material properties of concrete and reinforcement used in the current collapse analysis are selected according to the design codes or specifications, but the material properties of concrete actually vary with time once it is casted. The compressive strength of concrete can be enhanced by the confinement of stirrups, but such confinement effect can be considered only in terms of the empirical formula (Priestley et al. 2007) in the current collapse analysis. The strength of reinforcement can also be increased if it is embedded in concrete, but this strengthening effect can only be considered empirically. The internal forces in different components of a RC building structure may redistribute because of different construction procedures and/or the shrinking and creeping effects of concrete, but such effects cannot be taken into consideration in the current collapse analysis. Furthermore, a RC building structure may already suffer from some damage during its service time and its material properties are no longer linear and elastic, but such damaged conditions cannot be estimated and taken into account in the current collapse analysis. All these uncertainties involved in the current collapse analysis of RC structures make the collapse analysis questionable or incorrect.

As a cutting-edge technology, the structural health monitoring (SHM) system has been installed on a number of building structures and bridge structures. The SHM system is used to monitor the loading conditions of a structure, to measure various structural responses, to update the FE model of the structure, and to assess the performance of the structure during its service life. As demonstrated in Chapter 5, the actual material properties of a RC structure can be identified through a linear model updating using the linear structural responses measured by the SHM system installed in the structure. Chapter 6 also manifests that the damage conditions of a RC structure caused by previous earthquakes can also be identified in terms of the evolution of envelop curves of both concrete and reinforcement through a nonlinear model updating using the nonlinear structural responses measured by the SHM system installed in the structure. Therefore, if the seismic collapse analysis of a RC structure is performed based on its linear and nonlinear updated FE model, the adverse effects of the aforementioned uncertainties can be eliminated and the accuracy of collapse prognosis results is enhanced.

In this connection, a SHM-based seismic collapse analysis is proposed in this chapter for not only RC building structures but also RC bridge structures. A nonlinear model updating analysis is first performed to identify the key parameters of the FE model of the RC cable-stayed bridge subjected to a large earthquake. The failure criteria for the zero-length failure elements are then determined based on the updated FE model and in terms of the provisions described in Chapter 3. Finally, a number of seismic collapse analyses are performed against a number of earthquake excitations of different intensity levels to find out which earthquake will finally cause the true collapse of the bridge. Such a seismic collapse analysis is also called the collapse prognosis of a RC structure.

7.2 Nonlinear Model Updating and Results

To prognosticate whether a RC bridge will collapse or not when it is subjected to an assumed future earthquake excitation, the current damaged conditions of the bridge should be identified. By recalling the shaking table tests of the RC bridge model described in Chapter 4, a large earthquake test was arranged before the collapse earthquake test. Therefore, the measured seismic responses of the bridge due to the large earthquake will be used in this chapter for the nonlinear model updating of the bridge to determine the current damaged conditions of the bridge. Once the current damaged conditions are quantified, the failure criteria of the failure elements can be determined and the collapse prognosis can be subsequently conducted.

Prior to conducting the nonlinear model updating of the bridge, the key parameters of materials to be updated and the key sensor locations from which the measured responses can be used for updating should be determined. The determination of the key parameters of materials to be updated can be made in a similar way as used in Chapter 6 through a nonlinear analysis of the FE model of the bridge under the large earthquake excitation. The 58 key parameters to be updated in this chapter are selected and listed in Table 7.1. The key parameters are classified into the five groups: (1) all the fiber elements in the transverse beams, twin-girder, and north side piers; (2) the failure-vulnerable fiber elements in the two tower legs; (3) the failure-vulnerable fiber elements in the southeast pier; (4) the failure- vulnerable fiber elements in the southwest pier; (5) all the other fiber elements in the tower legs and the southwest and southeast piers except for their failure-vulnerable elements. Because the excessive local deformations of the bridge due to the large earthquake occurred at the strain gauges n7 and s2, the two strain gauges were damaged and no strain responses were recorded in these two locations during the shake table test. The strain gauges at n8, s8 and e1 together with the accelerometers at A6, A8 and A9 have to be taken as key sensor locations for the nonlinear model updating.

7.2.1 Optimization objective function

The accelerometers at the sensor locations A6, A8 and A9 and the strain gauges at the sensor locations n8, s8 and e1 are selected as key sensor locations for the nonlinear model updating in this chapter, as shown in Figure 7.1. The optimization objective function employed in Chapter 6 can be used in this chapter although some of the sensors used in this chapter are different from those in Chapter 6.

$$Min(J(\mathbf{r})) = Min(w_1 J^1 + w_2 J^2) \tag{7.1}$$

subject to $\left|1 - r_{\mathrm{k}}^{\mathrm{a}} / r_{\mathrm{k}}^{\mathrm{e}}\right| \le 60\%$, k=1, 2, …, n_{p}

where the weighting factors for the objective function are set as $w_1 = w_2 = 0.5$, and J^1 and J^2 are the functions associated with acceleration and reinforcement strain responses, respectively.

$$J^1 = \sum_{\mathrm{i}=1}^{3} \left(\frac{\sum_{\mathrm{n}=1}^{\mathrm{N_t}} \left(\ddot{u}_{\mathrm{i}}^{\mathrm{a}}(t_{\mathrm{n}}, \mathbf{DV}) - \ddot{u}_{\mathrm{i}}^{\mathrm{e}}(t_{\mathrm{n}}) \right)^2}{\sum_{\mathrm{n}=1}^{N_{\mathrm{t}}} \left(\ddot{u}_{\mathrm{i}}^{\mathrm{e}}(t_{\mathrm{n}}) \right)^2} \right) \tag{7.2}$$

$$J^2 = \sum_{\mathrm{i}=1}^{3} \left(\frac{\sum_{\mathrm{n}=1}^{\mathrm{N_t}} \left(\varepsilon_{\mathrm{i}}^{\mathrm{a}}(t_{\mathrm{n}}, \mathbf{DV}) - \varepsilon_{\mathrm{i}}^{\mathrm{e}}(t_{\mathrm{n}}) \right)^2}{\sum_{\mathrm{n}=1}^{N_{\mathrm{t}}} \left(\varepsilon_{\mathrm{i}}^{\mathrm{e}}(t_{\mathrm{n}}) \right)^2} \right) \tag{7.3}$$

where $\mathrm{N_t}$ denotes the time steps in the response time history used for optimization, $\ddot{u}_{\mathrm{i}}^{\mathrm{a}}(t_{\mathrm{n}}, \mathbf{DV})$ is the computed acceleration response at the location of the ith accelerometer at the time t_{n} with respect to the key parameter vector **DV,** $\ddot{u}_{\mathrm{i}}^{\mathrm{e}}(t_{\mathrm{n}})$ is the measured acceleration response from the ith accelerometer at the time t_{n}, and

$\varepsilon_{\mathrm{i}}^{\mathrm{a}}(t_{\mathrm{n}}, \mathbf{DV})$ and $\varepsilon_{\mathrm{i}}^{\mathrm{e}}(t_{\mathrm{n}})$ are the ith computed and measured reinforcement strains at the time t_{n}, respectively.

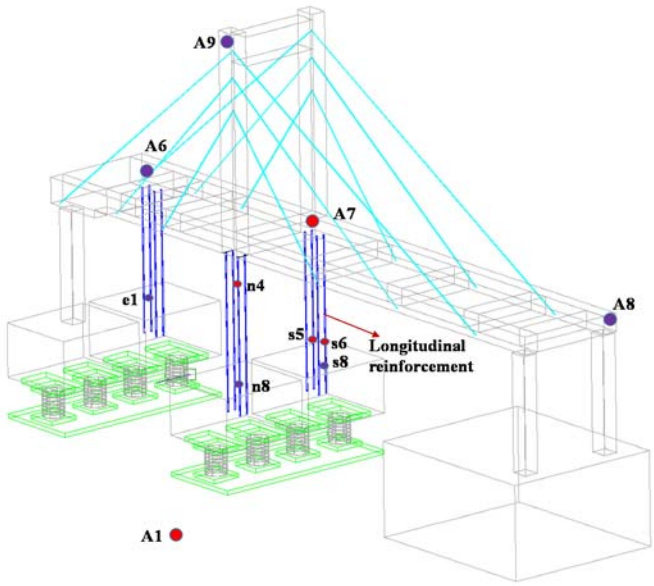

Figure 7.1 Key sensor locations for model updating

7.2.2 Updated results of key parameters

Figure 7.2 shows the current large earthquake ground motion applied to the bridge structure for the nonlinear model updating. The peak acceleration and duration of the large earthquake are 4.758m/s^2 and 19.53 seconds, respectively. The sampling frequency of the large earthquake ground excitation is 256 Hz. The updated results of the 56 key parameters for the envelop curves of the materials of the damaged RC bridge due to the previous earthquakes are tabulated in Table 7.1, in which the alphabet A, A1, B1 and C1 represent the key points on the envelop curves shown in Figure 7.3 (a) and Figure 7.3 (b). Table 7.2 lists the updated two Rayleigh damping coefficients. From Table 7.1, it can be seen that the compressive strength of the concrete and the yielding strength of the reinforcement of the failure-vulnerable fiber elements in the second, third and fourth groups decrease sharply due to the damage caused by previous earthquakes, whereas those of the fiber elements in the fifth group decrease slightly.

These changes are attributed to the strength degradations of both concrete and reinforcement. In Figure 7.3 (a) and Figure 7.3 (b), the envelop curves OA and AA' for concrete and reinforcement are for the undamaged southwest pier and they are determined through the linear model updating conducted in Chapter 5. The envelop curves A'OA and D''C''B''A''OABCD for concrete and reinforcement are for the damaged southwest pier and they are determined through the nonlinear model updating in this chapter. It can be seen that the envelop curves of the confined concrete and the reinforcement in the undamaged southwest pier are significantly different from those of the damaged southwest pier due to previous earthquakes. The envelop curves evolve clearly. The maximum compressive strength of the confined concrete sharply decreases from 58.7MPa to 8.3MPa. The compressive strength 8.3MPa is actually the residual strength of the concrete that experienced all the previous earthquakes. For reinforcement, the yielding strength of the reinforcement sharply decreases from 589.9MPa to 206.5MPa, and the modulus of the reinforcement substantially decreases from 2.96×10^5 MPa to 1.03×10^5 MPa. It is interesting to know from Table 7.2 that the updated Rayleigh damping coefficients for the damaged structure are much larger than those of the undamaged structure. From Table 7.1, it can also be seen that most groups of the compressive strength of concrete and the modulus of reinforcement are decreased remarkably compared with the ones identified in Chapter 6. This is because the current damage of the bridge results from the accumulation of damage due to all the previous earthquakes including those used in Chapter 6.

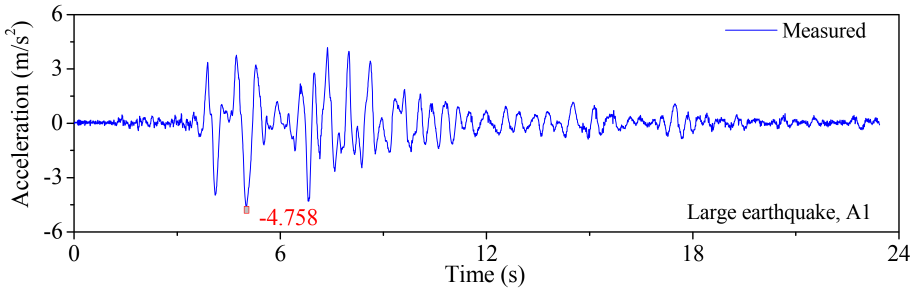

Figure 7.2 Ground acceleration recorded at station A1

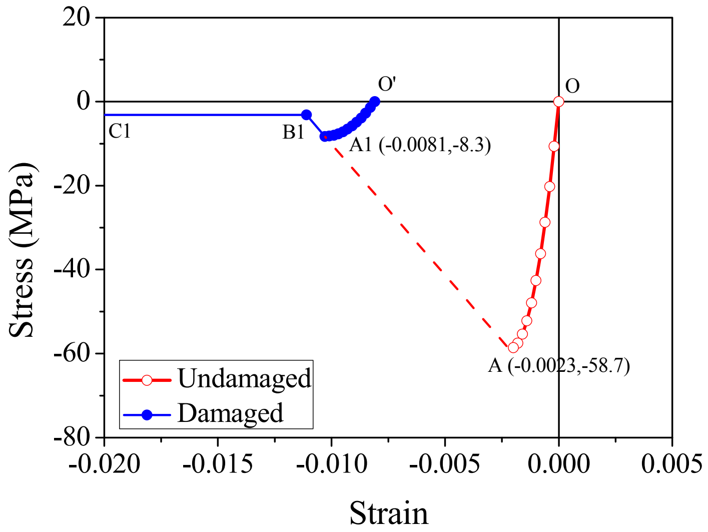

(a)

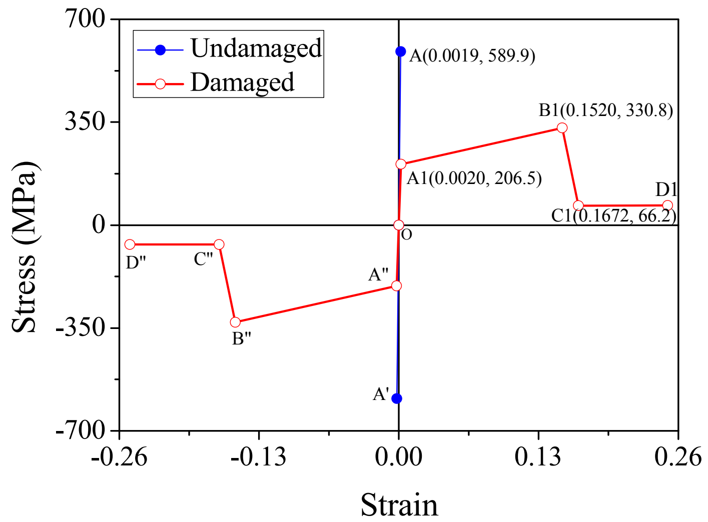

(b)

Figure 7.3 Evolution of envelop curves (a) Confined concrete (b) Reinforcement

Table 7.1 Updated key parameters

Parameter No.	Description	Linear model updated	Nonlinear model updated		
		A	A1	B1	C1
1-2	Confined concrete compressive stress of the slightly damaged tower and pier (MPa)	-58.7	-51.9	-3.2	
3-4	Confined concrete compressive strain of the slightly damaged tower and pier	-0.0023	-0.0021	-0.0108	
5-6	Cover concrete compressive stress of the slightly damaged tower and pier (MPa)	-52.6	-51.1	0.0	
7-8	Cover concrete compressive strain of the slightly damaged tower and pier	-0.0033	-0.0027	-0.0069	
9-10	Confined concrete compressive stress of the southeast severe damaged pier (MPa)	-58.7	-14.9	-3.2	
11-12	Confined concrete compressive strain of the southeast severe damaged pier	-0.0023	-0.0024	-0.0111	
13-14	Cover concrete compressive stress of the southeast severe damaged pier (MPa)	-52.6	-7.5	0.0	
15-16	Cover concrete compressive strain of the southeast severe damaged pier	-0.0033	-0.0024	-0.0328	
17-18	Confined concrete compressive stress of the severe damaged tower (MPa)	-58.7	-20.7	-3.2	
19-20	Confined concrete compressive strain of the severe damaged tower	-0.0023	-0.0018	-0.0105	
21-22	Cover concrete compressive stress of the severe damaged tower (MPa)	-52.6	-3.9	0.0	
23-24	Cover concrete compressive strain of the severe damaged tower	-0.0033	-0.0025	-0.0637	
25-26	Confined concrete compressive stress of the southwest severe damaged pier (MPa)	-58.7	-8.3	-3.2	
27-28	Confined concrete compressive strain of the southwest severe damaged pier	-0.0023	-0.0022	-0.0111	
29-30	Cover concrete compressive stress of the southwest severe damaged pier (MPa)	-52.6	-7.5	0.0	
31-32	Cover concrete compressive strain of the southwest severe damaged pier	-0.0033	-0.0022	-0.0337	
33-35	Yielding stress of reinforcement in the slightly damaged tower and pier (MPa)	589.9	600.4	916.0	183.2
36-38	Yielding strain of reinforcement in the slightly damaged tower and pier	0.0019	0.0023	0.1520	0.1672
39-41	Yielding stress of reinforcement in the severe damaged southeast pier (MPa)	589.9	697.8	875.6	175.1
42-44	Yielding strain of reinforcement in the severe damaged southeast pier	0.0019	0.0046	0.1520	0.1672
45-47	Yielding stress of reinforcement in the severe damaged tower (MPa)	589.9	667.0	801.8	160.4
48-50	Yielding strain of reinforcement in the severe damaged tower	0.0019	0.0058	0.1520	0.1672
51-53	Yielding stress of reinforcement in the severe damaged southwest pier (MPa)	589.9	206.5	330.8	66.2
54-56	Yielding strain of reinforcement in the severe damaged southwest pier	0.0019	0.0020	0.1520	0.1672

Table 7.2 Updated key parameters

Parameter No.	Description	Linear model updated	Nonlinear model updated
57	Rayleigh damping coefficient of mass	1.921 (rad/s)	10.175 (rad/s)
58	Rayleigh damping coefficient of stiffness	0.0002 (s/rad)	0.0003 (s/rad)

7.3 Validation

The multi-start method, as used in Chapter 6, is also employed in this chapter to find the nonlinear model updating solution. With many sets of initial values within the pre-set domain, only one set yielding the achievable minimum value of the objective function is regarded as the global solution. To validate the correctness of the nonlinear model updating results in this chapter, the computed seismic responses are compared with the measured responses which are not used in the model updating. One acceleration response at A7, ten reaction forces and two reinforcement strain responses at n4 and s5 are employed for such comparison. To quantify the difference between the computed and measured responses, the following index is again used in this chapter.

$$J = \frac{\sum_{\mathrm{n}=1}^{N_{\mathrm{t}}} \left(Mea(t_{\mathrm{n}}) - Ana(t_{\mathrm{n}}) \right)^2}{\sum_{\mathrm{n}=1}^{N_{\mathrm{t}}} \left(Mea(t_{\mathrm{n}}) \right)^2} \tag{7.4}$$

where *Mea* and *A*na denote the measured and the calculated results, respectively, and the index *J* actually represents the relative average error of the computed response.

7.3.1 Comparison of acceleration responses

The acceleration response of A7 computed from the updated nonlinear FE model of the bridge is plotted in Figure 7.4 together with the measured one. The computed acceleration response matches well with the measured one. The peak acceleration responses and the average errors are presented in Table 7.3. The average error index *J* is small, but the difference in the peak acceleration response is considerable.

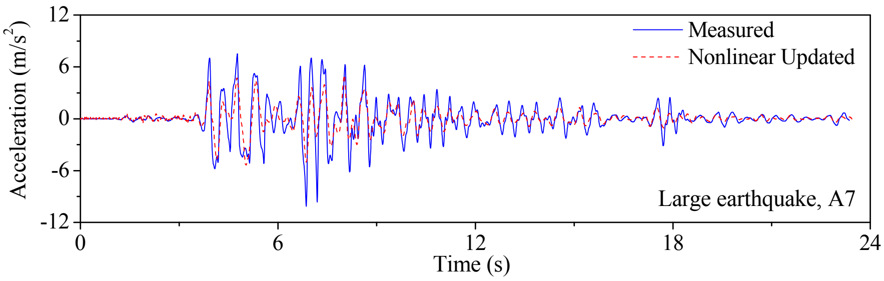

Figure 7.4 Comparison of acceleration response time histories at A7

Table 7.3 Comparison of acceleration responses

Station No.	Peak Acceleration (m/s^2)		J
	Measured	Nonlinear Updated	
A7	10.137	5.365	0.390
Mean			0.390

7.3.2 Comparison of reaction forces

Figure 7.5 demonstrates the locations and positive directions of the reaction forces (i.e., shear force, axial force, bending moment and torsion moment). The reaction forces at the north and south tower legs and the southeast pier calculated from the updated nonlinear FE model of the bridge are plotted in Figures 7.6, 7.8 and 7.10, respectively, together with the measured ones. The peak reaction forces and the average errors are summarized in Table 7.4. The computed reaction force time-histories are in good agreement with the measured ones except for the axial force and the shear force of the south tower leg. The calculated peak reaction forces also match with measured ones in general and the maximum error occurs in the axial force of the three components and the shear force of the south tower leg. As mentioned in Chapter 4, the channels for measuring the axial force from the load cells may not be sensitive enough to measure axial forces. Although the average error values (J) are quite large, the actual errors between the measured and calculated results are not so large. This is because the error J is defined in the time domain for the entire response time history. The hysteretic responses of the computed bending moment versus the curvature at the bottom of the two tower legs, the southeast pier and southwest pier are plotted in Figures 7.7, 7.9, 7.11 and 7.12, respectively. It can be clearly seen that the two RC tower legs and the two south RC piers all experienced material nonlinearity and exhibit plump hysteretic loops under the large earthquake. Therefore, the degradations of both stiffness and strength must be considered in the nonlinear model updating.

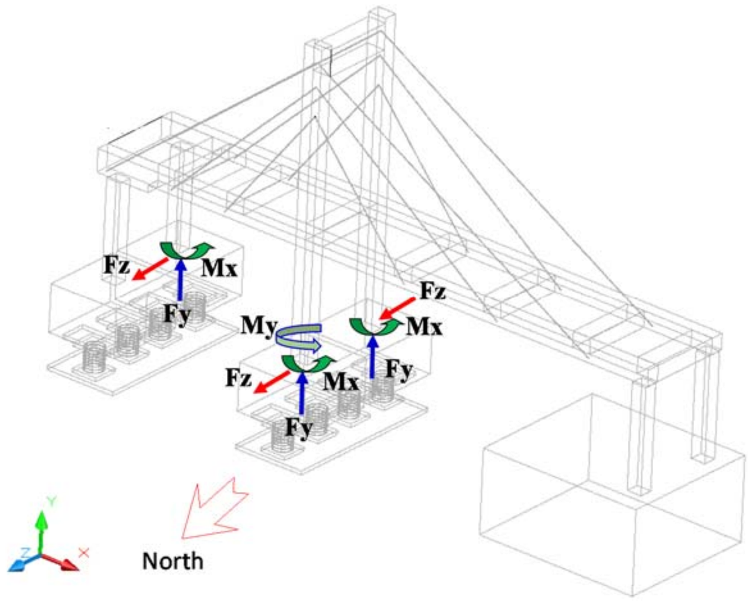

Figure 7.5 Locations for recorded reaction forces

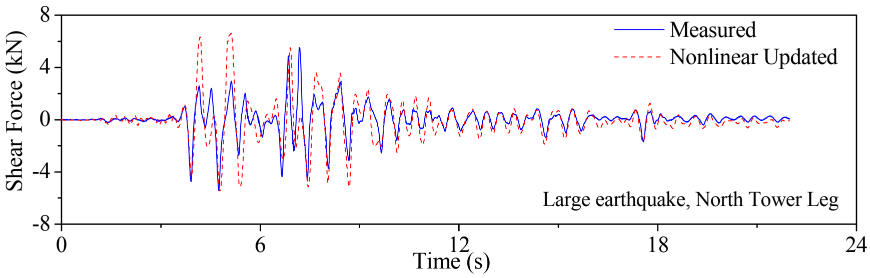

(a)

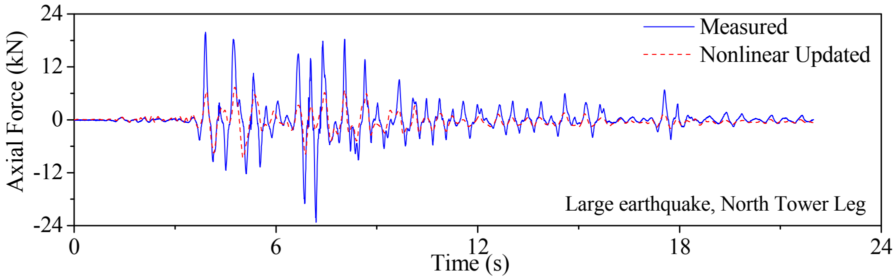

(b)

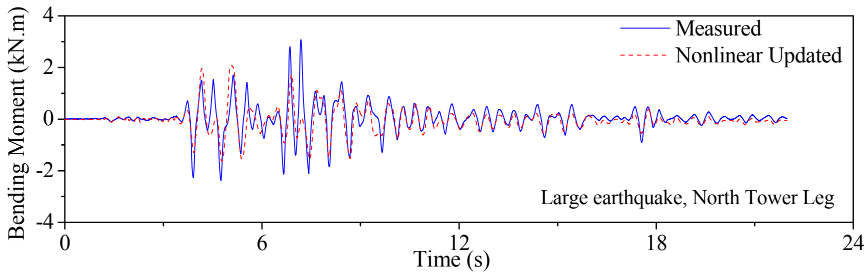

(c)

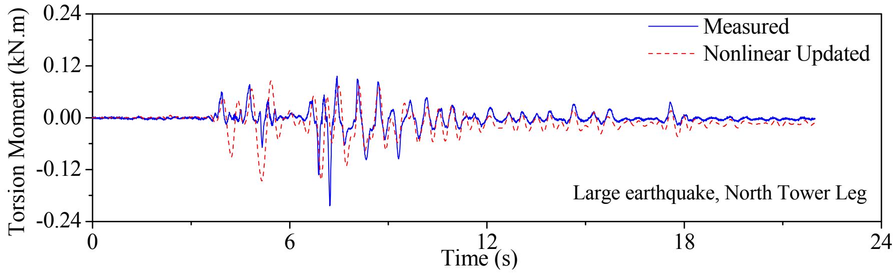

(d)

Figure 7.6 Comparison of reaction forces at the bottom of the north tower leg

(b) Shear force (b) Axial force (c) Bending moment (d) Torsion moment

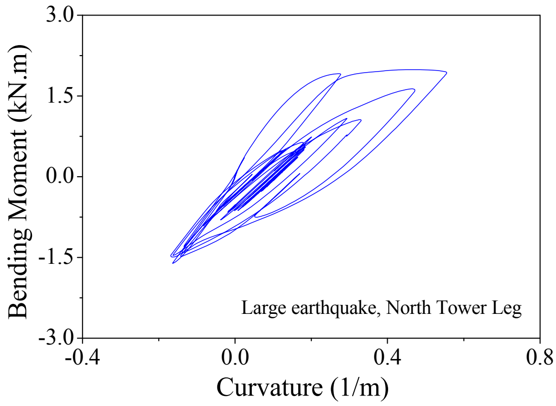

Figure 7.7 Hysteretic response of the bending moment vs. curvature

at the bottom of the north tower leg

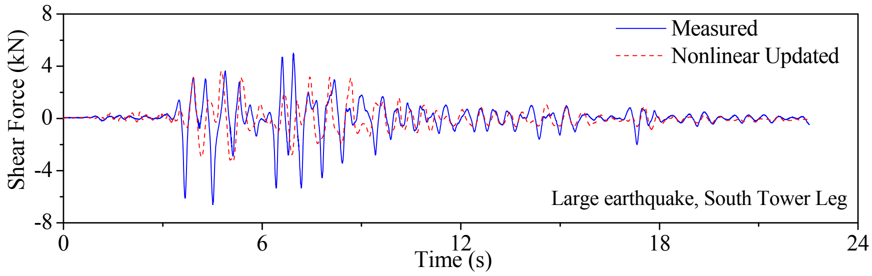

(a)

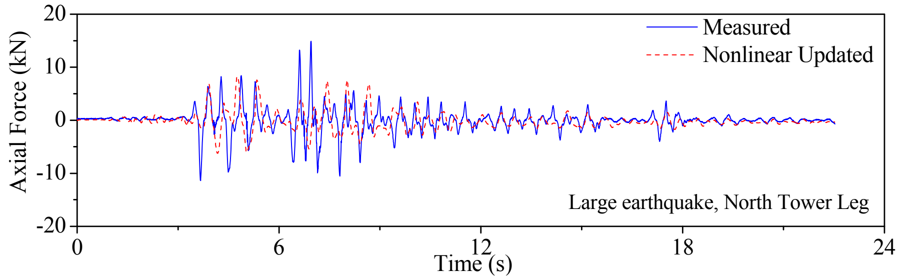

(b)

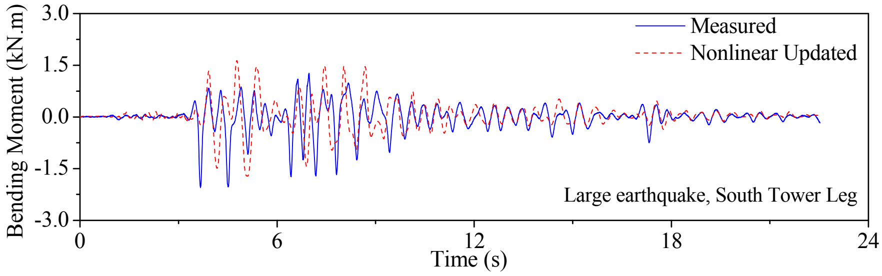

(c)

Figure 7.8 Comparison of reaction forces at the bottom of the north tower leg

(c) Shear force (b) Axial force (c) Bending moment

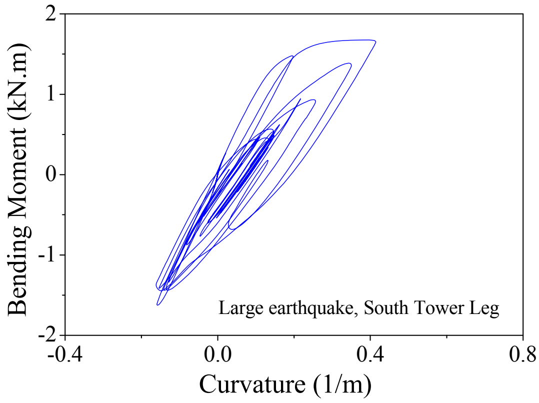

Figure 7.9 Hysteretic response of the bending moment vs. curvature

at the bottom of the south tower leg

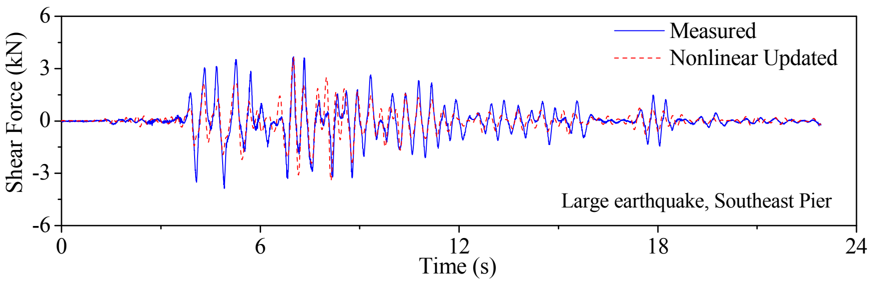

(a)

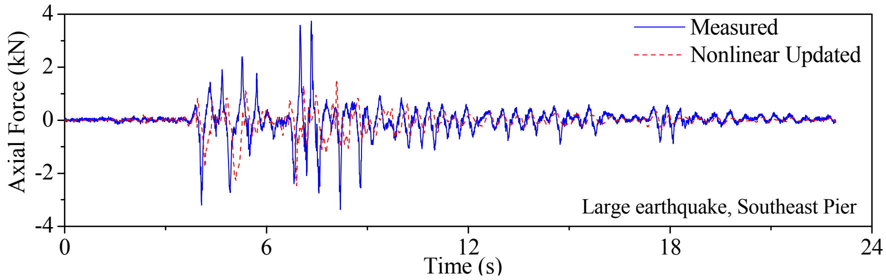

(b)

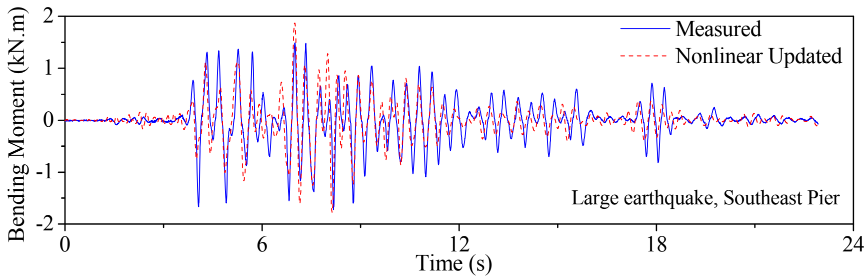

(c)

Figure 7. 10 Comparison of reaction forces at the bottom of the north tower leg

(a) Shear force (b) Axial force (c) Bending moment

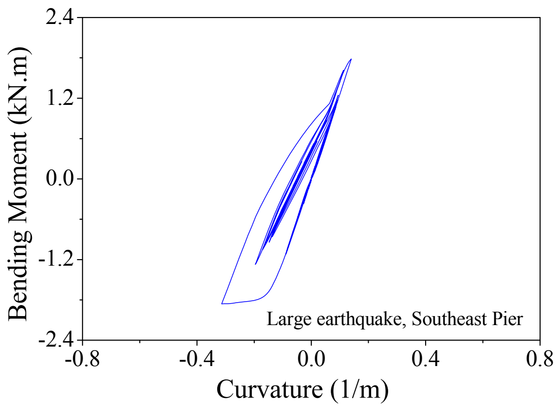

Figure 7.11 Hysteretic response of the bending moment vs. curvature

at the bottom of the southeast pier

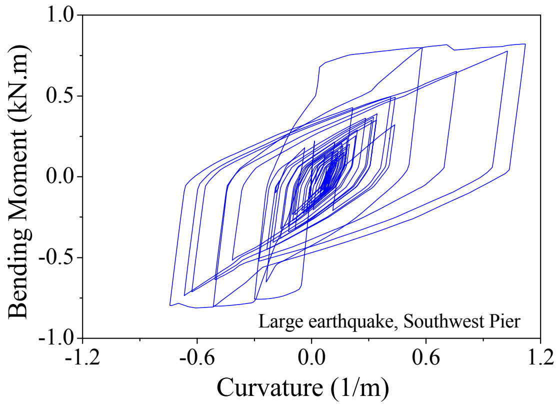

Figure 7.12 Hysteretic response of the bending moment vs. curvature at the bottom of the southwest pier

Table 7.4 Comparison of reaction forces (Moments)

Location	Force Type	Peak Forces (Moments)		J
		Measured	Nonlinear Updated	
North Tower Leg	Shear Force	5.532kN	6.627kN	1.129
	Axial Force	23.229kN	8.579kN	0.538
	Bending Moment	3.075kN.m	2.069kN.m	0.558
	Torsion Moment	0.204kN.m	0.146kN.m	1.528
South Tower Leg	Shear Force	6.600kN	3.272kN	1.173
	Axial Force	14.912kN	8.274kN	1.282
	Bending Moment	2.055kN.m	1.717kN.m	1.558
Southeast Pier	Shear Force	3.873kN	3.342kN	0.406
	Axial Force	3.738kN	2.476kN	1.401
	Bending Moment	1.721kN.m	1.735kN.m	0.548
Mean				1.014

7.3.3 Comparison of reinforcement strains

Figure 7.13 shows the strain responses of the reinforcement at the north and south tower legs close to the girder calculated from the updated nonlinear FE model of the bridge, and the corresponding measured strain responses are also plotted in Figure 7.13. The measured and computed strain response time histories are similar in pattern. The peak reinforcement strain responses and the average errors of strain responses are summarized in Table 7.5. From Table 7.5, it can be seen that the average error associated with the strain response at s5 is the smallest and the average error associated with the strain response at n4 is the largest with the *J* index of 2.42. The measured maximum reinforcement strain response is 0.01 at the sensor location s5, indicating that the deformation of the reinforcement at the location s7 is larger than the other location. It is of interest that the absolute tensile peak strain is larger than the absolute compressive peak strain because the reinforcement sustains all the tension force, yet the concrete does not bear tension force.

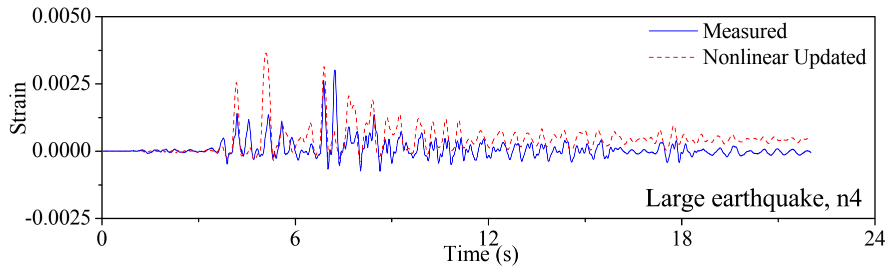

(a)

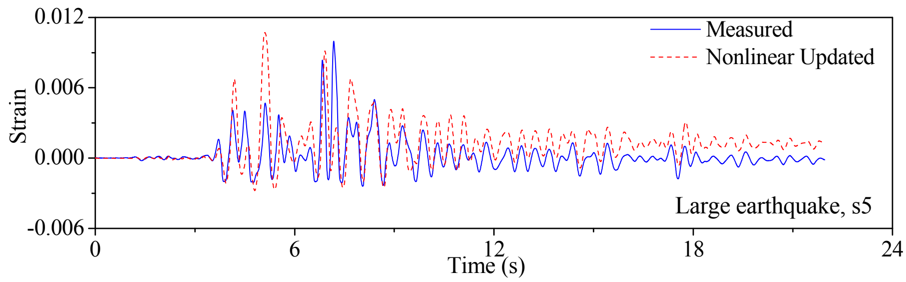

(b)

Figure 7.13 Comparison of reinforcement strain time histories (a) n4 (b) s5

Table 7.5 Comparison of reinforcement strains

Component	Location	Peak Strain		*J*
		Measured	Nonlinear Updated	
North Tower Leg	n4	0.0030	0.0036	2.420
South Tower Leg	s5	0.0100	0.0107	1.532
Mean				1.976

7.4 Failure Criteria for Failure Elements

As described in Chapter 3, one failure element composed of a zero-length failure element will be assigned at one appropriate failure-vulnerable location of the updated FE model for seismic collapse prognosis. The failure criteria for the failure elements are closely related to the updated damage conditions of the failure-vulnerable elements. According to the updated key parameters of materials, the failure modes of the southeast and southwest RC piers are flexure failure modes. The corresponding failure criteria are determined through a standard section analysis by virtue of OpenSees (McKenna et al. 2007) as listed in Table 7.6. The failure criteria for the undamaged materials are also listed in Table 7.6 for the piers in bracket. It can be seen in Table 7.6 that the values of failure criteria for flexure failure of the southeast RC pier without damage are 0.083 rad for rotation and 0.606kN.m for bending moment respectively, whereas the same quantities with considering material damage are 0.080 rad and 0.538kN.m respectively. Clearly, the values of failure criteria are reduced for the damaged materials slightly. However, for the southwest pier the values of failure criteria for flexure failure without considering damage are 0.084 rad for rotation and 0.617kN.m for bending moment respectively, but the same quantities with considering damage are 0.030 rad and 0.169kN.m only. This is because the southwest pier is damaged severely. For the two RC tower legs, they experience flexure-shear-axial modes according to the updated key parameters of materials. The thresholds of the failure criteria are determined by Eqs. (3.3) and (3.4) and the results are listed in Table 7.6 together with the threshold values of the failure criteria for the undamaged materials of the two RC tower legs in bracket. Δ_s / L and Δ_a / L in Table 7.6 indicate the thresholds of drift ratio triggering the flexure-shear and flexure-shear-axial failures, respectively. It can be seen that for the flexure-shear failure, the threshold values increase slightly compared with those without considering material damage. However, for the flexure-shear-axial failure, the threshold values decrease moderately compared with those without considering material damage. Once the failure criteria for the four failure elements are given, the collapse prognosis of the RC bridge can be performed.

Table 7.6 Failure modes and failure criteria

Location	Failure Mode	Failure Criteria		Threshold of Failure	
		Rotation (rad)	Bending moment	Δ_s / L	Δ_a / L
Southeast Pier	Flexure Failure	0.080 (0.083)	0.538 (0.606)kN.m		
Southwest Pier	Flexure Failure	0.030 (0.084)	0.169 (0.617)kN.m		
South Tower Leg	Flexure-Shear-Axial Failure			0.042 (0.039)	0.075 (0.089)
North Tower Leg	Flexure-Shear-Axial Failure			0.042 (0.039)	0.075 (0.089)

Note: value inside bracket is the failure criteria or threshold of undamaged component.

7.5 Seismic Collapse Prognosis

The updated FE model with 4 zero-length failure elements, as shown in Figure 7.14, is now used for seismic collapse prognosis. Generally, a number of earthquake ground motions of different peak ground accelerations (PGAs) will be applied to the updated FE model of the bridge to find which one will cause the collapse of the bridge.

In this chapter, based on the information obtained from the shake table tests, only two earthquake ground motions of different intensities are considered in determining which one will cause the collapse of the bridge. The first and second earthquake excitations for collapse prognosis are plotted in Figures 7.15 and 7.16, respectively. The PGA and the duration of the first earthquake ground motion excitation are 3.307m/s^2 and 12.0 seconds, respectively. The PGA and the duration of the second earthquake ground motion excitation are 4.633 m/s^2 and 11.719 seconds, respectively.

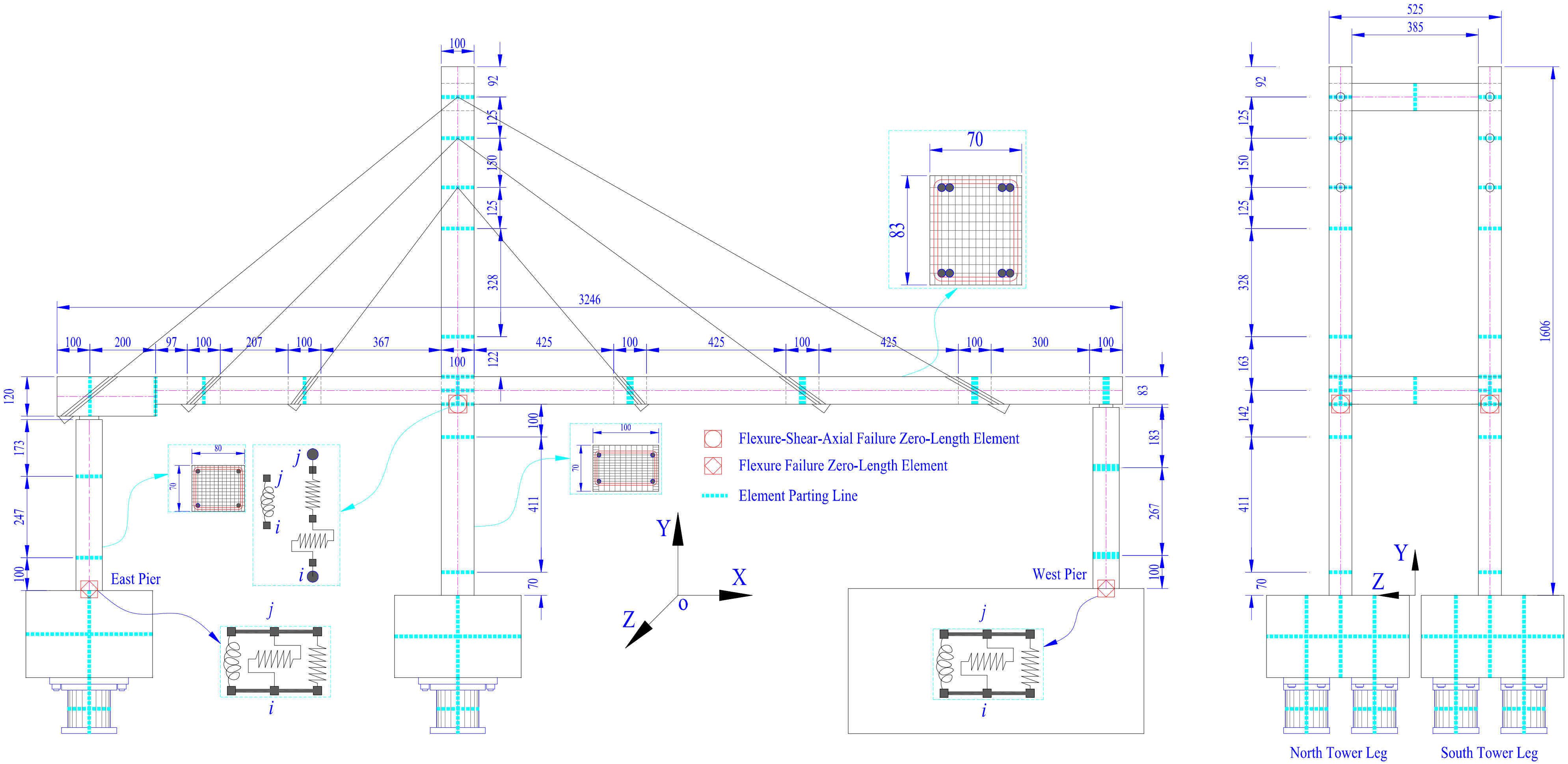

Figure 7.14 3-D FE model for seismic analysis (Unit: mm)

The sampling frequency of the two earthquake excitations are 50Hz and 256 Hz, respectively. It should be mentioned that the first earthquake ground motion excitation is used to prognosticate the future behavior of the damaged RC bridge. The second earthquake ground motion is also used to prognosticate the future behavior of the damaged RC bridge but it was actually recorded by the accelerometer at A1 during the collapse shaking table test of the bridge. Therefore, the second earthquake ground motion is actually the one causing the bridge collapse. A series of measured results from the test can then be employed to make comparison with the simulated seismic results of the bridge subject to the second earthquake so that the feasibility and accuracy of the proposed collapse prognosis can be examined.

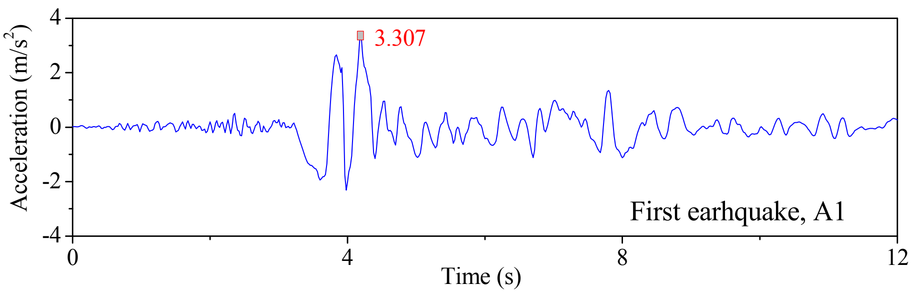

Figure 7.15 First earthquake ground motion excitation

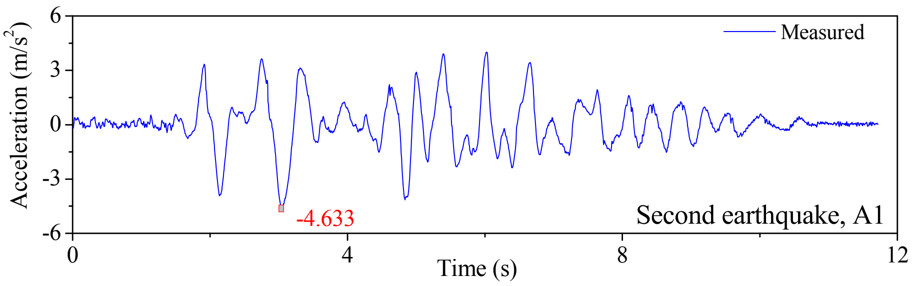

Figure 7.16 Second earthquake ground motion excitation recorded at A1

7.5.1 Collapse prognosis for the first earthquake excitation

To prognosticate whether the RC bridge collapse or not when subjected to the first earthquake ground excitation, the seismic responses of the zero-length failure elements are investigated. The bending moments versus rotations at the bottom of the southeast and southwest piers are plotted in Figure 7.17. It can be seen in Figure 7.17 that the seismic response of the southeast pier is still linear and the seismic response of the southwest is nonlinear but within the failure envelop curves. The absolute rotation responses of the southeast and southwest piers subject to the first earthquake are, respectively, 0.011 and 0.020 rad, which are less than the corresponding failure criteria of 0.080 and 0.030 rad, respectively. The shear forces versus drift ratios of the north and south tower legs are plotted in Figure 7.18. The absolute drift ratio responses of the north and south tower legs are respectively 0.011 and 0.012, which are far less than the flexure-shear failure criterion of 0.042. As a result, although the four zero-length failure elements accumulate unrecoverable damage due to the first earthquake, the RC bridge does not collapse.

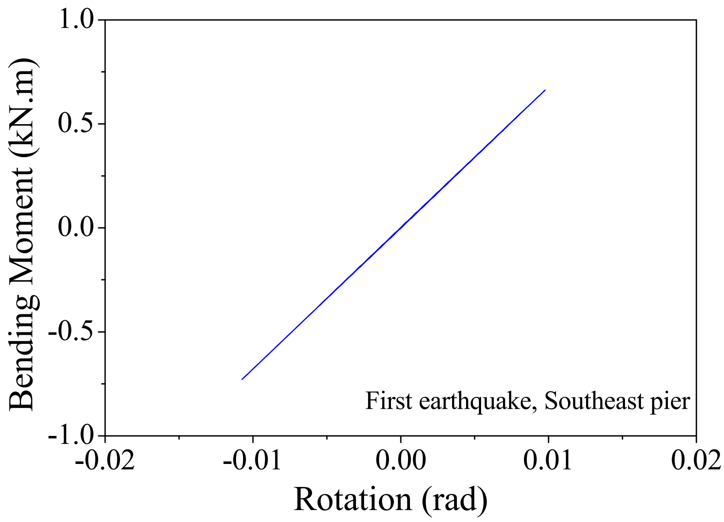

(a)

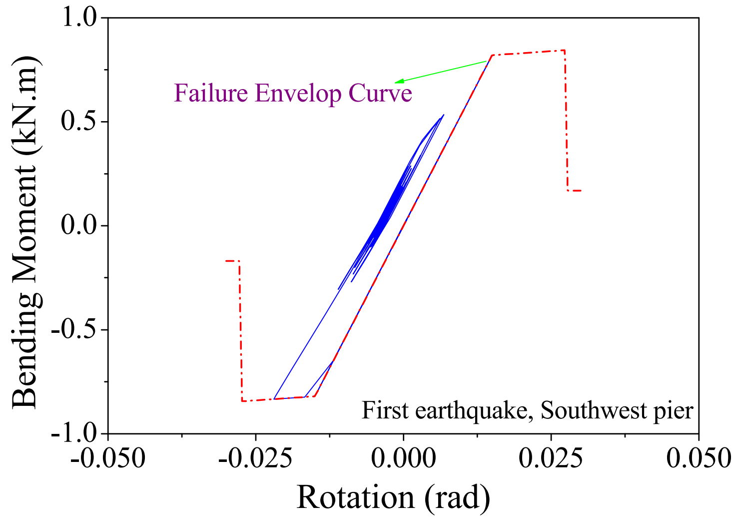

(b)

Figure 7.17 Hysteretic response of the bending moment vs. rotation

(a) At the bottom of the southeast pier (b) At the bottom of the southwest pier

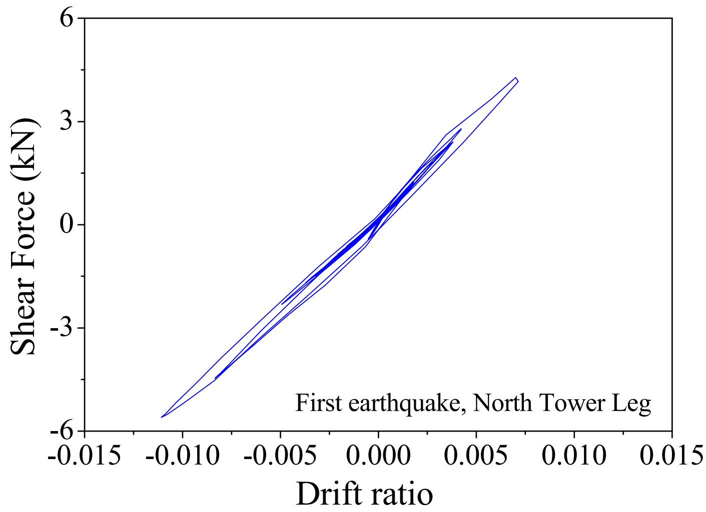

(a)

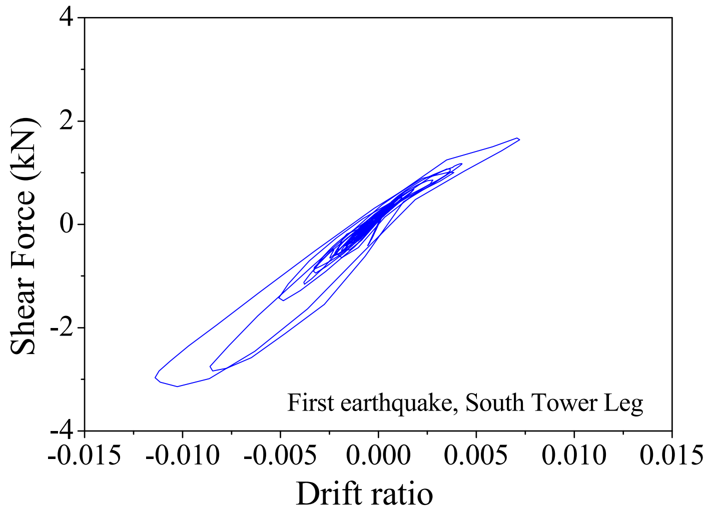

(b)

Figure 7. 18 Hysteretic response of the shear force vs. drift ratio

(a) The north tower leg (b) The south tower leg

7.5.2 Collapse prognosis for the second earthquake excitation

The results presented in Section 7.5.1 show that the RC cable-stayed bridge does not collapsed when it is subjected to the first earthquake ground excitation of a relatively small intensity. Nevertheless, the shake table tests described in Chapter 4 showed that the RC cable-stayed bridge experienced partially collapse when it was subjected to the second earthquake ground excitation. The second earthquake excitation is therefore called the collapse earthquake excitation in Chapter 4. The shake table tests showed that the southwest RC pier suffered from severe damage at the zero-length failure element (plastic hinge zone): the concrete crushed, the longitudinal reinforcing steels yielded and the stirrup fractured. The southwest RC pier was finally separated from the twin-girder. The concrete in the plastic hinge zones of the southeast RC pier and the two tower legs also cracked remarkably. In other parts of the two south piers and the two tower legs, the concrete also experienced more severe damage than that under the moderate earthquake. The concrete in the twin-girder and transverse beams, however, experienced only slight damage similar to that under the moderate earthquake.

7.5.2.1 Collapse prognosis

The collapse prognosis of the RC bridge subject to the collapse (second) earthquake excitation is now performed based on the nonlinearly updated FE model. The southwest RC pier reaches its flexure failure criteria at about 3.133 second. As a result, the southwest RC pier fails and is removed from the entire bridge structure according to the provisions of seismic collapse analysis proposed in Chapter 3. The maximum displacement at the top of the southwest pier is about 0.032m and the southwest pier is separated from the girder, which is similar to what was observed from the shake table tests. Each RC tower leg beneath the girder also experiences flexure-shear-axial damage and the southeast RC pier experiences flexure damage. Nevertheless, the two north piers experience very small inertial forces because their connections with the girder are free in both longitudinal and transverse directions. Consequently, they are less damaged. The entire seismic collapse process of the RC cable-stayed bridge is demonstrated in Figure 7.19 (a), (b) and (c), respectively.

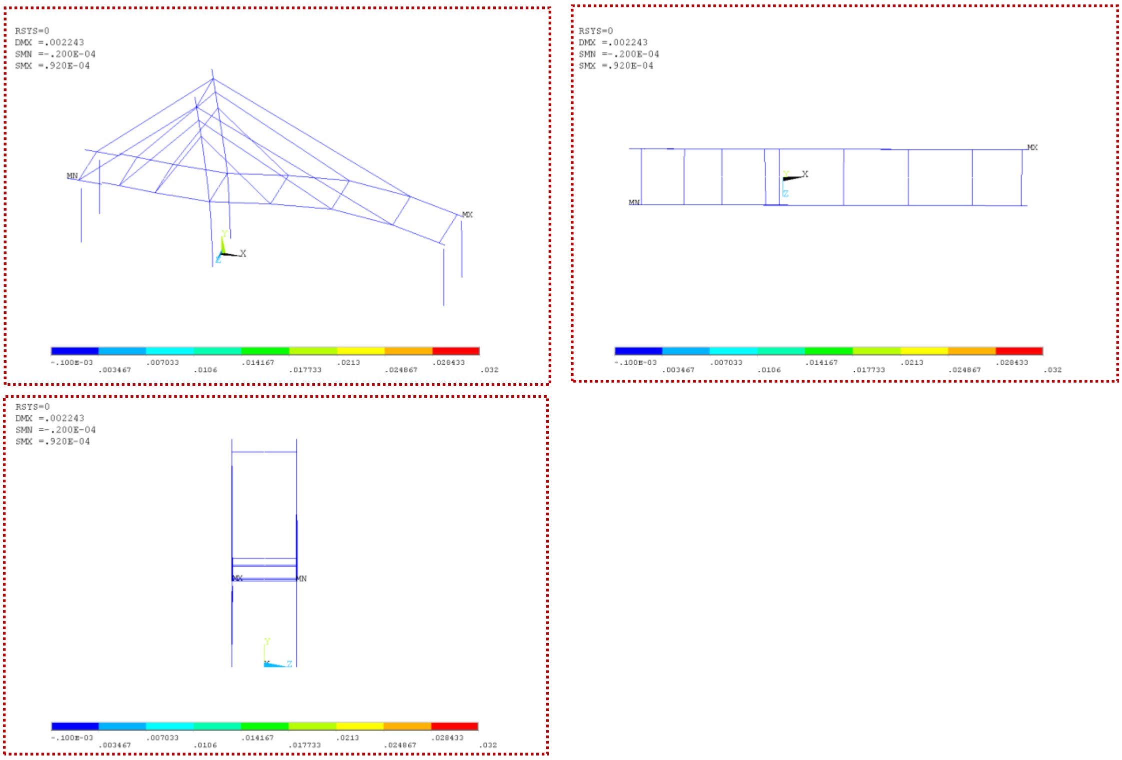
RSYS=0
DMX =.002243
SMN =-.200E-04
SMX =.920E-04
MN
MX

(a)

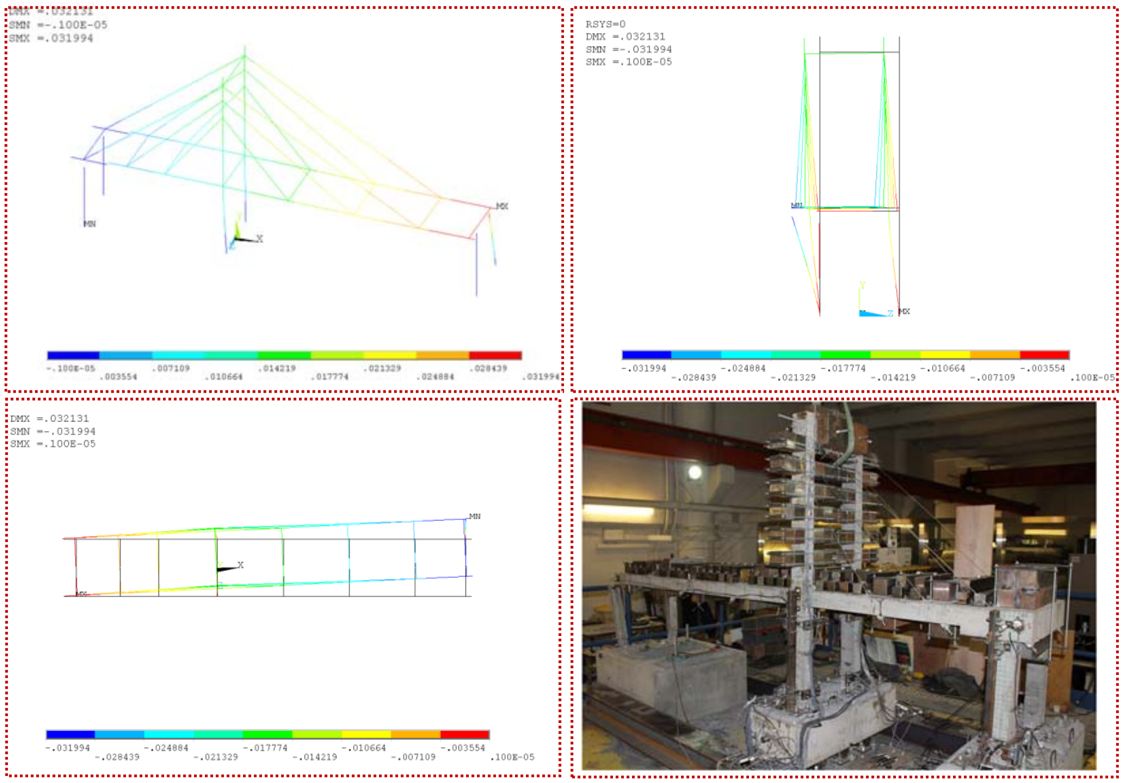
SMN =-.100E-05
SMX =.031994
RSYS=0
DMX =.032131
SMN =-.031994
SMX =.100E-05
MN
MX

(b)

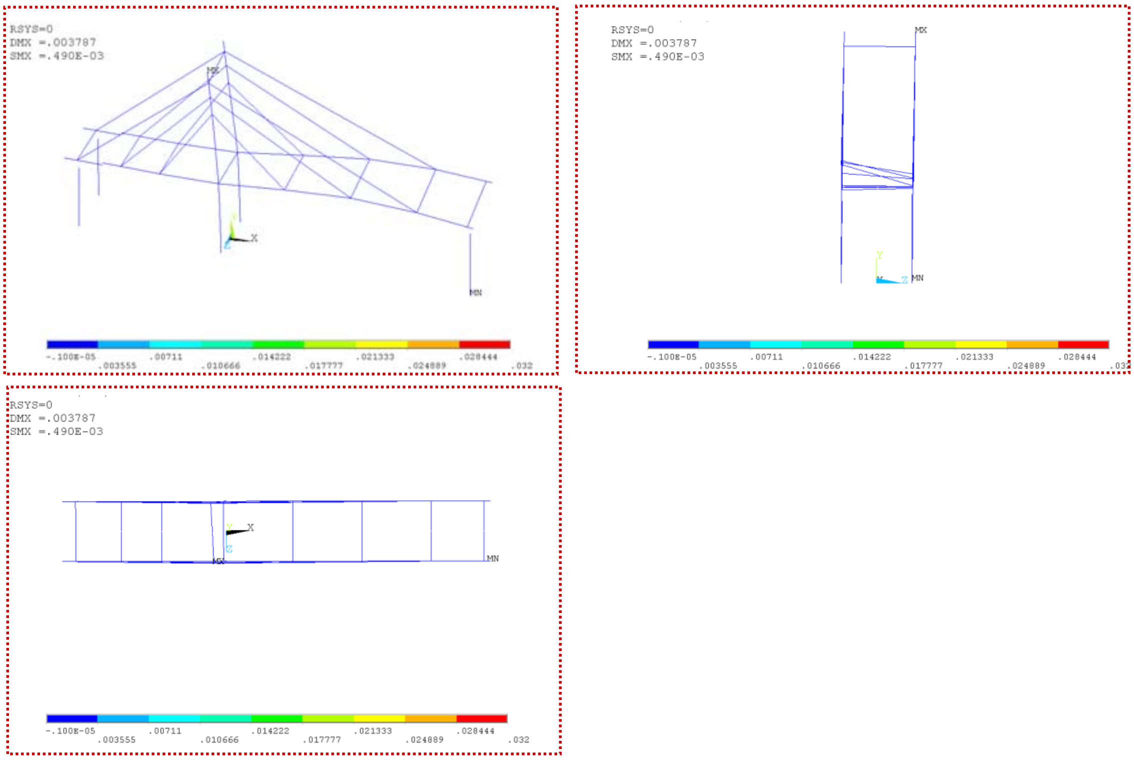

(c)

Figure 7.19 Seismic collapse process of the RC cable-stayed bridge

(a) Before earthquake event (b) Partial collapse (c) After earthquake event

7.5.2.3 Comparison of acceleration response

To demonstrate the accuracy of the collapse prognosis carried out by using the updated FE model, the computed structural responses of the RC bridge subject to the collapse earthquake excitation are compared with the measured results from the shake table tests in the following sub sections.

The acceleration responses at the sensor locations A6, A7, A8 and A9 computed from the updated nonlinear FE model of the RC bridge are plotted in Figure 7.20 together with the measured ones. From Figure 7.20, it can be seen that the computed acceleration responses match well with the measured ones. The peak acceleration responses and the average errors are presented in Table 7.7. Although the average error indexes J are small, the discrepancies in the peak acceleration responses are considerable. This is because the nonlinear model updating becomes more difficult when the RC bridge experiences more severe damage than one with slight damage.

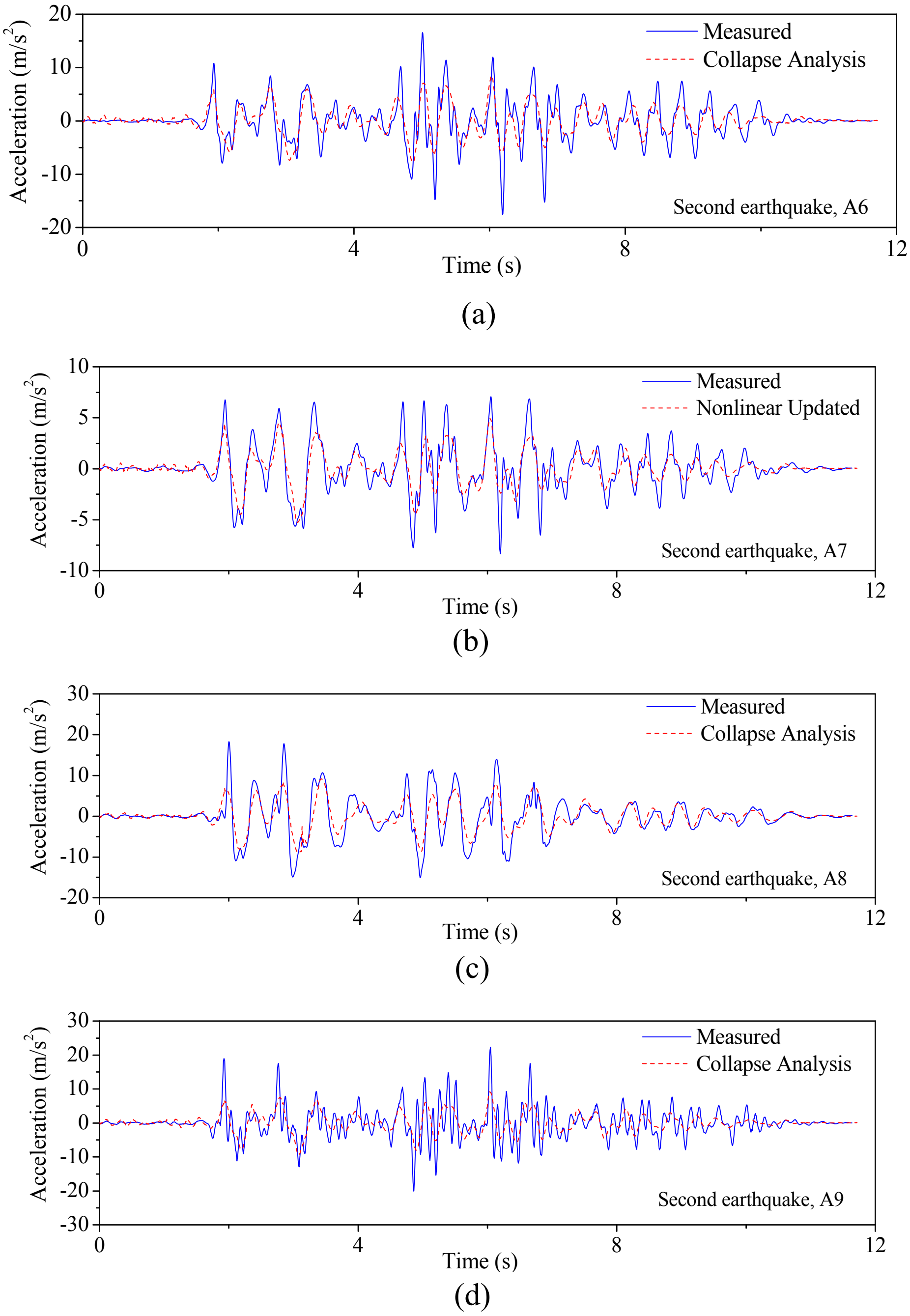

Figure 7.20 Comparison of acceleration response time histories

(a) A6 (b) A7 (c) A8 (d) A9

Table 7.7 Comparison of acceleration responses

Station No.	Peak Acceleration (m/s^2)		J
	Measured	Collapse Analysis	
A6	17.546	7.834	0.432
A7	8.351	5.262	0.297
A8	18.316	9.200	0.327
A9	22.298	8.473	0.670
	Mean		0.432

7.5.2.2 Comparison of reaction forces

Figure 7.5 demonstrates the locations and positive directions of the reaction forces (i.e., shear force, axial force, bending moment and torsion moment). The reaction forces at the north and south tower legs and the southeast pier calculated from the updated nonlinear FE model of the bridge are plotted in Figures 7.21, 7.23 and 7.25, respectively, together with the measured ones. The peak reaction forces and the average errors are summarized in Table 7.8. The computed reaction force time-histories are in good agreement with the measured ones. The calculated peak reaction forces also match with measured ones in general, and the maximum error occurs in the axial force of the north tower leg. The hysteretic responses of the computed bending moment versus the curvature at the bottom of the two tower legs and the southeast pier are plotted in Figures 7.22, 7.24 and 7.26, respectively. It can be clearly seen that the two RC tower legs and the southeast RC pier all experience material nonlinearity and exhibit hysteretic loops under the second earthquake excitation.

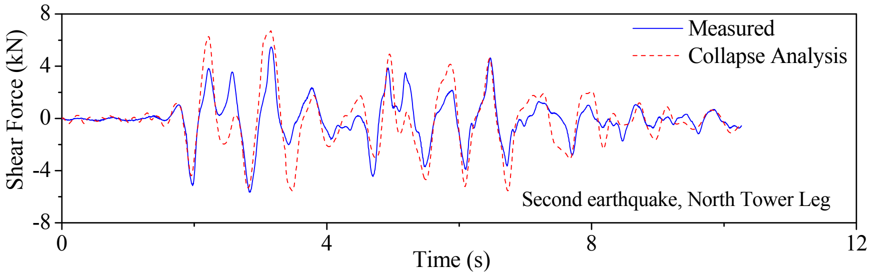

(a)

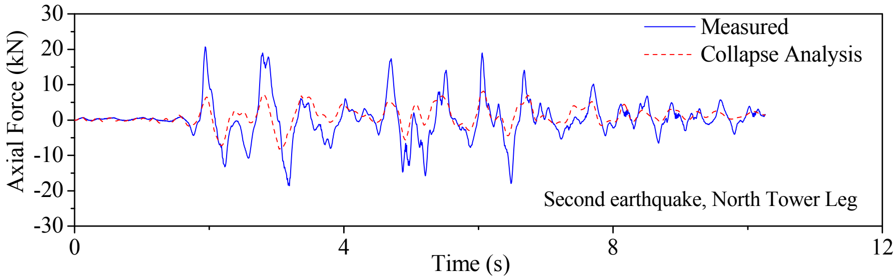

(b)

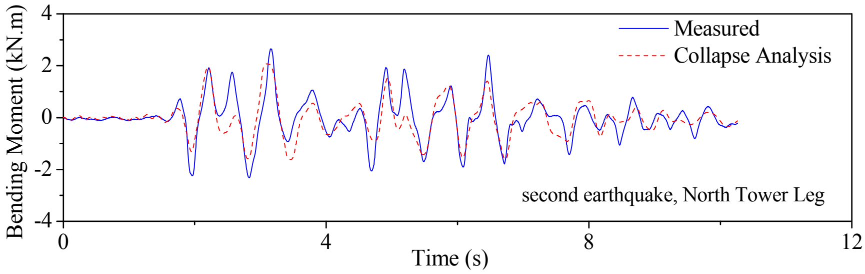

(c)

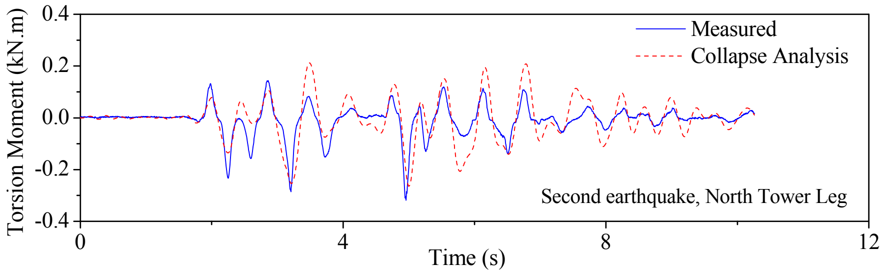

(d)

Figure 7.21 Comparison of reaction forces at the bottom of the north tower leg

(a) Shear force (b) Axial force (c) Bending moment (d) Torsion moment

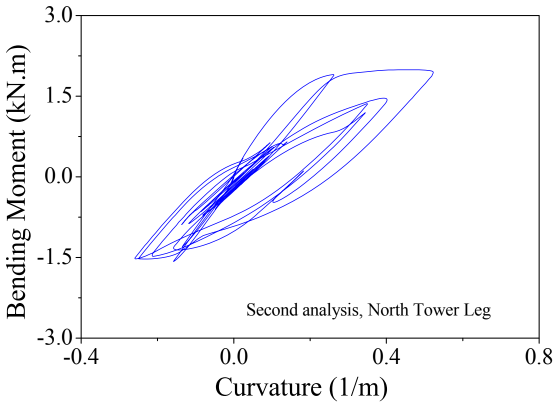

Figure 7.22 Hysteretic response of the bending moment vs. curvature at the bottom of the north tower leg

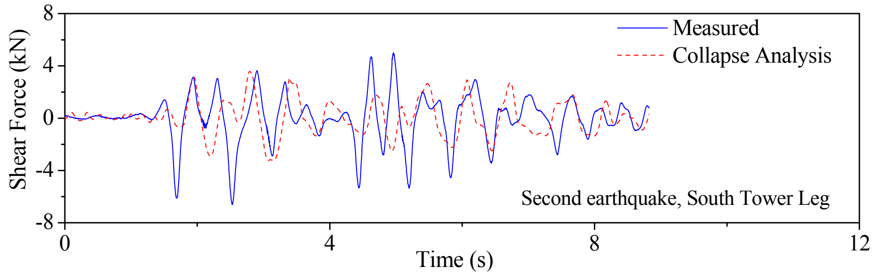

(a)

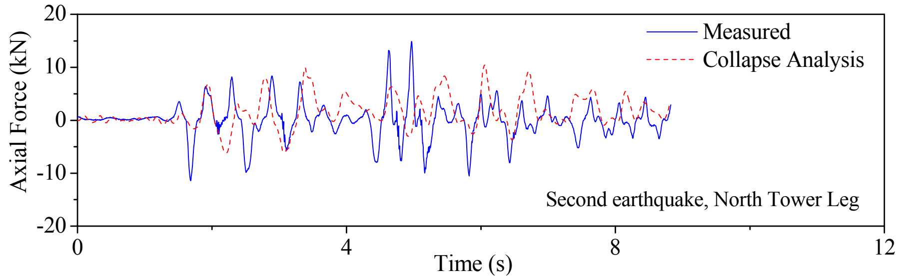

(b)

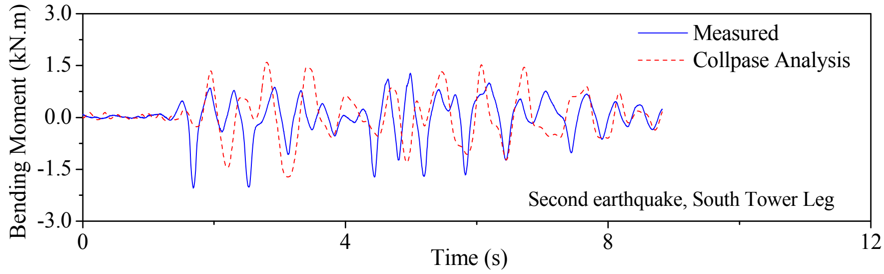

(c)

Figure 7.23 Comparison of reaction forces at the bottom of the south tower leg

(a) Shear force (b) Axial force (c) Bending moment

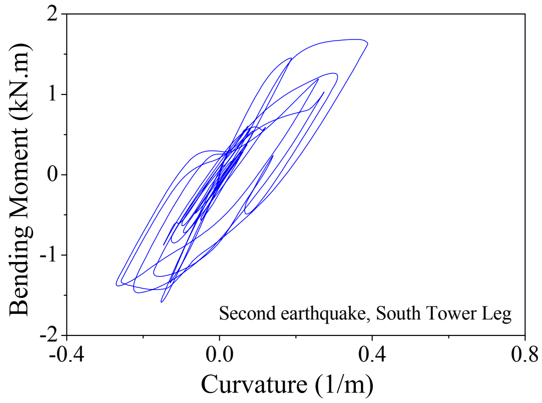

Figure 7.24 Hysteretic response of the bending moment vs. curvature at the bottom of the south tower leg

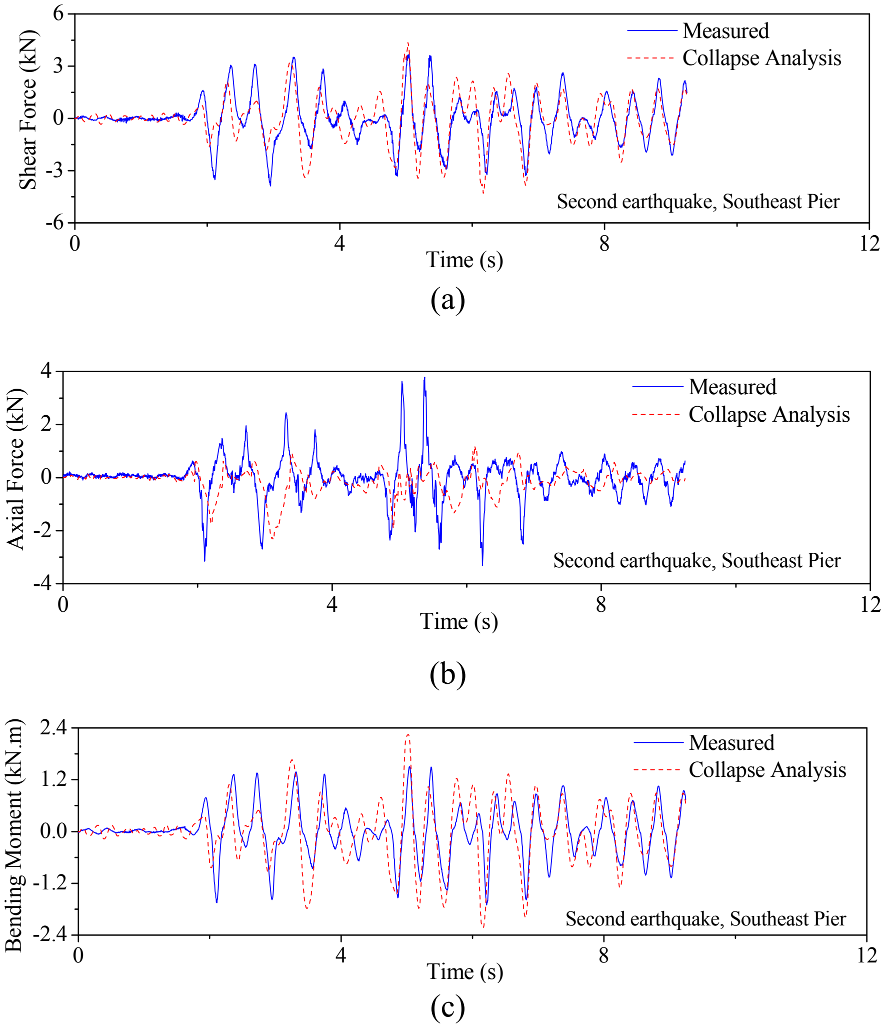

Figure 7.25 Comparison of reaction forces at the bottom of the southeast pier

(a) Shear force (b) Axial force (c) Bending moment

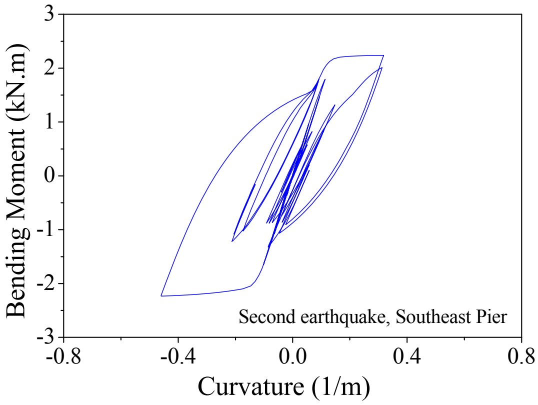

Figure 7.26 Hysteretic response of the bending moment vs. curvature at the bottom of the southeast pier

Table 7.8 Comparison of reaction forces

Location	Force Type	Peak Forces (Moments)		*J*
		Measured	Nonlinear Updated	
North Tower Leg	Shear Force	5.651kN	6.175kN	0.681
	Axial Force	20.712kN	8.372kN	0.593
	Bending Moment	2.657kN.m	2.072kN.m	0.408
	Torsion Moment	0.319kN.m	0.265kN.m	0.865
South Tower Leg	Shear Force	6.602kN	3.228kN	1.234
	Axial Force	14.893kN	10.419kN	1.733
	Bending Moment	2.046kN.m	1.721kN.m	1.731
Southeast Pier	Shear Force	3.882kN	4.306kN	0.637
	Axial Force	3.782kN.m	1.201kN	1.453
	Bending Moment	1.704kN.m	2.224kN.m	1.013
	Mean			1.035

7.5.2.3 Comparison of reinforcement strains

Figure 7.27 shows the strain responses of the reinforcement at the bottoms of the north and south tower legs, at the south tower leg close to the girder, and at the bottom of the southeast pier calculated from the updated nonlinear FE model of the bridge, and the corresponding measured strain responses are also plotted in Figure 7.27. The measured and computed strain response time histories are similar in pattern. The peak reinforcement strain responses and the average errors of strain responses are summarized in Table 7.9. From Table 7.9, it can be seen that the average error associated with the strain response at s8 is the smallest and the average error associated with the strain response at s5 is the largest with the *J* index of 1.359. The measured maximum reinforcement strain response is 0.010 at the sensor location s5, indicating that the deformation of the reinforcement at the location s5 is the largest among the five locations. It is of interest that the absolute tensile peak strain is larger than the absolute compressive peak strain because the reinforcement sustains all the tension force, yet the concrete does not bear tension force.

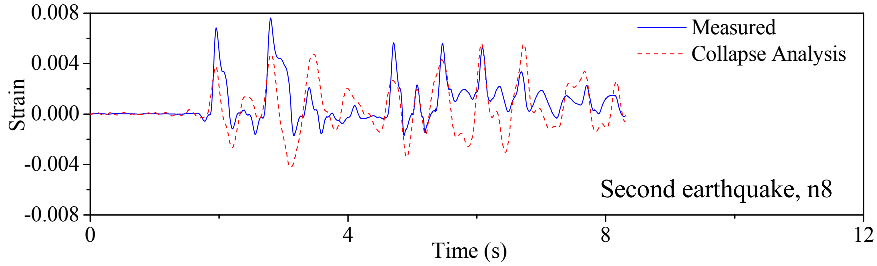

(a)

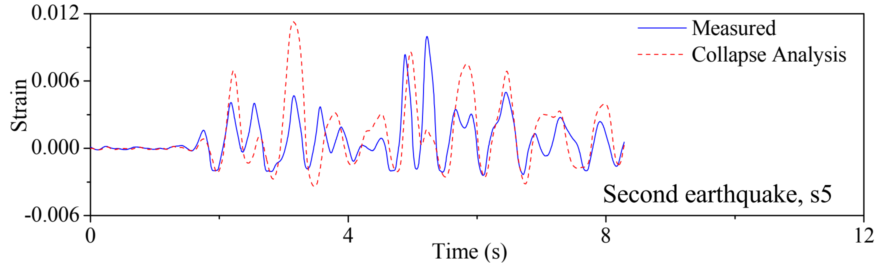

(b)

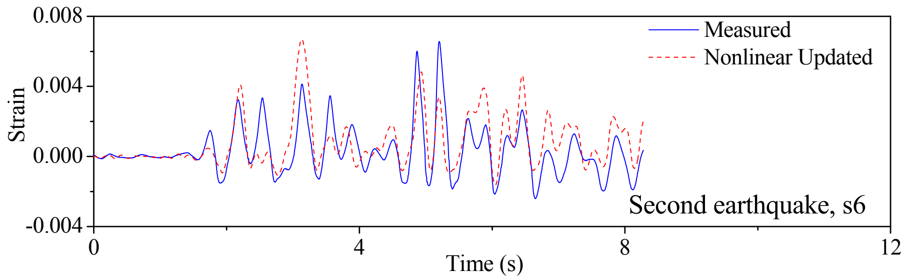

(c)

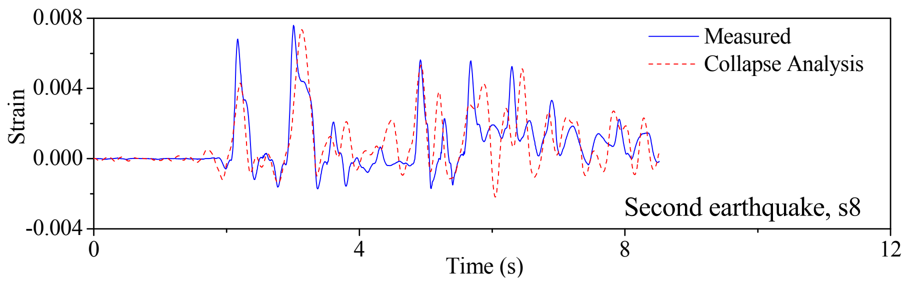

(d)

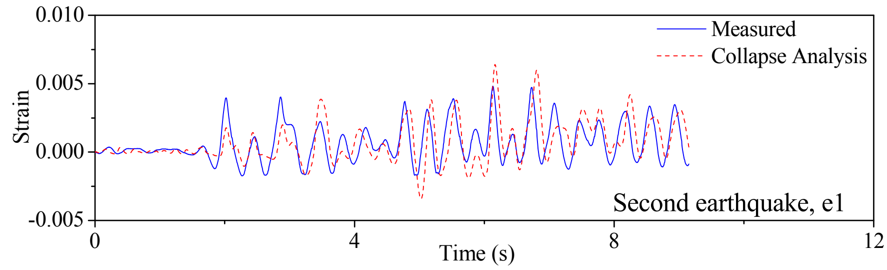

(e)

Figure 7.27 Comparison of reinforcement strain time histories:

(a) n8 (b) s5 (c) s6 (d) s8 (e) e1

Table 7.9 Comparison of reinforcement strains

Component	Location	Peak Strain		*J*
		Measured	Collapse Analysis	
North Tower Leg	n8	0.0076	0.0056	1.026
South Tower Leg	s5	0.0100	0.0113	1.359
	s6	0.0066	0.0067	0.778
	s8	0.0076	0.0074	0.590
Southeast Pier	e1	0.0048	0.0064	0.796
	Mean			0.910

7.5.2.4 Responses of zero-length failure elements

There are four zero-length failure elements in the FE model for collapse prognosis. The seismic responses of these failure elements can be investigated to find which failure element fails during the collapse earthquake excitation. The shear force and drift ratio relationships of the zero-length failure elements at the north and the south tower legs are plotted in Figures 7.28 (a) and (b), respectively. The maximum drift ratios of the north and south tower legs are 0.0245 and 0.0247, respectively, and both are less than the threshold value of 0.042 which triggers the flexure-shear failure mode.

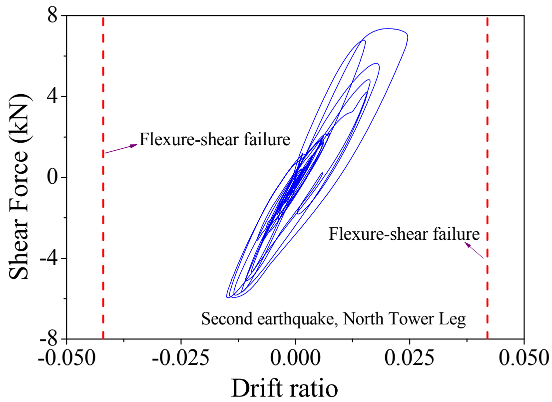

(a)

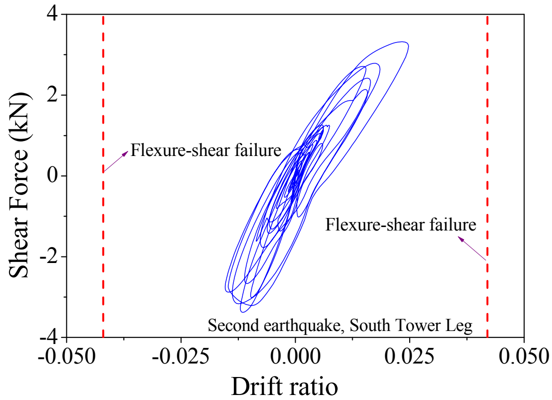

(b)

Figure 7.28 Hysteretic response of the shear force vs. drift ratio

(a) The north tower leg (b) The south tower leg

The stress versus strain hysteretic response of the reinforcement in the southwest RC pier is plotted in Figure 7.29. From Figure 7.29, it can be seen that the reinforcing steel experiencing yielding and the maximum strain reaches 0.0245. The bending moment versus rotation at the bottom of the southwest RC pier is plotted in Figure

7.30. Figure 7.30 shows that the maximum rotation is 0.03 and the corresponding residual bending moment is 0.17kN.m, which triggers the criterion of the flexure failure. This is why the southwest RC pier is removed from the RC cable-stayed bridge, leading to a partial collapse of the RC bridge structure at 3.113 second of the collapse earthquake excitation.

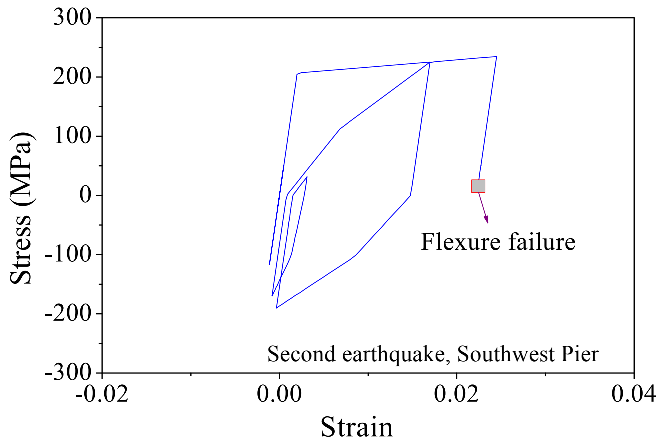

Figure 7.29 Hysteretic response of the stress vs. strain

at the bottom of the north tower leg

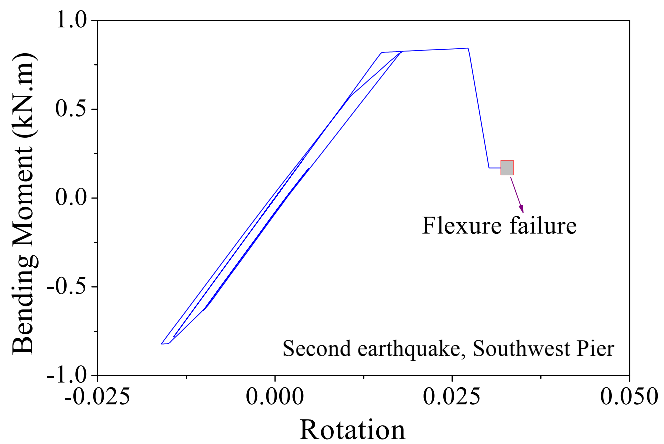

Figure 7.30 Hysteretic response of the bending moment vs. rotation

at the bottom of the southwest pier

7.7 Summary

The SHM-based seismic collapse prognosis method has been proposed in this chapter and applied to the RC bridge tested in Chapter 4. Since the seismic collapse prognosis of a structure will be carried out based on the current damage conditions of the structure, the SHM-based nonlinear model updating is necessary to find out the current damage conditions of the structure. In this regard, the 58 key parameters of the RC bridge were updated by considering the bridge subject to the latest earthquake ground motion and using the nonlinear model updating method proposed in Chapter 6. The results showed that the values of the most updated parameters of the bridge under the latest large earthquake excitation became much smaller compared with those identified in Chapter 6 for the bridge subject to a moderate earthquake excitation. The values/thresholds of the failure criteria of the four zero-length failure elements of the RC bridge were also determined based on the current damaged conditions and compared with those from the undamaged conditions. The comparative results showed that the values/thresholds of the failure criteria of the four zero-length failure elements of the RC bridge determined based on the current damaged conditions are very different from those based on the undamaged conditions. The collapse prognosis of the RC bridge subject to two future earthquake ground excitations were finally performed base on the updated FE model of the bridge to find out which earthquake will cause the true bridge collapse. The computed results showed that the RC bridge did not collapse when it was subjected to the first future earthquake excitation of relatively small intensity. The computed results showed that when the bridge was subjected to the second earthquake excitation of relatively large intensity, the RC southwest pier, as one of the failure-vulnerable component, triggered the flexure failure at 3.133 second of the earthquake excitation and it was separated from the RC bridge structure. The other three failure-vulnerable components experienced severe damage but did not failed. A series of computed seismic responses such as acceleration, strain and reaction force of the RC bridge subject to the second earthquake excitation were compared with the shake table test results recorded by the SHM system installed on the bridge. The comparison results showed that the computed results and collapse process are compatible with the test results recorded by the SHM system. The SHM-based collapse prognosis proposed in this chapter is feasible and effective.

Clearly, the SHM system plays an important role in the seismic collapse analysis and prognosis of the RC bridge subject to earthquake excitations. The next chapter will discuss how to establish a SHM system for the prototype RC cable-stayed bridge for the collapse prognosis and how to apply the SHM-based collapse analysis method to the prototype RC cable-stayed bridge for collapse prognosis.

CHAPTER 8

SHM-BASED SEISMIC COLLAPSE PROGNOSIS OF A RC CABLE-STAYED BRIDGE

8.1 Introduction

Prognosis is an advanced technique for assessing future behavior of a structure based on an accurate calibration of present conditions of the structure. Three factors are critical to make accurate prognosis for a structure: (1) a set of SHM system including appropriate sensor number and sensor placement; (2) a reliable and accurate method for calibration of current conditions of the structure; (3) a series of evolution rules for materials and computational capacity of large deformation of structure. An accurate prognosis of a structure is very important for authorities to know the performance of the structure timely for maintenance or make decision to deal with any accidental damage. The current seismic collapse analysis of an RC bridge is a direct analysis process that begins from intact condition of the bridge to collapse, which is applicable for the bridge at design stage. That is to say, the current collapse analysis based on an ideal condition of the bridge, which cannot reflect the real conditions of the bridge, is incapable of making prognosis for the bridge. The current SHM systems installed on important bridges are mainly used to monitor the linear performance of the bridge under specific service loadings. However, these systems provide insufficient information for predicting the collapse of bridges subject to future earthquakes.

Therefore, an SHM system for the collapse prognosis of bridges subject to earthquakes is essential to be proposed. A numerical study on the seismic collapse of the 1:12 scaled RC cable-stayed bridge has been presented in Chapter 7. However, the FE model of the scaled bridge cannot replace that of the prototype bridge for seismic collapse analysis because the similarity laws of the scaled bridge cannot fully satisfied. Therefore, a collapse analysis of the prototype bridge is essential to be performed. In this regards, an SHM-based seismic collapse prognosis method that considers the present damage conditions of the RC bridge need to be proposed. The damage conditions of the bridge can be determined by using the nonlinear model updating method presented in Chapter 6 as well as by virtue of the information acquired from the SHM systems installed on the bridge.

In this chapter, a three dimensional FE model of the prototype RC stay-cable bridge is firstly established for the SHM system design and the seismic collapse prognosis. Then, two set of SHM systems are designed according to two different methods, respectively. Finally, the current seismic collapse method is used to perform the collapse analysis of the prototype bridge. The proposed collapse prognosis method is subsequently demonstrated based on the prototype bridge with specified damage.

8.2 FE Model of the Prototype Bridge for SHM System Design and Collapse Analysis

The detailed as-built drawing information of the prototype RC cable-stayed bridge is described in Chapter 4. An FE model of the bridge is established to facilitate the sensor placement either for the existing SHM system to assess the linear performance of the bridge under specific service loadings or for the proposed SHM system to predict the collapse of the bridge under future seismic loadings. Similar to the FE model of the scaled bridge applied in Chapter 5, two RC tower legs, two girders, nine transverse beams, and four side piers of the prototype cable-stayed bridge are all modeled by the nonlinear beam-column fiber element in OpenSees (McKenna et al. 2007), whereas the stay cables are modeled by the tension-only truss element. The connection conditions of the bearings at the top of the four side piers are identical to those in the FE model of the scaled bridge in Chapter 5. The pile foundations, which are applied to the tower and side piers of the prototype bridge, are assumed rigid. Therefore, the tower and piers are fixed at their bottoms. For the prototype RC cable-stayed bridge, the potential failure-vulnerable components and their failure modes can be predicted by referring to the provisions presented in Chapter 3. The prediction results show that the two RC piers at the south side of the bridge will suffer from flexure failure at their bottoms and that the tower legs beneath the girder will suffer from flexure-shear-axial failure during an earthquake. Therefore, two zero-length elements are inserted into the bottom of each south side pier to detect their potential flexure failure, and another two zero-length elements are inserted into the section of each tower leg beneath the tower-girder joint to detect their flexure-shear-axial failure (see Figure 8.1). The two nodes of the zero-length elements i and j have identical coordinates. The earthquake excitations in this study are only inputted along the transverse direction (Z axis). The zero-length elements that link

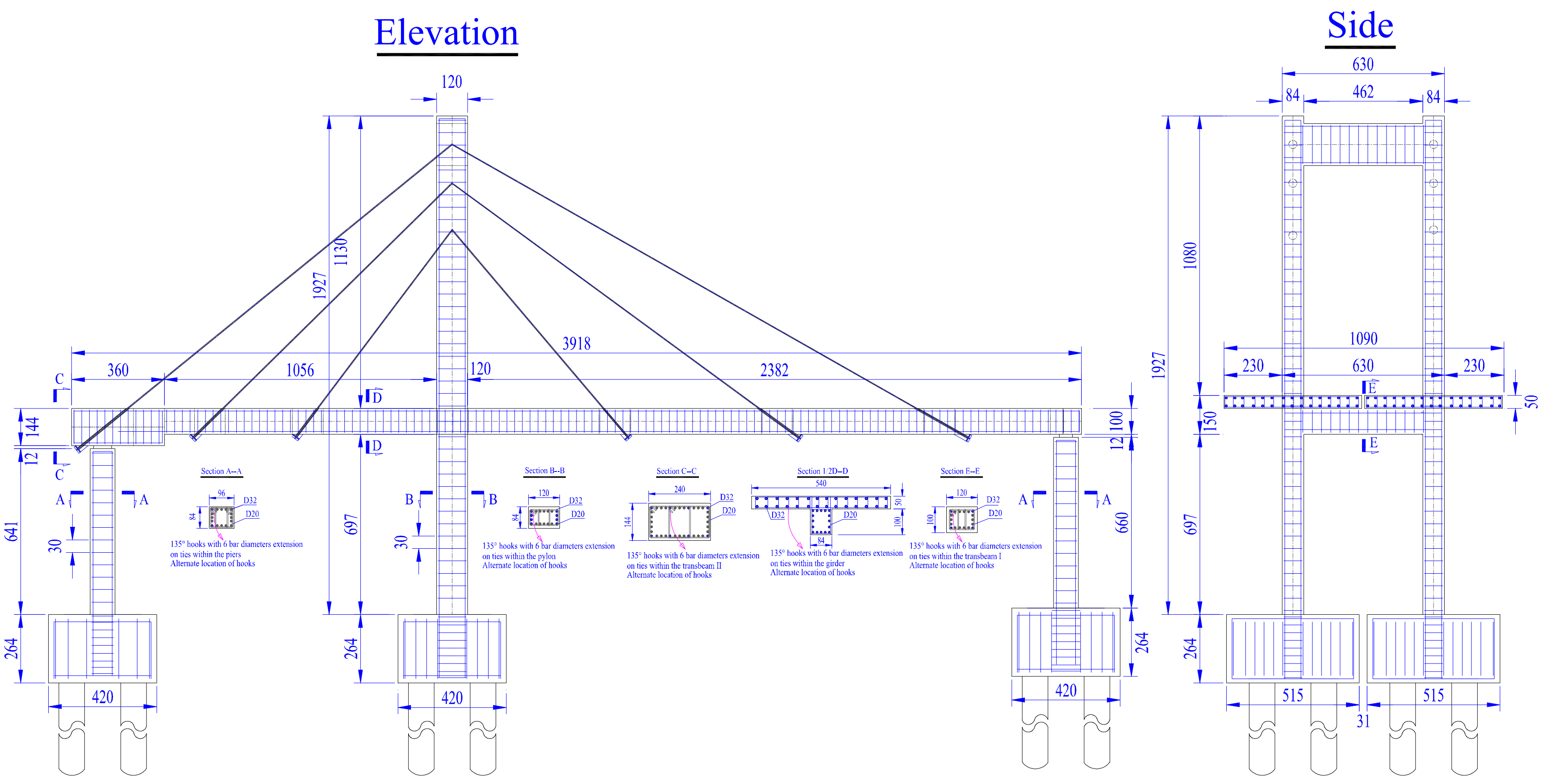

Figure 8.1 3-D nonlinear FE model for seismic collapse prognosis (unit: cm)

nodes *i* and *j* include the three DOFs that correspond to Y, Z, and ROTX. The other three DOFs (i.e., X, ROTY, and ROTZ) between nodes *i* and *j* are connected by rigid zero-length springs. A 3-D nonlinear FE model with 72 nonlinear fiber beam-column elements, 12 truss elements, and 4 zero-length failure elements is eventually established as shown in Figure 8.1.

8.3 SHM System Design

8.3.1 SHM system design for assessing linear performance of bridge

The number of sensors and their placement must be determined when designing an SHM system for a bridge structure. An effective independence (EFI) method that considered the contribution of each sensor location to the linear independence of the identified modes to optimize the placement of sensors was proposed by Kammer (1991). The EFI method to consider the effects of measurement noise and proposed a pre-determined level of signal-to-noise ratio that was described in the modal coordinates to determine the number of sensors was further developed by Kammer (1992). However, the EFI method can only be applied for the placement of only one type of sensor, which is difficult to accomplish in large-scale civil structures. Zhang (2012) addressed such limitation by proposing a method for the placement of multi-type sensors on civil structures. The locations of these sensors are selected in such a way that the measured data from these locations can be fused together for the best possible reconstruction of the key structural responses for multi-scale structural monitoring. The Kalman filter algorithm is utilized to construct the optimization objective function, and a constraint function is provided to determine the number of sensors. The reconstruction method for sensor placement aims to match the summation of standard deviation between the calculated values and measured ones at the sensor placement of the bridge that is subjected to an earthquake. Therefore, the multi-type sensor placement method (Zhang 2012) is used in this paper. The Kobe earthquake ground motion (see Figure 8.2) with a peak ground acceleration (PGA) of 0.834 g is used as the seismic loading input for the response reconstruction of the bridge. The earthquake has a sample frequency of 50Hz. The measured data for response reconstruction are assumed as noise-free responses that are added by normally distributed random noises. The noise and noise-free responses have a standard deviation of 0.05. A total of 16 strain gauges (s1 to s16) and 12 accelerometers (A1 to A12) are eventually selected for the SHM system as shown in Figure 8.3. Figure 8.3 shows three accelerometers (A5, A7, and A8) and six strain gauges (s1 to s3 and s5 to s7) installed on the tower legs, four accelerometers (A1, A4, A9, and A10) and one strain gauge (s4) that are installed on the girders, two accelerometers (A2 and A3), and three strain gauges (s11 to s13) installed on the transverse beams, two accelerometers (A11 and A12) and two strain gauges (s8 and s9) that are installed on the west piers, and three strain gauges (s14 to s16) that are mounted on three stay cables.

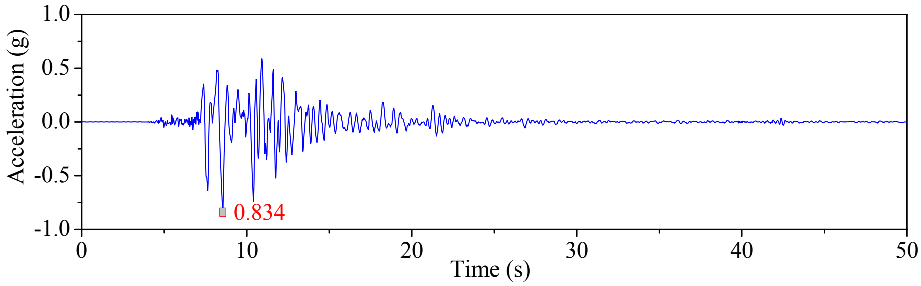

Figure 8.2 History of the Kobe earthquake ground motion with a PGA of 0.834 g

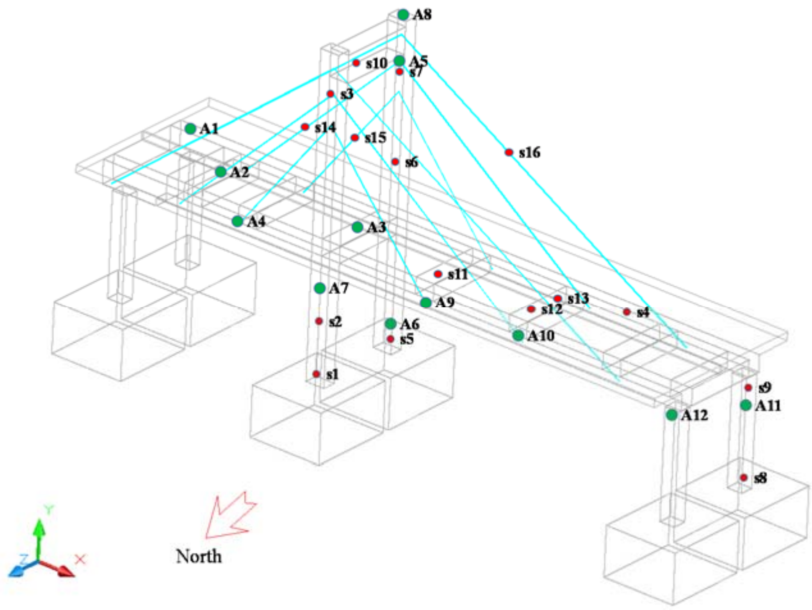

Figure 8.3 Key sensor locations as proposed by the multi-sensor placement method (Zhang 2012)

8.3.2 SHM system design for seismic collapse prognosis of bridge

The earthquake is assumed to excite in the transverse direction of the bridge for the collapse prognosis. The earthquake excitations on the bridge foundations must be recorded to facilitate a seismic collapse prognosis. Therefore, A1 to A6 are installed on the six foundations of the two east side piers, and two tower legs and two side west piers are used to record the earthquake excitations that will be used as the input earthquake loadings for the collapse analysis. A nonlinear seismic analysis need to be conducted before the collapse analysis is performed to facilitate the sensor placement. The Kobe earthquake ground motion in Figure 8.2 is used as the seismic loading for the nonlinear seismic analysis. Accelerators are installed on the top of the east pier (A7), tower (A10), and west pier (A8) to record the global information of the bridge.

An accelerometer is also installed on the joint of the tower and the south girder (A9) to verify the feasibility and accuracy of the proposed collapse prognosis method. Local damage detection must also be performed because a bridge structure begins to collapse when one or some of its failure-vulnerable components suffers from local damages, which eventually spread into the other failure-vulnerable components. As mentioned in Chapter 3, the failure-vulnerable components of the bridge and their corresponding failure modes can be predicted. The southeast pier, the lower parts of the two tower legs beneath the girder, and the southwest pier are identified as the four failure-vulnerable components. The failure mode of the two side piers is flexure failure, while that of the two tower legs is flexure-shear-axial failure. Therefore, the two ends of the reinforcement in each plastic hinge of the failure-vulnerable components are selected as sensor locations for the strain gauge to monitor the local seismic strain response information that will be used for predicting the collapse of the bridge. As shown in Figure 8.4, 24 strain gauges are attached to the reinforcement in the six plastic hinges of the four failure-vulnerable components. These gauges may be damaged during earthquakes, especially when the bridge nearly collapses. When some strain gauges are damaged during the earthquake, the other gauges can be used to record the seismic responses.

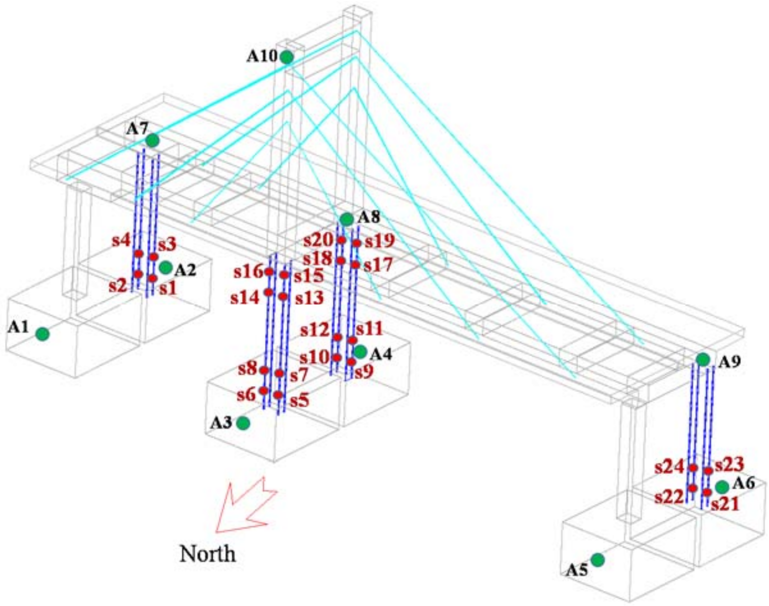

Figure 8.4 Key sensor locations for collapse prognosis

8.3.3 Comparison of two sets of SHM systems

Two sets of SHM systems with different purposes have been established. The SHM system that applies the multi-sensor placement method (Zhang 2012) includes 16 strain gauges and 12 accelerometers. The reconstruction response method for sensor placement aims to determine those locations with relatively large acceleration or strain responses during the linear stage. Six accelerometers and seven strain gauges are mounted on the girder and the stay cable although they always perform in linear and elastic states. However, the proposed SHM system of the bridge includes 24 strain gauges and 10 accelerometers and most sensors in the SHM system are mounted on the failure-vulnerable components, except for six accelerometers that are respectively installed on the six foundations to record the external seismic loadings. The proposed SHM system aims to predict the collapse of the RC bridge subjected to earthquakes. If the sensors in these two separate SHM systems can complement each other and be appropriately integrated, a new and highly effective SHM system not only for assessing the linear performance of the bridge under specific service loadings but also for predicting the collapse of the bridge under severe seismic loadings can be established.

8.4 SHM-Based Seismic Collapse Prognosis

8.4.1 Material properties of the damaged RC bridge

An RC bridge tends to be damaged during its service time, thereby rendering its material properties non-linear and inelastic. In this study, the prototype RC bridge is damaged by a Kobe earthquake with a PGA of 1.360 g as shown in Figure 8.5. The seismic responses of stress versus strain of the unconfined concrete at the plastic hinge of the southwest pier are plotted in Figures 8.6 (a) and (b), respectively. Figure 8.6 (a) shows that the compressive strength of the unconfined concrete has decreased from 36.7MPa to 23.7MPa after the earthquake. Figure 8.6 (b) shows that the reinforcement yielded and maximum strain have reached approximately 0.01.

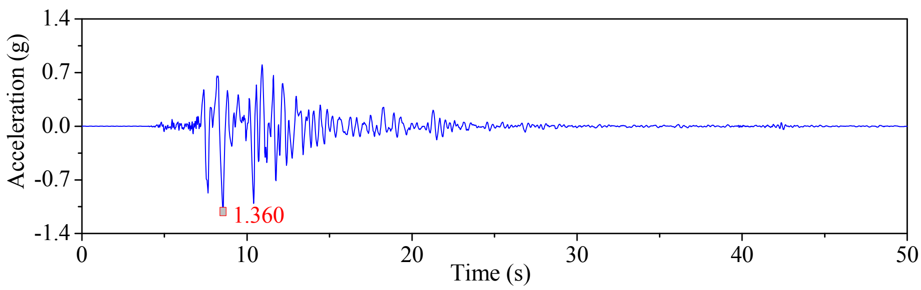

Figure 8.5 History of the Kobe earthquake excitation with a PGA of 1.360g

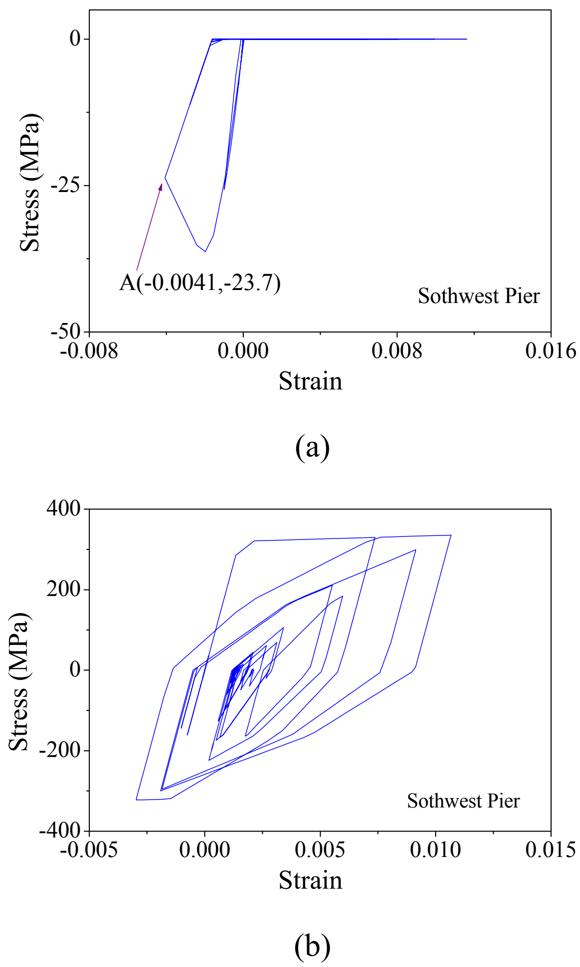

Figure 8.6 Hysteretic response of stress versus strain

(a) Unconfined concrete (b) Reinforcement

The damaged conditions of the RC bridge are not considered in the current numerical collapse analysis. However, the SHM-based collapse prognosis method proposed in this chapter can be applied to address this issue. The proposed nonlinear model in Chapter 6 can be applied to update the key parameters of the damaged materials and to provide an accurate FE model for further collapse prognosis. To update the key parameters of the materials conveniently, the fiber elements are classified into five groups: (1) all fiber elements in the transverse beams, twin-girder, and north side piers, (2) the failure-vulnerable fiber elements in the two tower legs, (3) the failure-vulnerable fiber elements in the southeast pier, (4) the failure-vulnerable fiber elements in the southwest pier, and (5) all other fiber elements in the tower legs and the southwest and southeast piers except for their failure-vulnerable elements. The fiber elements in the first group are in linear states, and their key parameters are presented in Section 8.6.1. Fourteen key parameters must be updated for each of the four groups of nonlinear fiber elements, of which six parameters are for reinforcement, four parameters are for the confined concrete, and four parameters are for the unconfined concrete. As aforementioned, a specified Kobe earthquake with a PGA of 1.36g is employed to get a damaged state of the bridge to demonstrate the SHM-based collapse prognosis of the bridge. The seismic responses of the materials of each group of the bridge at the end of the earthquake are assumed as the updated results of the materials. Then, the updated results of the 56 key parameters for the envelop curves of the materials of the earthquake-damaged RC bridge are tabulated in Table 8.1, in which A, A1, B1, and C1 represent the key points on the envelop curves shown in Figures 8.7 (a) and (b). Table 8.2 lists the updated two Rayleigh damping coefficients. In Figures 8.7 (a) and (b), the envelop curves OAB1C1 and D’C’B’A’OABC D of the unconfined concrete and reinforcement of the intact southwest pier are determined following the specifications or the design codes. The envelop curves O’A1B1C1 and D”C”B”A”OA1B1C1D1 of the unconfined concrete and reinforcement of the damaged southwest pier are determined through the nonlinear model updating. The envelop curves of the unconfined concrete and the reinforcement in the undamaged southwest pier were significantly different from those of the earthquake-damaged southwest pier. These envelop curves also evolved clearly. The maximum compressive strength of the unconfined concrete sharply decreased from 36.7MPa to 23.7MPa. The yielding strength of the reinforcement increased from 320.0MPa to 335.6MPa, whereas the corresponding modulus of the reinforcement slightly decreased from 2.13×10^5MPa to 2.11×10^5MPa. Interestingly, Table 8.6 shows that the updated Rayleigh damping coefficients for the damaged bridge are larger than those for the undamaged bridge.

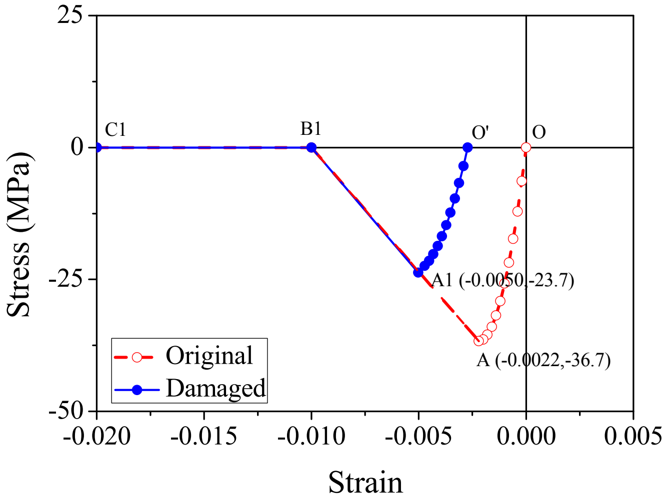

(a)

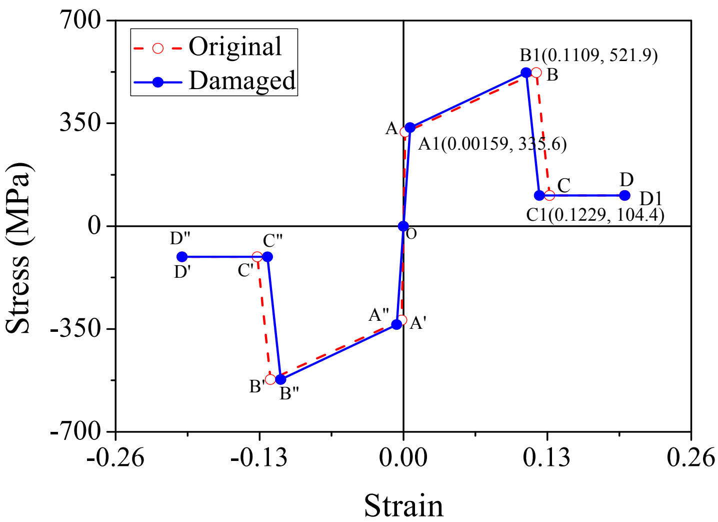

(b)

Figure 8.7 Envelop curves of materials (a) Unconfined concrete (b) Reinforcement.

Table 8.1 Original key parameters of materials

Parameter No.	Description	A1	B1	C1
1–2	Confined concrete compressive stress of the slightly damaged tower and pier (MPa)	-36.5	-3.7	
3–4	Confined concrete compressive strain of the slightly damaged tower and pier	-0.0022	-0.0100	
5–6	Cover concrete compressive stress of the slightly damaged tower and pier (MPa)	-33.0	0.0	
7–8	Cover concrete compressive strain of the slightly damaged tower and pier	-0.0024	-0.0075	
9–0	Confined concrete compressive stress of the southeast damaged pier (MPa)	-35.6	-3.6	
11–12	Confined concrete compressive strain of the southeast damaged pier	-0.0022	-0.0100	
1–14	Cover concrete compressive stress of the southeast damaged pier (MPa)	-21.5	0.0	
15–16	Cover concrete compressive strain of the southeast damaged pier	-0.0028	-0.0075	
17–18	Confined concrete compressive stress of the damaged tower (MPa)	-35.5	-3.6	
19–20	Confined concrete compressive strain of the damaged tower	-0.0022	-0.0100	
21–22	Cover concrete compressive stress of the damaged tower (MPa)	-31.2	0.0	
23–24	Cover concrete compressive strain of the damaged tower	-0.0024	-0.0075	
25–26	Confined concrete compressive stress of the southwest damaged pier (MPa)	-36.5	-3.7	
27–28	Confined concrete compressive strain of the southwest damaged pier	-0.0022	-0.0100	
29–30	Cover concrete compressive stress of the southwest damaged pier (MPa)	-23.7	0.0	
31–32	Cover concrete compressive strain of the southwest damaged pier	-0.0026	-0.0075	
33–35	Yielding stress of the reinforcement in the slightly damaged tower and pier (MPa)	320.3	521.9	104.4
36–38	Yielding strain of the reinforcement in the slightly damaged tower and pier	0.00151	0.1198	0.1318
39–41	Yielding stress of the reinforcement in the damaged southeast pier (MPa)	338.3	521.9	104.4
42–44	Yielding strain of the reinforcement in the damaged southeast pier	0.00159	0.1094	0.1214
45–47	Yielding stress of the reinforcement in the damaged tower (MPa)	334.5	521.9	104.4
48–50	Yielding strain of the reinforcement in the damaged tower	0.00159	0.1116	0.1236
51–53	Yielding stress of the reinforcement in the damaged southwest pier (MPa)	335.6	521.9	104.4
54–56	Yielding strain of the reinforcement in the damaged southwest pier	0.00159	0.1109	0.1229

Table 8. 2 Updated key parameters

Parameter No.	Description	Nonlinear model updating
57	Rayleigh damping coefficient of mass	0.3926 (s/rad)
58	Rayleigh damping coefficient of stiffness	0.0067 (s/rad)

8.4.2 Failure criteria and thresholds

Table 8.3 presents that the flexure failure criteria of the southeast and southwest RC piers without damage are 0.0362rad and 0.0375rad for rotation and 377.0kN.m and 384.2kN.m for bending moment. The thresholds of the failure criteria are determined by Eqs. (3.3) and (3.4) and the results are listed in Table 8.3. Δ_s / L and Δ_a / L

indicate the thresholds of drift ratio that trigger the flexure-shear and flexure-shear-axial failures, respectively. Obviously, the failure criteria or thresholds for the damaged bridge are smaller than those for the intact bridge.

Table 8.3 Failure modes with their failure criteria and thresholds

Location	Failure Mode	Failure Criteria		Failure Threshold	
		Rotation	Bending Moment	Δ_s / L	Δ_a / L
Southeast Pier	Flexure Failure	0.0362 rad	377.0kN.m		
Southwest Pier	Flexure Failure	0.0375 rad	384.2kN.m		
South Tower Leg	Flexure-Shear-Axial Failure			0.0320	0.0475
North Tower Leg	Flexure-Shear-Axial Failure			0.0320	0.0475

8.4.3 Collapse prognosis of the entire bridge

To conduct a seismic collapse prognosis of the damaged RC cable-stayed bridge, the Kobe earthquake excitation with an adjusted PGA of 0.56 g is selected as the input seismic loading as shown in Figure 8.8. The earthquake excitation has a sample frequency of 34Hz. The collapse prognosis of the RC bridge subject to the Kobe earthquake excitation is then performed based on the updated FE model of the damaged bridge.

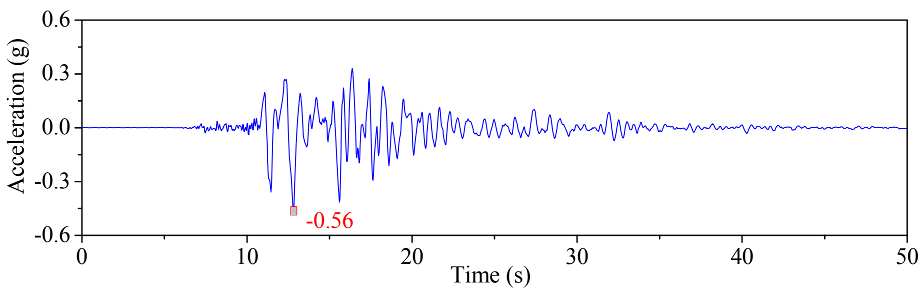

Figure 8. 8 History of the Kobe earthquake excitation with a PGA of 0.56 g

8.4.3.1 Collapse process

The collapse analysis results for the RC cable-stayed bridge are tabulated in Table 8.4

and shown in Figures 8.9 (a), (b), and (c). Figure 8.9 (a) shows that the maximum camber of the girder is located 1.96 cm near the middle main span of the intact bridge after its construction. Figure 8.9 (b) shows that the flexure-shear failure at each RC tower leg beneath the girder is initially detected at 12.96 seconds. Both tower legs beneath the girders partially failed because of the flexure-shear failure that was detected at 13.05 seconds, during which the maximum deformation of the two tower legs in the transverse direction exceeded 0.4m. Therefore, the shear DOF of both tower legs were released at 13.05 seconds following the provisions of the refined seismic collapse analysis method proposed in Chapter 3. Figure 8.9 (c) shows that the southwest pier has failed because of the excessive rotation of 0.0439rad, thereby triggering flexure failure (0.0375rad). Therefore, the southwest RC pier was removed from the RC cable-stayed bridge, which led to a partial collapse at 13.08 seconds following the earthquake excitation.

Table 8.4 Seismic collapse process

Time	Failure condition	Rotation (rad)	Drift ratio	Failure location
12.96 s	Detect flexure-shear failure		0.0341	North tower leg
12.96 s	Detect flexure-shear failure		0.0345	South tower leg
13.05 s	Flexure-shear failure		0.0380	North tower leg
13.05 s	Flexure-shear failure		0.0384	South tower leg
13.08 s	Flexure failure	0.0439		Southwest pier

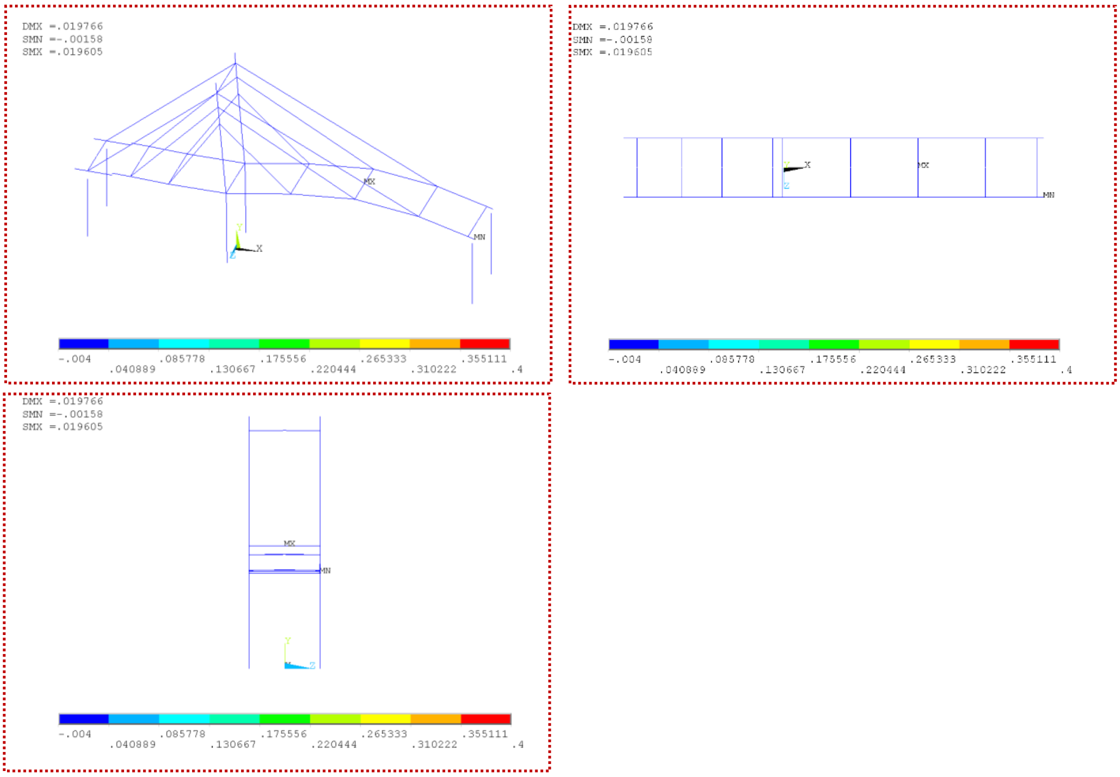
DMX =.019766
SMN =-.00158
SMX =.019605
MX
MN
-.004 .040889 .085778 .130667 .175556 .220444 .265333 .310222 .355111 .4
DMX =.019766
SMN =-.00158
SMX =.019605
MX
MN
-.004 .040889 .085778 .130667 .175556 .220444 .265333 .310222 .355111 .4
DMX =.019766
SMN =-.00158
SMX =.019605
MX
MN
-.004 .040889 .085778 .130667 .175556 .220444 .265333 .310222 .355111 .4

(a)

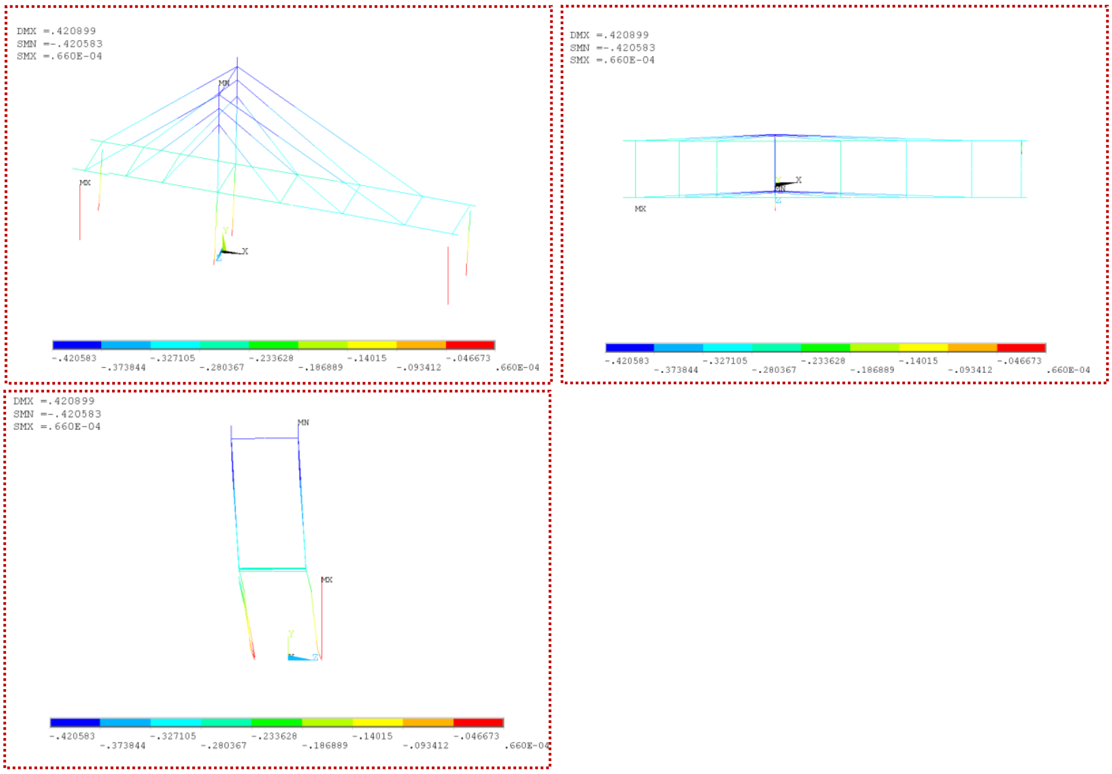
DMX =.420899
SMN =-.420583
SMX =.660E-04
MX
MN
-.420583 -.373844 -.327105 -.280367 -.233628 -.186889 -.14015 -.093412 -.046673 .660E-04
DMX =.420899
SMN =-.420583
SMX =.660E-04
MX
-.420583 -.373844 -.327105 -.280367 -.233628 -.186889 -.14015 -.093412 -.046673 .660E-04
DMX =.420899
SMN =-.420583
SMX =.660E-04
MN
MX
-.420583 -.373844 -.327105 -.280367 -.233628 -.186889 -.14015 -.093412 -.046673 .660E-04

(b)

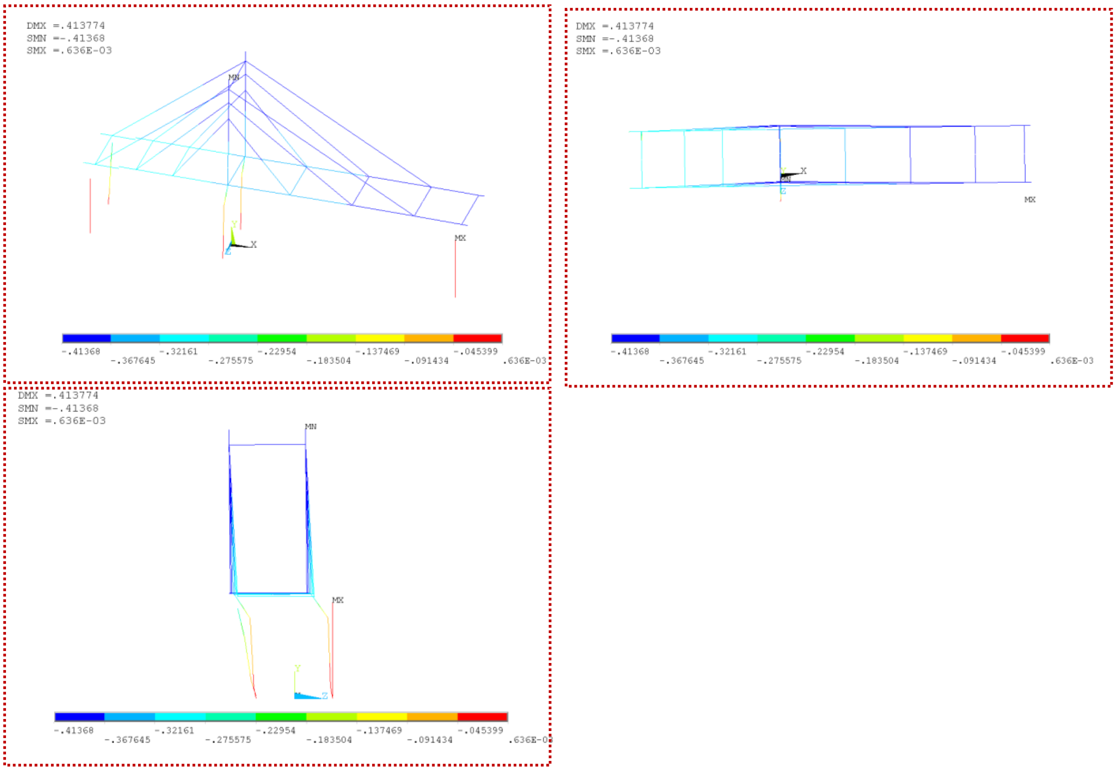

(c)

Figure 8.9 Seismic collapse process of the RC cable-stayed bridge

(b) Before the earthquake (b) Flexure-shear damage of the tower

(c) Flexure damage of the southwest pier

8.4.3.2 Responses of the zero-length failure elements

The seismic responses of bending moment versus the rotation of the southeast and southwest piers are plotted in Figures 8.10 (a) and (b), respectively. Figure 8.10 (a) shows that the peak rotation response of the southwest pier reaches 0.0281rad, which is much smaller than the corresponding failure criterion of 0.0418rad. Therefore, the southwest pier can sustain seismic loading despite accumulating severe damage. Figure 8.10 (b) shows that the resistant capacity of the bending moment decreases sharply when the rotation of the southwest pier reaches 0.0358rad. The southeast piers failed after the rotation increased to 0.0439rad and the bending moment remained

364.0kN.m, thereby triggering flexure failure (0.0375rad).

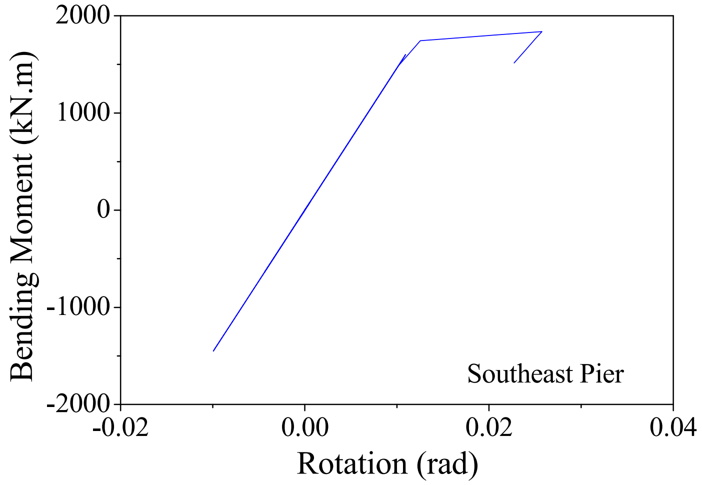

(a)

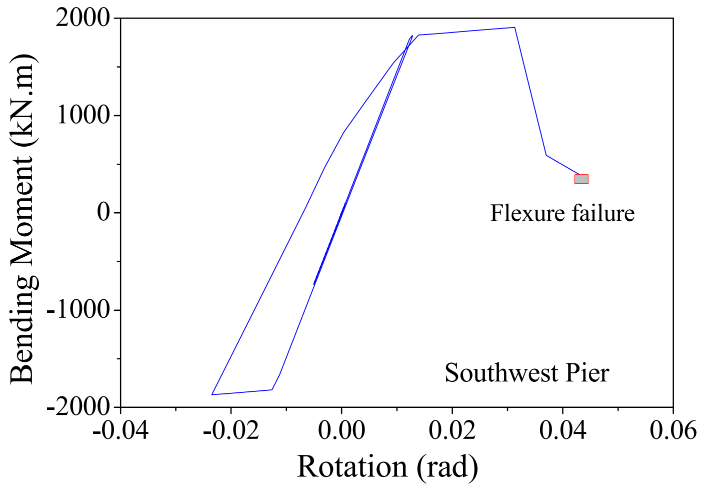

(b)

Figure 8.10 Rotation versus moment hysteretic curves

(a) Southeast pier (b) Southwest pier

The shear force and drift ratio relationships of the zero-length failure elements attached to the north and the south tower legs beneath the girders are plotted in Figures 8.11 (a) and (b), respectively. The peak drift ratios of the north and south tower legs were 0.0380 and 0.0384, respectively, both of which are larger than the threshold flexure-shear failure (0.032) and smaller than the threshold of the flexure-shear-axial failure (0.0475), respectively.

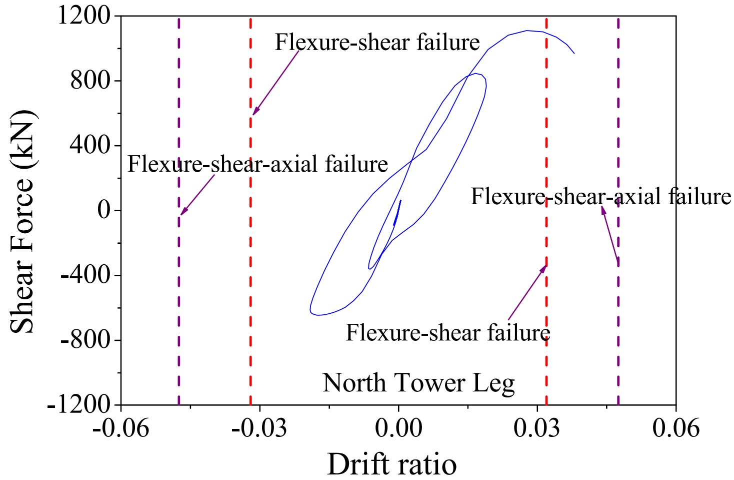

(a)

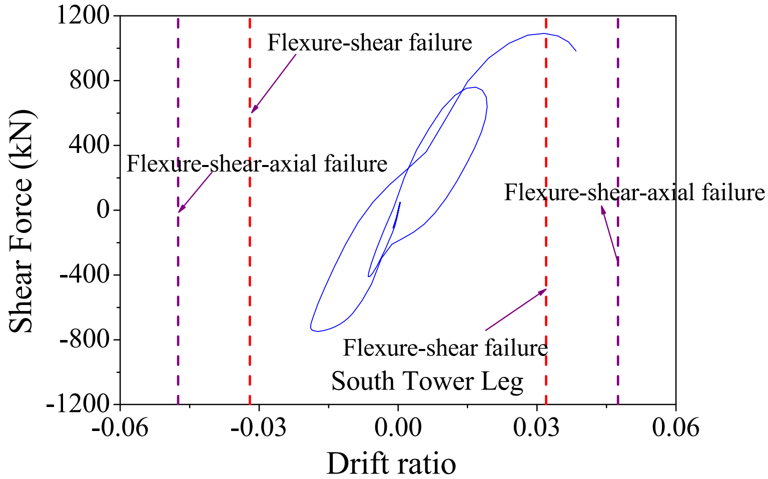

(b)

Figure 8.11 Hysteretic response of shear force versus drift ratio

(b) North tower leg (b) South tower leg

The hysteretic responses of stress versus strain of the reinforcement in the southeast and southwest piers are plotted in Figures 8.12 (a) and (b), respectively. The reinforcing steel in the southeast and southwest piers experienced yielding and maximum strain that reached 0.0043 and 0.0034, respectively.

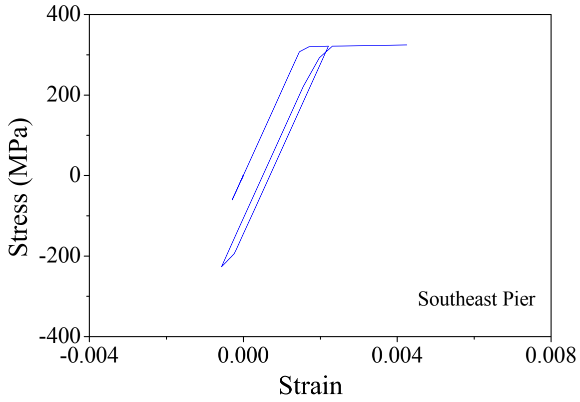

(a)

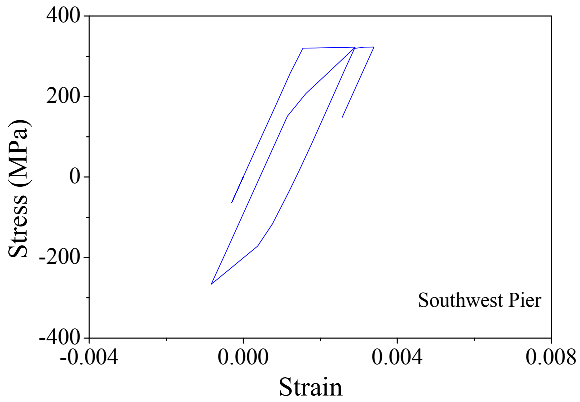

(b)

Figure 8.12 Hysteretic response of stress versus strain

(a) Southeast pier (b) Southwest pier

8.5 Current Method for Seismic Collapse Analysis

8.5.1 Material properties of an intact RC bridge

The current seismic collapse analysis method for an RC bridge begins from the intact structure of the bridge to collapse, which is applicable for the bridge at design stage. The material properties of concrete and reinforcement refer to the as-built drawing information of the bridge or the specifications of related design codes. All the concrete and reinforcement properties of different components of the bridge are identical and are tabulated in Table 8.5. The envelop curves of the unconfined concrete and the reinforcement of the intact RC bridge are graphed in Figures 8.13(a) and 8.13(b), respectively. The original values of key points A1 and B1 of the concrete and the original values of key points A1, B1, and C1 of the reinforcement in their envelop curves are presented in Table 8.5. The Rayleigh damping coefficients are tabulated in Table 8.6 to form the damping matrix for the collapse analysis of the intact bridge.

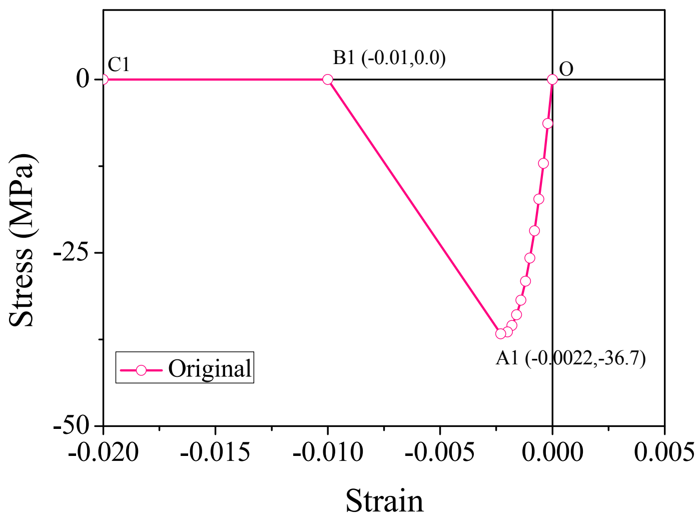

(a)

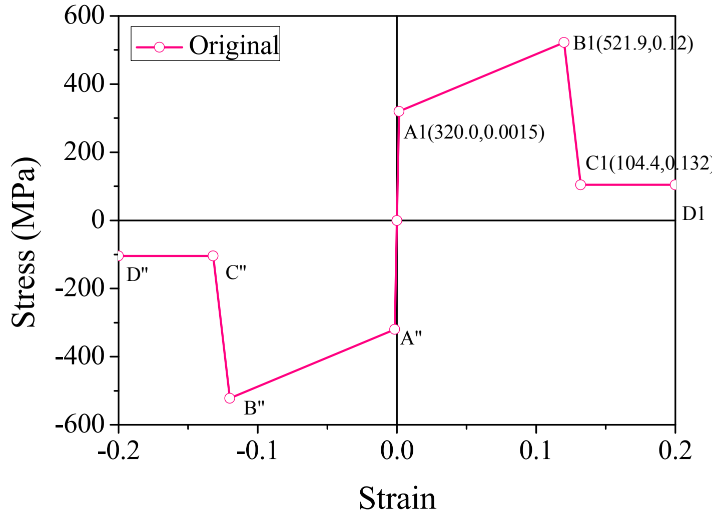

(b)

Figure 8.13 Envelop curves of materials (a) Unconfined concrete (b) Reinforcement

Table 8.5 Original key parameters of materials

Parameter No.	Description	A1	B1	C1
1–2	Confined concrete compressive stress of the intact tower, girder, and pier (MPa)	-36.9	-3.7	
3–4	Confined concrete compressive strain of the intact tower, girder, and pier	-0.0022	-0.0100	
5–6	Cover concrete compressive stress of the intact tower, girder, and pier (MPa)	-36.7	0.0	
7–8	Cover concrete compressive strain of the intact tower, girder, and pier	-0.0022	-0.0075	
9–11	Yielding stress of the reinforcement in the intact tower, girder, and pier (MPa)	320.0	521.9	104.4
12–14	Yielding strain of the reinforcement in the intact tower, girder, and pier	0.0015	0.1200	0.1320

Table 8.6 Original damping coefficients

Parameter No.	Description	Original value
15	Rayleigh damping coefficient of mass	0.3795 (s/rad)
16	Rayleigh damping coefficient of stiffness	0.0065 (s/rad)

8.5.2 Failure criteria and thresholds

The failure criteria for the failure elements are closely related to the current behavior of the failure-vulnerable components. The southeast and southwest RC piers demonstrate the flexure failure mode, and their failure criteria can be determined through a standard section analysis by virtue of OpenSees (McKenna et al. 2007). Table 8.7 presents that the criteria for the flexure failure of the southeast and southwest RC piers without damage are 0.0426rad and 0.0487rad for rotation and 413.4kN.m and 415.6kN.m for the bending moment. The two RC tower legs experience flexure-shear-axial modes according to the key parameters of the materials. The thresholds of the failure criteria are determined by Eqs. (3.3) and (3.4), and the results are listed in Table 8.7. Δ_s / L and Δ_a / L in Table 8.3 indicate the thresholds of drift ratio that trigger the flexure-shear and flexure-shear-axial failures, respectively. The collapse prognosis can be conducted after determining the failure criteria for the four failure elements.

Table 8.7 Failure modes with their failure criteria and thresholds

Location	Failure Mode	Failure Criteria		Failure Threshold	
		Rotation	Bending Moment	Δ_s / L	Δ_a / L
Southeast Pier	Flexure Failure	0.0426rad	413.4kN.m		
Southwest Pier	Flexure Failure	0.0487rad	415.6kN.m		
South Tower Leg	Flexure-Shear-Axial Failure			0.033	0.048
North Tower Leg	Flexure-Shear-Axial Failure			0.033	0.048

8.5.3 Collapse analysis of the entire bridge

To conduct a seismic collapse analysis of the intact RC cable-stayed bridge, the Kobe earthquake excitation with an adjusted PGA of 1.408 g is selected as the input seismic loading as shown in Figure 8.14. The earthquake excitation has a sample frequency of 50Hz. The collapse prognosis of the RC bridge subject to the Kobe earthquake excitation is performed based on the nonlinearly original FE model of the intact bridge. The material properties of the FE model refer to the as-built drawing or design codes.

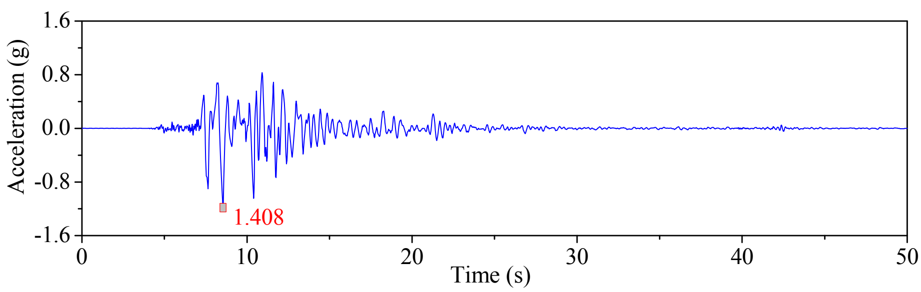

Figure 8.14 History of the Kobe earthquake excitation with a PGA of 1.408g

8.5.3.1 Collapse process

The collapse analysis results for the RC cable-stayed bridge are tabulated in Table 8.8 and demonstrated in Figures 8.15 (a), (b), and (c). Figure 8.15 (a) shows that the maximum camber of the girder is located 1.96 cm near the middle main span of the as-built bridge. Figure 8.15 (b) shows that the flexure-shear failure at each RC tower leg beneath the girder is initially detected at 8.34 seconds. Both tower legs beneath the girders partially failed because of the flexure-shear failure that was detected at 8.38 seconds, and the two tower legs demonstrated a maximum deformation of over 0.4 m in the transverse direction. Therefore, the shear DOF of both tower legs were released at 8.38 seconds following the provisions of the refined seismic collapse analysis method in Chapter 3. Figure 8.15 (c) shows that the southeast pier has failed because of the excessive rotation of 0.044rad, thereby triggering flexure failure (0.0426rad). Therefore, the southeast RC pier was removed from the RC cable-stayed bridge, which led to the partial collapse of the RC bridge at 9.20 seconds after the earthquake excitation.

Table 8.8 Seismic collapse process

Time	Failure condition	Rotation	Drift ratio	Failure location
8.34 s	Detect flexure-shear failure		0.0354	North tower leg
8.34 s	Detect flexure-shear failure		0.0381	South tower leg
8.38 s	Flexure-shear failure		0.0386	North tower leg
8.38 s	Flexure-shear failure		0.0407	South tower leg
9.20 s	Flexure failure	0.0440 rad		Southeast pier

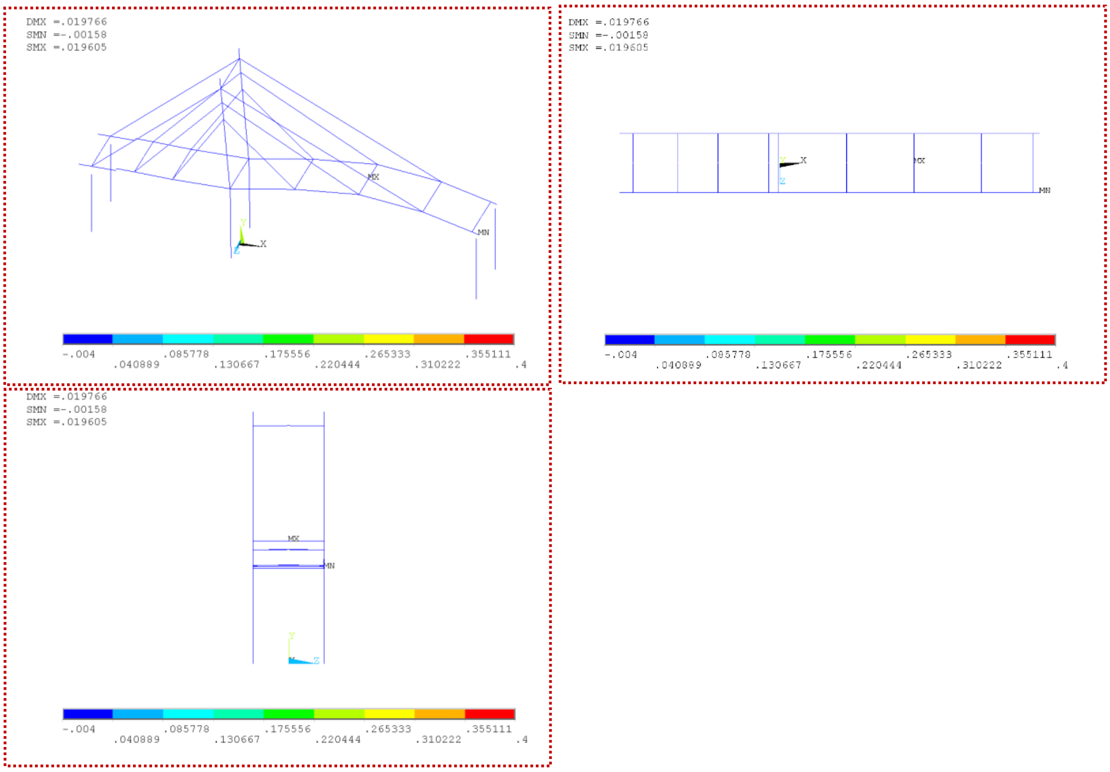
DMX =.019766
SMN =-.00158
SMX =.019605
MX
MN
-.004 .040889 .085778 .130667 .175556 .220444 .265333 .310222 .355111 .4
DMX =.019766
SMN =-.00158
SMX =.019605
MX
MN
-.004 .040889 .085778 .130667 .175556 .220444 .265333 .310222 .355111 .4
DMX =.019766
SMN =-.00158
SMX =.019605
MX
MN
-.004 .040889 .085778 .130667 .175556 .220444 .265333 .310222 .355111 .4

(a)

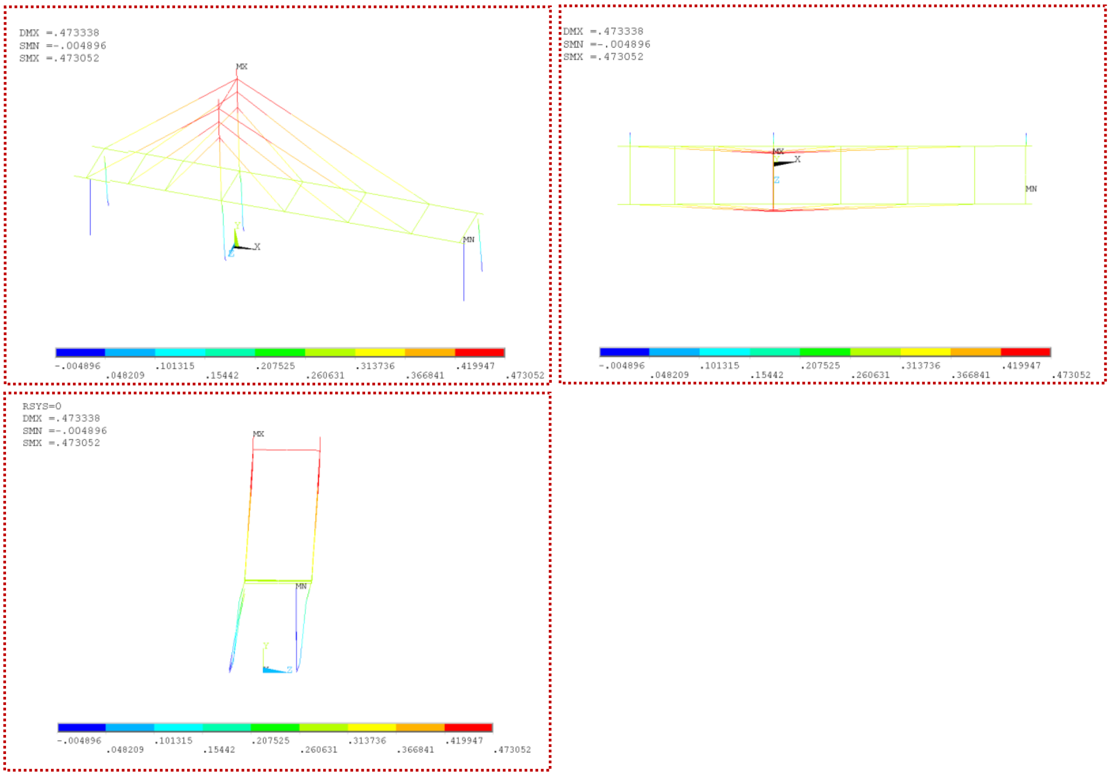
DMX =.473338
SMN =-.004896
SMX =.473052
MX
MN
-.004896 .048209 .101315 .15442 .207525 .260631 .313736 .366841 .419947 .473052
DMX =.473338
SMN =-.004896
SMX =.473052
MX
MN
-.004896 .048209 .101315 .15442 .207525 .260631 .313736 .366841 .419947 .473052
RSYS=0
DMX =.473338
SMN =-.004896
SMX =.473052
MX
MN
-.004896 .048209 .101315 .15442 .207525 .260631 .313736 .366841 .419947 .473052

(b)

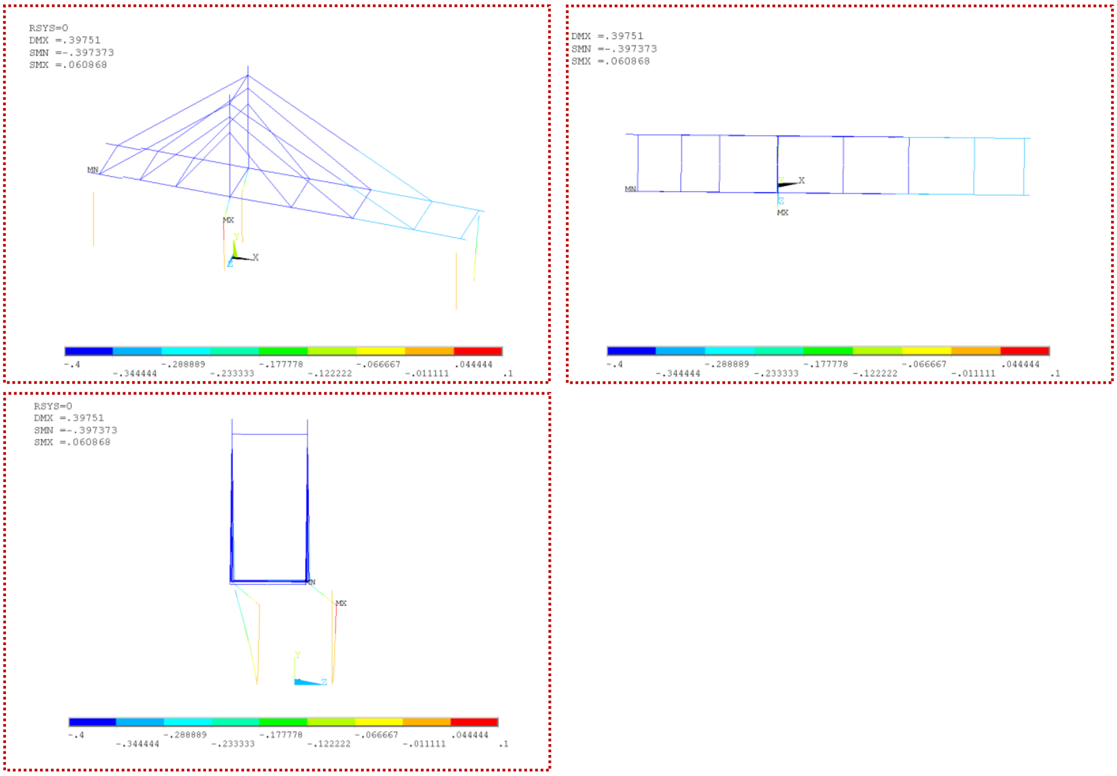

(c)

Figure 8.15 Seismic collapse process of the RC cable-stayed bridge

(a) Before the earthquake (b) Flexure-shear damage of the tower

(c) Flexure damage of the southeast pier

8.5.3.2 Responses of the zero-length failure elements

Four zero-length failure elements are included in the FE model for the collapse prognosis. Investigating the seismic responses of these failure elements can provide an extensive insight into the seismic collapse of a bridge. The seismic responses of bending moment versus the rotation of the southeast and southwest piers are plotted in Figures 8.16 (a) and (b), respectively. Figure 8.16 (a) shows that the resistant capacity of the bending moment decreases sharply when the rotation of the southeast pier reaches 0.0388rad. The southeast piers failed after the rotation exceeded 0.044rad and the bending moment remained at 413.4kN.m, thereby triggering flexure failure

(0.0426rad). Figure 8.16 (b) shows that the peak rotation response of the southwest pier is 0.0386rad, which is much smaller than the corresponding failure criterion of 0.0487rad. Therefore, the southwest pier can continually sustain seismic loadings despite suffering from severe damage.

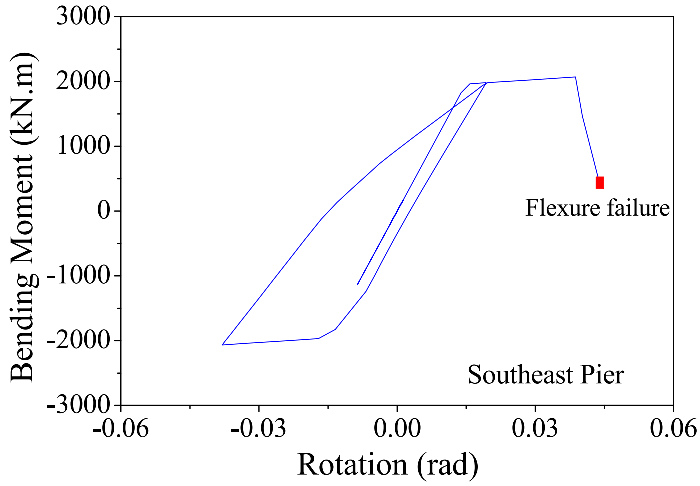

(a)

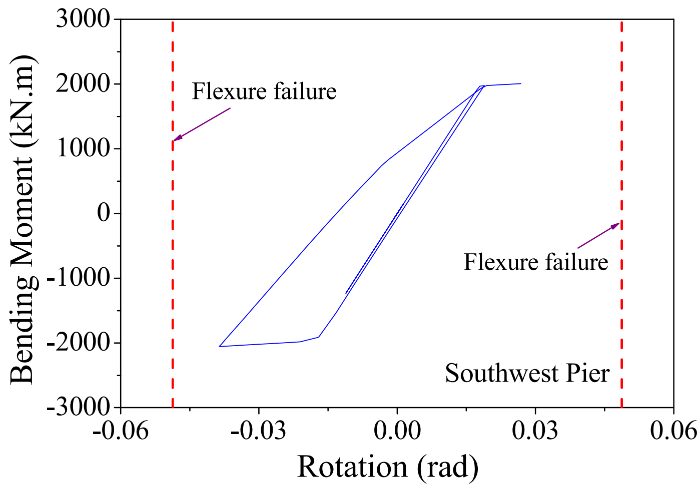

(b)

Figure 8.16 Rotation versus moment hysteretic curves

(b) Southeast pier (b) Southwest pier

The shear force and drift ratio relationships of the zero-length failure elements that are attached to the north and the south tower legs beneath the girders are plotted in

Figures 8.17 (a) and (b), respectively. The peak drift ratios of the north and south tower legs were 0.0385 and 0.0406, respectively, which were both larger than the threshold of flexure-shear failure (0.033) and smaller than the threshold of flexure-shear-axial failure (0.048), respectively.

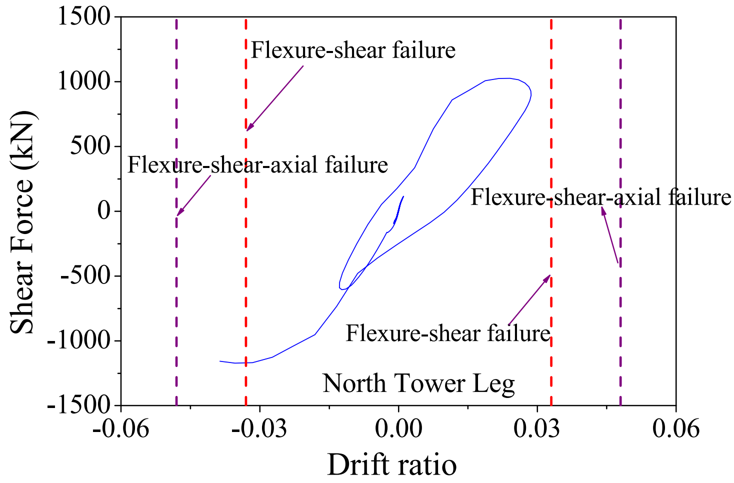

(a)

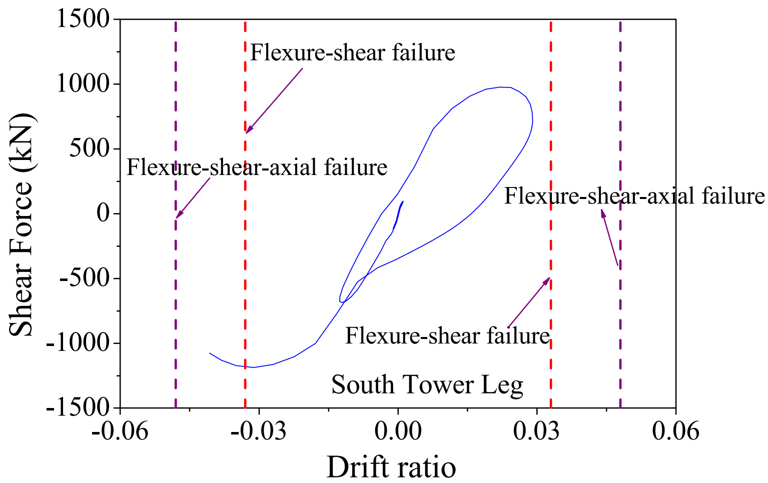

(b)

Figure 8.17 Hysteretic response of shear force versus drift ratio

(a) North tower leg (b) South tower leg

The hysteretic responses of stress versus the strain of the reinforcement in the southeast and southwest piers are plotted in Figures 8.18 (a) and (b), respectively. The reinforcing steel in the southeast and southwest piers experienced yielding and maximum strain that reached 0.006 and 0.0053, respectively.

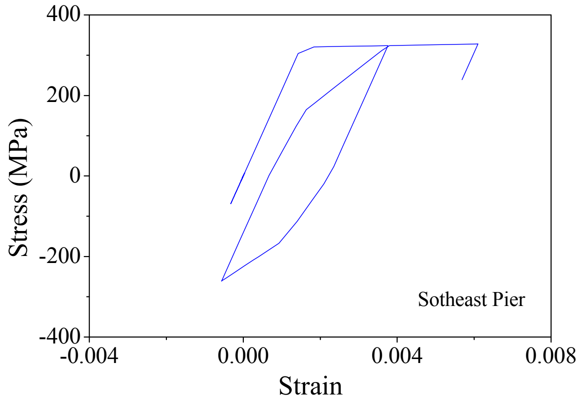

(a)

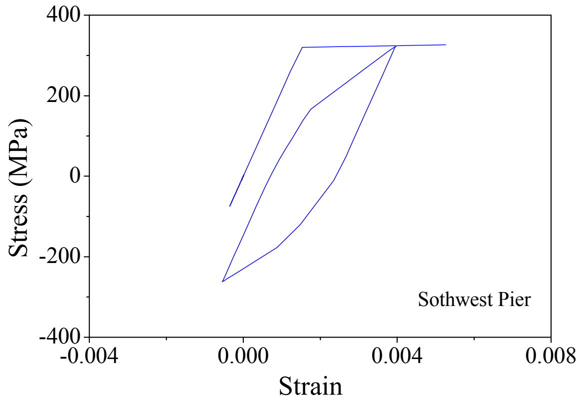

(b)

Figure 8.18 Hysteretic response of stress versus strain

(a) Southeast pier (b) Southwest pier

8.5.4 Comparison of collapse analysis and collapse prognosis

From the collapse analysis/prognosis results obtained from Sections 8.5.2 and 8.5.3, two points are summarized: first, the seismic intensities of the Kobe earthquake, resulting in the collapse of the bridge, used in the two methods are considerably different. The seismic intensity used for the current collapse analysis method is larger than that used for the proposed SHM-based collapse prognosis method; second, the collapse processes are remarkably different. The flexure failure of the southeast pier triggered the partial collapse of the bridge, whereas the flexure failure of the southwest pier caused the partial collapse of the bridge. The reason for the first point can be interpreted that the damaged bridge is easier to collapse than the intact one. The reason for the second point is that the dynamic properties of the intact bridge and the damaged bridge are different, which is prone to yield different collapse modes.

8.6 Conclusions

An ideal SHM system installed on a bridge is useful in monitoring the loading conditions, updating the FE model, assessing the linear and nonlinear performance, and making collapse prognosis of the bridge. Two sets of SHM systems for the prototype RC bridge are established using two different methods. These systems have demonstrated significantly different results in terms of sensor location and sensor number. The SHM system that uses the multi-sensor placement method includes 16 strain gauges and 12 accelerometers, whereas the proposed SHM system includes 24 strain gauges and 10 accelerometers. The sensors of the strain gauge in the proposed SHM system are all placed in the failure-vulnerable components, such as the tower legs beneath the girder and the two south piers, whereas only several strain gauges in the current SHM system are placed on the girder, transverse beam, and stay cable. These differences can be attributed to the fact that the current SHM system is utilized to assess the linear performance of the bridge under service loadings, whereas the proposed SHM system is used to make a collapse prognosis of the RC bridge under seismic loadings.

To demonstrate the difference of the current collapse analysis method and the proposed SHM-based collapse analysis method, an SHM-based collapse prognosis of the earthquake-damaged bridge was conducted. In reality, the damage condition of the bridge can be determined using the nonlinear model updating technique in Chapter 6 and the information that is acquired from the proposed SHM system installed on the bridge. In this way, the uncertainties in the FE model of the bridge can be eliminated and provide a critical support for the collapse prognosis. In this study, the damaged state was specified by conducting a nonlinear seismic analysis for absence of SHM system. For comparison, a collapse analysis of the prototype RC bridge is also conducted using the current collapse analysis method. The entire collapse processes from the two collapse analysis/prognosis methods are significantly different: (1) the seismic intensity used for the current collapse analysis method is larger than that used for the proposed SHM-based collapse prognosis method; and (2) the proposed method has detected a partial collapse in the southwest pier, whereas the current collapse analysis method has detected a partial collapse in the southeast pier. Therefore, the proposed SHM-based collapse prognosis is a promising method to prognosticate the behavior of the existing RC bridges under future earthquakes, whereas the current collapse analysis can be only used for the bridge at design stage.

CHAPTER 9

CONCLUSIONS AND RECOMMENDATIONS

9.1 Conclusions

This thesis is a study of structural health monitoring (SHM)-based seismic collapse analysis of reinforced concrete (RC) bridge structures. In particular, this study is devoted to: (1) proposing a rigorous seismic collapse analysis method by introducing a concept of degree of freedom (DOF) release for RC structures; (2) designing and constructing a 1/12 scaled RC bridge model installed with a sophisticated SHM system for conducting seismic collapse tests on a shake table; (3) establishing a nonlinear fibre-element (FE) model of the scaled bridge and performing the linear model updating of the FE model in the time domain to obtain an accurate FE model of the intact bridge; (4) conducting the nonlinear model updating of the FE model in the time domain to obtain an accurate FE model of the currently damaged bridge; (5) conducting seismic collapse analysis of the damaged bridge based on the updated FE model of the damaged bridge; and (6) establishing a nonlinear FE model of the prototype bridge and demonstrating the SHM-based seismic collapse prognosis method by virtue of the FE model of the prototype bridge. The main conclusions of this study are summarized below:

1. A new refined method for FE-method-based seismic collapse simulation of RC

structures is proposed by introducing the concept of DOF release. This refined method can consider the catenary effect for RC beams and the effect of axial forces on the failure modes of RC columns. The refined method has been implemented in an open source finite element code of OpenSees (McKenna et al. 2007). The numerical results of the seismic collapse of a two-span RC continuous beam with its two ends fixed under a concentrated static load was first compared with the test results. The comparison results show that the DOF release method gives a better agreement with the measured results than the traditional element removal method. Then, the refined seismic analysis method was applied to a two-story RC frame structure to demonstrate the entire progress of dynamic collapse. The numerical results again demonstrate that the proposed method gives more reasonable progressive collapse results by taking the catenary effect into account than the traditional element removal method. At last, a two-span continuous RC bridge with a two-column pier at its middle was taken as an example to demonstrate the applicability of the refined method to RC bridge structures. The results show that the collapse of the RC columns did not occur immediately after the DOFs associated with bending moment and shear force of the two columns were released, and that the final collapse of the two columns was due to excessive axial loads. This failure mode could not be predicted by the traditional element removal method. Therefore, the refined method based on DOF release is preferable for the seismic collapse analysis of RC structures including RC bridge structures.

2. A 1:12 scaled RC cable-stayed bridge was firstly elaborately designed and

constructed to experimentally study the seismic collapse of the RC bridge that was not designed for seismic resistance. A comprehensive SHM system was designed and installed on the RC bridge to record both the global responses and local responses of the bridge. Before the shaking table tests, each cable force of the as-built RC bridge was measured by the frequency method to ensure that the bridge configuration meets the design requirement. The dynamic characteristic test was then conducted to gain an insight of the properties of the bridge. Finally, a series of earthquake tests, which include small earthquake, moderate earthquake, large earthquake and collapse earthquake in terms of the peak ground acceleration (PGA) and spectrum, were conducted. It was observed from the four shake table tests that: (1) the RC bridge performed linearly and elastically under the small earthquake excitation and the RC bridge kept intact conditions after the small earthquake excitation; (2) the RC bridge behaved slightly nonlinearly and plastically under the moderate earthquake excitation. The concrete in the failure-vulnerable components cracked slightly; (3) the RC bridge performed severely nonlinearly and plastically under the large earthquake excitation. The concrete in the failure-vulnerable components crushed severely and the reinforcement in the failure-vulnerable components yielded severely; and (4) the RC bridge partially collapsed under the collapse earthquake excitation. The concrete in the failure-vulnerable components crushed severely and the reinforcement in the failure-vulnerable components yielded severely.

3. A new two-stage model updating strategy (linear model updating and nonlinear

model updating) is proposed. Two types of objective functions: the objective function based on natural frequencies and the objective function based on acceleration and strain responses, were used to conduct the linear model updating of the scaled bridge. The comparison results indicated that both of the two objective functions can improve the quality of the FE model. The second objective function can not only be used as an alternate of the first one for nonlinear model updating but also provide better updating results than the first objective function. As demonstrated by the success of the linear updating of the three dimensional (3-D) FE model using acceleration and reinforcement strain responses in the time domain, the second objective function can be used for the nonlinear model updating.

4. A nonlinear model updating method by using the measured responses of acceleration and strain of reinforcement of the bridge in the time domain to update the envelop curves of the materials of the bridge without knowing its previous loading history is proposed. In the nonlinear model updating, the degradations of both unloading stiffness and reloading stiffness are accomplished in addition to the strength degradation by using the rules of the Concrete01 and the hysteretic material model provided in OpenSees (McKenna et al. 2007). Various seismic response time histories computed using the nonlinear updated results are compared with the measured responses. The comparison results indicate that the updated results of the key parameters are correct and the nonlinear model updating method is feasible. As demonstrated by the success of the nonlinear model updating of the 3-D nonlinear FE model by using acceleration and reinforcement strain responses

in the time domain, it can be used as a useful tool for the further seismic collapse analysis.

5. The new SHM-based seismic collapse prognosis method is proposed and applied to the scaled RC bridge. Since the seismic collapse prognosis of a structure will be carried out based on the current damage conditions of the structure, the SHM-based nonlinear model updating is necessary to find out the current damage conditions of the structure. A total of 58 parameters are selected for updating. The results showed that the values of the most updated parameters of the bridge under the latest large earthquake excitation became much smaller compared with those identified for the bridge subject to a moderate earthquake excitation. The values/thresholds of the failure criteria of the four zero-length failure elements of the RC bridge were also determined based on the current damaged conditions and compared with those from the undamaged conditions. The comparative results showed that the values/thresholds of the failure criteria of the four zero-length failure elements of the RC bridge determined based on the current damaged conditions are very different from those based on the undamaged conditions. The collapse prognosis of the RC bridge subject to two future earthquake ground excitations were finally performed based on the updated FE model of the bridge to find out which earthquake will cause the true bridge collapse. The computed results showed that the RC bridge did not collapse when it was subjected to the first future earthquake excitation of relatively small intensity. The computed results showed that when the bridge was subjected to the second earthquake excitation of relatively large

intensity, the RC southwest pier, as one of the failure-vulnerable component, triggered the flexure failure at 3.133 second of the earthquake excitation and it was separated from the RC bridge structure. The other three failure-vulnerable components experienced severe damage without any failure. A series of computed seismic responses such as acceleration, strain and reaction force of the RC bridge subject to the second earthquake excitation were compared with the shake table test results recorded by the SHM system installed on the bridge. The comparison results showed that the computed results and collapse process are compatible with the test results recorded by the SHM system. The SHM-based collapse prognosis proposed in this chapter is therefore feasible and effective for as-built RC bridges. Clearly, the SHM system plays an important role in the seismic collapse analysis/prognosis of the RC bridge subject to earthquake excitation.

6. An ideal SHM system installed on a bridge is useful in monitoring the loading conditions, updating the FE model, assessing the linear and nonlinear performance, and making collapse prognosis of the bridge. Two sets of SHM systems for the prototype RC bridge are established using two different methods. These systems have demonstrated significantly different results in terms of sensor location and sensor number. The SHM system that uses the multi-sensor placement method includes 16 strain gauges and 12 accelerometers, whereas the proposed SHM system includes 24 strain gauges and 10 accelerometers. The sensors of the strain gauge in the proposed SHM system are all placed in the failure-vulnerable components, such as the tower legs beneath the girder and the two south piers,

whereas only several strain gauges in the current SHM system are placed on the girder, transverse beam, and stay cable. These differences can be attributed to the fact that the current SHM system is utilized to assess the linear performance of the bridge under service loadings, whereas the proposed SHM system is used to make a collapse prognosis of the RC bridge under seismic loadings.

To demonstrate the difference of the current collapse analysis method and the proposed SHM-based collapse analysis method, an SHM-based collapse prognosis of the earthquake-damaged bridge was conducted. In reality, the damage condition of the bridge can be determined using the nonlinear model updating technique in Chapter 6 and the information that is acquired from the proposed SHM system installed on the bridge. In this way, the uncertainties in the FE model of the bridge can be eliminated and provide a critical support for the collapse prognosis. In this study, the damaged state was specified by conducting a nonlinear seismic analysis for absence of SHM system. For comparison, a collapse analysis of the prototype RC bridge is also conducted using the current collapse analysis method. The entire collapse processes from the two collapse analysis/prognosis methods are significantly different: (1) the seismic intensity used for the current collapse analysis method is larger than that used for the proposed SHM-based collapse prognosis method; (2) the proposed method has detected a partial collapse in the southwest pier, whereas the current collapse analysis method has detected a partial collapse in the southeast pier. Therefore, the proposed SHM-based collapse prognosis is a promising method to prognosticate the behavior of the existing RC bridges under future earthquakes, whereas the current collapse analysis can be only used for the bridge at design stage.

9.2 Recommendations for Future Studies

Although progress has been made in this thesis for the development and application of seismic collapse analysis of RC bridges under earthquake excitations, several important issues remain to be further studied.

1. A large number of RC component (beam, column and joint) tests should be designed and conducted with respect to the different failure modes considering the failing sequence of the DOFs to strongly support the rules for release sequence of the DOFs as presented in Chapter 3.
2. A large number of RC component (beam, column and joint) tests should be designed and conducted with respect to the different accumulated damage conditions of the RC components to gain an insight of the unloading/reloading path of the components.
3. The hysteretic curves of force/bending moment versus deformation/curvature at critical sections of the bridge should be measured to better investigate the behavior of the components during earthquake.
4. A prototype RC bridge installed with a specially designed SHM system for seismic collapse analysis should be established for conducting seismic collapse test on shake table to verify the proposed SHM-based seismic collapse prognosis method.
5. It is necessary to develop and implement a practical numerical model to account for failed element (debris) spread and impact for a thorough seismic collapse

analysis of RC bridges.

6. It is necessary to propose an algorithm to optimize the sensor number and sensor placement for collapse prognosis of the RC bridge.
7. It is necessary to propose a group of algorithms that help the SHM practitioner from data to a decision.

APPENDIX A. CHANNEL ARRANGEMENT

Channel No.	Instrument Type	Description	Name
1	Load cell	At the north tower leg foundation	Fx_1
2	Load cell	At the north tower leg foundation	Fy_1
3	Load cell	At the north tower leg foundation	Fz_1
4	Load cell	At the north tower leg foundation	Mx_1
5	Load cell	At the north tower leg foundation	My_1
6	Load cell	At the north tower leg foundation	Fx_2
7	Load cell	At the north tower leg foundation	Fy_2
8	Load cell	At the north tower leg foundation	Fz_2
9	Load cell	At the north tower leg foundation	Mx_2
10	Load cell	At the north tower leg foundation	My_2
11	Load cell	At the south tower leg foundation	Fx_3
12	Load cell	At the south tower leg foundation	Fy_3
13	Load cell	At the south tower leg foundation	Fz_3
14	Load cell	At the south tower leg foundation	Mx_3
15	Load cell	At the south tower leg foundation	Fx_4
16	Load cell	At the south tower leg foundation	Fy_4
17	Load cell	At the south tower leg foundation	Fz_4
18	Load cell	At the south tower leg foundation	Mx_4
19	Load cell	At the southeast pier foundation	Fx_5
20	Load cell	At the southeast pier foundation	Fy_5
21	Load cell	At the southeast pier foundation	Fz_5
22	Load cell	At the southeast pier foundation	Mx_5
23	Load cell	At the southeast pier foundation	Fx_6
24	Load cell	At the southeast pier foundation	Fy_6
25	Load cell	At the southeast pier foundation	Fz_6
26	Load cell	At the southeast pier foundation	Mx_6
27	Strain Gage	At the north tower leg	n1
28	Strain Gage	At the north tower leg	n2
29	Strain Gage	At the north tower leg	n3
30	Strain Gage	At the north tower leg	n4
31	Strain Gage	At the north tower leg	n5
32	Strain Gage	At the north tower leg	n6
33	Strain Gage	At the north tower leg	n7
34	Strain Gage	At the north tower leg	n8
35	Strain Gage	At the south tower leg	s1
36	Strain Gage	At the south tower leg	s2
37	Strain Gage	At the south tower leg	s3
38	Strain Gage	At the south tower leg	s4
39	Strain Gage	At the south tower leg	s5
40	Strain Gage	At the south tower leg	s6

APPENDIX A. CHANNEL ARRANGEMENT (continued)

Channel No.	Instrument Type	Description	Name
41	Strain Gage	At the south tower leg	s7
42	Strain Gage	At the south tower leg	s8
43	Strain Gage	At the southeast pier	s21
44	Strain Gage	At the southeast pier	s22
45	Strain Gage	At the southeast pier	s23
46	Trigger	Computer 1	
47	Trigger	Computer 2	
48	Accelerometer	On board of the shake table	A1
49	Accelerometer	At the southeast foundation	A2
50	Accelerometer	At the northeast foundation	A3
51	Accelerometer	At the south tower leg foundation	A4
52	Accelerometer	At the north tower leg foundation	A5
53	Accelerometer	At the top of the southeast pier	A6
54	Accelerometer	At joint of the tower and south girder	A7
55	Accelerometer	At the top of the southwest pier	A8
56	Accelerometer	At top of the north tower leg	A9
57	Accelerometer	At top of the south tower leg	A10
58	Accelerometer	At top of the north tower leg	A11
59	Accelerometer	At top of the south girder	A12
60	Accelerometer	At top of the north girder	A13

REFERENCES

ACI/318 "Building code requirements for structural concrete (ACI 318-05) and commentary (ACI 318R-05)." American Concrete Institute.

Administration, G. S. (2003). "Progressive collapse analysis and design guidelines for new federal office buildings and major modernization projects." Office of Chief Architect, Washington, DC.

Aktan, A. E., Farhey, D. N., Brown, D. L., Dalal, V., Helmicki, A. J., Hunt, V. J., and Shelley, S. J. (1996). "Condition assessment for bridge management." *Journal of Infrastructure Systems*, 2(3), 108-117.

Alexandris, A., Protopapa, E., and Psycharis, I. "Collapse mechanisms of masonry buildings derived by the distinct element method." *Proc., Proceedings of the 13th World Conference on Earthquake Engineering*.

Allahabadi, R., and Powell, G. H. (1988). *DRAIN-2DX user guide*, University of California, Earthquake Engineering Research Center, College of Engineering.

Andersen, E., and Pedersen, L. (1994). "Structural monitoring of the great belt east bridge." *Strait crossings*, 94, 189-195.

ASCE. (2010). "Minimum design loads for buildings and other structures." American Society of Civil Engineers, Reston, Virginia.

ASCE/SEI (2007). "Seismic Rehabilitation of Existing Buildings (ASCE/SEI 41-06)." *American Society of Civil Engineers, Reston, VA.*

Asgarieh, E., Moaveni, B., and Stavridis, A. (2014). "Nonlinear finite element model updating of an infilled frame based on identified time-varying modal parameters during an earthquake." *Journal of Sound and Vibration*, 333(23), 6057-6073.

Aviram, A., Mackie, K. R., and Stojadinović, B. (2008). *Guidelines for nonlinear analysis of bridge structures in California*, Pacific Earthquake Engineering Research Center.

Azevedo, N. M. M. (2003). "A rigid particle discrete element model for the fracture analysis of plain and reinforced concrete." Heriot-Watt University.

Baggio, C., and Trovalusci, P. (2000). "Collapse behaviour of three-dimensional brick-block systems using non-linear programming." *Structural Engineering and Mechanics*, 10(2), 181.

Banon, H., Irvine, H. M., and Biggs, J. M. (1981). "Seismic damage in reinforced concrete frames." *Journal of the Structural Division*, 107(9), 1713-1729.

Bao, Y., Kunnath, S. K., El-Tawil, S., and Lew, H. (2008). "Macromodel-based simulation of progressive collapse: RC frame structures." *Journal of Structural Engineering*, 134(7), 1079-1091.

Beardsley, P., Hemez, F. M., and Doebling, S. W. "Updating nonlinear finite element models in the time domain." *Proc., 2nd International Workshop on Structural Health Monitoring*, 8-10.

Brownjohn, J., Moyo, P., Omenzetter, P., and Chakraborty, S. (2005). "Lessons from monitoring the performance of highway bridges." *Structural Control and Health Monitoring*, 12(3‐4), 227-244.

Brownjohn, J. M., and Xia, P.-Q. (2000). "Dynamic assessment of curved cable-stayed bridge by model updating." *Journal of Structural Engineering*, 126(2), 252-260.

Brownjohn, J. M., Xia, P.-Q., Hao, H., and Xia, Y. (2001). "Civil structure condition assessment by FE model updating:: methodology and case studies." *Finite Elements in Analysis and Design*, 37(10), 761-775.

Cantieni, R. "Updating of analytical models of existing large structures based on modal testing." *Proc., Recent Advances in Bridge Engineering. Proceedings of the US-Europe Workshop on Bridge Engineering.*

Casciati, F. (2003). *An overview of structural health monitoring expertise within the European Union*, Swets and Zeitlinger, Lisse.

Catbas, F. N., and Aktan, A. E. (2002). "Condition and damage assessment: issues and some promising indices." *Journal of Structural Engineering*, 128(8), 1026-1036.

Catbas, F. N., Ciloglu, S. K., Hasancebi, O., Grimmelsman, K., and Aktan, A. E. (2007). "Limitations in structural identification of large constructed structures." *Journal of Structural Engineering*, 133(8), 1051-1066.

Chajes, M. J., Mertz, D. R., and Commander, B. (1997). "Experimental load rating of a posted bridge." *Journal of Bridge Engineering*, 2(1), 1-10.

Cheung, M., and Naumoski, N. "The first smart long-span bridge in Canada—health monitoring of the Confederation Bridge." *Proc., Structural Health Monitoring Workshop*, 31-44.

Chopra, A. K. (1995). *Dynamics of structures*, Prentice Hall New Jersey.

Chung, Y., Meyer, C., and Shinozuka, M. (1987). "Seismic damage assessment of reinforced concrete members."

Coffin Jr, L. F., and Wesley, R. (1952). "An Apparatus for the Study of the Effects of Cyclic Thermal Stresses on Ductile Metals." Knolls Atomic Power Lab.

Council, B. S. S. (2000). "Prestandard and commentary for the seismic rehabilitation of buildings." *Report FEMA-356, Washington, DC.*

Crisfield, M. A. (1990). "A consistent co-rotational formulation for non-linear, three-dimensional, beam-elements." *Computer Methods in Applied Mechanics and Engineering*, 81(2), 131-150.

Cundall, P. A. (1971). "A Computer model for simulating progressive large scale movements in blocky rock systems." *Proceedings of the symposium of the international society for rock mechanics*.

De Witte, F., and Kikstra, W. (2005). "DIANA finite element analysis." *User's Manual: Release*, 9.

DoD (2009). "Design of building to resist progressive collapse." UFC.

Elwood, K. J., Matamoros, A. B., Wallace, J. W., Lehman, D. E., Heintz, J. A., Mitchell, A. D., Moore, M. A., Valley, M. T., Lowes, L. N., and Comartin, C. D. (2007). "Update to ASCE/SEI 41 concrete provisions." *Earthquake Spectra*, 23(3), 493-523.

Elwood, K. J., and Moehle, J. P. (2003). "Shaking Table Tests and Analytical Studies on the Gravity Load Collapse of Reinforced Concrete Frames." University of

California, Berkeley, PEER.

Elwood, K. J., and Moehle, J. P. (2005). "Drift capacity of reinforced concrete columns with light transverse reinforcement." *Earthquake Spectra*, 21(1), 71-89.

Enevoldsen, I., Pedersen, C., Axhag, F., Johansson, Ö., and Töyrä, B. (2002). "Assessment and measurement of the Forsmo Bridge, Sweden." *Structural engineering international*, 12(4), 254-257.

Farnam, Y., Mohammadi, S., and Shekarchi, M. (2010). "Experimental and numerical investigations of low velocity impact behavior of high-performance fiber-reinforced cement based composite." *International Journal of Impact Engineering*, 37(2), 220-229.

Friswell, M., and Mottershead, J. E. (1995). *Finite element model updating in structural dynamics*, Springer Science & Business Media.

Fujino, Y., and Abe, M. "Structural health monitoring-current status and future." *Proc., Proceedings of the 2nd European workshop on structural health monitoring. Lancaster (PA): DEStech*, 3-10.

Galambos, T. V. (2000). "Recent research and design developments in steel and composite steel–concrete structures in USA." *Journal of Constructional Steel Research*, 55(1), 289-303.

Ghannoum, W. M. (2007). "Experimental and analysis dynamic collapse study of a reinforced concrete frame with light transverse reinforcement." Ph. D, University of California, Berkeley.

Gill, P. E., Murray, W., and Saunders, M. A. (2002). "SNOPT: An SQP algorithm for large-scale constrained optimization." *SIAM journal on optimization*, 12(4), 979-1006.

Gosain, N. K., Jirsa, J. O., and Brown, R. H. (1977). "Shear requirements for load reversals on RC members." *Journal of the Structural Division*, 103(7), 1461-1476.

Grierson, D., Xu, L., and Liu, Y. (2005). "Progressive‐failure analysis of buildings subjected to abnormal loading." *Computer‐Aided Civil and Infrastructure Engineering*, 20(3), 155-171.

GSA (2003). "Progressive collapse design guide line." General Services Administration, Washington, DC.

Gu, Q., Barbato, M., Conte, J. P., Gill, P. E., and McKenna, F. (2011). "OpenSees-SNOPT framework for finite-element-based optimization of structural and geotechnical systems." *Journal of Structural Engineering*, 138(6), 822-834.

Hakuno, M. (1996). "Simulation of 3-D concrete-frame collapse due to dynamic loading." *11th World Conference on Earthquake Engineering*.

Hallquist, J. O. (2006). "LS-DYNA theory manual." *Livermore Software Technology Corporation*, 3.

Hao, H., and Tang, E. K. (2010). "Numerical simulation of a cable-stayed bridge response to blast loads, Part II: Damage prediction and FRP strengthening." *Engineering Structures*, 32(10), 3193-3205.

Helmy, H., Salem, H., and Tageldin, H. "Numerical simulation of charlotte coliseum demolition using the applied element method." *Proc., USNCCM-10 conference-Ohio-USA*.

Hemez, F. M., and Doebling, S. W. (2001). "Review and assessment of model updating for non-linear, transient dynamics." *Mechanical Systems and Signal Processing*, 15(1), 45-74.

Ibarra, L. F., Medina, R. A., and Krawinkler, H. (2005). "Hysteretic models that incorporate strength and stiffness deterioration." *Earthquake engineering & structural dynamics*, 34(12), 1489-1511.

Imai, K., and Frangopol, D. M. (2000). "Geometrically nonlinear finite element reliability analysis of structural systems. I: theory." *Computers & Structures*, 77(6), 677-691.

Iwashita K., and Hakuno M. (1988). "Granular assembly simulation for dynamic cliff collapse due to earthquake." *Procedding of 9 WCEE*, 175-180.

Jaishi, B., and Ren, W.-X. (2005). "Structural finite element model updating using ambient vibration test results." *Journal of Structural Engineering*, 131(4), 617-628.

Kabeyasawa, T., Tasai, A., and Igarashi, S. (2002). "An economical and efficient method of strengthening reinforced concrete columns against axial load collapse during major earthquake." *PEER Report*, 2, 399-412.

Kaewkulchai, G., and Williamson, E. B. (2004). "Beam element formulation and solution procedure for dynamic progressive collapse analysis." *Computers & Structures*, 82(7), 639-651.

Kammer, D. C. (1991). "Sensor placement for on-orbit modal identification and correlation of large space structures." *Journal of Guidance, Control, and Dynamics*, 14(2), 251-259.

Kammer, D. C. (1992). "Effects of noise on sensor placement for on-orbit modal identification of large space structures." *Journal of dynamic systems, measurement, and control*, 114(3), 436-443.

Kato, D., and Ohnishi, K. "Axial load carrying capacity of R/C columns under lateral load reversals." *Proc., Proceedings of the Third US-Japan Workshop on Performance-Based Earthquake Engineering Methodology for Reinforced Concrete Building Structures*, 247-255.

Kent, D. C., and Park, R. (1971). "Flexural members with confined concrete." *Journal of the Structural Division*, 97(7), 1969-1990.

Khandelwal, K., El-Tawil, S., Kunnath, S. K., and Lew, H. (2008). "Macromodel-based simulation of progressive collapse: Steel frame structures." *Journal of structural engineering*, 134(7), 1070-1078.

Kim, H.-S., Kim, J., and An, D.-W. (2009). "Development of integrated system for progressive collapse analysis of building structures considering dynamic effects." *Advances in Engineering Software*, 40(1), 1-8.

Kim, Y., Kabeyasawa, T., and Igarashi, S. (2012). "Dynamic collapse test on eccentric reinforced concrete structures with and without seismic retrofit." *Engineering Structures*, 34, 95-110.

Kim, Y., Kabeyasawa, T., Matsumori, T., and Kabeyasawa, T. (2012). "Numerical study of a full - scale six - story reinforced concrete wall - frame structure tested at E - Defense." *Earthquake Engineering & Structural Dynamics*, 41(8), 1217-1239.

Ko, J., and Ni, Y. (2005). "Technology developments in structural health monitoring of large-scale bridges." *Engineering structures*, 27(12), 1715-1725.

Koh, H., Choo, J., Kim, S., and Kim, C. (2003). "Recent application and development of structural health monitoring systems and intelligent structures in Korea." *Proc. SHMII-1, Structural Health Monitoring and Intelligent Infrastructures*, 1, 99-112.

Kunnath S. K., Ei-Bahy A., Taylor A. W., and Stone W. C. (1991). "Cumulative Damage of Reinforced Concrete Bridge Piers." National Institute of Standards and Technology.

Kunnath, S. K., Mander, J. B., and Fang, L. (1997). "Parameter identification for degrading and pinched hysteretic structural concrete systems." *Engineering Structures*, 19(3), 224-232.

Kwasniewski, L. (2010). "Nonlinear dynamic simulations of progressive collapse for a multistory building." *Engineering Structures*, 32(5), 1223-1235.

Lemos, J. V. (2007). "Discrete element modeling of masonry structures." *International Journal of Architectural Heritage*, 1(2), 190-213.

Li, J., and Hao, H. (2013). "Influence of brittle shear damage on accuracy of the two-step method in prediction of structural response to blast loads." *International Journal of Impact Engineering*, 54, 217-231.

Li, J., and Hao, H. (2013). "Numerical study of structural progressive collapse using substructure technique." *Engineering Structures*, 52, 101-113.

Li, Q., Xu, Y.-l., Zheng, Y., Guo, A.-x., Wong, K.-y., and Xia, Y. (2011). "SHM-based F-AHP bridge rating system with application to Tsing Ma Bridge." *Frontiers of Architecture and Civil Engineering in China*, 5(4), 465-478.

Lignos, D., Krawinkler, H., and Whittaker, A. (2011). "Prediction and validation of sidesway collapse of two scale models of a 4‐story steel moment frame." *Earthquake Engineering & Structural Dynamics*, 40(7), 807-825.

Liu, P.-L., and Kiureghian, A. D. (1991). "Finite element reliability of geometrically nonlinear uncertain structures." *Journal of engineering mechanics*, 117(8), 1806-1825.

Lu, X., Lu, X., Guan, H., and Ye, L. (2013). "Collapse simulation of reinforced concrete high‐rise building induced by extreme earthquakes." *Earthquake Engineering & Structural Dynamics*, 42(5), 705-723.

Lu X. (2013). <http://blog.sina.com.cn/s/blog_6cdd8dff0101n4zp.html>.

Lynn, A. C. (2001). "Seismic evaluation of existing reinforced concrete building columns." UNIVERSITY of CALIFORNIA at BERKELEY.

Lynn, A. C., Moehle, J. P., Mahin, S. A., and Holmes, W. T. (1996). "Seismic evaluation of existing reinforced concrete building columns." *Earthquake Spectra*, 12(4), 715-739.

Marc, M. (2010). "Volume A: Theory and user information." *MSC. Software Corporation*.

Marjanishvili, S. (2004). "Progressive analysis procedure for progressive collapse." *Journal of Performance of Constructed Facilities*, 18(2), 79-85.

McKenna, F., Fenves, G., and Scott, M. (2007). "Open system for earthquake engineering simulation." *University of California, Berkeley, CA*.

Meguro, K., and Tagel-Din, H. (2001). "Applied element simulation of RC structures under cyclic loading." *Journal of structural engineering*, 127(11), 1295-1305.

Meguro, K., and Tagel-Din, H. (2002). "Applied element method used for large displacement structural analysis." *Journal of Natural Disaster Science*, 24(1), 25-34.

Meguro K., and Hakuno M. (1988). "Fracture analysis of concrete structures by granular analysis simulation." *Bulletin of The Earthquake Research Instiute*, 63, 409-468.

Meguro K., and Hakuno M. (1989). "Fracture analysis of media composed of irregularly shaped regions by the extended distinct element method."

Structural Engineering and Earthquake Engineering, 8(3), 131-142.

Meyer, S., and Link, M. (2003). "Modelling and updating of local non-linearities using frequency response residuals." *Mechanical Systems and Signal Processing*, 17(1), 219-226.

Mitra, N., and Lowes, L. N. (2007). "Evaluation, calibration, and verification of a reinforced concrete beam–column joint model." *Journal of Structural Engineering*, 133(1), 105-120.

Moncarz, P. D., and Krawinkler, H. (1981). *Theory and application of experimental model analysis in earthquake engineering*, Stanford University.

Mottershead, J., and Friswell, M. (1993). "Model updating in structural dynamics: a survey." *Journal of sound and vibration*, 167(2), 347-375.

Mufti, A. A. (2002). "Structural health monitoring of innovative Canadian civil engineering structures." *Structural Health Monitoring*, 1(1), 89-103.

Myrvoll, F., Aarnes, K., Larssen, R., and Gjerding-Smith, K. "Full scale measurements for design verification of bridges." *Proc., SPIE proceedings series*, Society of Photo-Optical Instrumentation Engineers, 827-835.

Neuenhofer, A., and Filippou, F. C. (1997). "Evaluation of nonlinear frame finite-element models." *Journal of Structural Engineering*, 123(7), 958-966.

Newmark, N. M. "A method of computation for structural dynamics." *Proc., Proc. ASCE*, 67-94.

Nigbor, R., and Diehl, J. (1997). "Two year's experience using OASIS real-time remote condition monitoring system on two large bridges." *Structural Health Monitoring, Current Status and Perspectives*, 1, 410-417.

Okamura, H., and Maekawa, K. (1991). "Nonlinear analysis and constitutive models of reinforced concrete." *Gihodo, Tokyo*.

Ou, J. (2004). "The state-of-the-art and application of intelligent health monitoring systems for civil infrastructures in mainland of China." *Progress in Structural Engineering, Mechanics and Computation*, 599-608.

Papantonopoulos, C., Psycharis, I., Papastamatiou, D., Lemos, J., and Mouzakis, H. (2002). "Numerical prediction of the earthquake response of classical columns using the distinct element method." *Earthquake engineering & structural dynamics*, 31(9), 1699-1717.

Park, Y.-J., and Ang, A. H.-S. (1985). "Mechanistic seismic damage model for reinforced concrete." *Journal of Structural Engineering*, 111(4), 722-739.

Park, Y., Ang, A. H., and Wen, Y. (1987). "Damage-limiting aseismic design of buildings." *Earthquake spectra*, 3(1), 1-26.

Pavic, A., Hartley, M. J., and Waldron, P. "Updating of the analytical models of two footbridges based on modal testing of full-scale structures." *Proc., PROCEEDINGS OF THE INTERNATIONAL SEMINAR ON MODAL ANALYSIS*, KATHOLIEKE UNIVERSITEIT LEUVEN, 1111-1118.

Pines, D., and Aktan, A. E. (2002). "Status of structural health monitoring of long‐span bridges in the United States." *Progress in Structural Engineering and materials*, 4(4), 372-380.

Priestley, M. (1997). "Displacement-based seismic assessment of reinforced concrete buildings." *Journal of earthquake Engineering*, 1(1), 157-192.

Priestley, M., Calvi, G., and Kowalsky, M. "Direct displacement-based seismic design of structures." *Proc., 2007 NZSEE Conference*.

Pujol, S. (2002). "Drift capacity of reinforced concrete columns subjected to displacement reversals."

Pujol, S., Ramfrez, J., and Sozen, M. A. (1999). "Drift capacity of reinforced concrete columns subjected to cyclic shear reversals." *ACI Special Publication*, 187.

Ren, W.-X., and Chen, H.-B. (2010). "Finite element model updating in structural dynamics by using the response surface method." *Engineering Structures*, 32(8), 2455-2465.

Ristic, D., Yamada, Y., and Iemura, H. (1986). "Stress-strain based modeling of hysteretic structures under earthquake induced bending and varying axial loads." *Research Rep. No. 86-ST*, 1.

Sagiroglu, S. (2012). "Analytical and experimental evaluation of progressive collapse resistance of reinforced concrete structures." Ph. D, Northeastern

University.

Salem, H. (2011). "Computer-aided design of framed reinforced concrete structures subjected to flood scouring." *J Am Sci*, 7(10), 191-200.

Salem, H., El-Fouly, A., and Tagel-Din, H. (2011). "Toward an economic design of reinforced concrete structures against progressive collapse." *Engineering Structures*, 33(12), 3341-3350.

Sasani, M. (2008). "Response of a reinforced concrete infilled-frame structure to removal of two adjacent columns." *Engineering Structures*, 30(9), 2478-2491.

Sasani, M., Bazan, M., and Sagiroglu, S. (2007). "Experimental and analytical progressive collapse evaluation of actual reinforced concrete structure." *ACI Structural Journal*, 104(6).

Sasani, M., and Sagiroglu, S. (2008). "Progressive collapse resistance of hotel San Diego." *Journal of Structural Engineering*, 134(3), 478-488.

Schlune, H., Plos, M., and Gylltoft, K. (2009). "Improved bridge evaluation through finite element model updating using static and dynamic measurements." *Engineering structures*, 31(7), 1477-1485.

Sezen, H., and Moehle, J. P. (2004). "Shear strength model for lightly reinforced concrete columns." *Journal of Structural Engineering*, 130(11), 1692-1703.

Sivaselvan, M. V., and Reinhorn, A. M. (2000). "Hysteretic models for deteriorating inelastic structures." *Journal of Engineering Mechanics*, 126(6), 633-640.

Song, J.-K., and Pincheira, J. (2000). "Spectral displacement demands of stiffness-and strength-degrading systems." *Earthquake Spectra*, 16(4), 817-851.

Song, W., Dyke, S., and Harmon, T. (2012). "Application of Nonlinear Model Updating for a Reinforced Concrete Shear Wall." *Journal of Engineering Mechanics*, 139(5), 635-649.

Song, W., So, M., Dyke, S., Harmon, T., and Yun, G. (2008). "Nonlinear RC structure model updating using ambient vibration data." *ACI Special*

Publication, 252.

Spacone, E., Filippou, F. C., and Taucer, F. F. (1996). "Fibre beam-column model for non-linear analysis of R/C frames: Part I. Formulation." *Earthquake engineering and structural dynamics*, 25(7), 711-726.

Stavridis, A., Koutromanos, I., and Shing, P. B. (2012). "Shake‐table tests of a three‐story reinforced concrete frame with masonry infill walls." *Earthquake Engineering & Structural Dynamics*, 41(6), 1089-1108.

Su, R., and Wong, S. (2007). "Seismic behaviour of slender reinforced concrete shear walls under high axial load ratio." *Engineering Structures*, 29(8), 1957-1965.

Tagel-Din, H., and Meguro, K. (2000). "Applied element method for dynamic large deformation analysis of structures." *STRUCTURAL ENGINEERING EARTHQUAKE ENGINEERING*, 17(2), 215s-224s.

Tagel-Din, H., and Meguro, K. (2000). "Applied Element Method for simulation of nonlinear materials: theory and application for RC structures." *Structural Eng./Earthquake Eng., JSCE*, 17(2).

Tagel-Din, H., and Rahman, N. (2004). "Extreme loading: breaks through finite element barriers." *Struct Eng*, 5(6), 32-34.

Talaat, M., and Mosalam, K. M. (2009). "Modeling progressive collapse in reinforced concrete buildings using direct element removal." *Earthquake Engineering & Structural Dynamics*, 38(5), 609-634.

Tang, E. K., and Hao, H. (2010). "Numerical simulation of a cable-stayed bridge response to blast loads, Part I: Model development and response calculations." *Engineering Structures*, 32(10), 3180-3192.

Tasai, A. "Residual axial capacity and restorability of reinforced concrete columns damaged due to earthquake." *Proc., US-Japan Workshop on Performance-Based Earthquake Engineering Methodology for Reinforced Concrete Building Structures*, 191-202.

Thomson, P., Casas, J. M., Arbelaez, J. M., and Caicedo, J. "Real-time health monitoring of civil infrastructure systems in Colombia." *Proc., 6th Annual International Symposium on NDE for Health Monitoring and Diagnostics*, International Society for Optics and Photonics, 113-121.

Toussi S., and Yao I. T. P. (1983). "Hysteretic identification of exciting structures." *Journal of Engineering Mechanics, ASCE*, 109(5), 1189-1203.

Uenishi, K., Takahashi, H., Yamachi, H., and Sakurai, S. (2010). "PC-based simulations of blasting demolition of RC structures." *Construction and Building Materials*, 24(12), 2401-2410.

Wahab, M. A., and De Roeck, G. (1999). "Damage detection in bridges using modal curvatures: application to a real damage scenario." *Journal of Sound and Vibration*, 226(2), 217-235.

Wang, Y., Li, Z., Wang, C., and Wang, H. (2013). "Concurrent multi-scale modelling and updating of long-span bridges using a multi-objective optimisation technique." *Structure and Infrastructure Engineering*, 9(12), 1251-1266.

Watanabe, F., and Ichinose, T. "Strength and ductility design of RC members subjected to combined bending and shear." *Proc., Proceeding, Workshop Concrete Shear Earthquake, University of Houston, Houstin, Tex*, 429-438.

Wenzel, H. (2008). *Health monitoring of bridges*, John Wiley & Sons.

Wibowo, H., Reshotkina, S. S., and Lau, D. T. "Modelling progressive collapse of RC bridges during earthquakes." *Proc., CSCE Annual General Conference 2009*, 27-30.

Williams, M. S., and Sexsmith, R. G. (1995). "Seismic damage indices for concrete structures: a state-of-the-art review." *Earthquake spectra*, 11(2), 319-349.

Wong, K. Y. (2004). "Instrumentation and health monitoring of cable‐supported bridges." *Structural control and health monitoring*, 11(2), 91-124.

Wu, C. l., Kuo, W. W., Yang, Y. S., Hwang, S. J., Elwood, K. J., Loh, C. H., and Moehle, J. P. (2009). "Collapse of a nonductile concrete frame: Shaking table tests." *Earthquake Engineering & Structural Dynamics*, 38(2), 205-224.

Wu, Z., and Fujino, Y. (2005). "Structural health monitoring and intelligent infrastructure." *Smart Materials and Structures*, 14(3), null.

Xiang, H. "Health monitoring status of long-span bridges in China." *Proc., Proceedings of the workshop on research and monitoring of long span bridge*, 24-31.

Xiao, X., Xu, Y., and Zhu, Q. (2014). "Multiscale modeling and model updating of a cable-stayed bridge. II: Model updating using modal frequencies and influence lines." *Journal of Bridge Engineering*.

Xu Y. L. (2015). "SHMS-based prognosis and rating of long-span suspension bridges." *IStructE*Shang hai.

Xu, Y. L., and Xia, Y. (2011). *Structural health monitoring of long-span suspension bridges*, CRC Press.

Yavari, S., Elwood, K. J., and Wu, C. l. (2009). "Collapse of a nonductile concrete frame: Evaluation of analytical models." *Earthquake Engineering & Structural Dynamics*, 38(2), 225-241.

Yun, C.-B., Lee, J.-J., Kim, S.-K., and Kim, J.-W. (2003). "Recent R&D activities on structural health monitoring for civil infra-structures in Korea." *KSCE journal of civil engineering*, 7(6), 637-651.

Zhang, X. H. (2012). "Multi-sensing and multi-scale monitoring of long-span suspension bridges." Ph. D, The Hong Kong Polythenic University.

Zhu, L., Elwood, K., and Haukaas, T. (2007). "Classification and seismic safety evaluation of existing reinforced concrete columns." *Journal of Structural Engineering*, 133(9), 1316-1330.